Enhanced Noninvasive Imaging of Acoustic Biomolecules

Thesis by

Daniel Patrick Sawyer

In Partial Fulfillment of the Requirements for the Degree of

Doctor of Philosophy in Biological Engineering

CALIFORNIA INSTITUTE OF TECHNOLOGY

Pasadena, California

2021

Defended December 11, 2020

Daniel Patrick Sawyer
ORCID: 0000-0003-2926-191X

ACKNOWLEDGEMENTS

My doctoral education at Caltech has been everything I could have hoped for and more, and I owe it all to the people around me. Throughout my education, I have had the annoying tendency to change the discipline of my career ambitions every few years, and so I owe a debt of gratitude to the mentors who believed in my potential and provided a path forward despite my haphazard record. First, I want to thank my PhD advisor, Mikhail Shapiro. You supported and believed in me every step of the way, starting with my first conversation with you as a waitlisted electrical engineering applicant. You supported my subsequent interest in machine learning, allowing me to explore orthogonal opportunities by taking classes and doing an internship. You were always generous with your time, giving me regular guidance and feedback to help me learn and grow in my research and communication. You provided the most creative, collaborative, and friendly interdisciplinary lab culture I could have asked for. Thank you for helping me live my dream of pursuing groundbreaking research and exploring exciting ideas with the smartest and kindest people I know.

I also want to thank my undergraduate advisor at Simon's Rock, Ret. Col. Patty Dooley, for patiently teaching a naïve homeschooled student from Indiana the skills and discipline to succeed in the structured environment of higher education.

I would also like to thank my undergraduate advisor at Columbia, Ken Shepard, for welcoming an ex-pre-med transfer student from a liberal arts college into his electrical engineering lab to gain extensive research experience on projects that sounded like science fiction.

I would like to thank my committee members, Rob Phillips, Michael Roukes, and Lulu Qian for their guidance and enthusiastic interest throughout this project.

I am grateful for the happy and thoughtful mentorship that David Maresca provided in teaching me about ultrasound from the ground up and jump-starting my research by giving me a central a role on the project you had just started, which resulted in Chapter 1 of this thesis.

I cannot express enough gratitude for the friendships I have made at the Shapiro lab. Thank you, David Mittelstein and Di, for being my steadfast partners in crime, from fearless adventures in exciting classes that were over our heads, to whirlwind escapades all over Japan. Thank you, Arash and Anu, for being great officemates. I benefited from your advice and experience and already miss our conversations. Thank you, Avinoam, for being a fantastic friend as well as co-author.

Thank you, Bill and Lealia, for your friendship and support from the start of our Caltech PhD journeys together. I am also grateful to Audrey, Rob, Dan, Gabrielle, and all the other current and former Shapiro Lab members for making these last four years the happiest and most rewarding of my life.

I am honored to have received funding from the National Science Foundation Graduate Research Fellowship, which has bolstered my confidence and sense of independence in research and has opened doors to a number of opportunities.

I am also incredibly grateful for the people at the Caltech Y and IMPLiCIT, who provided opportunities to skillfully venture outside my comfort zone with outdoor adventures and improv comedy, and who provided a reliable source of happiness in times when good research results were few and far between.

I have profound loving gratitude for Betty Jin, whose quick wit, loving care, beautiful companionship, and uncanny intuition have both kept me motivated and moderated some of my less-wise ideas and tendencies.

Finally, I would like to thank my parents. I can never fully express my gratitude toward my mother, Nancy Sawyer, for having the courage to leave her job in elementary education and devote herself full-time to providing me and my siblings with the radically divergent education that she knew would best preserve our natural curiosity and love of learning. The same is true of my father, Patrick Sawyer, whom I still look to as a role model of diligence, honesty, playful curiosity, and healthy disregard for the status quo. Though I will never get to show you what I've accomplished, I could not have done it without you.

ABSTRACT

The extensive scientific interest in cellular and biomolecular processes is due in large part to the importance of such processes deep inside living organisms, in the context of both health and disease. However, most methods for imaging cellular processes such as gene expression have relied on fluorescent proteins and other optical reporters that, while providing a direct optical readout of the biomolecular environment in cells readily exposed to light, have greatly limited performance in large animals due to the poor penetration of visible light beyond 1 mm of biological tissue. In contrast, ultrasound is widely used to noninvasively image tissue deep inside living organisms but has rarely been used to investigate cellular function due a lack of acoustic reporters whose production and properties are coupled to biomolecular events. Recently, the first acoustic reporter genes (ARGs) were developed for ultrasound imaging of a unique class of air-filled protein nanostructures known as gas vesicles, or GVs, which scatter sound waves when expressed in bacterial and mammalian cells. ARGs allow gene expression to be visualized with ultrasound similar to how green fluorescent protein (GFP) allowed gene expression to be visualized with light. However, ARGs will have limited utility in practical applications involving living organisms without ultrasound imaging methods providing the specificity to reliably distinguish GVs from surrounding tissue and the sensitivity to detect GVs at low concentrations.

In this thesis, we present two novel ultrasound imaging methods that exploit the unique nonlinear physical properties of gas vesicles to enhance image quality in situations that pose challenges for conventional imaging methods. In Chapter 1, we provide a brief background and introduction to methods for enhancement of ultrasound imaging of biological structure and function through contrast agents. In Chapter 2, we address the problem of distinguishing GVs from tissue with cross-Amplitude Modulation (xAM), an ultrasound pulse sequence that uses X-waves to isolate the signal generated by reversible buckling of the GV shell while cancelling scattering and artifacts from tissue. In Chapter 3, we present an application of xAM to imaging of dynamic biomolecular processes. We show that, when GVs are engineered such that buckling is induced by enzyme activity, xAM can visualize enzymatic processes deep inside living animals. In Chapter 4, we address the problem of detecting very low concentrations of ARG-expressing cells with Burst Ultrasound Reconstructed with Signal Templates (BURST), an imaging method that exploits the strong, transient signals

generated during sudden GV collapse under acoustic pressure by unmixing the temporal dynamics of such signals from background scattering. BURST imaging improves cellular sensitivity by more than 1000-fold and, in dilute cell suspensions, enables the detection of gene expression in individual bacteria and mammalian cells. In Chapter 5, we present an application of an early formulation of BURST to imaging gene expression in mammalian cells. We use this imaging method to visualize vascularization patterns in tumors containing mammalian cells expressing acoustic reporter genes.

PUBLISHED CONTENT AND CONTRIBUTIONS

1.
Maresca, D., Sawyer, D. P., Renaud, G., Lee-Gosselin, A. & Shapiro, M. G. Nonlinear X-wave ultrasound imaging of acoustic biomolecules. *Phys. Rev. X* **8**, 041002 (2018). https://link.aps.org/doi/10.1103/PhysRevX.8.041002
D.M. and D.P.S. contributed equally to this work. D.M., D.P.S., and M.G.S. conceived and planned the project. D.M. and D.P.S. planned and conducted the experiments, designed and optimized the ultrasound pulse sequences, and analyzed the data. D.M., D.P.S., and M.G.S. wrote the manuscript with input from all authors.

2.
Lakshmanan, A., Jin, Z., Nety, S., Sawyer, D. P., Lee-Gosselin, A., Malounda, D., Swift, M., Maresca, D. & Shapiro, M. G. Acoustic biosensors for ultrasound imaging of enzyme activity. *Nature Chemical Biology* **16**, 988–996 (2020). https://doi.org/10.1038/s41589-020-0591-0
A.L., Z.J., S.P.N., D.P.S., A.L-G., M.B.S. and D. Mal. conducted the experiments. Z.J., D.P.S. and D. Mar. wrote the MATLAB scripts for ultrasound imaging and data processing.

3.
Sawyer, D. P., Bar-Zion, A., Farhadi, A., Lee-Gosselin, A., Shrivaei, S. & Shapiro, M. G. Ultrasensitive ultrasound imaging of gene expression with signal unmixing. Accepted for publication in *Nature Methods*.
D.P.S. and M.G.S. conceived and planned the project. D.P.S. planned and conducted the experiments, designed and optimized the ultrasound pulse sequences, and analyzed the data. D.P.S. and M.G.S. wrote the manuscript with input from all authors.

4.
Farhadi, A., Ho, G. H., Sawyer, D. P., Bourdeau, R. W. & Shapiro, M. G. Ultrasound imaging of gene expression in mammalian cells. *Science* **365**, 1469–1475 (2019). https://doi.org/10.1126/science.aax4804
A.F. and D.P.S. designed and optimized the ultrasound imaging sequences. D.P.S. assisted A.F. and M.G.S. with writing the manuscript.

TABLE OF CONTENTS

LIST OF ILLUSTRATIONS

LIST OF TABLES

Chapter 1

METHODS FOR CONTRAST-ENHANCED ULTRASOUND IMAGING OF BIOLOGICAL STRUCTURE AND FUNCTION

1.1 Introduction

In this chapter, I provide an overview of the field of contrast-enhanced ultrasound, emphasizing the pulse sequences and image processing algorithms that exploit the unique properties of ultrasound contrast agents. I first provide a brief background on the principles of ultrasound imaging, including the relevant physical properties of sound waves, common pulse sequences used to generate echoes from the sample, and the data processing pipeline by which the echoes are used to reconstruct an image. Next, I introduce microbubbles, the most widely-used synthetic ultrasound contrast agent. I then describe how novel pulse sequences and algorithms designed to exploit the unique physical properties of these contrast agents have enhanced the capabilities of contrast-enhanced ultrasound. Finally, I introduce gas vesicles as the first genetically encodable ultrasound contrast agents, compare their properties with those of synthetic ultrasound contrast agents, discuss existing methods for imaging them, and present some remaining challenges for ultrasound imaging with gas vesicles. Throughout, I compare the development of microbubbles and gas vesicles in ultrasound imaging to the development of synthetic dyes and fluorescent proteins used in optical imaging to place these technologies in the broader context of imaging of biomolecular and cellular function.

1.2 Principles of Biomedical Ultrasound Imaging

Ultrasound has been widely used as a portable and low-cost imaging technique in the medical field since the 1960s and is currently the most prescribed diagnostic modality[1]. However, while diagnostic medical ultrasound is generally considered a mature technology in some applications, recent advances in computational processing power and contrast agents have ushered in a large number of novel research directions[2]. Here, I provide a brief overview of acoustic waves in biological tissue and biomedical ultrasound imaging on programmable systems in sufficient detail to confer a conceptual understanding.

1.2.1 Properties of acoustic waves and propagation media

Ultrasound is a form of energy manifested as a compressive wave consisting of periodic regions of compression and rarefaction, or peaks of high and low pressure, in a medium such as air or water (of course, this is also a description of audible sound: ultrasound is distinguished by having a frequency above the upper audible range in humans of roughly 20 kHz). The basic principle that makes ultrasound imaging possible is the reflection or scattering of acoustic waves at boundaries of media with different material properties. Specifically, the density and compressibility of a medium determine its *acoustic impedance*[3], a property analogous to the index of refraction in optics. The greater the mismatch in acoustic impedance between two media, the greater the fraction of energy of an ultrasound wave that will be reflected when it encounters that boundary. The acoustic impedances of different types of soft biological tissue are relatively similar, resulting in a small fraction of an acoustic wave's energy being backscattered at each interface[4]. For example, at a boundary between muscle and fat tissue, on the order of 1% of the acoustic energy is backscattered. This allows ultrasound to remain coherent and pass through multiple layers of tissue while sending backscattered echoes back toward the ultrasound probe, providing the information necessary to reconstruct an image. When a boundary consists of a particle on the order of ten times smaller than the wavelength of ultrasound propagating through it (such as a fiber, cell, or organelle), an omnidirectional scattering event occurs instead of a directional reflection[5]. Most soft biological tissues include many such scatterers, creating a pattern known as *speckle* between tissue interfaces[4] whose intensity is mostly independent of the orientation of the transducer with respect to the tissue.

Finally, an important acoustic property is *nonlinearity*. In a perfectly linear medium with linear scatterers, an acoustic wave and its backscattered echoes will have the same frequency components as the transmitted wave. However, in nonlinear media and scatterers, for instance those whose speed of sound and attenuation change in response to the amplitude of an acoustic wave, the shape of the acoustic wave becomes distorted[6–8], creating new frequency components in the frequency spectrum of both the backscattered and propagating waves. As a rough rule of thumb, nonlinearity occurs when the properties of a medium or a scatterer change in response to the properties of an acoustic wave. In reality, all media, including water and biological tissue, have some degree of nonlinearity. However, the strongest commonly-encountered sources of nonlinearity are ultrasound contrast agents, discussed in the next section. While the effects of nonlinearity can be undesirable[9], we will see later how they represent some of the most interesting opportunities for improving ultrasound imaging with novel pulse sequences and algorithms.

1.2.2 Data processing pipeline

A typical programmable ultrasound system consists of a probe connected to a scanner system communicating with a host computer. The probe contains a linear array of piezoelectric transducer elements (often 128 or 256 of them) that can both transmit and receive analog ultrasound signals[10], which is sent to the scanner system

for low-level signal processing operations such as amplification, analog-to-digital conversion, and filtering. In most clinical equipment, the scanner system also performs the higher-level image reconstruction and processing operations using dedicated digital signal processing chips to minimize latency for real-time imaging. The conventional sequence for these operations includes beamforming, envelope detection, interpolation, and dynamic range compression (often by conversion to dB scale). Beamforming is the process by which the times of flight of the received echoes and the positions of the receiving probe elements are used to compute the origin in the imaging plane of every echo. In recent decades, popular platforms for preclinical ultrasound research began implementing these higher-level processing functions in software on the host computer[11], allowing users to access raw data and implement custom reconstruction algorithms. These systems, along with advances in computing power, have accelerated research on novel pulse sequences and image reconstruction algorithms[12] due to their programmability, versatility, and general lack of proprietary processing steps. The following discussion on pulse sequences assumes such a programmable ultrasound system connected to a linear array probe.

1.2.3 Pulse sequences

A *pulse sequence* is, at a basic level, a pattern of voltage values applied to each probe element as a function of time and element position. A pulse sequence usually consists of several *transmits*, each of which represents a pattern of *transmit waveforms* applied to one or more of the probe elements.

Each transmit waveform is a function of pressure over time that is typically parameterized by frequency, number of cycles, amplitude, and phase. Frequency is an important property of the acoustic wave itself that determines its wavelength ($\lambda = c/f$, where c is the speed of sound in the medium and f is the frequency of the ultrasound wave), which determines a lower limit for the resolution of conventional imaging and ranges from 500 μm in clinical imaging to 50 μm in microscanning of small animals[13]. Because attenuation increases with frequency as mentioned above, there is an inherent trade-off between resolution and penetration depth. If the transmit waveform contains more than one cycle, the axial (depth-wise) resolution will be reduced in proportion to the number of cycles, though signal-to-noise ratio of the imaging (SNR) increases with number of cycles. The amplitude of a transmit waveform, determined primarily by the voltage applied to the probe, also affects the SNR, as well as the strength of nonlinear distortion. Moreover, as described in the next section, even small differences in amplitude can result in qualitatively different acoustic phenomena when imaging with contrast agents. The phase of a transmit waveform does not typically affect the image on its own because phase information in the received echoes is usually lost during envelope detection, but it can be useful for techniques such as phase inversion[14] where RF echoes from transmits with opposite phases are combined to highlight nonlinear signal. Most commonly, a single set of waveform parameters is applied across all probe elements active during a transmit event.

During a transmit event, a set of delays is applied to all active probe elements as they transmit the specified waveform, after which the probe elements all wait to receive echoes generated in the region to be imaged before initiating any other transmit events in the pulse sequence. The (usually contiguous) set of active elements is called the *aperture* and the set of delays applied to these elements is called the *delay law*. Together, the aperture and delay law determine the shape of the ultrasound beam, which is formed by constructive interference of the quasi-spherical waves generated by each element after the programmed delay.

Most pulse sequences utilize some variation of one of two types of ultrasound beam: focused (or parabolic) beams, and plane waves. Conventional brightness-mode (B-mode) images rely on focused beams, which involve a parabolic delay law that ensures the acoustic waves transmitted by each active element arrive simultaneously at a target focal depth at the center of the aperture. For a given aperture size and waveform amplitude, focused beams maximize the peak acoustic pressure experienced at the target location. During a beamforming process known as *delay and sum*, delays are applied to echoes received by all the active elements to account for different travel times from the aperture bisector. The delayed echoes are then summed together to generate a 1-dimensional signal known as a *ray line*. In pulse sequences relying on focused beams, a 2-dimensional image is generated by successively shifting the aperture by a single element prior to each transmit until the maximum number of ray lines is acquired. For instance, a focused beam pulse sequence with a 64-element aperture implemented on a 128-element array will generate an image from $128 - 64 + 1 = 65$ ray lines. In this example, an image with up to the full 128 ray lines could be formed by continuing to transmit with progressively truncated apertures at the edges of the array, but this would result in lower, nonuniform contrast in the rightmost and leftmost 32 ray lines.

Plane waves, formed using a flat or linear delay law, allow images encompassing the probe's maximum lateral field of view to be reconstructed from the echoes of as few as one transmit, allowing for ultrafast imaging with frame rates improved by two orders of magnitude relative to focused beams (7,700 Hz compared to 59 Hz for a 10-cm-deep image with a 128-element probe)[15]. Plane wave image reconstruction is accomplished through a process called *synthetic aperture beamforming*, in which delay-and-sum beamforming is successively applied to the RF recordings of subsets of the probe elements in a convolution-like process. Consequently, the computational intensity of reconstruction in plane wave imaging increases in proportion to the higher frame rate, which made recent improvements in computer hardware crucial for the advance of ultrafast imaging. While images acquired with single plane waves have low contrast compared to those acquired with focused beams, images from a small number of plane waves tilted at different angles can be combined to improve contrast while maintaining ultrafast framerates[16]. Ultrafast plane wave imaging has been the basis for several recent advances in ultrasound, including functional doppler imaging of blood flow in the brain, in which shifts in the scattering signal from red blood cells between frames is used to estimate

the blood flow velocity in the brain vasculature over time with high SNR[17,18]. Ultrafast imaging has also enabled advances when combined with contrast agents, as described below.

1.3 Synthetic Contrast Agents

While the relative homogeneity of acoustic impedance across soft biological tissues provides conventional ultrasound with its signature advantage of large penetration depth, it also results in relatively low contrast. This causes an inability to distinguish tissue features with scattering properties similar to those of their surroundings, such as tumors, or those with small size and low scattering levels relative to their surroundings, such as small blood vessels[3].

In the field of microscopy, similar limitations, resulting from the small difference in optical properties between spatially co-localized tissues, cells, and organelles, were addressed with synthetic dyes that allowed distinct chemical and structural properties to be coupled to large changes in optical properties. For example, the Golgi stain allowed visualization of the axons and dendrites of individual neurons, which are small and whose weak levels of absorbance and scattering of visible light are similar to those of other neurons and glial cells. The stain accomplishes this by producing a large increase in absorbance confined to the cytoplasm of the target neuron[19].

In both ultrasound and microscopy, then, there is often an overlap between the imaging target's properties of interest and its hidden properties, namely those that are not detectable or distinguishable by the respective imaging modality. In this way, for a given biomedical imaging modality, we can view a good contrast agent as a substance or particle with one or more physical properties that are 1) detectable by the imaging modality, 2) distinguishable from the target's background signal, and 3) dependent on one or more of the imaging target's hidden properties of interest. In addition, the contrast agent should be robust in the sense that its presence should not change the target's properties of interest to an extent that is confounding of the results of experiments or, for *in vivo* imaging, harmful to the subject. Of course, the utility of a contrast agent depends on other factors such as cost and ease of use, but a simplified framework of detectability, distinguishability, dependence, and robustness is a helpful way to conceptualize the differences among contrast agents between and within imaging modalities.

1.3.1 Microbubbles

To address the limitations of ultrasound imaging mentioned above, researchers and clinicians have for several decades used synthetic microscale bubbles, typically stabilized lipid membranes, a type of ultrasound contrast

agent known as microbubbles[20–22]. The Golgi stain had a spatial distribution of absorbance that was detectable by visible light, distinguishable from neural tissue, and dependent on the structure of neurons. Similarly, microbubbles have a spatial distribution of scattering that is detectable by ultrasound, distinguishable from most types of soft tissue, and dependent on the structure of blood vessels in the vascular system. In addition, the safety and robustness of microbubbles in clinical imaging has been long-established[20,23].

The size and composition of microbubbles represent two characteristics that are virtually essential for any ultrasound contrast agent. Ultrasound contrast agents are designed to be no larger than red blood cells[3], allowing them to pass through the smallest capillaries and scatter omnidirectionally even for the higher range of frequencies used in ultrasound imaging. Second, ultrasound contrast agents are almost always gas-filled inclusions. Because gas is dramatically more compressible and less dense than biological tissue, an inclusion filled with gas maximizes the acoustic impedance mismatch and thus also the amount of scattering for a scatterer of a given radius.

1.3.2 Imaging methods for microbubbles

While microbubbles were initially developed to exploit the linear acoustic properties mentioned above for use with existing imaging methods[3], novel imaging methods continue to be developed that exploit these properties in new ways. The high linear scattering of microbubbles allows ultrafast plane wave imaging to maintain good contrast at high frame rates[24], and their small size results in signals with high spatiotemporal frequency that can be unmixed from tissue background signal[25]. Together, these properties have enabled super-resolution methods that track the motion of individual microbubbles to produce images of the brain or tumors at the organ scale with resolutions of less than 10 μm[16,26].

In addition to the linear acoustic properties, the size and composition of microbubbles also endows them with interesting nonlinear properties that became some of their most useful features as novel pulse sequences were developed to exploit them[14,27,28]. The sub-wavelength size of microbubbles allows them to be fully exposed to each cycle of compression and rarefaction in an acoustic wave, while their highly-compressible gaseous composition allows their size to fluctuate in response to these rapid pressure changes. These changes in the radius of the scatterers in response to incident acoustic waves generate nonlinearity in the form of harmonic frequencies[29].

Because biological tissue has weak nonlinearity, nonlinear contrast agents present an opportunity to improve imaging specificity by separating contrast agent signal from the tissue background. The method of *pulse inversion* does this by successively sending two transmits in which the phase of the waveforms are shifted by one half-cycle relative to each other[14]. The coherent sum of the echoes from these two pulses cancels the fundamental frequency component and preserves the second harmonic signal produced

by the contrast agent. Another method is *amplitude modulation*, in which echoes from two low-pressure transmits are coherently subtracted from the echoes of a high-pressure transmit whose beam is the sum of the first two[30,31]. This cancels the linear signals and preserves nonlinear signal present in both the fundamental and second harmonic frequencies.

1.3.3 Current limitations of microbubbles

Despite their many capabilities and remaining opportunities for improvement, there are a number of limitations intrinsic to all forms of synthetic microbubbles. The imaging methods for microbubbles we have discussed have all functioned to expand their detectability and distinguishability across spatial and temporal dimensions and across imaging contexts. However, none of these have expanded the dependence of microbubbles to biological phenomena other than blood flow and vascular structure.

While microbubbles have been functionalized to bind to specific molecular targets in the blood stream[20,22,27], their microscale size and limited stability after injection create significant challenges for their use in molecular imaging of targets outside the bloodstream and of dynamic cellular processes. Enabling robust noninvasive imaging of biological processes at the cellular and biomolecular levels will require an ultrasound contrast agent whose physical properties are intrinsically dependent on such processes.

1.4 Genetically Encodable Contrast Agents

To provide context and tentative outlook for biomolecular ultrasound imaging, we return to our analogy with optical microscopy. In 1994, the gene encoding green fluorescent protein (GFP) was expressed in *E. coli* and *C. elegans* and shown to generate fluorescence in these non-native organism for the first time[32,33], allowing a plethora of questions in the burgeoning field of molecular biology to be answered with the well-established tools of optical microscopy. As a fluorescent protein whose gene could be readily expressed in non-native prokaryotic and eukaryotic cells, GFP created a robust dependence between detectable and distinguishable optical signal and the processes that define the central dogma of molecular biology. Moreover, because GFP is built with the same well-characterized molecular machinery and building blocks common to all forms of life, the goals of creating dependence between optical signals and other biomolecular processes, such as Ca^{2+} signaling[34], without exogenous agents were transformed from open scientific problems to engineering challenges. While GFP and an increasing number of engineered variants demonstrated the exciting potential of this class of tools with conventional microscopy techniques, innovations in optical imaging such as PALM[35], STORM[36], light-sheet microscopy[37], and multiphoton microscopy[38] were developed to exploit the

unique physical properties of these proteins. This resulted in the ever-increasing resolution, scope, information content, and robustness of fluorescent protein imaging technologies that made them the mainstays of scientific and industrial biotechnology they are today.

However, as fluorescent protein imaging has matured, so has recognition of its limitations. Because the physical nature of visible light limits ballistic penetration past approximately 1 mm of biological tissue[39], it appears clear that biomolecular and cellular processes occurring deep inside the body are unlikely ever to be noninvasively imaged *in situ* using optical methods. This is an important problem because most of the cellular and biomolecular processes investigable by optical methods are interesting because of their roles deep inside the bodies of living animals.

1.4.1 Gas vesicles and acoustic reporter genes

In 2014, gas vesicles, a unique class of gas-filled protein nanostructures that scatter acoustic waves, were presented as the first biomolecular ultrasound contrast agents[40]. The native function of gas vesicles is to regulate buoyancy in photosynthetic microbes for optimal access to light[41,42]. In a process that remains to be fully understood, chaperones and other assembly factor proteins nucleate and assemble the hollow gas vesicle shell out of repeating subunits of a protein called GvpA, an amphiphilic protein whose hydrophobic residues face the inside of the shell and prevent the condensation of water while leaving the shell selectively permeable to gas. A second protein, GvpC, acts as an outer scaffold that increases the structural integrity of the shell. This structure allows water vapor and gas dissolved in the surrounding media to equilibrate with the gas in the gas vesicle on a microsecond timescale, leaving no pressure differential across the shell at equilibrium and providing long-term stability in contrast to microbubbles, which typically dissolve in under 6 minutes[20]. In recent years, the gene cluster encoding gas vesicles and the auxiliary proteins has been engineered to develop the first acoustic reporter genes for imaging gene expression of gut bacteria in mammalian hosts[43]. In this way, gas vesicles have shown the potential to do for ultrasound what GFP and its derivatives have done for optical imaging.

1.4.2 Imaging methods for gas vesicles

As sub-wavelength, gas-filled inclusions, gas vesicles share many of the advantageous linear acoustic properties of microbubbles. As with microbubbles, the size and composition of gas vesicles also create interesting nonlinear properties. However, the encasement in a gas-permeable protein shell and the consequent lack of surface tension give gas vesicles unique nonlinear properties distinct from those of microbubbles. The most important of these from the perspective of contrast-enhanced imaging are *collapse* and *buckling*, both of

which are genetically determined and can be modulated by the biomolecular environment[40,44–47]. Irreversible collapse of the gas vesicle shell occurs when it is exposed to positive acoustic pressures above a genetically determined threshold, liberating the gas inside as nanobubbles[48] and erasing any ultrasound contrast. Reversible buckling of the gas vesicle shell occurs at acoustic pressures above a genetically determined buckling threshold (but below the collapse threshold) at ultrasound frequencies above 1 MHz[47], where the time between ultrasound cycles is short enough that the internal pressure of the gas vesicle is maintained despite the free gas exchange across the shell, which occurs on the order of 10^{-5} seconds[41].

Unlike the nonlinear behavior of microbubbles, which occurs even at low acoustic pressures[7], the nonlinear phenomena of buckling and collapse in gas vesicles occur at sharply-defined acoustic pressure thresholds due to the rigid structure of the gas vesicle shell. For gas vesicle collapse, this property allows for multiplexed imaging of gas vesicle variants with different collapse profiles[44]. This method works by applying successively higher acoustic pressures to collapse one gas vesicle variant population at a time, followed by linear unmixing to isolate the total signal due to each variant for every image pixel. For gas vesicle buckling, the sharp threshold property allows signal from different engineered gas vesicle variants to be distinguished on the basis of nonlinear harmonic generation[44,47], including with the use of the amplitude modulation method discussed above in the context of microbubbles.

1.4.3 Limitations of gas vesicle imaging methods

Despite the demonstrated potential of gas vesicles and acoustic reporter genes, a number of challenges remain that limit their practical utility. First, while amplitude modulation imaging of harmonic gas vesicles improves contrast relative to tissue, use of this technique to image targets *in vivo* showed the presence of strong nonlinear propagation artifacts in tissue downstream of gas vesicle inclusions[47]. Because the spatial distribution of gas vesicles will not be known *a priori*, such artifacts compromise the specificity of this technique. Second, while B-mode ultrasound imaging was shown to detect engineered bacteria expressing gas vesicles inside the mouse colon at 10^9 cells/ml, endogenous targets of interest such as immune cells and certain gut microbes are present at concentrations orders of magnitude smaller[49,50].

As was the case with GFP and optical imaging methods, the full realization of the potential of acoustic reporter genes requires ultrasound imaging methods that exploit the unique physical properties of gas vesicles to address these outstanding limitations and augment advances in the engineering of these acoustic proteins. In this thesis, I present the development and application of two such methods.

References

1. Liang, H.-D., Noble, J. A. & Wells, P. N. T. Recent advances in biomedical ultrasonic imaging techniques. *Interface Focus* **1**, 475–476 (2011).
2. Seo, J. & Kim, Y. *Ultrasound imaging and beyond: recent advances in medical ultrasound*. (Springer, 2017).
3. Szabo, T. L. *Diagnostic ultrasound imaging: inside out*. (Academic Press, 2004).
4. Azhari, H. *Basics of Biomedical Ultrasound for Engineers*. (John Wiley & Sons, 2010).
5. Cobbold, R. S. C. *Foundations of Biomedical Ultrasound*. (Oxford University Press, 2006).
6. Wu, J. & Tong, J. Measurements of the nonlinearity parameter BA of contrast agents. *Ultrasound in medicine & biology* **24**, 153–159 (1998).
7. Emmer, M. *et al.* Pressure-dependent attenuation and scattering of phospholipid-coated microbubbles at low acoustic pressures. *Ultrasound in medicine & biology* **35**, 102–111 (2009).
8. Tang, M.-X. & Eckersley, R. J. Frequency and pressure dependent attenuation and scattering by microbubbles. *Ultrasound in medicine & biology* **33**, 164–168 (2007).
9. ten Kate, G. L. *et al.* Far-Wall Pseudoenhancement During Contrast-Enhanced Ultrasound of the Carotid Arteries: Clinical Description and In Vitro Reproduction. *Ultrasound in Medicine & Biology* **38**, 593–600 (2012).
10. Powers, J. & Kremkau, F. Medical ultrasound systems. *Interface Focus* **1**, 477–489 (2011).
11. Daigle, R. E. Ultrasound imaging system with pixel oriented processing. (2012).
12. Boni, E. *et al.* A reconfigurable and programmable FPGA-based system for nonstandard ultrasound methods. *IEEE Transactions on Ultrasonics, Ferroelectrics, and Frequency Control* **59**, 1378–1385 (2012).
13. Foster, F. S., Pavlin, C. J., Harasiewicz, K. A., Christopher, D. A. & Turnbull, D. H. Advances in ultrasound biomicroscopy. *Ultrasound in Medicine & Biology* **26**, 1–27 (2000).

14. Simpson, D. H., Chien Ting Chin & Burns, P. N. Pulse inversion Doppler: a new method for detecting nonlinear echoes from microbubble contrast agents. *IEEE Transactions on Ultrasonics, Ferroelectrics, and Frequency Control* **46**, 372–382 (1999).
15. Tanter, M. & Fink, M. Ultrafast imaging in biomedical ultrasound. *IEEE Transactions on Ultrasonics, Ferroelectrics, and Frequency Control* **61**, 102–119 (2014).
16. Errico, C. *et al.* Ultrafast ultrasound localization microscopy for deep super-resolution vascular imaging. *Nature* **527**, 499–502 (2015).
17. Macé, E. *et al.* Functional ultrasound imaging of the brain. *Nature Methods* **8**, 662–664 (2011).
18. Mace, E. *et al.* Functional ultrasound imaging of the brain: theory and basic principles. *IEEE Transactions on Ultrasonics, Ferroelectrics, and Frequency Control* **60**, 492–506 (2013).
19. Finger, S. *Origins of Neuroscience: A History of Explorations Into Brain Function*. (Oxford University Press, 2001).
20. Unnikrishnan, S. & Klibanov, A. L. Microbubbles as Ultrasound Contrast Agents for Molecular Imaging: Preparation and Application. *American Journal of Roentgenology* **199**, 292–299 (2012).
21. Paefgen, V., Doleschel, D. & Kiessling, F. Evolution of contrast agents for ultrasound imaging and ultrasound-mediated drug delivery. *Front. Pharmacol.* **6**, (2015).
22. Ferrara, K., Pollard, R. & Borden, M. Ultrasound Microbubble Contrast Agents: Fundamentals and Application to Gene and Drug Delivery. *Annual Review of Biomedical Engineering* **9**, 415–447 (2007).
23. Feinstein Steven B. *et al.* Safety and efficacy of a new transpulmonary ultrasound contrast agent: Initial multicenter clinical results. *Journal of the American College of Cardiology* **16**, 316–324 (1990).
24. Couture, O. *et al.* Ultrafast Imaging of Ultrasound Contrast Agents. *Ultrasound in Medicine & Biology* **35**, 1908–1916 (2009).
25. Demené, C. *et al.* Spatiotemporal Clutter Filtering of Ultrafast Ultrasound Data Highly Increases Doppler and fUltrasound Sensitivity. *IEEE Transactions on Medical Imaging* **34**, 2271–2285 (2015).

26. Lin, F. *et al.* 3-D Ultrasound Localization Microscopy for Identifying Microvascular Morphology Features of Tumor Angiogenesis at a Resolution Beyond the Diffraction Limit of Conventional Ultrasound. *Theranostics* **7**, 196–204 (2017).
27. Dayton, P. A. & Rychak, J. J. Molecular ultrasound imaging using microbubble contrast agents. *Front Biosci* **12**, 5124–5142 (2007).
28. Errico, C. *et al.* Transcranial functional ultrasound imaging of the brain using microbubble-enhanced ultrasensitive Doppler. *NeuroImage* **124**, 752–761 (2016).
29. Hoff, L. *Acoustic characterization of contrast agents for medical ultrasound imaging*. (Springer Science & Business Media, 2001).
30. Mor-Avi Victor *et al.* Combined Assessment of Myocardial Perfusion and Regional Left Ventricular Function by Analysis of Contrast-Enhanced Power Modulation Images. *Circulation* **104**, 352–357 (2001).
31. Brock-Fisher, G. A., Poland, M. D. & Rafter, P. G. Means for increasing sensitivity in non-linear ultrasound imaging systems. (1996).
32. Chalfie, M., Tu, Y., Euskirchen, G., Ward, W. W. & Prasher, D. C. Green fluorescent protein as a marker for gene expression. *Science* **263**, 802–805 (1994).
33. Inouye, S. & Tsuji, F. I. Aequorea green fluorescent protein. *FEBS Letters* **341**, 277–280 (1994).
34. Tian, L. *et al.* Imaging neural activity in worms, flies and mice with improved GCaMP calcium indicators. *Nat Methods* **6**, 875–881 (2009).
35. Betzig, E. *et al.* Imaging Intracellular Fluorescent Proteins at Nanometer Resolution. *Science* **313**, 1642–1645 (2006).
36. Rust, M. J., Bates, M. & Zhuang, X. Sub-diffraction-limit imaging by stochastic optical reconstruction microscopy (STORM). *Nat Methods* **3**, 793–796 (2006).
37. Keller, P. J., Schmidt, A. D., Wittbrodt, J. & Stelzer, E. H. K. Reconstruction of Zebrafish Early Embryonic Development by Scanned Light Sheet Microscopy. *Science* **322**, 1065–1069 (2008).

38. Zipfel, W. R., Williams, R. M. & Webb, W. W. Nonlinear magic: multiphoton microscopy in the biosciences. *Nature Biotechnology* **21**, 1369–1377 (2003).

39. Ntziachristos, V. Going deeper than microscopy: the optical imaging frontier in biology. *Nature Methods* **7**, 603–614 (2010).

40. Shapiro, M. G. *et al.* Biogenic gas nanostructures as ultrasonic molecular reporters. *Nature Nanotechnology* **9**, 311–316 (2014).

41. Walsby, A. E. Gas vesicles. *Microbiology and Molecular Biology Reviews* **58**, 94–144 (1994).

42. Pfeifer, F. Distribution, formation and regulation of gas vesicles. *Nature Reviews Microbiology* **10**, 705–715 (2012).

43. Bourdeau, R. W. *et al.* Acoustic reporter genes for noninvasive imaging of microorganisms in mammalian hosts. *Nature* **553**, 86–90 (2018).

44. Lakshmanan, A. *et al.* Molecular Engineering of Acoustic Protein Nanostructures. *ACS Nano* **10**, 7314–7322 (2016).

45. Zhang, S. *et al.* The Vibration Behavior of Sub-Micrometer Gas Vesicles in Response to Acoustic Excitation Determined via Laser Doppler Vibrometry. *Advanced Functional Materials* **30**, 2000239 (2020).

46. Lakshmanan, A. *et al.* Preparation of biogenic gas vesicle nanostructures for use as contrast agents for ultrasound and MRI. *Nature Protocols* **12**, 2050–2080 (2017).

47. Maresca, D. *et al.* Nonlinear ultrasound imaging of nanoscale acoustic biomolecules. *Appl. Phys. Lett.* **110**, 073704 (2017).

48. Bar-Zion, A. *et al.* Acoustically Detonated Biomolecules for Genetically Encodable Inertial Cavitation. *bioRxiv* 620567 (2019).

49. Guarner, F. & Malagelada, J.-R. Gut flora in health and disease. *The Lancet* **361**, 512–519 (2003).

50. Simon, G. L. & Gorbach, S. L. Intestinal flora in health and disease. *Gastroenterology* **86**, 174–193 (1984).

Chapter 2

NONLINEAR X-WAVE ULTRASOUND IMAGING OF ACOUSTIC BIOMOLECULES

This chapter is in large part a reformatted version of the manuscript entitled "Nonlinear X-Wave Ultrasound Imaging of Acoustic Biomolecules" published by Maresca, D., Sawyer, D. P., Renaud, G., Lee-Gosselin, A. & Shapiro, M. G. in *Physical Review X*. Under the supervision of Mikhail Shapiro, my contributions to this work were to conceive, design, and conduct the experiments, design and optimize the ultrasound pulse sequence and reconstruction algorithm, analyzed the data, and write the manuscript alongside David Maresca. Thanks to Guillaume Renaud for performing the ultrasound simulations and to Audrey Lee-Gosselin for assistance with the animal experiments.

2.1 Abstract

The basic physics of sound waves enables ultrasound to visualize biological tissues with high spatial and temporal resolution. Recently, this capability was enhanced with the development of acoustic biomolecules – proteins with physical properties enabling them to scatter sound. The expression of these unique air-filled proteins, known as gas vesicles (GVs), in cells allows ultrasound to image cellular functions such as gene expression *in vivo*, providing ultrasound with its analog of optical fluorescent proteins. Acoustical methods for the *in vivo* detection of GVs are now required to maximize the impact of this technology in biology and medicine. We previously engineered GVs exhibiting a nonlinear scattering behavior in response to acoustic pressures above 300 kPa, and showed that amplitude-modulated (AM) ultrasound pulse sequences that both excite the linear and nonlinear GV scattering regimes were highly effective at distinguishing GVs from linear scatterers like soft biological tissues. Unfortunately, the *in vivo* specificity of AM ultrasound imaging is systematically compromised by the nonlinearity added by the GVs to propagating waves, resulting in strong image artifacts from linear scatterers downstream of GV inclusions. To address this issue, we present an imaging paradigm, cross-amplitude modulation (xAM), which relies on cross-propagating plane-wave transmissions of finite aperture X-waves to achieve quasi artifact-free *in vivo* imaging of GVs. The xAM method derives from counter-propagating wave interaction theory which predicts that, in media exhibiting quadratic elastic nonlinearity like biological tissue, the nonlinear interaction of counter-propagating acoustic waves is inefficient. By transmitting cross-propagating plane-waves, we minimize cumulative nonlinear interaction effects due to collinear wave propagation, while generating a transient wave-amplitude modulation

at the two plane-waves' intersection. We show in both simulations and experiments that residual xAM nonlinearity due to wave propagation decreases as the plane-wave cross-propagation angle increases. We demonstrate in tissue-mimicking phantoms that imaging artifacts distal to GV inclusions decrease as the plane-wave cross-propagation angle opens, nearing complete extinction at angles above 16.5 degrees. Finally, we demonstrate that xAM enables highly specific *in vivo* imaging of GVs located in the gastrointestinal tract, a target of prime interest for future cellular imaging. These results advance the physical facet of the emerging field of biomolecular ultrasound, and are also relevant to synthetic ultrasound contrast agents.

2.2 Introduction

Green fluorescent protein (GFP) and its analogs serve as irreplaceable tools allowing biologists to visualize gene expression and other cellular processes using optical microscopes[1]. However, the microstructure of biological tissues restricts a photon's transport mean free path to about 1 mm[2], limiting *in vivo* optical imaging applications. In contrast, the physics of ultrasonic waves allow them to propagate centimeters deep into biological tissues without losing their coherence, and enable tissue scanning at the organ scale. Very recently, the first acoustic biomolecules for ultrasound, analogous to GFP for optics, were developed[3] based on a unique class of air-filled protein nanostructures called gas vesicles, or GVs[4], making it possible to use ultrasound to visualize the function of cells deep inside tissues.

To maximize the impact of acoustic biomolecules in biology and medicine, physical methods are needed to discriminate GV scattering from tissue scattering, analogous to previous developments in the imaging of synthetic microbubble contrast agents[5–11]. GVs are air-filled nanocompartments with dimensions on the order of 200 nm, enclosed by a rigid 2 nm-thick protein shell[12,13]. In 2014, it was reported that GVs could be imaged with ultrasound[4], and it was recently shown that gene clusters encoding GVs could be expressed heterologously in engineered cells and serve as acoustic reporter genes[3]. While most natural GVs behave as linear ultrasound scatters, Lakshmanan et al.[14] engineered harmonic GV variants (hGVs) that buckle and scatter higher harmonics at acoustic pressures above 320 kPa, corresponding to a mechanical index of 0.08, well below the FDA safety requirement of 1.9[15]. Amplitude modulation (AM) ultrasound pulse sequences emerged as logical candidates to exploit dissimilar hGV responses below and above buckling and enabled nonlinear imaging of hGVs *in vitro*, *in ovo*, and *in vivo*[15]. In AM, backscattered echoes of two half-amplitude transmissions are digitally subtracted from echoes of a third, full-amplitude transmission. The full-amplitude transmission creates pressures above the hGV buckling threshold, triggering hGV harmonic scattering, while the half-amplitude transmissions create pressures below hGV buckling and trigger hGV linear scattering. This scattering response difference in hGV echoes persists after the subtraction, while linear echoes from surrounding tissue scale in amplitude and are cancelled. However, we observed that the *in vivo* specificity of

AM imaging of hGVs was systematically compromised by nonlinear wave propagation artifacts that lead to the misclassification of biological tissue as hGVs[15].

In a highly nonlinear medium such as buckling hGVs or resonant microbubbles (nonlinearity parameter B/A two orders of magnitude higher than tissue)[16], ultrasonic waves experience amplitude-dependent attenuation and amplitude-dependent speed of sound[17,18]. In consequence, the high amplitude pulse of the AM sequence gets distorted in proportions that to not scale linearly with the low amplitude pulse of the sequence. Ultrasonic waves carry that distortion as they travel forward in the medium. We hypothesized that this phenomenon, reported in microbubble inclusions[19], is also the cause of nonlinear artifacts distal to GV inclusions.

It is established that in a medium exhibiting quadratic elastic nonlinearity, the interaction of two ultrasonic waves propagating in the same direction exhibits a cumulative nonlinear interaction[20]. With a conventional AM pulse sequence, images are reconstructed line-by-line along the wave propagation direction. The high amplitude pulse of the sequence can be seen as the sum of two pulses of half amplitude that co-propagate and are subject to cumulative nonlinear interaction effects. It is less well known that the nonlinear interaction of ultrasonic waves propagating in opposite directions is inefficient[21]. In a pioneering proof-of-concept, Renaud et al.[22] showed that a pair of subwavelength elements of an ultrasound transducer array could be used to transmit circular wave pulses that are quasi counter-propagative in the near field of the array, allowing them to minimize nonlinear distortion, while generating a 2-fold higher amplitude at the moment of their intersection. Here we show that propagation nonlinearity (Fig. 2.1a) can be efficiently minimized with a non-collinear plane-wave transmission paradigm, which we call cross amplitude modulation, or xAM, while allowing depth-invariant, nonlinear imaging of acoustic biomolecules (Fig. 2.1b). We demonstrate in simulations and experiments that plane-wave cross-propagation prevents cumulative distortion of the AM wave code, suppresses nonlinear propagation artifacts distal to highly nonlinear hGV inclusions, and enables highly specific *in vivo* nonlinear ultrasound imaging of hGVs in mice.

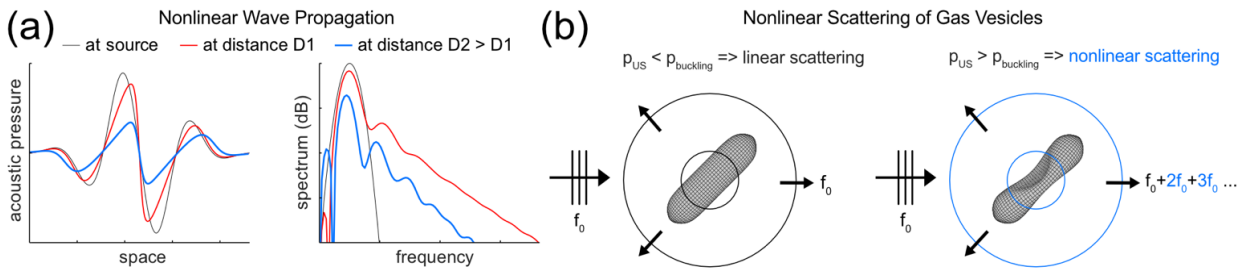

Figure 2.1 | Nonlinear acoustic phenomena. Sketch of the two nonlinear phenomena that take place while imaging a biological medium containing acoustic biomolecules. (a) Propagation history of a single plane wave: nonlinear frequency components accumulate with depth as the wave propagates through tissue before being attenuated. This phenomenon, amplified during the near-collinear interaction of two wavefronts, leads to nonlinear propagation artifacts distal to GV

inclusions. (b) Nonlinear scattering behavior of GVs insonified above their buckling pressure, enabling their detection with an amplitude modulation (AM) code.

2.3 Nonlinear Interaction of Cross-Propagating Plane Waves

2.3.1 The cross amplitude modulation sequence (xAM)

Cross amplitude modulation is a biomolecular ultrasound imaging paradigm that aims at minimizing wave propagation-related harmonics[23] using propagation symmetry considerations, while capturing local acoustic biomolecules' harmonics to ensure their specific *in vivo* detection. Considering an N-element aperture of a linear array of ultrasonic transducers, the xAM sequence consists in (1) using the elements 1 to N/2 to transmit a tilted plane-wave at an angle θ with respect to the array (Fig. 2.2a), (2) using the elements N/2+1 to N to transmit a symmetric plane-wave at an angle θ with the array (Fig. 2.2b), and (3) transmitting the previous two plane-waves simultaneously (Fig. 2.2 c). The two cross-propagating waves depicted in Fig. 2.2c interact along the virtual bisector that separates the two half-apertures. Particles of the insonified medium that are located along the bisector experience the same wave amplitude for steps (1) and (2), and a doubled wave-amplitude for step (3) as seen in Fig. 2.1d. This axisymmetric pulse sequence creates an AM code along the bisector that separates the two N/2 sub-apertures.

Our working hypothesis was that cumulative nonlinear plane-wave interaction arsing during wave propagation decreases as the cross-propagation angle θ increases. We therefore started by determining whether minimal AM code distortion could be achieved with xAM in a weakly nonlinear homogeneous/isotropic medium. To do so, we first evaluated xAM signal cancellation during plane-wave propagation in water using two-dimensional time-domain numerical simulations (see Methods)[24]. Keeping the experimental realization of the xAM sequence in mind, we assessed the directivity of individual elements of our transducer array[25] and set the maximal angle θ to 21° based on the array -3 dB directivity bandwidth (see Methods, Fig. 2.7). The simulation result displayed in Fig. 2.2d shows that, for a xAM sequence of angle θ = 18° at a depth of 3.6 mm, the residual peak wave amplitude is reduced by four orders of magnitude to 0.02% of the cross-propagating plane-waves peak amplitude (0.13 kPa compared to 747 kPa, respectively). As a comparison, a high-end commercial scanner provides an AM residual of the order of 0.5%.

Cross-propagating plane-waves, or X-waves, intersect with each other along a finite geometric distance which defines the depth of field Z_X of the xAM sequence,

$$Z_X = \frac{A}{2}\cot\theta, \quad (1)$$

where A is the full aperture used for the X-wave transmission. For an angle θ = 18° and an aperture A = 6.5 mm, Z_X equals 10 mm, which would for example enable scanning of a full mouse brain. Note that beyond Z_X, images could be reconstructed further down thanks to the diffraction of the wavefronts edges using spherical delay laws analogous to Renaud et al. [22].

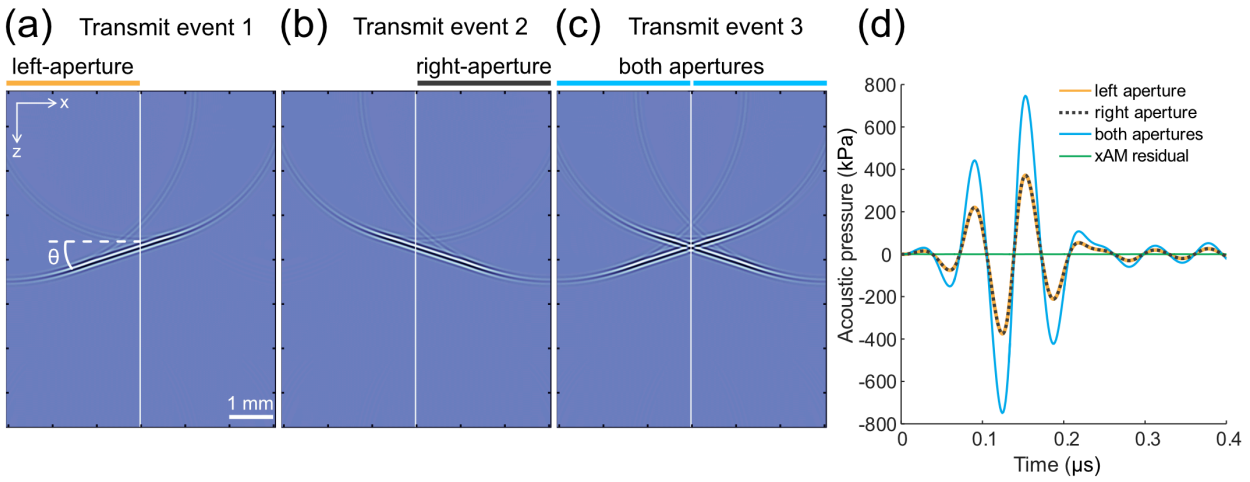

Figure 2.2 | xAM simulation. Simulation of the xAM sequence for θ = 18° in a homogeneous/isotropic water medium. (a) Half-aperture plane-wave transmission at an 18° angle with respect to the transducer array. (b) Axisymmetric half-aperture plane-wave transmission at an 18° angle with the other half of the array. (c) Cross-propagating plane-waves transmission at an 18° angle using both half-apertures. (d) Simulated waveforms at the bisector intersection for z = 3.6 mm. The cross-propagating plane-waves peak positive pressure was 747 kPa (blue curve), while the residue peak positive pressure (green curve) was 0.13 kPa, or 0.02% of the cross-propagating plane-waves peak positive pressure.

We further assessed the significance of nonlinear effects accumulating during plane-wave propagation as a function of θ (Figs. 3a- 3b). At low θ angles, which correspond to quasi co-propagation, residual AM nonlinearity clearly accumulated with depth (see Fig. 2.3a, θ = 0° and 5°). In particular, for plane-waves propagating in water with a peak amplitude of 400 kPa and at an angle θ = 0° (collinear propagation case), the residual AM peak amplitude reached 13.5 kPa at a distance z = 8 mm (Fig. 2.3a). As θ increased, the residual AM nonlinearity was significantly reduced, reaching a non-cumulative 0.3 kPa peak pressure at an angle θ = 20° (Fig. 2.3a). Fig. 2.3b reports the peak amplitude of the AM residue as a function of θ at the distances z = 4 mm and z = 6 mm from the array. Data reported in Figs 2.3a and 2.3b were obtained using a constant transmit peak pressure at 4 mm equal to 400 kPa. The simulations show that the amplitude of the xAM residue drops rapidly as θ increases, and converges below a threshold of 0.2 kPa for θ > 15°. These results support our hypothesis that nonlinear plane-wave interaction becomes less efficient as θ increases, and predict that in a weakly nonlinear homogeneous/isotropic medium as water (attenuation equal to 0.002 dB/MHz^2 cm), one can expect an AM code showing minimal wave distortion due to propagation at cross-propagation angles above 15°.

While a complete analytical treatment of this phenomenon has not been developed, some intuition can be obtained from the work of Hamilton et al.[26,27], who reported that the noncollinear nonlinear interaction of two plane wave fields results in an asynchronous interaction that generates a sum frequency wave whose amplitude oscillates with a spatial period of $2\pi/2k(1-\cos\theta)$, k being the wave vector of the plane waves. As the angle between the two waves increases, the phase mismatch increases, the spatial period of the nonlinear pressure field decreases, and the nonlinear interaction becomes less efficient. The same phenomenon is observed in our simulations: as the angle increases, the spatial period of oscillation and the amplitude of the nonlinear pressure field decrease (see Fig 2.3a, 10, 15 and 20 degree lines). The nonlinear pressure field is also expected to increase or decrease with the nonlinearity of the medium, as characterized by its shock length. With these considerations supporting the plausibility of our simulation results, we proceeded to implement the xAM concept experimentally. A full analytical treatment of this problem will be described in future work.

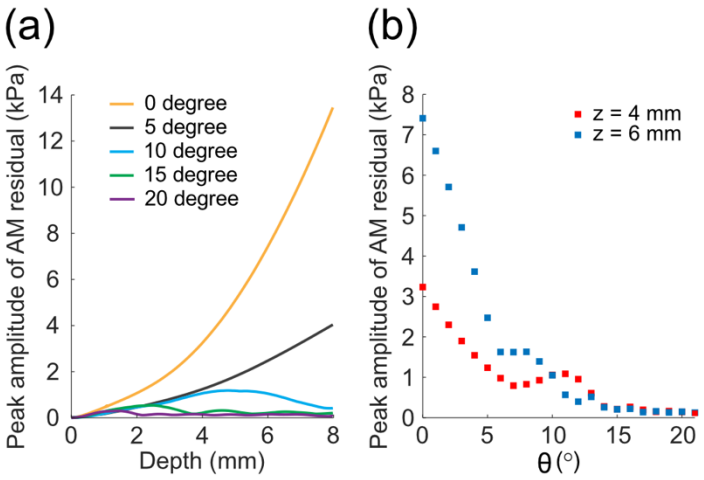

Figure 2.3 | Simulation of nonlinearity vs. angle. Simulation of nonlinear plane-wave interaction as a function of the cross-propagation angle θ. (a) Peak positive pressure of the xAM residual as a function of depth for five cross-propagation angles. (b) Peak positive pressure of the xAM residual as a function of θ at depths z equals 4 mm and 6 mm.

2.3.2 Experimental reduction of residual xAM nonlinearity as a function of θ

To assess experimentally the ability of higher-θ xAM pulses to minimize nonlinearity, we implemented the xAM imaging sequence and beamforming on a programmable ultrasound system with a 128-element linear array (see Methods) and measured the peak residual AM signal of a subwavelength linear scatterer immersed in water. This configuration enabled the assessment of the nonlinearity captured by the AM sequence that is solely due to wave propagation in a typical quasi-incompressible medium (water serves as a first-approximation model for sound wave propagation in soft biological tissues). A 10 µm diameter nickel wire was placed perpendicular to the imaging plane in phosphate buffer saline (PBS) at a depth of 4 mm. The wire

was imaged using xAM at θ values ranging from 1.5° to 21° (Fig. 2.4a). We measured the AM residual for each angle as the peak value of the beamformed radio-frequency (RF) data. The data show the same trend predicted by the simulations, with residual nonlinearity decreasing sharply with wider angles (Fig. 2.4b). To compare these results with a conventional AM imaging sequence, we implemented a standard parabolic amplitude modulation (pAM) code, in which half-amplitude transmissions were achieved by silencing the even or odd transmitting elements of the array and imaging lines were reconstructed along the wave propagation direction[15]. As of θ = 3°, xAM significantly outperformed pAM in reducing the residual AM signal (Fig. 2.4b). We measured the axial and lateral resolution of xAM using the full-width half-maximum (FWHM) of the point-spread function (PSF) along the respective directions. The mean axial resolution was 117 μm ± 16 μm, and the mean lateral resolution is 381 μm ± 42 μm, with values remaining constant across angles. The axial resolution of pAM was 103 μm and the lateral resolution was 250 μm.

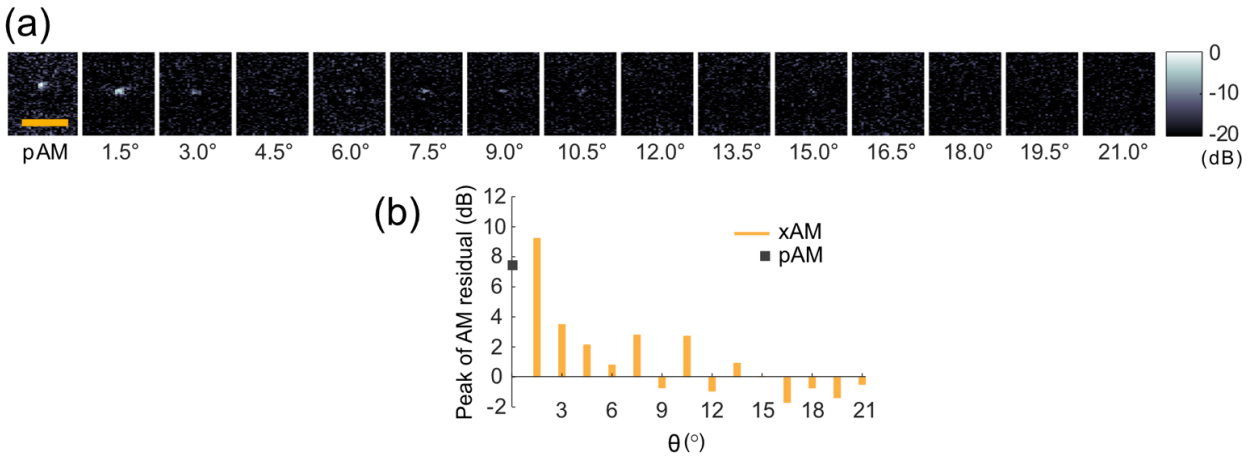

Figure 2.4 | xAM residual signal. xAM images of the cross section of a subwavelength nickel wire as a function of the cross-propagation angle θ. (a) Images reconstructed from the three component transmissions of the pAM code and xAM code at angles ranging from 1.5° to 21°. The wire was positioned at a depth of 4 mm. Each image depth ranges from 3.0 mm to 4.5 mm and width from -1.5 mm to 1.5 mm. Scale bar: 1 mm. (b) Peak AM residual signal as a function of the xAM sequence angle θ. xAM signals are labelled in orange, the pAM signal is labelled with a gray square symbol. Values in dB represent the peak value of the residual signal relative to the peak value of the noise.

2.4 Cross Amplitude Modulation Imaging of Acoustic Biomolecules

2.4.1 Angle-dependent xAM reduction of nonlinear propagation artifacts distal to GV inclusions

The xAM sequence was developed to detect hGVs with high specificity. The peak positive pressure of the single tilted plane-waves excites the hGVs in the linear scattering regime, while the doubled X-wave intersection amplitude excites the hGVs in the nonlinear scattering regime. By summing the echoes from the two plane-wave transmissions and then subtracting them from the echoes of the X-wave transmissions, we

solely retrieve non-zero differential GV signals while the echoes of surrounding linear scatterers cancel. To evaluate the effectiveness of xAM in reducing the nonlinear propagation artifact, we embedded a 2-mm wide cylindrical inclusion of hGVs in agar (at a concentration of 256 pM; see Section 2.6 for GV preparation) in a tissue-mimicking phantom consisting of agar and 3 μm aluminum oxide particles (a model linear scatterer). A second inclusion filled with a scatterer-free PBS/agar mixture was positioned 1 mm below the GVs (see schematic, Fig 2.5a). We imaged the phantom using the same sequence parameters used for the subwavelength scatterer measurements, with the top of the hGV inclusion positioned at 4 mm (Fig. 2.5], since X-waves provide extended depths of fields compared to parabolic beams[28].

With parabolic and low-θ xAM pulses, we observed significant nonlinear propagation artifact distal to hGV inclusions (Fig. 2.5a and 2.5b), confirming the high nonlinearity of hGV-filled media. The pAM and xAM images where quantified in terms of contrast-to-tissue ratios (CTR), contrast-to-artifact ratios (CAR), and artifact-to-tissue ratios (ATR) (Fig. 2.5b-d). For pAM and low θ angles, the artifact intensity was on par or above the hGV inclusion intensity (e.g. for θ = 1.5°, CAR = -1.6 dB at z = 4 mm), highlighting the specificity issue posed by collinear AM imaging. For angles above 15°, xAM produces images with a clear reduction in artifact signal while maintaining full contrast in the hGV inclusion. We also observed that, as in the simulation and subwavelength scatter results, the artifact reduction is a non-monotonic function of θ, with a local jump in xAM artifact at 10.5° (Fig. 2.5c). Overall, these results suggested that xAM provides the highest specificity for hGV signals at angles larger than 15°.

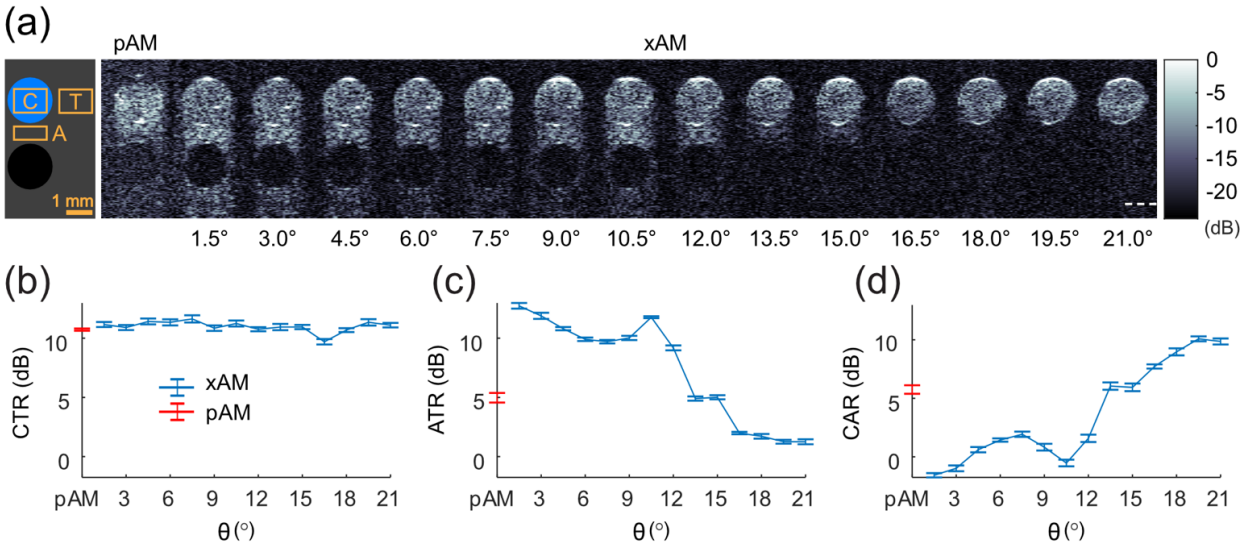

Figure 2.5 | *In vitro* pAM and xAM. *In vitro* pAM and xAM images of an hGV inclusion in a tissue-mimicking phantom. (a) Left, schematic of the phantom configuration: linearly scattering tissue-mimicking medium in gray, hGV inclusion in blue, anechoic agar-filled inclusion in black, and ROIs for contrast (C), tissue (T) and artifact (A) quantification. Right, set of pAM and xAM images of a representative well positioned at z = 4 mm. Separate images spanning depths of 3 mm

to 9 mm are concatenated. Scale bar: 1 mm. White dotted line: Z_X at θ = 21°. (b) Contrast-to-tissue ratio (CTR) as a function of θ. (c) Artifact-to-tissue ratio (ATR) as a function of θ. (d) Contrast-to-artifact ratio (CAR) as a function of θ. N = 6. Error bars: SEM.

2.4.2 *In vivo* xAM ultrasound imaging of acoustic biomolecules

Finally, to test the xAM imaging method *in vivo*, we injected into the gastrointestinal tract of a mouse a patterned agar-GV mixture that consisted of a core of wild-type linearly scattering GVs (wtGVs) surrounded by a circular layer of hGVs. We imaged the mouse abdomen using xAM at $\theta = 19.5°$, which yielded the highest contrast-to-artifact ratio in the phantom experiments, and compared the results to imaging with pAM with the focus adjusted to 4 mm and an aperture of 20 elements (f-number = 2.0) to align the depth-of-field with that of the xAM sequence. The parabolic B-mode (pBMode) image, i.e. the conventional anatomical ultrasound image, was sharper than the cross-propagating B-mode (xBMode) image, which is expected, as X-waves generate higher side lobes that reduce image contrast[29]. Only the top of the hGV inclusion was visible in the pAM image due to the narrow depth-of-field of parabolic beams (Fig. 2.6c). The pAM image also contained a large artifact below the inclusion (CTR = 2.8 dB, CAR = -2.6 dB), parts of which blended with the hGV signal, displaying a potentially misleading distribution of the contrast agent. In contrast, the annular hGV inclusion is almost entirely visible in the xAM image, with little-to-no artifact in the vicinity, and inner and outer contours more clearly delineated (Fig. 2.6e). The xAM CTR was 9.0 dB and the xAM CAR was 9.6 dB, demonstrating the superior performance of xAM over pAM in terms of specificity (Fig. 2.6f).

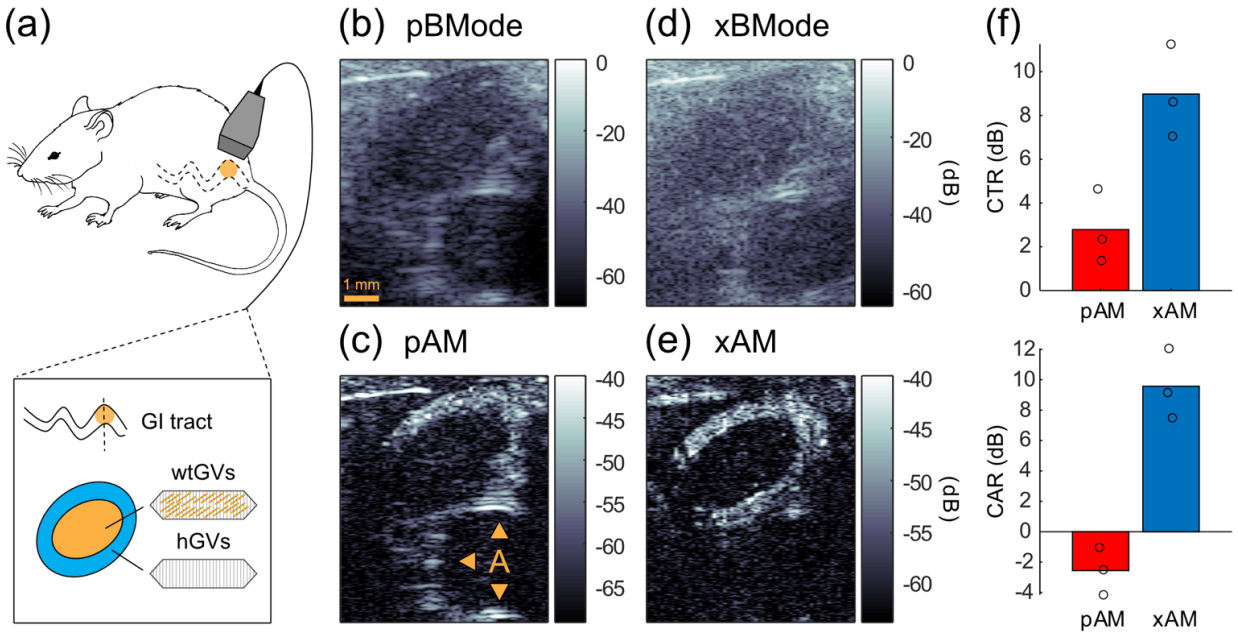

Figure 2.6 | *In vivo* pAM and xAM. *In vivo* pAM and xAM imaging of acoustic biomolecules. (a) Schematic of the experiment. A concentric mixture of nonlinearly scattering hGVs and linearly scattering wtGVs was injected in a mouse gastrointestinal (GI) tract and imaged with pAM and xAM. (b) pBMode image, focus = 4 mm, f-number = 2.0. (c) pAM image, arrows point at the artifact (A). (d) xBMode, θ = 19.5° (e) xAM image. pAM and xAM dynamic ranges are displayed relative to their respective BMode ranges. All images depth ranged from z = 2 mm to Z_X = 9.2 mm. (f) Comparison of xAM and pAM in terms of mean contrast-to-tissue ratios (CTR) and contrast-to-artifact ratios (CAR). N = 3. ROIs for CTR and CAR measurements are reported in Fig. 2.8, Methods.

2.5 Discussion

Taken together, our results suggest that the xAM ultrasound pulse sequence, based on one X-wave and two tilted plane-wave transmissions, achieves highly specific nonlinear imaging of acoustic biomolecules through wave-amplitude modulation. Two non-collinear plane waves interact to generate a two-fold amplitude modulation at their intersection with minimal nonlinear distortion for angles θ above 15°. This allows retrieval of non-zero differential hGV signals, while the echoes of surrounding linear scatterers cancel and propagation artifacts are reduced to the noise floor level (-10 dB at 18°). With a 6.4 mm aperture, this technique offers a depth-of-field suitable for small-animal imaging (10 mm at 18°). The xAM sequence proved to be robust enough to suppress *in vivo* artifacts present in pAM while distinguishing engineered nonlinear hGVs from linearly scattering wild type GV variants in the gastrointestinal tract of a mouse. While this manuscript is focused on introducing and thoroughly characterizing the xAM pulse sequence for use with non-linear contrast agents, with purified GVs as the model agent, these results are relevant to parallel work being done to apply GVs as functionalized contrast agents and as reporter genes expressed inside cells[3,13,30]. The xAM imaging method introduced here thus paves the way for *in vivo* biomolecular ultrasound studies of molecular and cellular processes based on visualization of acoustic biomolecules[13]. Interestingly, theory and simulations predict that the peak of the cross-propagating plane-waves travels at a supersonic velocity, increasing as θ opens (see Supplementary Material, Fig. 2.9), an effect that may be linked to the decreasing nonlinear interaction of the planar wavefronts. Coherent compounding of xAM data acquired at four different angles θ (see Supplementary Material, Fig. 2.10) was also shown to be a way to increase CTR and CAR further.

Potential limitations of this method include its reduced depth of field as the cross-propagating angle increases. The method appears therefore to be well suited for ultrasound biomicroscopy, small animal experiments and superficial examinations in humans. xAM image depth can be extended beyond the intersection distance of the X-wave by using spherical delay laws reported by Renaud et al.[22], but the quality of nonlinear artifact reduction will decline with depth. Another potential limitation of the method is that it relies on propagation symmetry in a homogeneous/isotropic medium to generate an amplitude-modulated code, and will therefore be impacted by dissymmetric phase-aberrating media like biological tissues. This issue could be tackled using

adaptive wavefront-shaping techniques developed in optics and acoustics[31,32]. In the near future, xAM could be implemented at ultrafast frame rates[33] by relying on 2D arrays of transducers[34] to improve the sensitivity or the temporal resolution of xAM further. Finally, while this study focused on the use of xAM to image nonlinear acoustic biomolecules, we expect this technology to propagate across as a general solution to the long-standing problem of distal nonlinear propagation artifacts in the field of synthetic microbubble-based ultrasound contrast agents.

2.6 Methods

2.6.1 k-Wave simulations

We investigated the influence of the transmit angle θ on the nonlinear interaction between two non-collinear plane waves emitted by two apertures using two-dimensional time-domain numerical simulations (k-Wave version 1.2,[24]). The transmit angle was varied from 1 to 21 degrees (Fig. 2.3). Transmit delays are calculated to generate a plane-waves with the proper angle θ. We simulated wave propagation in a homogeneous/isotropic medium (water) with a configuration corresponding to the setup reported experimentally in Fig. 2.4. Speed of sound in water was set to 1480 m/s, the attenuation to 0.002 dB/MHz^2 cm), and the nonlinear parameter B/A to 5. The size of the domain was 6.4 mm x 8 mm; it is discretized with a step size of 10 μm. Perfectly matched layers are used to absorb the waves at the edges of the domain. The source broadcasts a short pulse with a center frequency of 15 MHz. The acoustic pressure generated by the source is varied so that the peak acoustic pressure generated at 4 mm depth by a single aperture equals 400 kPa for all tested angles. For a given transmit angle, three simulations are required: 1) transmission with the right aperture only, 2) transmission with the left aperture only and 3) transmission with both apertures. The pressure field is recorded along the segment bisector (between the two transmit apertures). For a given transmit angle, the amplitude modulation scheme is applied to the recorded signals, then the result is band-pass filtered to reproduce the effect of the limited frequency bandwidth of the transducer with a 100% relative frequency bandwidth (the cutoff frequencies of the filter are 7.5 MHz and 22.5 MHz).

2.6.2 Engineering of harmonic acoustic protein nanostructures

Anabaena GVs were cultured and transferred to sterile separating funnels and the buoyant cells were allowed to float to the top and separate from the spent media over a 48h period. GVs were harvested by hypertonic lysis. Purification was done by repeated centrifugally assisted floatation followed by resuspension. Wild type Ana GVs were stripped of their outer GvpC layer by treatment with 6 M urea solution to obtain hGVs. Two

rounds of centrifugally assisted floatation followed by removal of the subnatant layer to ensure complete removal of native GvpC. For detailed information, see Lakshmanan et al.[30].

2.6.3 Tissue-mimicking phantom 3D design & preparation

Tissue-mimicking phantoms for imaging were prepared by melting 1% (w/v) agarose gel in PBS and with 0.2% (w/v) AlO_3. We used a custom 3D-printed mold to create a 2-by-2 grid of cylindrical wells with 2 mm diameter and 1 mm spacing between the outer radii in the bulk material. GVs were incubated at 42 °C for 1 minute and then mixed in a 1:1 ratio with molten agarose (at 42 °C) for a final GV concentration corresponding to 2.25 OD500nm and immediately loaded into the phantom. Wells not containing GVs were filled with plain 1% agar. The AlO_3 concentration was chosen to match the scattering echogenicity of the GV well as measured by the contrast-to-noise ratio of the respective regions in a B-mode ultrasound image. The phantoms used for the angle ramp images contained stripped Ana GVs in the upper-left well. The phantom used for the voltage ramp images contained wild type Ana GVs in the upper-left well and stripped Ana GVs in the upper-right well. All phantoms were imaged on top of an acoustic absorber material while immersed in PBS. Based on the elevation f-number of the probe, the elevation resolution (i.e. the thickness of the imaging plane) is 512 μm. The molarity of Ana GVs for a given OD value is 114 pM/OD[30]. Using these values and the dimensions of the hGV inclusion, we estimate that 2.47×10^5 GVs contribute to each image, or roughly 200 GVs for each pixel.

2.6.4 Ultrasound acquisition sequence

We used a Verasonics Vantage ultrasound system with a L22-14v probe (Verasonics Inc., Redmond, WA, USA) to implement the xAM and pAM imaging sequences. The probe is a linear array of 128 elements with a 0.10 mm pitch, an 8 mm elevation focus, a 1.5 mm elevation aperture, and a center frequency of 18.5 MHz with 67% -6 dB bandwidth. We applied a single-cycle transmit waveform at 15.625 MHz to each active array element to ensure our fundamental frequency divided four times with the 62.5 MHz sampling rate of the system. To provide a reasonable tradeoff between lateral field of view and axial depth of field, we used an aperture of 65 elements for the xAM sequence (with the center element silenced to allow for a symmetric AM code). This allowed for 64 ray lines per xAM image. The focus of the parabola used in the pAM sequence was set to 8 mm to match the probe's elevation focus. We used an aperture of 38 elements for the pAM sequence to maintain a f-number of 2, but limited the number of ray lines to 64 to match the xAM frames. To

control for variation in pressure across different beam profiles, we selected probe voltages for each xAM angle and for pAM that generated to a CTR of 10 dB in the hGV inclusion of the phantoms. The voltage table is provided in Section 2.7 Supplementary Material.

We collected raw RF data from our acquisitions and implemented a custom real-time image reconstruction pipeline, including a beamforming algorithm suited to the unique requirements of xAM. To reduce noise during live imaging while saving system memory, we applied a first-order infinite impulse response (IIR) filter to successive frames of RF data, according to the following difference equation

$$y[n] = \alpha y[n-1] + (1-\alpha)x[n], \qquad (1-A1)$$

where n is the frame index, α is the persistence coefficient, x is the unfiltered RF data, and y is the output of the filter. All RF data reported was acquired with $\alpha = 0.9$ except for the *in vivo* pAM image, which was acquired with $\alpha = 0.7$ to avoid blurring due to motion.

2.6.5 xAM beamforming

The novel cross-propagation paradigm necessitated adjustments to conventional beamforming for image reconstruction, as a particularity of this method is that xAM image lines are not formed along the propagation direction of the ultrasonic waves, but along the line along which the two cross-propagating plane-waves intersect. The linear array transmission configuration and directivity[25] can be modeled as in Fig. 2.7.

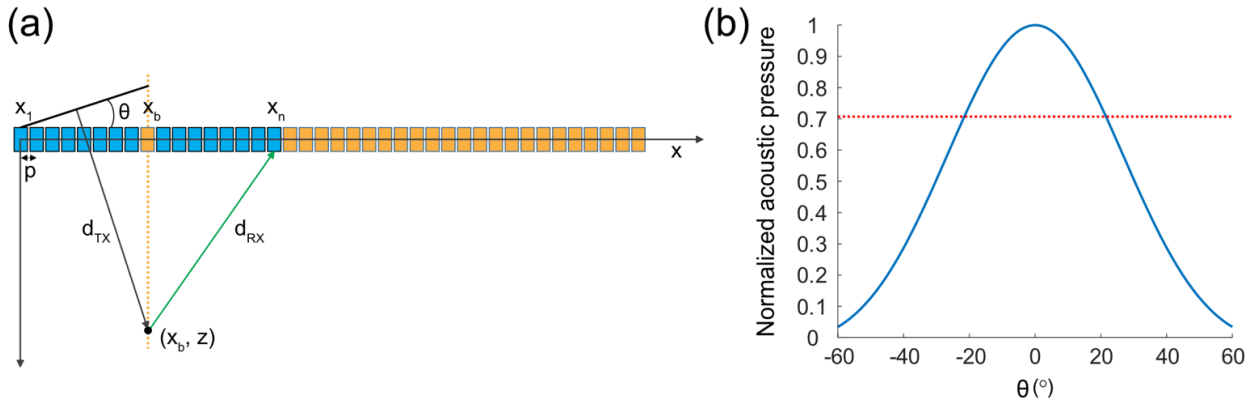

Figure 2.7 | Linear array aperture geometry and directivity. (a) Ultrasound imaging linear array configuration. θ is the cross-propagation angle, p the pitch of the linear transducer array, x_1 the first element of the active aperture (blue elements), x_b the element along the aperture, and x_n an arbitrary element along the array. d_{tx} is the distance from the planar wavefront to a point along the bisector, and d_{rx} is the return distance to the array. Silent elements are labelled in orange. (b) Directivity of an individual element of the linear transducer array (p = 0.1 mm, f = 15.6 MHz). The red dotted line indicates the – 3 dB acoustic pressure level.

The distance from either angled wavefront to the point (x_b, z) and the return trip distance of the echo received by array element x_n are, respectively,

$$d_{TX}(\theta, x_b, z) = (x_b - x_1)p \sin\theta + z\cos\theta\,, \qquad (1-A2)$$

$$d_{RX}(x_b, x_n, z) = \sqrt{(x_n - x_b)^2 p^2 + z^2}. \qquad (1-A3)$$

Hence, the two-way travel time to element x_n is

$$\tau_{\mathrm{T}/R\to x_n} = \frac{1}{c}[(x_b - x_1)p \sin\theta + z\cos\theta] + \frac{1}{c}\sqrt{(x_n - x_b)^2 p^2 + z^2}, \qquad (1-A4)$$

whereas the observed arrival time of this echo on the bisector element is

$$\tau_{\mathrm{T}/R\to x_b} = \frac{1}{c}[(x_b - x_1)p \sin\theta + z\cos\theta + z]. \qquad (1-\mathrm{A}5)$$

We can then derive the depth of the echo signal from its arrival time on the bisector as

$$z = \frac{c\tau_{\mathrm{T}/R\to x_b} - (x_b - x_1)p \sin\theta}{\cos\theta + 1}, \qquad (1-A6)$$

and, finally, obtain the time delay to apply to the received signal for dynamic focusing:

$$\delta(x_n, z) = \tau_{\mathrm{T}/R\to x_n} - \tau_{\mathrm{T}/R\to x_b} = \frac{1}{c}\left[\sqrt{(x_n - x_b)^2 p^2 + z^2} - z\right] \qquad (1-\mathrm{A}7)$$

These beamforming equations are valid in the region over which the waves are cross-propagating. The depth of field (equation (1)) to which this region extends is given by $(x_n - x_b)\cot\theta$.

2.6.6 *In vivo* ultrasound imaging

The *in vivo* experiment was performed on a C57BL/6J male mouse (Jackson Laboratory) under a protocol approved by the Institutional Animal Care and Use Committee of the California Institute of Technology. No randomization or blinding were necessary in this study. Ultrasound imaging was performed as follows: the mouse was anaesthetized with 2–3% isoflurane, depilated over the imaged region, and imaged using an L22-14v transducer with the pulse sequence described above. For imaging of GVs in the gastrointestinal tract, the mouse was placed in a supine position, with the ultrasound transducer positioned on the lower abdomen, transverse to the colon. Prior to imaging, wild type and stripped Ana GVs were mixed in a 1:1 ratio with 42 °C 4% agarose–PBS for a final GV OD_{500nm} equal to 2.25. An 8-gauge needle was filled with the mixture of agarose and stripped Ana GVs. Before it solidified, a 14-gauge needle was placed inside the 8-gauge needle to form a hollow lumen within the gel. After the agarose–GV mixture solidified at room temperature for 10 min, the 14-gauge needle was removed. The hollow lumen was then filled with the agarose mixture containing the wild type Ana GVs. After it solidified, the complete cylindrical agarose gel was injected into the colon of the mouse with a PBS back-filled syringe. Additional PBS was then injected into the colon to remove air bubbles in the vicinity of the gel.

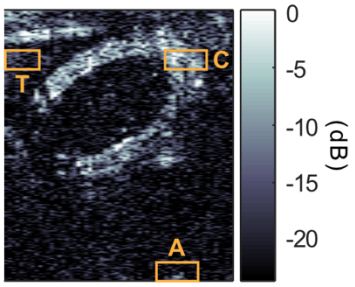

Figure 2.8 | *In vivo* regions of interest. Tissue (T), Contrast (C) and Artifact (A) regions of interest used for the ratios displayed in Fig. 2.6.

2.7 Supplementary Material

2.7.1 Supersonic cross-propagating plane-waves intersection

Interestingly, as both plane-waves cross-propagate, local coordinates of each wave-front interact with their axisymmetric counterpart, but contrary to co-propagating plane waves, it is a transient interaction. The plane-waves intersection velocity c_X is given by,

$$c_X = c_0/\cos\theta\,, \qquad (1-B1)$$

where c_0 is the speed of sound in the propagation medium. It can readily be seen from (2) that the plane-waves intersection velocity c_X is supersonic for θ > 0 as reported by Lu and Greenleaf[28], and seen in Fig. 2.9. The third transmission event of the xAM sequence (Fig. 2.2c) corresponds to a finite aperture forward propagating X-wave solution of the homogeneous/isotropic wave equation with the form $f(x, z - c_X t)$, where f represents a scalar function (e.g. the acoustic pressure pulse) of space and time[28], although in our case X-wave pressure distribution is constant along its branches.

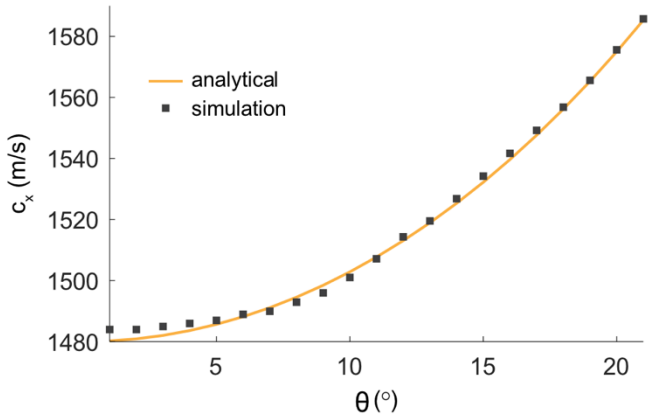

Figure 2.9 | X-wave intersection velocity. Analytical and simulated cross-propagating plane-waves intersection velocity as a function of θ.

2.7.2 Coherent compounding

We tested the effect of coherent compounding[35] of the RF data from multiple xAM acquisitions with different angles. Due to the difference in interaction velocity for different angles, the RF data from individual acquisitions was first aligned to the peak of the average autocorrelation function of the individual beamformed ray lines composing the images. The best results were achieved by compounding of four adjacent angles. This improved the average CTR by 1.7 dB and the peak CAR by 0.5 dB (Fig. 2.10).

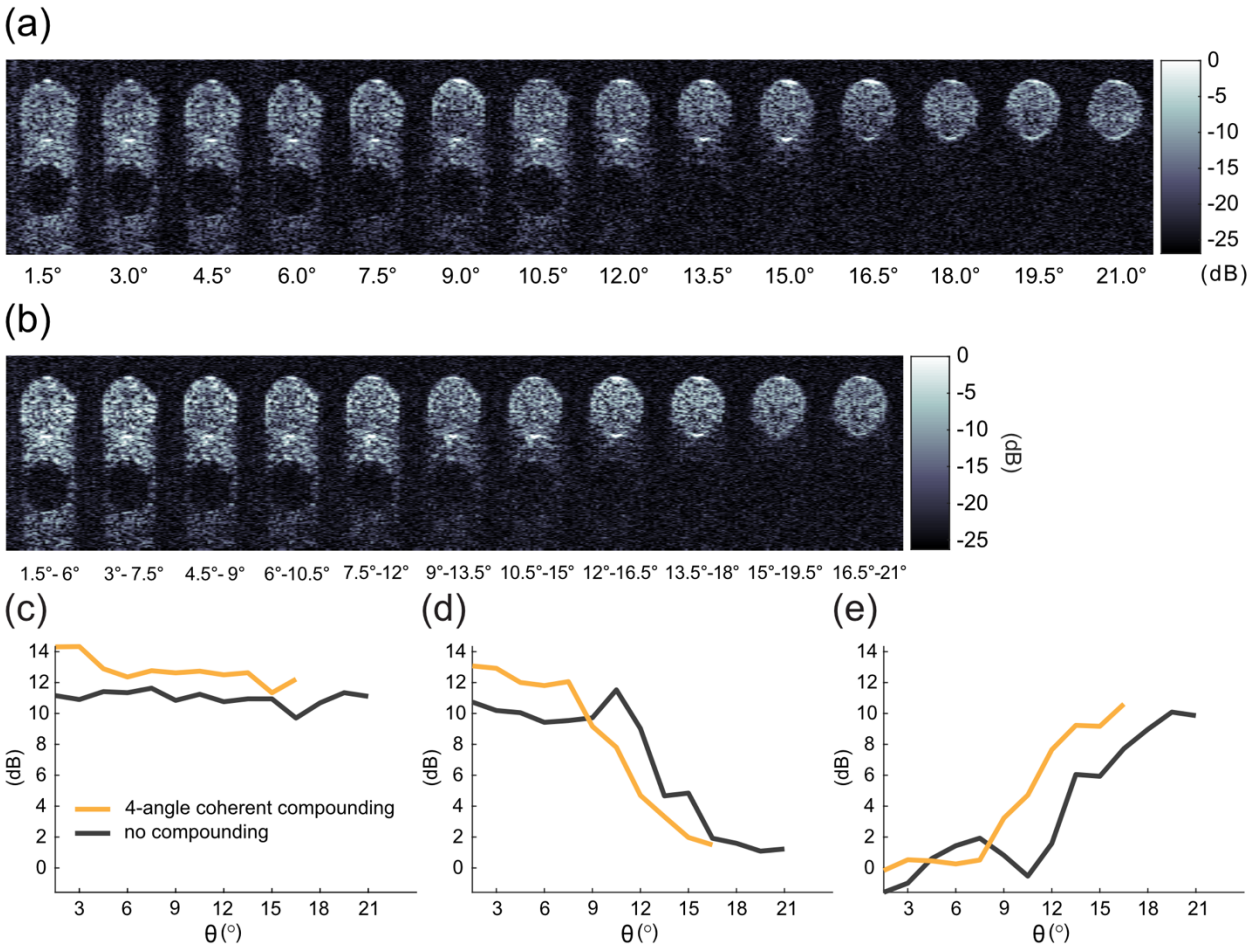

Figure 2.10 | Coherently compounded xAM. Comparison of coherently compounded and to single-acquisition xAM images the *in vitro* data at 4 mm. (a) A set of xAM images from the experiment depicted in Fig. 2.5. (b) The same images with coherent compounding applied to successive sets of four acquisitions. (c) Contrast-to-tissue ratio of single-acquisition xAM compared with coherently compounded data as a function of angle. (d) Artifact-to-tissue ratio. (e) Contrast-to-artifact ratio. n = 6. Error bars not shown for ease of comparison.

2.7.3 Voltage-pressure table

The phantom images reported in Fig. 2.5 were acquired using the following voltage table that ensured a 10 dB CTR across images and therefore enable for the comparison of the artifact intensity across cross-propagation angles.

Table 2.1 pAM (orange) and xAM (white) input transducer voltages generating a 10 dB CTR at 4 mm.

θ (°)	pAM	1.5	3.0	4.5	6.0	7.5	9.0	10.5	12.0	13.5	15.0	16.5	18.0	19.5	21.0
V_4 mm	1.9	4.6	4.3	3.7	3.3	3.4	3.8	3.9	4.2	4.1	4.5	4.5	4.7	5.0	5.5

References

1. Tsien, R. Y. The Green Fluorescent Protein. *Annual Review of Biochemistry* **67**, 509–544 (1998).

2. Ntziachristos, V. Going deeper than microscopy: the optical imaging frontier in biology. *Nature Methods* **7**, 603–614 (2010).

3. Bourdeau, R. W. *et al.* Acoustic reporter genes for noninvasive imaging of microorganisms in mammalian hosts. *Nature* **553**, 86–90 (2018).

4. Shapiro, M. G. *et al.* Biogenic gas nanostructures as ultrasonic molecular reporters. *Nature Nanotechnology* **9**, 311–316 (2014).

5. Ferrara, K., Pollard, R. & Borden, M. Ultrasound microbubble contrast agents: fundamentals and application to gene and drug delivery. *Annu. Rev. Biomed. Eng.* **9**, 415–447 (2007).

6. Faez, T. *et al.* 20 years of ultrasound contrast agent modeling. *IEEE transactions on ultrasonics, ferroelectrics, and frequency control* **60**, 7–20 (2012).

7. Rafter, P. G., Brock-Fisher, G. A. & Poland, M. D. User controlled destructive waveform routine for ultrasound systems. (2002).

8. Simpson, D. H., Chien Ting Chin & Burns, P. N. Pulse inversion Doppler: a new method for detecting nonlinear echoes from microbubble contrast agents. *IEEE Transactions on Ultrasonics, Ferroelectrics, and Frequency Control* **46**, 372–382 (1999).

9. Hansen, R. & Angelsen, B. A. J. Contrast imaging by non-overlapping dual frequency band transmit pulse complexes. *IEEE Transactions on Ultrasonics, Ferroelectrics, and Frequency Control* **58**, 290–297 (2011).

10. Maresca, D. *et al.* Contrast-enhanced intravascular ultrasound pulse sequences for bandwidth-limited transducers. *Ultrasound in medicine & biology* **39**, 706–713 (2013).

11. Renaud, G. *et al.* Counter-propagating wave interaction for contrast-enhanced ultrasound imaging. *Physics in Medicine & Biology* **57**, L9 (2012).

12. Walsby, A. E. Gas vesicles. *Microbiology and Molecular Biology Reviews* **58**, 94–144 (1994).

13. Maresca, D. *et al.* Biomolecular Ultrasound and Sonogenetics. *Annu. Rev. Chem. Biomol. Eng.* (2018) doi:10.1146/annurev-chembioeng-060817-084034.

14. Lakshmanan, A. *et al.* Molecular Engineering of Acoustic Protein Nanostructures. *ACS Nano* **10**, 7314–7322 (2016).

15. Maresca, D. *et al.* Nonlinear ultrasound imaging of nanoscale acoustic biomolecules. *Appl. Phys. Lett.* **110**, 073704 (2017).

16. Wu, J. & Tong, J. Measurements of the nonlinearity parameter BA of contrast agents. *Ultrasound in medicine & biology* **24**, 153–159 (1998).

17. Emmer, M. *et al.* Pressure-dependent attenuation and scattering of phospholipid-coated microbubbles at low acoustic pressures. *Ultrasound in medicine & biology* **35**, 102–111 (2009).

18. Tang, M.-X. & Eckersley, R. J. Frequency and pressure dependent attenuation and scattering by microbubbles. *Ultrasound in medicine & biology* **33**, 164–168 (2007).

19. Gerrit, L. *et al.* Far-wall pseudoenhancement during contrast-enhanced ultrasound of the carotid arteries: clinical description and in vitro reproduction. *Ultrasound in medicine & biology* **38**, 593–600 (2012).

20. Aanonsen, S. I., Barkve, T., Tjo/tta, J. N. & Tjo/tta, S. Distortion and harmonic generation in the nearfield of a finite amplitude sound beam. *The Journal of the Acoustical Society of America* **75**, 749–768 (1984).

21. Gusev, V., Bailliet, H., Lotton, P. & Bruneau, M. Interaction of counterpropagating acoustic waves in media with nonlinear dissipation and in hysteretic media. *Wave Motion* **29**, 211–221 (1999).

22. Renaud, G., Bosch, J. G., Steen, A. F. W. van der & Jong, N. de. Increasing specificity of contrast-enhanced ultrasound imaging using the interaction of quasi counter-propagating wavefronts: a proof of concept. *IEEE Transactions on Ultrasonics, Ferroelectrics, and Frequency Control* **62**, 1768–1778 (2015).

23. Pasovic, M. *et al.* Second harmonic inversion for ultrasound contrast harmonic imaging. *Physics in Medicine & Biology* **56**, 3163 (2011).

24. Treeby, B. E., Jaros, J., Rendell, A. P. & Cox, B. T. Modeling nonlinear ultrasound propagation in heterogeneous media with power law absorption using a k-space pseudospectral method. *The Journal of the Acoustical Society of America* **131**, 4324–4336 (2012).

25. Selfridge, A. R., Kino, G. S. & Khuri-Yakub, B. T. A theory for the radiation pattern of a narrow-strip acoustic transducer. *Appl. Phys. Lett.* **37**, 35–36 (1980).

26. Hamilton, M. F. & TenCate, J. A. Sum and difference frequency generation due to noncollinear wave interaction in a rectangular duct. *The Journal of the Acoustical Society of America* **81**, 1703–1712 (1987).

27. Hamilton, M. F. & Blackstock, D. T. On the coefficient of nonlinearity β in nonlinear acoustics. *The Journal of the Acoustical Society of America* **83**, 74–77 (1988).

28. Lu, J.- & Greenleaf, J. F. Nondiffracting X waves-exact solutions to free-space scalar wave equation and their finite aperture realizations. *IEEE Transactions on Ultrasonics, Ferroelectrics, and Frequency Control* **39**, 19–31 (1992).

29. Lu, J.- & Greenleaf, J. F. Theory and acoustic experiments of nondiffracting X-waves (medical US imaging application). in *IEEE 1991 Ultrasonics Symposium,* 1155–1159 vol.2 (1991). doi:10.1109/ULTSYM.1991.234298.

30. Lakshmanan, A. *et al.* Preparation of biogenic gas vesicle nanostructures for use as contrast agents for ultrasound and MRI. *Nature Protocols* **12**, 2050–2080 (2017).

31. Wang, K. *et al.* Direct wavefront sensing for high-resolution in vivo imaging in scattering tissue. *Nature Communications* **6**, 7276 (2015).

32. Imbault, M. *et al.* Robust sound speed estimation for ultrasound-based hepatic steatosis assessment. *Phys. Med. Biol.* **62**, 3582–3598 (2017).

33. Tanter, M. & Fink, M. Ultrafast imaging in biomedical ultrasound. *IEEE Transactions on Ultrasonics, Ferroelectrics, and Frequency Control* **61**, 102–119 (2014).

34. Provost, J. *et al.* 3D ultrafast ultrasound imagingin vivo. *Phys. Med. Biol.* **59**, L1–L13 (2014).

35. Montaldo, G., Tanter, M., Bercoff, J., Benech, N. & Fink, M. Coherent plane-wave compounding for very high frame rate ultrasonography and transient elastography. *IEEE Transactions on Ultrasonics, Ferroelectrics, and Frequency Control* **56**, 489–506 (2009).

Chapter 3

ACOUSTIC BIOSENSORS FOR ULTRASOUND IMAGING OF ENZYME ACTIVITY

This chapter is in large part a reformatted version of the manuscript entitled "Acoustic Biosensors for Ultrasound Imaging of Enzyme Activity" published by Lakshmanan, A., Jin, Z., Nety, S., Sawyer, D. P., Lee-Gosselin, A., Malounda, D., Swift, M., Maresca, D. and Shapiro, M. G. in *Nature Chemical Biology*. Under the supervision of Mikhail Shapiro, my contributions to the work was to help optimize the xAM pulse sequence for the experimental setups and engineered GVs used, as well as to provide guidance on its use during experiments.

Working as a collaborator on this project taught me valuable lessons about what it takes for a novel tool to be impactful: namely the practicalities of learning, optimizing, and extending the tool. After developing xAM, I had to ensure that those leading the biosensors project, particularly Zhiyang, not only knew how to use xAM, but understood the scripts well enough to modify and extend them. This is important because, while the utility of a method over other tools may be enough to drive adoption despite a difficult learning curve, it may not be enough to facilitate further optimizations, extensions, and innovations that require an in-depth understanding of how the method works. In this sense, making the xAM code well-documented and the results reproducible ended up being just as important as the custom graphical user interface I implemented to allow easy plug-and-play use of xAM in live imaging experiments.

However, another point I recognized was that secondary engineering considerations can have just as large an impact on the utility of a method as its fundamental capabilities. Because we implemented the xAM reconstruction in MATLAB rather than a compiled language like C/C++, the frame rate was quite low at only 1-3 frames per second, which made dealing with tissue motion during *in vivo* imaging experiments challenging. This gave me an appreciation for how engineering challenges can be just as important as research challenges in determining the utility and impact of a novel method.

3.1 Abstract

Visualizing biomolecular and cellular processes inside intact living organisms is a major goal of chemical biology. However, existing molecular biosensors, based primarily on fluorescent emission, have limited utility in this context due to the scattering of light by tissue. In contrast, ultrasound can easily image deep tissue with high spatiotemporal resolution, but lacks the biosensors needed to connect its contrast to the activity of specific biomolecules such as enzymes. To overcome this limitation, we introduce the first

genetically encodable acoustic biosensors – molecules that 'light up' in ultrasound imaging in response to protease activity. These biosensors are based on a unique class of air-filled protein nanostructures called gas vesicles, which we engineered to produce non-linear ultrasound signals in response to the activity of three different protease enzymes. We demonstrate the ability of these biosensors to be imaged *in vitro*, inside engineered probiotic bacteria, and *in vivo* in the mouse gastrointestinal tract.

3.2 Introduction

Virtually every biological process in living organisms involves dynamic changes in the concentration or activity of specific molecules. Visualizing these changes within the context of intact living tissues is critical to expanding our understanding of biological function and developing next-generation medicines. A large repertoire of genetically encoded fluorescent sensors has been developed to image specific molecular and cellular events[1-4]. However, deploying such biosensors in living organisms is challenging due to the limited penetration of light in tissue[5]. In contrast, non-invasive techniques such as ultrasound are capable of imaging deep tissues with high spatial and temporal resolution (below 100 μm and 1 ms, respectively)[6]. However, ultrasound currently lacks the sensors needed to observe dynamic molecular activity.

Here, we introduce molecular biosensors for ultrasound based on gas vesicles (GVs), a unique class of air-filled protein nanostructures that were recently established as genetically encodable imaging agents for ultrasound[7,8]. GVs evolved in certain aquatic microbes as a means to regulate cellular buoyancy for optimal photosynthetic illumination[9]. GV nanostructures comprise a 2 nm-thick protein shell enclosing an air-filled compartment, with genetically determined widths between 45-250 nm and lengths of several hundred nm[9,10]. The low density and high compressibility of GVs relative to surrounding aqueous media allows these proteins to scatter sound waves and thereby produce ultrasound contrast when injected into the body or expressed heterologously in engineered cells[7,8,11,12].

We hypothesized that we could engineer GV-based biosensors that dynamically change their ultrasound contrast in response to the activity of specific biomolecules. This possibility arises from the recent discovery that GVs' acoustic properties can be modified at the level of their constituent proteins[12]. In particular, the scaffolding protein GvpC, which sits on the GV surface (**Fig. 3.1a**) and provides structural reinforcement[13], can be modified at the level of its amino acid sequence to change GV mechanics. For example, shortening or removing GvpC makes GVs less rigid, allowing them to buckle more easily under acoustic pressure[12,14]. This reversible buckling produces nonlinear ultrasound contrast, which appropriate ultrasound pulse sequences readily distinguish from the linear signals produced by non-buckling GVs and background tissue[14,15].

As an initial target for acoustic biosensor development, we chose proteases – an important class of enzymes involved in many aspects of cellular signaling, homeostasis, disease, therapy and synthetic

biology[16-22]. While these enzymes were the targets of some of the first fluorescent biosensors[23,24], and continue to be a major focus of sensor engineering[25], no acoustic biosensors of protease activity have been developed. We postulated that by engineering variants of GvpC incorporating amino acid sequences that are recognized and acted upon by specific proteases, we could generate GVs whose nonlinear ultrasound contrast becomes activated by protease activity. As representative targets, we selected the constitutively active tobacco etch virus (TEV) endopeptidase, the calcium-dependent mammalian protease calpain, and the processive bacterial protease ClpXP. We set out to test the ability of acoustic biosensors engineered to respond to each of these enzymes to reveal their activity under ultrasound, and to demonstrate biosensor imaging *in vitro*, in living engineered cells, and *in vivo* in the mouse gastrointestinal (GI) tract.

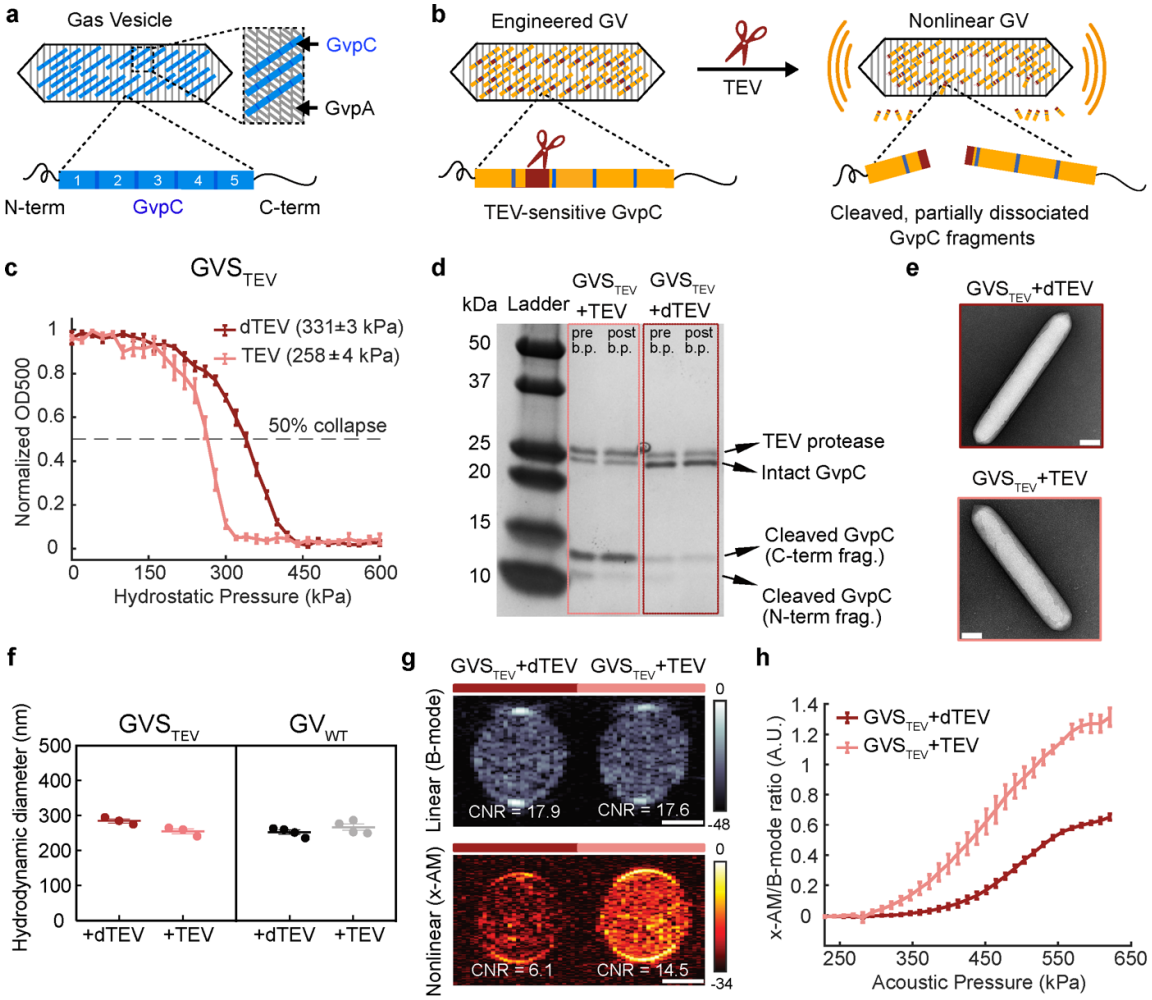

Figure 3.1: Acoustic biosensor of TEV endopeptidase. (**a**) Top: schematic of a gas vesicle (GV), including the primary shell protein GvpA (gray) and the reinforcing protein GvpC (blue). Bottom: schematic of GvpC structure, comprising five 33-amino acid repeats flanked by N-and C-terminal regions. (**b**) Schematic of GVS$_{TEV}$. (**c**) Normalized OD$_{500nm}$ of GVS$_{TEV}$ as a function of hydrostatic pressure, after incubation with active TEV or heat-inactivated TEV (dTEV). The legend lists the midpoint collapse pressure for each condition (±95% confidence interval), determined from fitting a Boltzmann sigmoid function (N = 3 biological replicates for GVS$_{TEV}$ + TEV and 4 for GVS$_{TEV}$ + dTEV). (**d**) Coomassie-stained SDS-PAGE gel of OD$_{500nm}$-matched samples of GVS$_{TEV}$ incubated with dTEV or active TEV protease, before and after buoyancy purification (labeled pre b.p. and post b.p., respectively). This experiment was

repeated 3 times with similar results. (**e**) Representative TEM images of GVS_{TEV} after incubation with dTEV or active TEV protease (N=3 biological replicates for GVS_{TEV} + TEV and 2 for GVS_{TEV} + dTEV; at least 100 GV particles were imaged for each condition). (**f**) DLS measurements of the average hydrodynamic diameter of GVS_{TEV} and GV_{WT} samples after protease incubation (N = 3 biological replicates for GVS_{TEV} and 4 for GV_{WT}; individual dots represent each N, and thick horizontal line indicates the mean). (**g**) Representative ultrasound images of agarose phantoms containing GVS_{TEV} incubated with TEV or dTEV protease at OD_{500nm} 2.2. The linear (B-mode) image was acquired at 132 kPa and the nonlinear (x-AM) image was acquired at 438 kPa. (**h**) Average ratio of x-AM to B-mode ultrasound signal as a function of applied acoustic pressure for GVS_{TEV}, after incubation with TEV or dTEV protease. N=3 biological replicates, with each N consisting of 2-3 technical replicates for **g** and **h**. For ultrasound images in **g**, CNR stands for contrast-to-noise-ratio, and color bars represent relative ultrasound signal intensity on the dB scale. Solid curves represent the mean in **c** and **h**. Error bars in **c**, **f** and **h** indicate SEM and were calculated from independent biological replicates. Scale bars in **e** represent 100 nm. Scale bars in **g** represent 1 mm. Individual data points for panels **c** and **h** shown as scatter plots in **Extended Data Figure 3.1**.

3.3 Results

3.3.1 Engineering an acoustic sensor of TEV endopeptidase

We selected the TEV endopeptidase as our first sensing target because of its well-characterized recognition sequence and widespread use in biochemistry and synthetic biology[26,27]. To sense TEV activity, we engineered a GvpC variant containing the TEV recognition motif ENLYFQ'G (**Fig. 3.1b**), hypothesizing that the cleavage of GvpC into two smaller segments would cause the GV shell to become less stiff, thereby allowing it to undergo buckling and produce enhanced nonlinear ultrasound contrast. We implemented this design *in vitro* using GVs from *Anabaena flos-aque* (Ana), whose native GvpC can be removed after GV isolation, and replaced with new versions expressed heterologously in *Escherichia coli*[12,28]. Ana GvpC comprises five repeats of a predicted alpha-helical polypeptide (**Fig. 3.1a**), and we tested insertions of the TEV recognition sequence, with and without flexible linkers of different lengths, at several locations within this protein. After incubating the engineered GVs with active TEV protease or a heat-inactivated "dead" control (dTEV), we measured their hydrostatic collapse using pressurized absorbance spectroscopy. This technique measures the optical density of GVs (which scatter 500 nm light when intact) under increasing hydrostatic pressure, providing a quick assessment of GV shell mechanics: GVs that collapse at lower pressures also produce more nonlinear contrast[7,8,12,28]. Using this approach, we identified an engineered GV variant that showed ~ 70 kPa reduction in its collapse pressure midpoint upon incubation with the active TEV protease (**Fig. 3.1c and Extended Data Fig. 3.1**), and selected it for further characterization. This GV sensor for TEV, hereafter referred to as GVS_{TEV}, has the TEV cleavage site on the second repeat of GvpC, flanked by flexible GSGSGSG linkers on both sides.

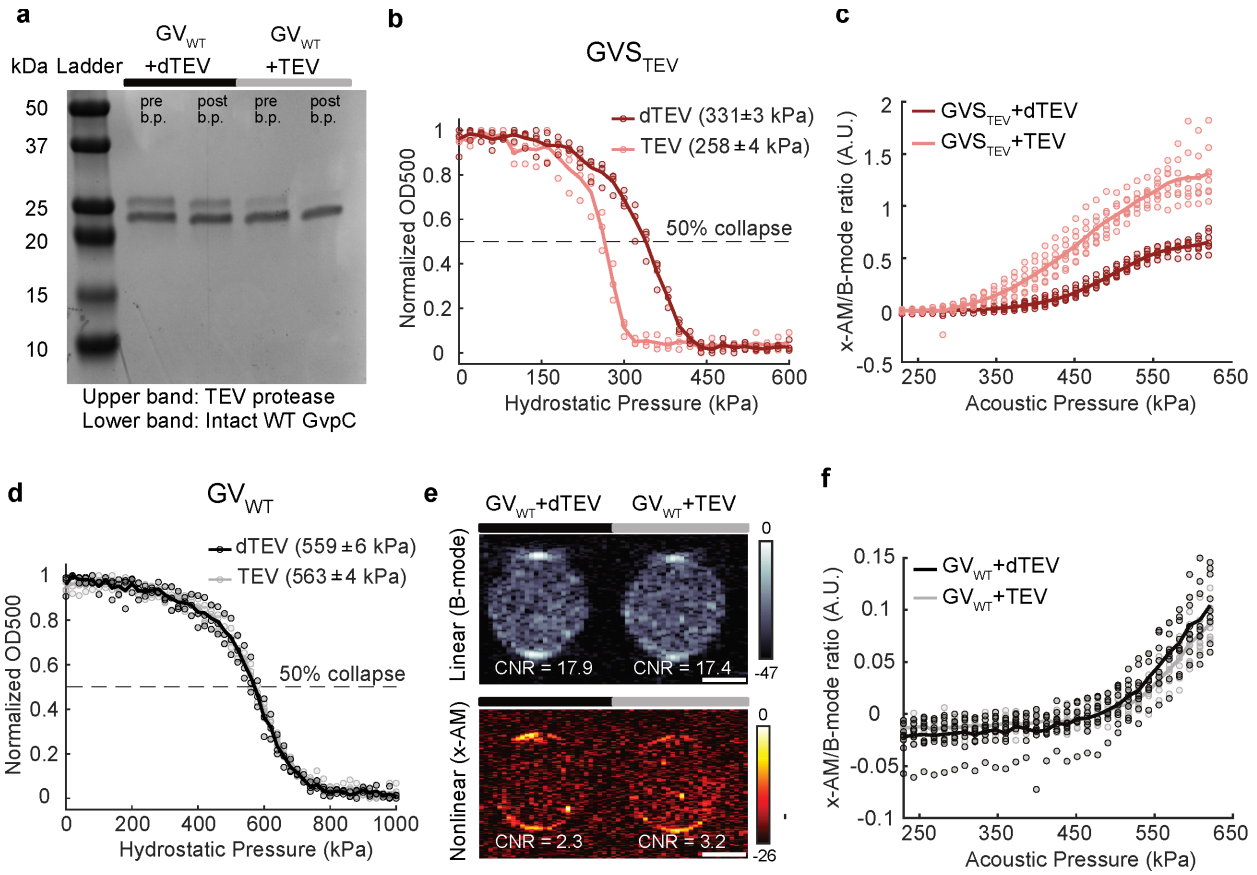

Extended Data Figure 3.1 | Engineering an acoustic sensor of TEV endopeptidase activity. (**a**) Coomassie-stained SDS-PAGE gel of OD_{500nm}-matched samples of GV_{WT} incubated with dTEV and TEV protease, before and after buoyancy purification (labeled pre b.p. and post b.p., respectively). N = 3 biological replicates. (**b**) Scatter plots showing normalized OD_{500nm} of GVS_{TEV} as a function of hydrostatic pressure. (N = 3 biological replicates for GVS_{TEV} + TEV and N =4 for GVS_{TEV} + dTEV.) (**c**) Scatter plots showing the ratio of nonlinear (x-AM) to linear (B-mode) ultrasound signal as a function of applied acoustic pressure for all the replicate samples used in the x-AM voltage ramp imaging experiments for GVS_{TEV}. N = 3 biological replicates and total number of replicates is 8. (**d**) Scatter plots showing normalized OD_{500nm} of GV_{WT} as a function of hydrostatic pressure. (N = 3 biological replicates for GV_{WT} +dTEV and N =4 for GV_{WT} + TEV.) (**e**) Representative ultrasound images of agarose phantoms containing GV_{WT} incubated with TEV or dTEV protease at OD_{500nm} 2.2. The B-mode image was acquired at 132kPa and the x-AM image at 569 kPa. Similar images acquired for N=3 biological replicates, with each N consisting of 3 technical replicates. CNR stands for contrast-to-noise-ratio, and color bars represent relative ultrasound signal intensity on the dB scale. Scale bars represent 1 mm (**f**) Scatter plots showing the ratio of nonlinear (x-AM) to linear (B-mode) ultrasound signal as a function of applied acoustic pressure for all the replicate samples used in the x-AM voltage ramp imaging experiments for GV_{WT}. N=3 biological replicates, with each N consisting of 3 technical replicates. Solid curve represents the mean of all the replicates.

TEV cleavage of the GvpC on GVS_{TEV} is expected to produce N- and C-terminal fragments with molecular weights of approximately 9 and 14 kDa, respectively. Indeed, gel electrophoresis of GVS_{TEV} after exposure to active TEV resulted in the appearance of the two cleaved GvpC fragments and a significant reduction in the intact GvpC band intensity (**Fig. 3.1d**). In addition, removal from solution of unbound fragments via buoyancy purification of the GVs resulted in a reduced band intensity for the N-terminal cleavage fragment, indicating its partial dissociation after cleavage (**Fig. 3.1d**). No significant changes in the GvpC band intensity were observed after incubation with dTEV. Transmission electron microscopy

(TEM) images showed intact GVs with similar appearance under both conditions, confirming that protease cleavage did not affect the structure of the underlying GV shell (**Fig. 3.1e**). Dynamic light scattering (DLS) showed no significant difference in the hydrodynamic diameter of the engineered GVs after incubation with dTEV and active TEV protease, confirming that the GVs remain dispersed in solution (**Fig. 3.1f**).

After confirming the desired mechanical and biochemical properties of GVS_{TEV}, we imaged it by ultrasound. Nonlinear imaging was performed in hydrogel samples containing the biosensor, using a recently developed cross-amplitude modulation (x-AM) pulse sequence[15]. x-AM uses pairs of cross-propagating plane waves to elicit highly specific nonlinear scattering from buckling GVs at the wave intersection, while subtracting the linear signal generated by transmitting each wave on its own[15]. Linear images were acquired using a conventional B-mode sequence. As hypothesized, exposing the GVS_{TEV} samples to TEV protease produced a strong nonlinear acoustic response, with a maximal contrast-to-noise ratio (CNR) enhancement of ~ 7 dB at an applied acoustic pressure of 438 kPa (**Fig. 3.1g**). Substantially less nonlinear contrast was observed in controls exposed to dTEV, while, as expected, both samples produced similar linear scattering. Consistent with the pressure-dependent mechanics of the GV shell, the differential nonlinear acoustic response of GVS_{TEV} became evident at pressures above 295 kPa, and kept increasing until 556 kPa, at which point the GVs began to collapse (**Fig. 3.1h and Extended Data Fig. 3.1**). As an additional control, we found that GVs with the wild-type GvpC sequence (GV_{WT}) showed no difference in their hydrostatic collapse pressure or nonlinear acoustic contrast in response to TEV protease (**Extended Data Fig. 3.1**), and no wild-type GvpC cleavage was seen upon gel electrophoresis (**Extended Data Fig. 3.1**). These results established GVS_{TEV} as an acoustic biosensor of the TEV protease enzyme, and additionally provided an experimental template to develop additional sensors.

3.3.2 Engineering an acoustic sensor of calpain

After validating our basic acoustic biosensor design using the model TEV protease, we examined its generalizability to other endopeptidases. As our second target, we selected the calcium-dependent cysteine protease calpain, a mammalian enzyme with critical roles in a wide range of cell types [29-31]. The two most abundant isoforms of this protease, known as μ-calpain and m-calpain, are expressed in many tissues and involved in processes ranging from neuronal synaptic plasticity to cellular senescence[29,30]. We designed an acoustic biosensor of μ-calpain by inserting the α-spectrin-derived recognition sequence QQEVY'GMMPRD[32] into Ana GvpC (**Fig. 3.2a**). We screened several versions of GvpC incorporating this cleavage sequence, flanked by GSG or GSGSG linkers, at different positions within the second helical repeat. Pressurized absorbance spectroscopy performed in buffers with and without calpain and Ca^{2+} allowed us to identify a GV sensor for calpain (GVS_{calp}), showing an approximately 50 kPa decrease in hydrostatic collapse pressure in the presence of the enzyme and its ionic activator (**Fig. 3.2b and Extended**

Data Fig. 3.2). Electrophoretic analysis confirmed cleavage and partial dissociation of the cleaved fragments from the GV surface (**Extended Data Fig. 3.2**), while TEM showed no change in GV morphology (**Extended Data Fig. 3.2**).

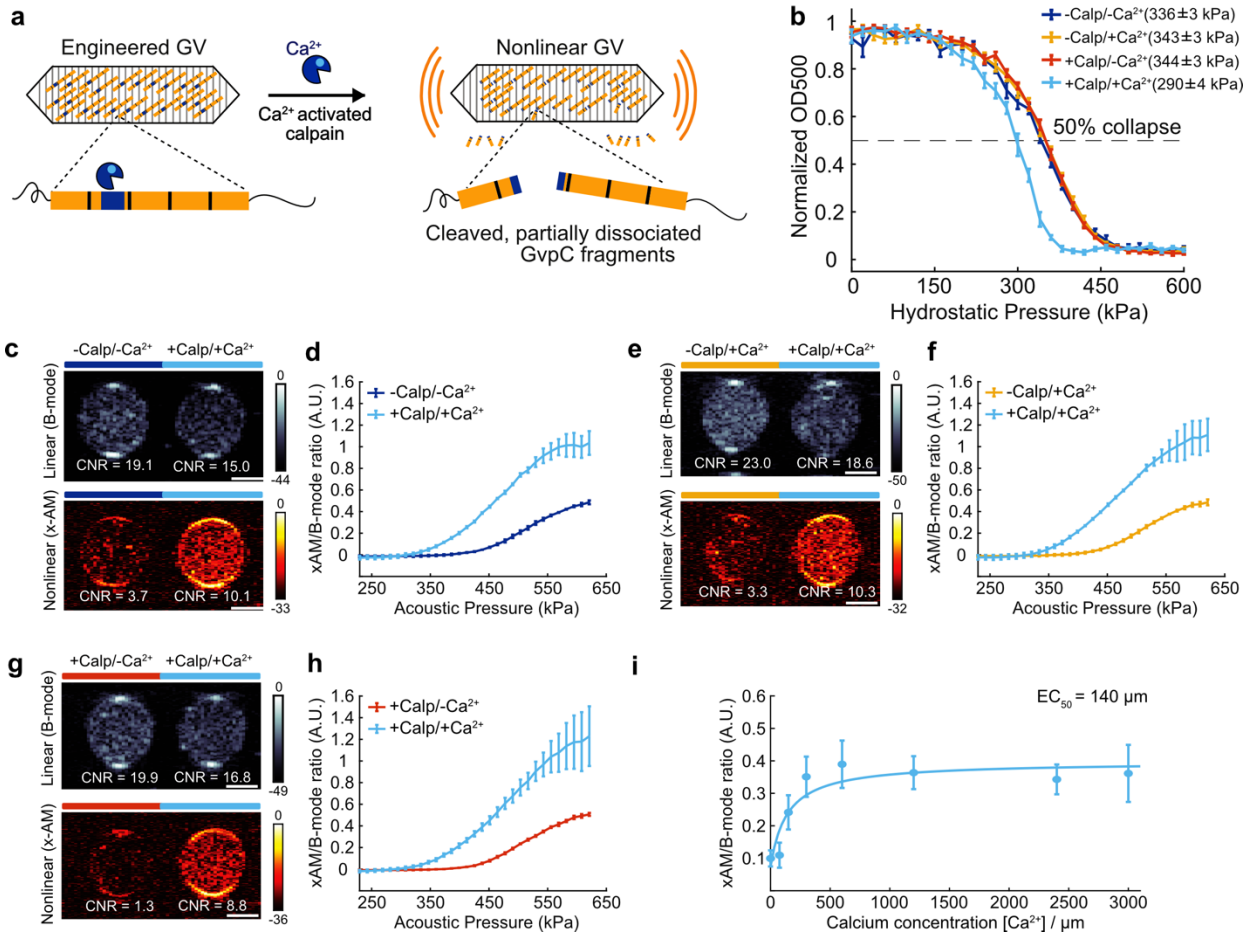

Figure 3.2 | Acoustic biosensor of calcium-activated calpain protease. (a) Schematic illustration GVS_{calp}. (**b**) Hydrostatic collapse curves of GVS_{calp} after incubations in the presence or absence of calpain and calcium. The legend lists the midpoint collapse pressure for each condition (±95% confidence interval) determined from fitting a Boltzmann sigmoid function N = 5 biological replicates for +Calp/+Ca^{2+}, 6 for -Calp/+Ca^{2+} and +Calp/-Ca^{2+}, and 7 for -Calp/-Ca^{2+}. (**c, e, g**) Representative ultrasound images of agarose phantoms containing GVS_{calp} incubated with and without calpain and/or calcium at OD_{500nm} 2.2. The B-mode images were taken at 132 kPa for **c**, **e** and **g**, and the x-AM images were taken at 438 kPa for **c**, **e** and at 425 kPa for **g**. CNR stands for contrast-to-noise-ratio, and color bars represent relative ultrasound signal intensity on the dB scale. Scale bars represent 1 mm. (**d, f, h**) Average ratio of x-AM to B-mode ultrasound signal as a function of applied acoustic pressure for GVS_{calp} after incubation in the presence or absence of calpain and/or calcium. N=3 biological replicates, with each N consisting of 2 technical replicates for **c-h**. Solid curves represent the mean and error bars indicate SEM. Statistics were performed on independent biological replicates for **b, d, f** and **h**.(**i**) Calcium-response curve for GVS_{calp} in the presence of µ-calpain, showing the ratio of x-AM to B-mode ultrasound signal at 425 kPa as a function of calcium concentration. The mean values are fitted to a Hill equation with a coefficient of 1, giving a half-maximum response concentration (EC_{50}) of 140 µm (N = 3 biological replicates, individual dots represent the mean values with the solid blue line showing the fitted curve). Error bars indicate SEM. Individual scatter plots for **d**, **f**, **h** and **i** are shown in **Extended Data Figure 3.2**.

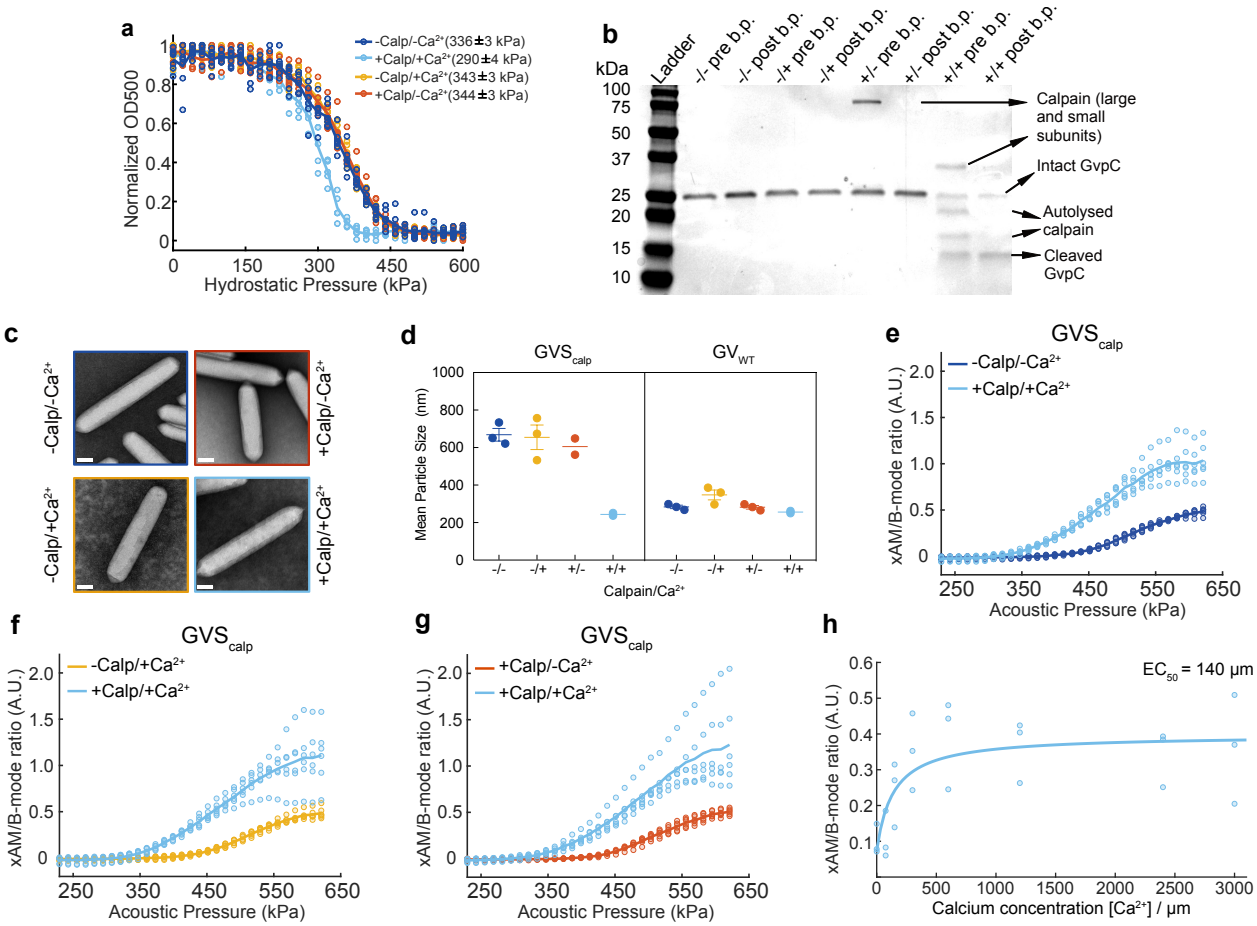

Extended Data Figure 3.2 | Engineering an acoustic sensor of calpain activity. (a) Individual scatter plots for **Fig. 3.2(b)**. N = 5 biological replicates for +Calp/+Ca^{2+}, 6 for -Calp/+Ca^{2+} and +Calp/-Ca^{2+}, 7 for -Calp/-Ca^{2+}. **(b)** Coomassie-stained SDS-PAGE gel of OD_{500nm}-matched samples of GVS_{calp} incubated in the presence (+) or absence (-) of calpain (first +/-) and calcium (second +/-), before and after buoyancy purification (labeled pre b.p. and post b.p. respectively). N = 3 biological replicates. (**c**) Representative TEM images of GVS_{calp} after incubations in the presence or absence of calpain and/or calcium. Scale bars represent 100 nm. At least 20 GV particles were imaged for each condition. (**d**) DLS measurements showing the average hydrodynamic diameter of GVS_{calp} and GV_{WT} samples after calpain/calcium incubations (N = 2 biological replicates for GVS_{calp} +/-, +/+, GV_{WT} +/+ and 3 for other conditions, individual dots represent each N and horizontal line indicates the mean). Error bars indicate SEM when N = 3. (**e, f, g**) Individual scatter plots for **Fig. 3.2(d, f, h)**. N = 3 biological replicates with each N consisting of 2 technical replicates (total number of replicates is 18 for +/+ and 6 for each of the remaining conditions). Solid line represents the mean of all the replicates for (**a, e-g**). (**h**) Scatter plots for **Fig. 3.2i**; N = 3 biological replicates, individual dots represent each N and solid blue line showing the fitted curve (a Hill equation with a coefficient of 1, with a half-maximum response concentration (EC_{50}) of 140 µm).

Ultrasound imaging of GVS_{calp} revealed a robust nonlinear acoustic response when both calpain and calcium were present (**Fig. 3.2, c, e, g**), but not in negative controls lacking either or both of these analytes. A slight clustering tendency of GVS_{calp} nanostructures, which was attenuated by incubation with activated calpain (**Extended Data Fig. 3.2**), resulted in a slightly higher B-mode signal for the negative controls. However, this did not significantly affect the maximal nonlinear sensor contrast of GVS_{calp} of approximately 7dB (**Fig. 3.2, c, e, g**). This contrast increased steeply beyond an applied acoustic pressure

of 320 kPa (**Fig. 3.2, d, f, h and Extended Data Fig. 3.2**). Using this biosensor, ultrasound imaging could be used to visualize the dynamic response of calpain to Ca^{2+}, with a half-maximal response concentration of 140 µM (**Fig. 3.2i and Extended Data Fig. 3.2**). Additional control experiments performed on GVs with wild-type GvpC showed no proteolytic cleavage, change in GV collapse pressure or ultrasound response, after incubation with calcium-activated calpain (**Extended Data Fig. 3.3**). These results show that acoustic biosensor designs based on GvpC cleavage can be generalized to a mammalian protease and used to sense the dynamics of a conditionally active enzyme.

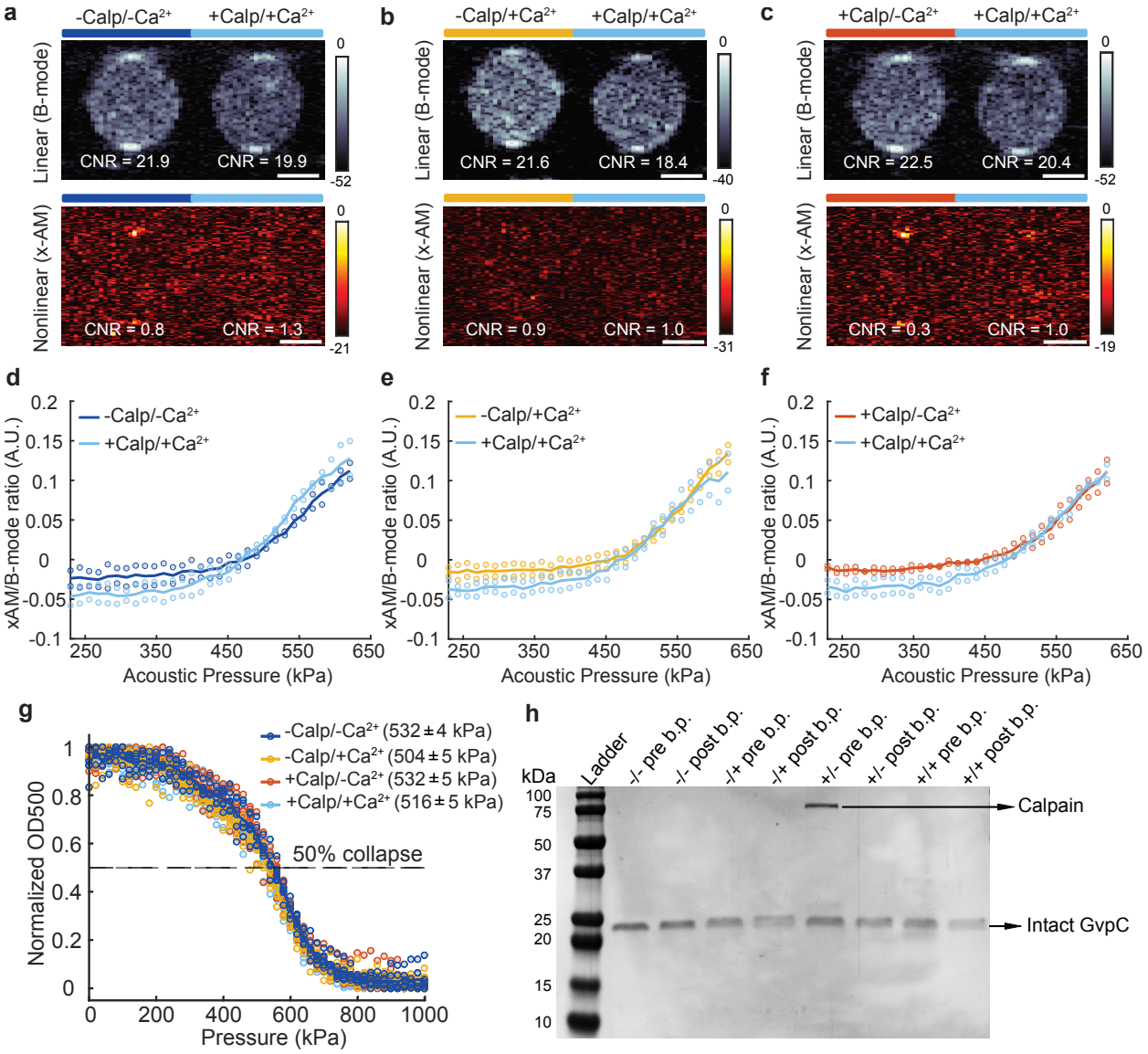

Extended Data Figure 3.3 | Characterization of GV_{WT} sample with calpain protease. (**a**, **b**, **c**) Representative ultrasound images of agarose phantoms containing GV_{WT} incubated in the presence (+) or absence (-) of calpain (first +/-) and calcium (second +/-), at OD_{500nm} 2.2. The B-mode images were taken at 132 kPa for **a**, **b** and **c** and the x-AM images corresponding to the maximum difference in non-linear contrast between the +/+ sample and the negative controls were taken at 438 kPa for **a** and **b** and at 425 kPa for **c**. CNR stands for contrast-to-noise-ratio and color bars represent ultrasound signal intensity in the dB scale. Scale bars represent 1 mm. N = 2 biological replicates for **a**, **b** and **c**. (**d**, **e**, **f**) Scatter plots showing the ratio of x-AM to B-mode ultrasound signal as a function of increasing acoustic

pressure for GV_{WT} after incubation in the presence or absence of calpain and/or calcium (N = 2 biological replicates). (**g**) Hydrostatic collapse curves of GV_{WT} after incubations in the presence (+) or absence (-) of calpain and/or calcium. The legend lists the midpoint collapse pressure for each condition (±95% confidence interval) determined from fitting a Boltzmann sigmoid function (N = 5 biological replicates for -/+ and N = 6 for other conditions) (**h**) Coomassie-stained SDS-PAGE gel of OD_{500nm}-matched samples of GV_{WT} incubated in the presence (+) or absence (-) of calpain/calcium, before and after buoyancy purification (labeled pre b.p. and post b.p., respectively, N=1). Individual dots in **d**, **e**, **f** and **g** represent each N and solid line represents the mean of all the replicates.

3.3.3 Building an acoustic sensor of the protease ClpXP

In addition to endopeptidases, another important class of enzymes involved in cellular protein signaling and homeostasis is processive proteases, which unfold and degrade full proteins starting from their termini[33]. To determine whether GV-based biosensors could be developed for this class of enzymes, we selected ClpXP, a processive proteolytic complex from *E. coli* comprising the unfoldase ClpX and the peptidase ClpP[34]. ClpX recognizes and unfolds protein substrates containing specific terminal peptide sequences called degrons. The unfolded proteins are then fed into ClpP, which degrades them into small peptide fragments[34]. We hypothesized that the addition of a degron to the C-terminus of GvpC would enable ClpXP to recognize and degrade this protein, while leaving the underlying GvpA shell intact, resulting in GVs with greater mechanical flexibility and nonlinear ultrasound contrast (**Fig. 3.3a**).

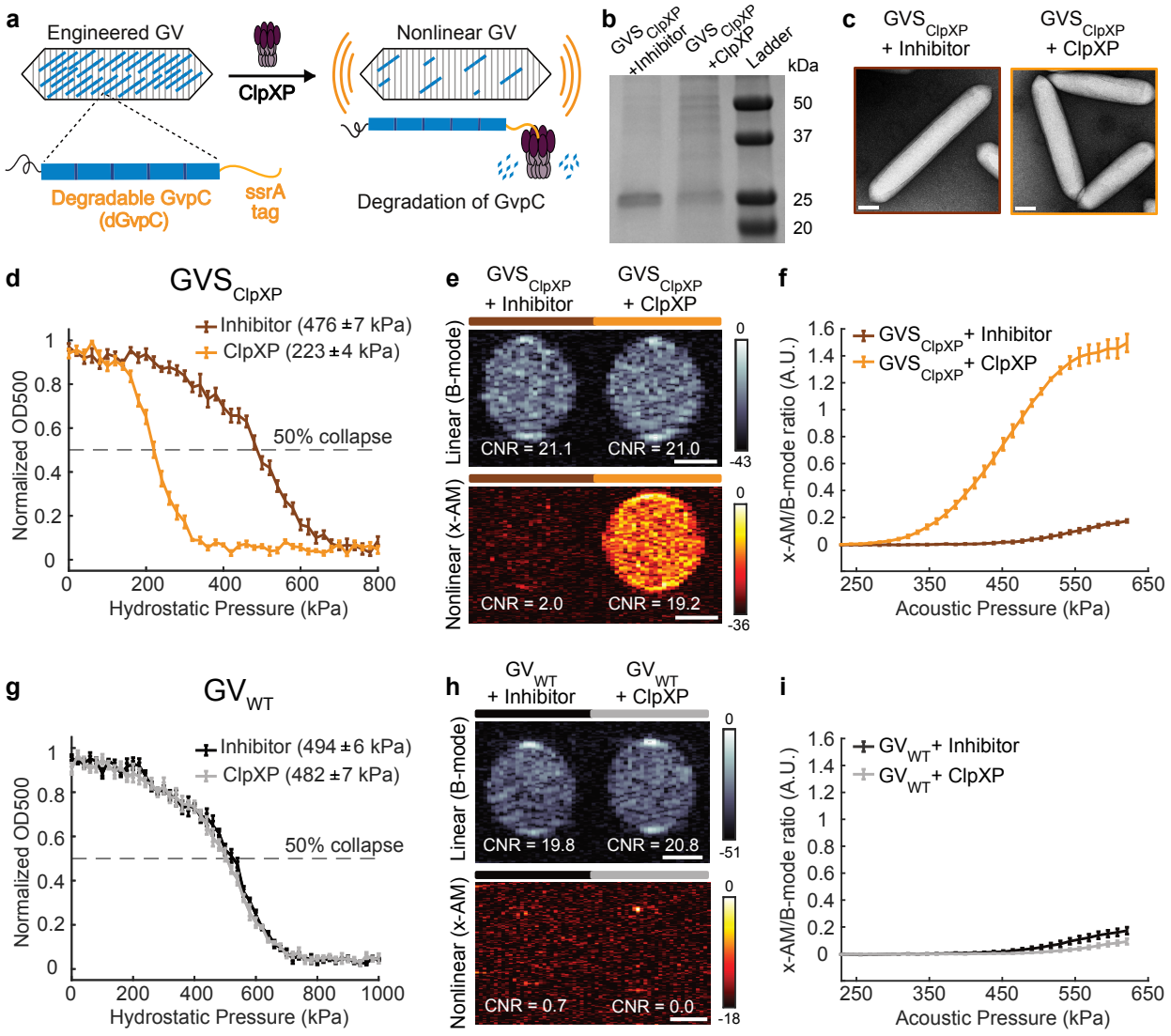

Figure 3.3: Acoustic biosensor of ClpXP protease. (**a**) Schematic of GVS_{ClpXP}. (**b**) Coomassie-stained SDS-PAGE gel of OD_{500nm}-matched GVS_{ClpXP} samples, incubated in a reconstituted cell-free transcription-translation (TX-TL) system containing a protease inhibitor cocktail or ClpXP (N= 3 biological replicates). Additional bands in these gels arise from components of the TX-TL system (**Extended Data Figure 3.4**) (**c**) Representative TEM images of GVS_{ClpXP} after incubations in the presence of a protease inhibitor or ClpXP. Scale bars represent 100 nm. A minimum of 100 GV particles were imaged for the +ClpXP condition and 50 particles for the +inhibitor control. (**d**) Normalized optical density (OD_{500nm}) measurements of GVS_{ClpXP} as a function of hydrostatic pressure after protease incubation (N=5 biological replicates). (**e**) Representative ultrasound images of agarose phantoms containing GVS_{ClpXP} incubated with the inhibitor cocktail or active ClpXP at OD_{500nm} 2.2. (**f**) Average x-AM/B-mode ratio as a function of applied acoustic pressure for GVS_{ClpXP}, after incubation with the protease inhibitor or active ClpXP. (**g**) Hydrostatic collapse pressure measurements for engineered Ana GVs with WT-GvpC (GV_{WT}) after protease incubation (N=5 biological replicates). For collapse pressure data in **d** and **g**, the legend lists the midpoint collapse pressure for each condition (±95% confidence interval), determined from fitting a Boltzmann sigmoid function. (**h**) Representative ultrasound images of agarose phantoms containing GV_{WT} incubated with the inhibitor cocktail or active ClpXP at OD_{500nm} 2.2. Scale bars in **e** and **h** represent 1mm. CNR stands for contrast-to-noise-ratio, and color bars represent relative ultrasound signal intensity on the dB scale. The B-mode images were acquired at 132 kPa and the x-AM images were acquired at 477 kPa. (**i**) Average ratio of x-AM to B-mode acoustic signal as a function of applied acoustic pressure for GV_{WT} after incubation with the inhibitor cocktail or ClpXP protease. For **e**, **f**, **h** and **i**, N=3 biological replicates, with each N having 3 technical replicates. For **d**, **f**, **g** and **i**, solid curves represent the mean and error bars indicate

SEM, which were calculated from independent biological replicates. Individual scatter plots for **d, f**, **g** and **i** are shown in **Extended Data Figure 3.4**.

To test this hypothesis, we appended the ssrA degron, AANDENYALAA, via a short SG linker, to the C-terminus of Ana GvpC, resulting in a sensor that we named GVS_{ClpXP} (**Fig. 3.3a**). We tested the performance of this biosensor *in vitro* using a reconstituted cell-free transcription-translation system comprising *E. coli* extract, purified ClpX, and a ClpP-expressing plasmid. Gel electrophoresis performed after incubating GVS_{ClpXP} with this cell-free extract showed significant degradation of the engineered GvpC, compared to a negative control condition in which the extract was pre-treated with a protease inhibitor (**Fig. 3.3b**). TEM images showed intact GVs under both conditions, confirming that GvpC degradation left the underlying GV shell uncompromised (**Fig. 3.3c**). Pressurized absorbance spectroscopy indicated a substantial weakening of the GV shell upon ClpXP exposure, with the hydrostatic collapse midpoint shifting by nearly 250 kPa (**Fig. 3.3d and Extended Data Fig. 3.4**). Ultrasound imaging revealed a 17dB enhancement in the nonlinear contrast produced by GVS_{ClpXP} at an acoustic pressure of 477 kPa, in response to ClpXP activity (**Fig. 3.3, e-f and Extended Data Fig. 3.4**). Control GVs containing wild type GvpC showed no sensitivity to ClpXP (**Fig. 3.3, g-i and Extended Data Fig. 3.4**). These results establish the ability of GV-based acoustic biosensors to visualize the activity of a processive protease as turn-on sensors.

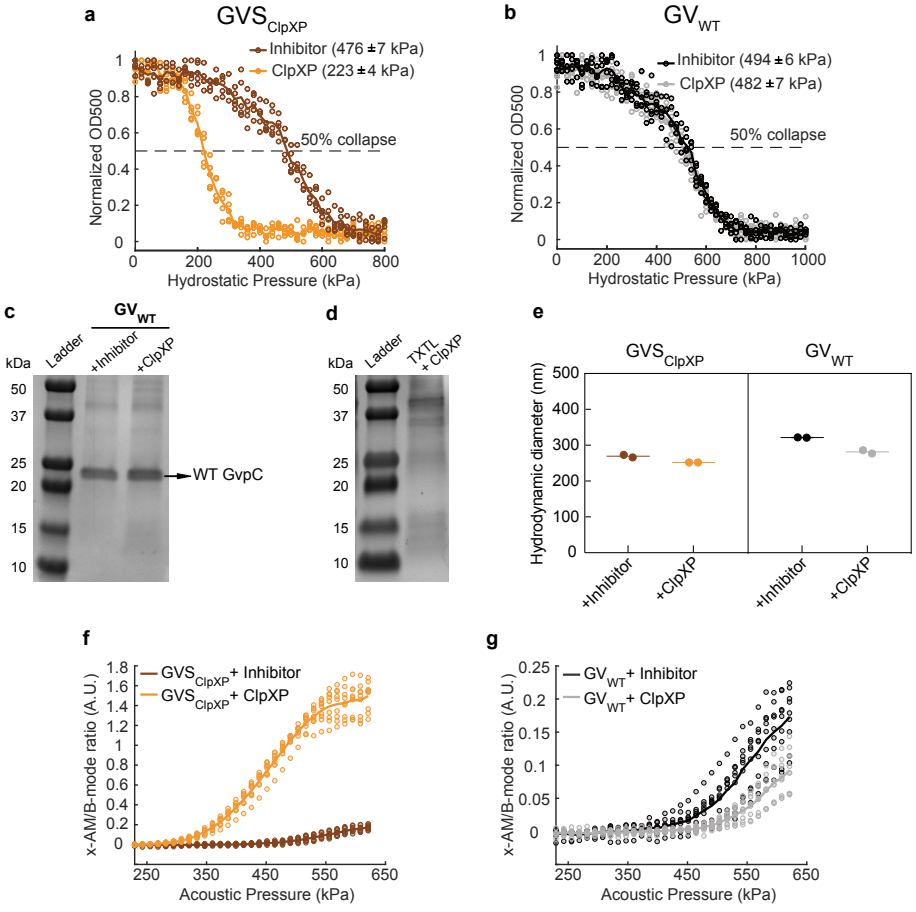

Extended Data Figure 3.4 | Engineering an acoustic sensor of ClpXP proteolytic activity. (**a, b**) Scatter plots for Figure. 3(**d, g**). N = 5 biological replicates. (**c**) Coomassie-stained SDS-PAGE gel of OD_{500nm}-matched GV_{WT} samples incubated in a reconstituted cell-free transcription-translation (TX-TL) system containing a protease inhibitor cocktail or ClpXP. N = 3 biological replicates. (**d**) Coomassie-stained SDS-PAGE gel of 30x diluted content of TX-TL system containing ClpXP. N = 2 biological replicates(**e**) DLS measurements showing the average hydrodynamic diameter of GVS_{ClpXP} and GV_{WT} samples, after incubations with protease inhibitor or ClpXP (N = 2 biological replicates, individual dots represent each N and horizontal line indicates the mean). (**f**, **g**) Scatter plots showing the ratio of x-AM to B-mode acoustic signal as a function of applied acoustic pressure for all the replicate samples used in the x-AM voltage ramp experiments for GVS_{ClpXP} (**f**) and GV_{WT} (**g**). N = 3 biological replicates, with each N consisting of 3 technical replicates. Individual dots represent each N and solid line represents the mean of all the replicates for **a**, **b, f** and **g**.

3.3.4 Constructing intracellular acoustic sensor genes

After demonstrating the performance of acoustic biosensors *in vitro*, we endeavored to show that they could respond to enzymatic activity inside living cells. As the cellular host, we chose *E. coli* Nissle 1917. This probiotic strain of *E. coli* has the capacity to colonize the mammalian gastrointestinal tract, and is widely used as a chassis for the development of microbial therapeutics[35-37], making it a valuable platform for intracellular biosensors. Recently, an engineered operon comprising GV-encoding genes from *Anabaena flos-aquae* and *Bacillus megaterium* was expressed in Nissle cells as acoustic reporter genes (*ARGs*), allowing gene expression to be imaged with linear B-mode ultrasound[8]. To develop an intracellular acoustic sensor gene targeting ClpXP (ASG_{ClpXP}), we swapped the wild type *gvpC* in the *ARG* gene cluster (ARG_{WT}) with the modified *gvpC* from GVS_{ClpXP} (dGvpC) (**Fig. 3.4a**). For a first test of this intracellular biosensor, we transformed it into wild-type (WT) Nissle cells, which natively express ClpXP protease, hypothesizing that it would show a reduced intracellular collapse pressure and enhanced nonlinear contrast compared to ARG_{WT}. Indeed, pressurized absorbance spectroscopy on intact cells expressing ASG_{ClpXP} revealed a reduction in the hydrostatic collapse pressure midpoint of ~ 160 kPa relative to cells expressing ARG_{WT} (**Extended Data Fig. 3.5**). In ultrasound imaging, live cells expressing ASG_{ClpXP} showed an enhancement in nonlinear contrast of approximately 13 dB (**Extended Data Fig. 3.5**), while linear B-mode signal was similar. The nonlinear response of ASG_{ClpXP} expressing cells was strongest beyond an acoustic pressure of 784 kPa (**Extended Data Fig. 3.5**).

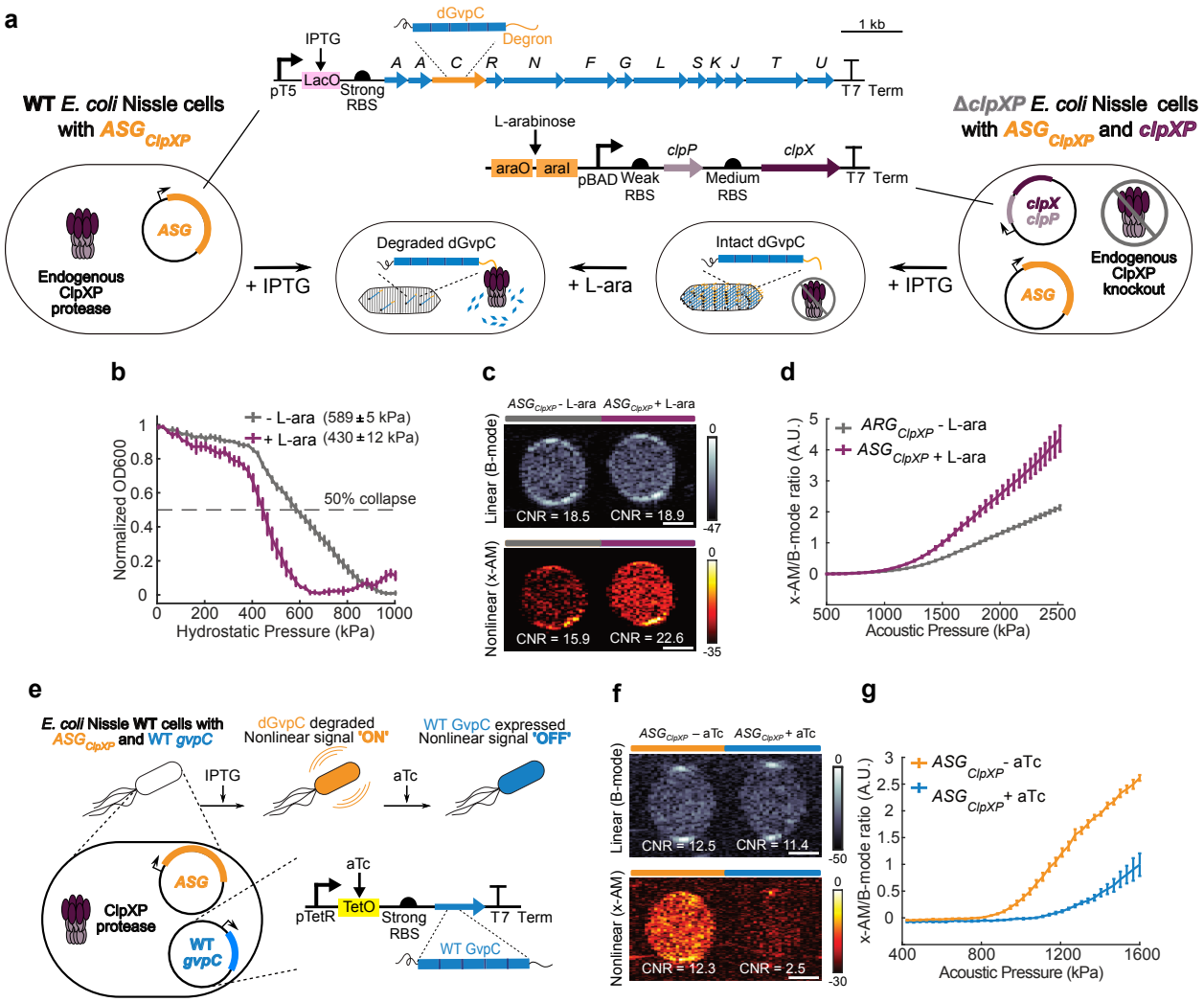

Figure 3.4: Monitoring intracellular protease activity and circuit-driven gene expression in engineered cells. (**a**) Schematic of *E. coli* Nissle cells expressing the acoustic sensor gene construct for ClpXP. In some cases, the Nissle cells are genomically modified to lack the *clpX* and *clpP* genes (Δ*clpXP*), and co-transformed with a plasmid encoding L-arabinose (L-ara) driven ClpXP. (**b**) Normalized pressure-sensitive optical density at 600 nm of Δ*clpXP* Nissle cells expressing ASG_{ClpXP} with or without L-ara induction of ClpXP protease expression. The legend lists the midpoint collapse pressure for each cell type (±95% confidence interval) determined from fitting a Boltzmann sigmoid function (N = 3 biological replicates). (**c**) Representative ultrasound images of Δ*clpXP* Nissle cells expressing ASG_{ClpXP} with or without L-ara induction of ClpXP protease at OD_{600nm} 1.5. (**d**) Average x-AM/B-mode ratio as a function of applied acoustic pressure for Δ*clpXP* Nissle cells expressing ASG_{ClpXP} with or without L-ara induction of ClpXP expression at OD_{600nm} 1.5. N=3 biological replicates, with each N having 3 technical replicates for **c** and **d**. (**e**) Schematic of pT5-LacO driven ASG_{ClpXP} and pTet-TetO driven WT *gvpC* gene circuits co-transformed into Nissle cells for dynamic switching of non-linear acoustic signals from the intracellular GV sensors in response to circuit-driven gene expression. (**f**) Representative ultrasound images of Nissle cells (OD_{600nm} 1) expressing ASG_{ClpXP}, with or without aTc induction to drive expression of WT GvpC. (**g**) Average x-AM/B-mode ratio as a function of applied acoustic pressure for Nissle cells expressing ASG_{ClpXP}, with or without aTc induction. N=5 biological replicates for **f** and **g**. CNR stands for contrast-to-noise-ratio, and color bars represent relative ultrasound signal intensity in the dB scale. The B-mode images were acquired at 309 kPa for (**c**) and 132 kPa for (**f**). The x-AM images were acquired at 1.61 MPa for (**c**), and 1.34 MPa for (**f**). Scale bars in **c** and **f** represent 1 mm.For **b**, **d** and **g**, solid curves represent the mean and error bars indicate SEM. Statistics were performed on data from independent biological replicates. Individual scatter plots for **b,d** and **g** are shown in **Extended Data Figure 3.5**.

Next, to examine the ability of *ASG*$_{ClpXP}$ to respond to intracellular enzymatic activity in a dynamic manner, we generated a ClpXP-deficient strain of Nissle cells (Δ*clpXP*) through genomic knock-out of the genes encoding ClpX and ClpP, and created a plasmid containing these two genes under the control of an arabinose-inducible promoter (**Fig. 3.4a**). This allowed us to externally control the activity of the ClpXP enzyme. Δ*clpXP* Nissle cells were co-transformed with an inducible *clpX-clpP* (*clpXP*) plasmid and *ASG*$_{ClpXP}$. ClpXP production in these cells after induction with L-arabinose resulted in an approximately 160 kPa reduction in the hydrostatic collapse pressure midpoint (**Fig. 3.4b and Extended Data Fig. 3.5**). Under ultrasound imaging, cells with induced ClpXP activity showed substantially stronger nonlinear contrast (+6.7 dB) compared to cells uninduced for this protease (**Fig. 3.4c**), while showing a similar B-mode signal. This enhancement in nonlinear signal was detectable with acoustic pressures above 950 kPa (**Fig. 3.4d and Extended Data Fig. 3.5**). These experiments demonstrate the ability of *ASG*$_{ClpXP}$ to function as an intracellular acoustic sensor to monitor variable enzyme activity.

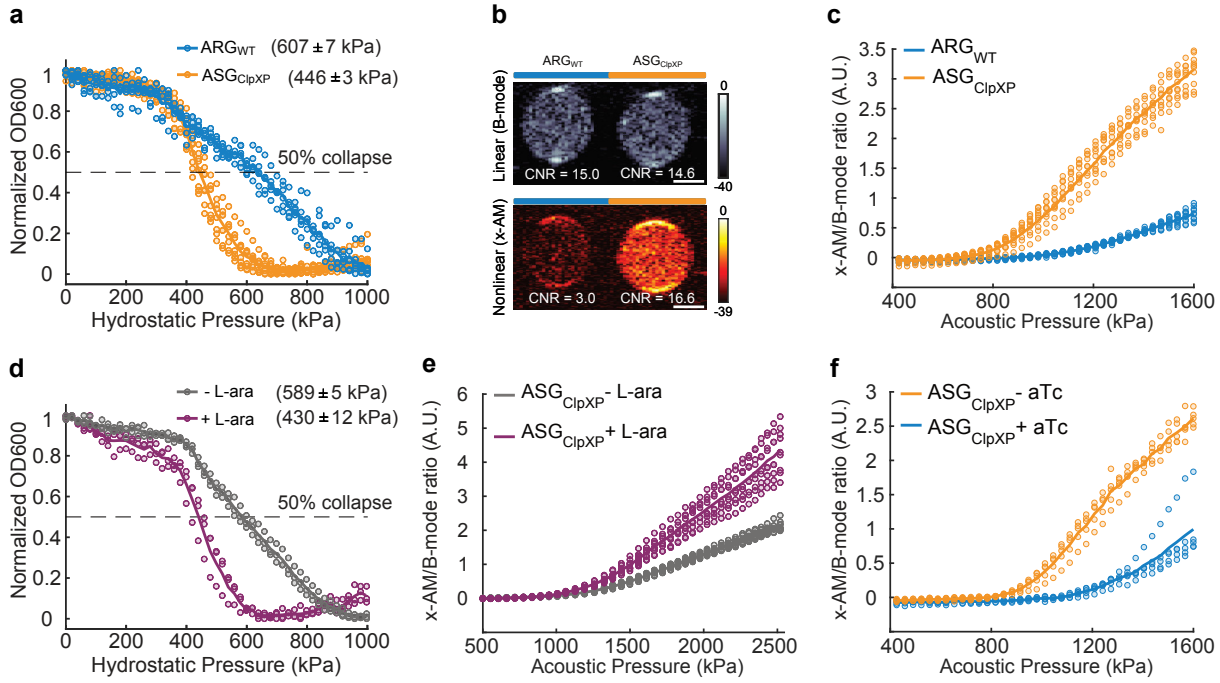

Extended Data Figure 3.5 | Constructing intracellular acoustic sensor genes for dynamic monitoring of protease activity and circuit-driven gene expression. (**a**) Normalized pressure-sensitive optical density at 600 nm of WT Nissle cells expressing either *ARG*$_{WT}$ or *ASG*$_{ClpXP}$. The legend lists the midpoint collapse pressure for each cell type (±95% confidence interval) determined from fitting a Boltzmann sigmoid function (N = 5 biological replicates and 8 total replicates for *ASG*$_{ClpXP}$; N = 3 biological replicates for *ARG*$_{WT}$ and 6 total replicates). (**b**) Representative ultrasound images of WT Nissle cells expressing either *ARG*$_{WT}$ or *ASG*$_{ClpXP}$ at OD$_{600nm}$ 1.5 (N = 4 biological replicates and the number of total replicates is 10). (**c**) Scatter plots showing x-AM/B-mode ratio as a function of applied acoustic pressure for WT Nissle cells expressing either *ARG*$_{WT}$ or *ASG*$_{ClpXP}$ at OD$_{600nm}$ 1.5 (N = 4 biological replicates and the number of total replicates is 10). (**d**) Scatter plots for Figure 3.4b, N = 3 biological replicates. (**e, f**) Scatter plots showing the ratio of x-AM to B-mode acoustic signal as a function of acoustic pressure for all the replicate samples used in the x-AM voltage ramp experiments for Δ*clpXP* Nissle cells expressing *ASG*$_{ClpXP}$ and araBAD driven *clpXP*, with or without L-arabinose induction (**e**) and WT Nissle cells expressing *ASG*$_{ClpXP}$ and pTet-TetO driven WT *gvpC*, with or without aTc induction (**f**). N = 3 biological replicates, with each N having 3 technical replicates for (**e**) and N

= 5 biological replicates for (**f**). Individual dots represent each N and solid line represents the mean of all the replicates for **a**, **c**, **d**, **e** and **f**.

A major application of dynamic sensors in cells is to monitor the activity of natural or synthetic gene circuits[38-40]. To test if our acoustic sensors could be used to track the output of a synthetic gene circuit in cells, we co-transformed WT Nissle cells with ASG_{ClpXP}, and a separate wild-type *gvpC* gene controlled by anhydrotetracycline (aTc) (**Fig. 3.4e**). Our hypothesis was that induction of this gene circuit only with IPTG would result in the production of GVs with ClpXP-degradable GvpC, resulting in nonlinear contrast, whereas the additional input of aTc would result in the co-production of non-degradable wild-type GvpC, which would take the place of any degraded engineered GvpC on the biosensor shell and lead to reduced nonlinear scattering (**Fig. 3.4e**). Indeed, when we induced cells with just IPTG we observed strong nonlinear contrast. However, when aTc was added to the cultures after IPTG induction, this contrast was reduced by approximately 10 dB (**Fig. 3.4f-g and Extended Data Fig. 3.5**). These results, together with our findings in Δ*clpXP* cells with inducible ClpXP, show that acoustic biosensors can be used to visualize the output of synthetic gene circuits.

3.3.5 Ultrasound imaging of intracellular ClpXP activity in vivo

Finally, after establishing the basic principles of acoustic biosensor engineering *in vitro* and demonstrating their performance in living cells, we assessed the ability of our sensor constructs to produce ultrasound contrast within a biologically relevant anatomical location *in vivo*. In particular, approaches to imaging microbes in the mammalian GI tract[8,41-43] are needed to support the study of their increasingly appreciated roles in health and disease[44,45] and the development of engineered probiotic agents[46,47]. The GI tract is also an excellent target for ultrasound imaging due to its relatively deep location inside the animal, and the use of ultrasound in clinical diagnosis and animal models of GI pathology, with appropriate measures taken to minimize potential interference from air bubbles and solid matter[48,49].

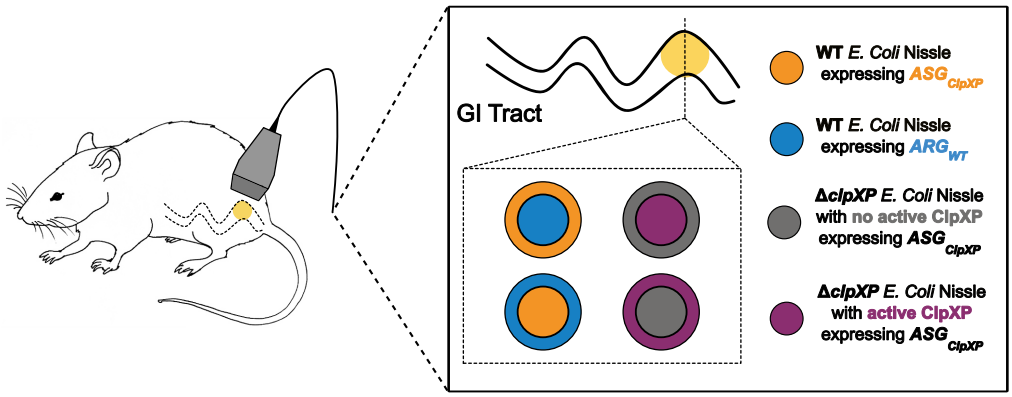

Extended Data Figure 3.6 | Schematic illustrating the *in vivo* ultrasound imaging experiment. Cells in cylindrical hydrogel with the indicated cross-sectional arrangements were injected into the GI tract of mice and imaged with ultrasound.

To demonstrate the ability of acoustic biosensors to produce nonlinear ultrasound contrast within the *in vivo* context of the mouse GI tract, we first co-injected WT Nissle cells expressing ASG_{ClpXP} and ARG_{WT} into the mouse colon (schematic shown in **Extended Data Fig. 3.6**), distributing one cell population along the lumen wall and the other in the lumen center. In these proof-of-concept experiments, the cells are introduced into the colon in a rectally-injected agarose hydrogel to enable precise positioning and control over composition. Using nonlinear ultrasound imaging, we could clearly visualize the unique contrast generated by the protease-sensitive *ASG*s as a bright ring of contrast lining the colon periphery (**Fig. 3.5a**). When the spatial arrangement was reversed, the bright nonlinear contrast was concentrated in the middle of the lumen (**Extended Data Fig. 3.7**). A comparison of ultrasound images acquired before and after acoustic collapse of the GVs, using a high-pressure pulse from the transducer, confirmed that the bright ring of nonlinear contrast was emanating from ASG_{ClpXP} -expressing cells (**Fig. 3.5a)**, and this result was consistent across independent experiments in 9 mice (**Fig. 3.5b).**

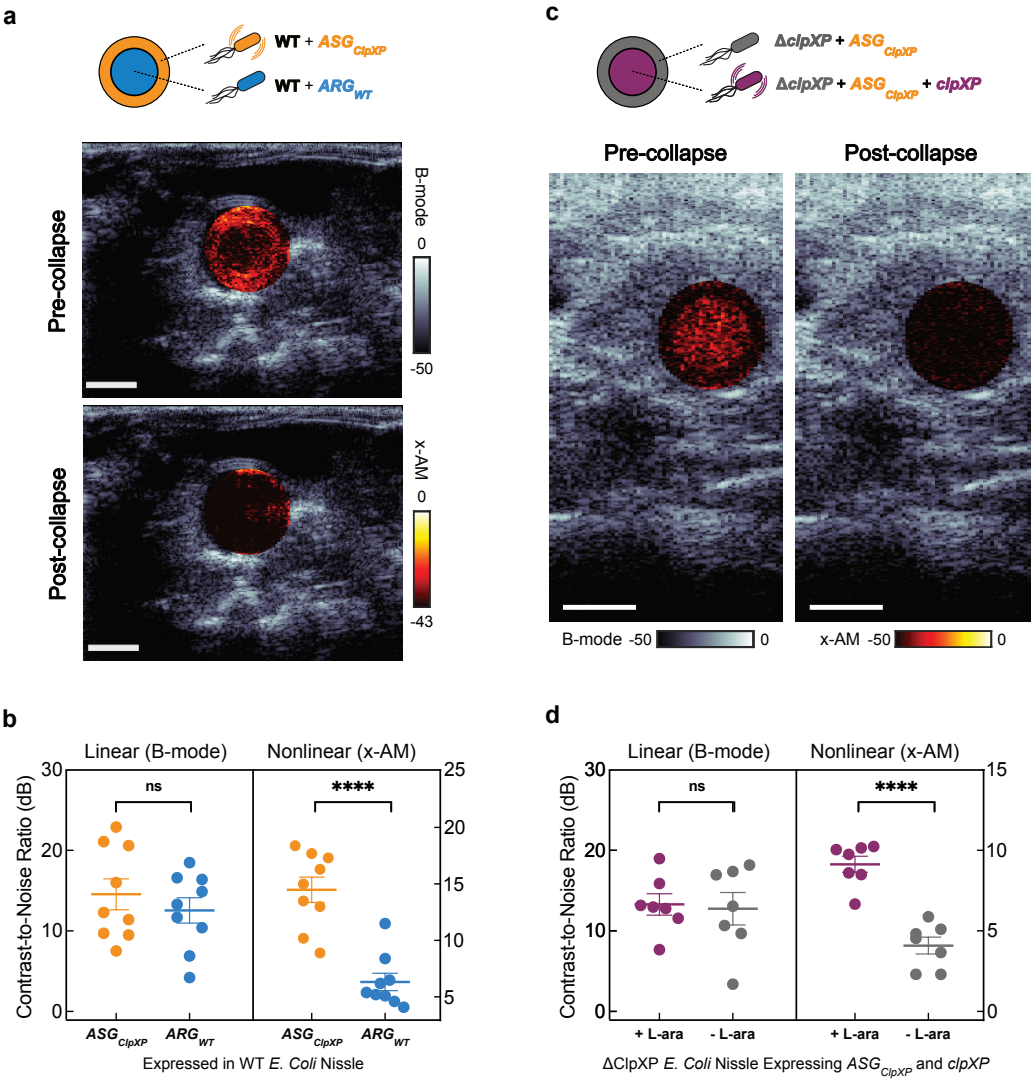

Figure 3.5: Ultrasound imaging of bacteria expressing acoustic sensor genes in the gastrointestinal tract of mice. (**a**) Transverse ultrasound image of a mouse whose colon contains WT Nissle cells expressing ARG_{WT} at the center of the lumen and the same strain expressing ASG_{ClpXP} at the periphery of the lumen. These imaging experiments were independently repeated 9 times with similar results. (**b**) B-mode and xAM contrast-to-noise ratio (CNR) *in vivo*, for WT Nissle cells expressing ARG_{WT} or ASG_{ClpXP}. N = 9 mice. P = 7.8E-5 for x-AM signal from cells expressing ASG_{ClpXP} versus the ARG_{WT} control and P = 0.2890 for B-mode signal. (**c**) Transverse ultrasound image of a mouse whose colon contains Δ*clpXP* Nissle cells expressing ASG_{ClpXP} with L-ara induction of ClpXP protease expression at the center and without L-ara induction at the periphery of the lumen. These imaging experiments were independently repeated 7 times with similar results. Cells were injected in agarose gel at a final concentration of 1.5E9 cells ml^{-1} for **a** and **c**. Nonlinear (x-AM) images of the colon, acquired at 1.27 MPa for (**a**) and 1.56 MPa for (**c**) before and after acoustic collapse (hot color map), are superimposed on linear (B-mode) anatomical images (bone colormap). Color bars represent relative ultrasound signal intensity on the dB scale. Scale bars represent 2 mm for **a** and **c**. (**d**) B-mode and xAM CNR *in vivo*, for Δ*clpXP* Nissle cells expressing ASG_{ClpXP} with or without L-ara induction of ClpXP expression. N = 7 mice. P = 1.8E-5 for x-AM signal from cells expressing ASG_{ClpXP} with ClpXP protease expression induced versus non- induced and P = 0.8293 for B-mode signal. Individual dots represent each N, and the thick horizontal line indicates the mean. Error bars indicate SEM. P-values were calculated using a two-tailed paired t-test.

To demonstrate *in vivo* imaging of enzyme activity, we introduced Δ*clpXP* Nissle cells expressing ASG_{ClpXP} into the mouse colon, with and without transcriptionally activating intracellular ClpXP (schematic shown in **Extended Data Fig. 3.6**) . As above, the cells were contained in an agarose hydrogel. Cells induced to express this enzyme showed enhanced nonlinear contrast compared to cells not expressing ClpXP (**Fig. 3.5c**). Acoustic collapse confirmed the acoustic biosensors as the primary source of nonlinear signal (**Fig. 3.5c**). This performance was consistent across 7 mice and 2 spatial arrangements of the cells (**Fig. 3.5d**). These results demonstrate the ability of acoustic biosensors to visualize enzyme activity within the context of *in vivo* imaging.

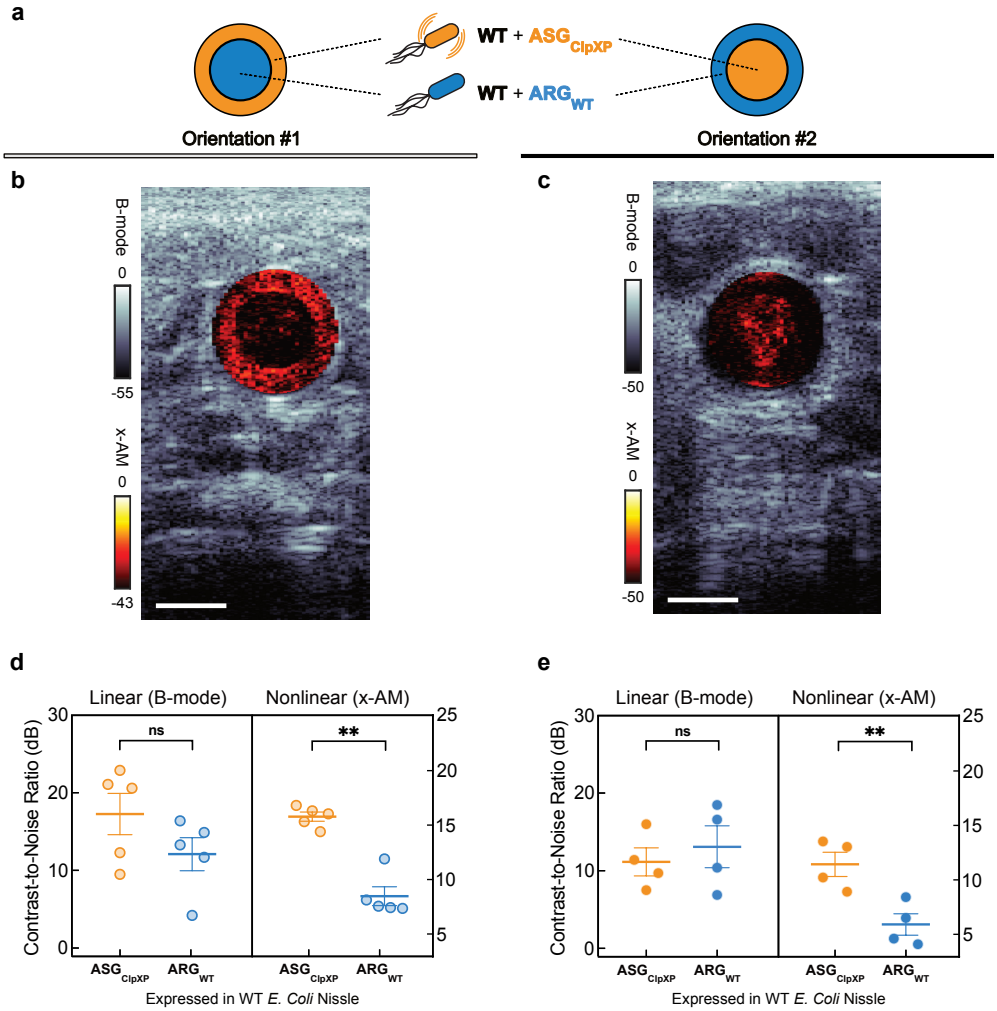

Extended Data Figure 3.7 | Ultrasound imaging of bacteria expressing acoustic sensor genes in the gastrointestinal tract of mice. (**a**) Schematic illustrating two orientations of the wild type (WT) *E. coli* Nissle cells expressing ARG_{WT} or ASG_{ClpXP} introduced into the mouse colon as a hydrogel. (**b, c**) Representative transverse ultrasound images of the colon for two mice used in the *in vivo* imaging experiments, with orientation #1 (**b**) and with orientation #2. (**c**). Cells are injected at a final concentration of 1.5E9 cells ml^{-1}. B-mode signal is displayed using the bone colormap and x-AM signal is shown using the hot colormap. Color bars represent B-mode and x-AM ultrasound signal intensity in the dB scale. Scale bars represent 2 mm. (**d, e**) B-mode and xAM contrast-to-noise ratio (CNR) *in vivo*, for WT Nissle cells expressing ARG_{WT} or ASG_{ClpXP} in orientation #1 (**d**) and orientation #2. (**e**). N = 5 mice for orientation #1 (**b, d**) and N = 4 mice for orientation #2 (**c, e**). Error bars indicate SEM. P = 0.0014 for x-AM signal from cells expressing ASG_{ClpXP} versus the ARG_{WT} control in orientation #1, and P = 0.0016 for that in orientation #2. P = 0.0570 for B-mode signal in orientation #1 and P = 0.3445 in orientation #2. P-values were calculated using a two-tailed paired t-test. Individual dots represent each N and horizontal line indicates the mean.

Besides molecular sensing, one additional benefit of the nonlinear contrast generated by ASG_{ClpXP} -expressing cells is to make the cells easier to detect relative to background tissue compared to linear B-mode imaging. Indeed, the nonlinear contrast of WT Nissle cells expressing ASG_{ClpXP} had a significantly higher contrast-to-tissue ratio than either the nonlinear contrast of ARG_{WT}-expressing cells, or the B-mode contrast of either of these two species (**Extended Data Fig. 3.8**).

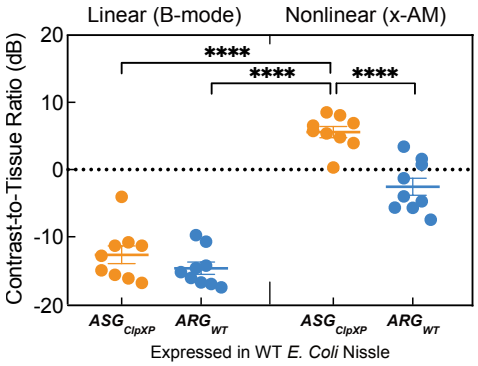

Extended Data Figure 3.8 | *ASG$_{ClpXP}$* -expressing cells showed higher contrast to tissue with nonlinear imaging. B-mode and xAM contrast-to-tissue ratio (CTR) *in vivo*, for WT Nissle cells expressing *ARG$_{WT}$* or *ASG$_{ClpXP}$* in both orientations. P = 7.8E-5 for the CTR from xAM imaging of cells expressing *ASG$_{ClpXP}$* versus CTR from xAM imaging of cells expressing *ARG$_{WT}$*. P = 1.4E-6 for the CTR from xAM imaging of cells expressing *ASG$_{ClpXP}$* versus CTR from B-mode imaging of cells expressing *ASG$_{ClpXP}$* and P = 4.9E-7 for the CTR from xAM imaging of cells expressing *ASG$_{ClpXP}$* versus CTR from B-mode imaging of cells expressing *ARG$_{WT}$*. Individual dots represent each N, and the thick horizontal line indicates the mean. Error bars indicate SEM. N = 9 mice. P-values were calculated using a two-tailed paired t-test for each comparison independently. Individual dots represent each N and horizontal line indicates the mean.

3.4 Discussion

Our results establish a paradigm for visualizing protease activity non-invasively with ultrasound imaging. This paradigm is enabled by the dependence of the buckling mechanics of GVs on the reinforcing protein GvpC, and the ability to turn this protein into a protease substrate by incorporating specific internal or terminal peptide sequences. Similar to the earliest work on fluorescent biosensors[23,24], this initial study has focused on proteases due to the importance of this class of enzymes in biology, their relatively compact recognition motifs, and the large impact of their activity on protein structure. Based on our success in sensing the function of three distinct proteases, we anticipate that the basic design strategy presented here should be applicable to many enzymes of this type.

Our study lends itself to numerous future investigations to extend the applications of acoustic protease sensors beyond the proof-of-concept demonstrations shown here. While our experiments in *E. coli* and within the mouse GI tract establish the critical ability of such biosensors to produce ultrasound contrast in relevant biological settings, additional application-centric optimizations would enable the use of these constructs to address specific problems in basic and synthetic biology. For example, purified acoustic biosensors could be designed to sense extracellular proteases, which play homeostatic and disease-causing roles in tissues ranging from extracellular matrix remodeling and blood clot formation to inter-cellular signaling. Meanwhile, the expression of acoustic biosensor genes in cells could be used to monitor natural cellular enzyme activity or serve as the output of synthetic signaling pathways. Intracellular use in bacteria could be particularly relevant in studying microbes in the mammalian GI tract, provided the successful adaptation of acoustic sensor genes to the relevant host species and ensuring successful delivery via oral gavage, colonization and metabolic viability. For potential applications in mammalian cells, acoustic protease sensor designs must be integrated into recently developed genetic programs enabling the expression of GVs in mammalian cells[50]. Successful use of acoustic sensors in this context will require increasing the level of mammalian GV expression to enable non-destructive nonlinear imaging.

In parallel, significant scope exists for further optimizing and generalizing the design of acoustic biosensors. While all three of our sensors produced detectable nonlinear contrast in response to protease activity, the changes exhibited by GVS_{ClpXP} were significantly larger than for the other two constructs. This is not surprising for an enzyme that processively degrades GvpC, and whose recognition motif can be incorporated outside the main GV-binding region of GvpC. Endopeptidase sensors could be optimized to reach similar performance by incorporating more than one cleavage site within the GvpC sequence and tuning the linkers connecting these sites to the rest of the protein. As with other protease biosensors, the irreversibility of proteolysis means that for repeated or continuous sensing, it is necessary for new sensor molecules to be synthesized or delivered. For genetically encoded biosensors, this occurs through gene expression, potentially posing a metabolic burden to the cell. For GVs, this burden could be reduced by re-expressing only the engineered GvpC rather than the full GV, since this protein can be added onto the shell of existing GVs, as demonstrated in this study and previous work[12]. Going beyond proteolytic sensors, we anticipate that our biosensor design strategy could be modified to enable allosteric conformational changes in GvpC, rather than its cleavage, to alter ultrasound contrast, thereby creating acoustic biosensors that respond reversibly to non-cleaving enzymes, ions or other signals of interest.

In addition to optimizing the biosensor constructs, it is also possible to improve the ultrasound techniques used for their visualization. In this study, we monitored the activation of our biosensors using a nonlinear x-AM pulse sequence, quantifying the resulting contrast relative to linear B-mode scattering. This ratiometric signal is advantageous for quantification in scenarios where the sensor concentration may vary. However, the dependence of the x-AM response on applied acoustic pressure introduces a variable that may differ across the ultrasonic field of view, and strategies involving dynamic pressure adjustment may be needed to obtain the optimal signal from each point in the imaged plane. In addition, normalization to B-mode signal in complex *in vivo* contexts may require methods to separate the linear scattering contributions of acoustic sensors from those of background tissue. With these improvements, acoustic biosensors promise to take dynamic imaging of molecular and cellular function to new depths.

References

1. Lin, M.Z. & Schnitzer, M.J. Genetically encoded indicators of neuronal activity. *Nature Neuroscience* **19**, 1142-1153 (2016).
2. Palmer, A.E., Qin, Y., Park, J.G. & McCombs, J.E. Design and application of genetically encoded biosensors. *Trends in Biotechnology* **29**, 144-152 (2011).
3. Rodriguez, E.A. et al. The growing and glowing toolbox of fluorescent and photoactive proteins. *Trends in Biochemical Sciences* **42**, 111-129 (2017).
4. Miyawaki, A. & Niino, Y. Molecular spies for bioimaging—fluorescent protein-based probes. *Molecular Cell* **58**, 632-643 (2015).
5. Piraner, D.I. et al. Going Deeper: Biomolecular Tools for Acoustic and Magnetic Imaging and Control of Cellular Function. *Biochemistry* (2017).
6. Maresca, D. et al. Biomolecular Ultrasound and Sonogenetics. *Annual Review of Chemical and Biomolecular Engineering* **9**, 229-252 (2018).
7. Shapiro, M.G. et al. Biogenic gas nanostructures as ultrasonic molecular reporters. *Nature Nanotechnology* **9**, 311-316 (2014).
8. Bourdeau, R.W. et al. Acoustic reporter genes for noninvasive imaging of microorganisms in mammalian hosts. *Nature* **553**, 86-90 (2018).
9. Walsby, A.E. Gas vesicles. *Microbiological Reviews* **58**, 94-144 (1994).
10. Pfeifer, F. Distribution, formation and regulation of gas vesicles. *Nature Reviews Microbiology* **10**, 705-715 (2012).
11. Farhadi, A. et al. Recombinantly Expressed Gas Vesicles as Nanoscale Contrast Agents for Ultrasound and Hyperpolarized MRI. *AIChE Journal* **64**, 2927-2933 (2018).
12. Lakshmanan, A. et al. Molecular Engineering of Acoustic Protein Nanostructures. *ACS Nano* **10**, 7314-7322 (2016).
13. Hayes, P., Buchholz, B. & Walsby, A. Gas vesicles are strengthened by the outer-surface protein, GvpC. *Archives of Microbiology* **157**, 229-234 (1992).
14. Maresca, D. et al. Nonlinear ultrasound imaging of nanoscale acoustic biomolecules. *Applied Physics Letters* **110**, 073701-073705 (2017).
15. Maresca, D., Sawyer, D.P., Renaud, G., Lee-Gosselin, A. & Shapiro, M.G. Nonlinear X-Wave Ultrasound Imaging of Acoustic Biomolecules. *Physical Review X* **8**, 041001-0410012 (2018).
16. Lopez-Otin, C. & Bond, J.S. Proteases: multifunctional enzymes in life and disease. *Journal of Biological Chemistry* **283**, 30433-7 (2008).

17. Drag, M. & Salvesen, G.S. Emerging principles in protease-based drug discovery. *Nature Reviews Drug Discovery* **9**, 690 (2010).
18. Sauer, R.T. & Baker, T.A. AAA+ proteases: ATP-fueled machines of protein destruction. *Annual Review of Biochemistry* **80**, 587-612 (2011).
19. Turk, B., Turk, D. & Turk, V. Protease signalling: the cutting edge. *The EMBO Journal* **31**, 1630-1643 (2012).
20. Stein, V. & Alexandrov, K. Protease-based synthetic sensing and signal amplification. *Proceedings of the National Academy of Sciences* **111**, 15934-15939 (2014).
21. Fernandez-Rodriguez, J. & Voigt, C.A. Post-translational control of genetic circuits using Potyvirus proteases. *Nucleic Acids Research* **44**, 6493-6502 (2016).
22. Gao, X.J., Chong, L.S., Kim, M.S. & Elowitz, M.B. Programmable protein circuits in living cells. *Science* **361**, 1252-1258 (2018).
23. Mitra, R.D., Silva, C.M. & Youvan, D.C. Fluorescence resonance energy transfer between blue-emitting and red-shifted excitation derivatives of the green fluorescent protein. *Gene* **173**, 13-17 (1996).
24. Heim, R. & Tsien, R.Y. Engineering green fluorescent protein for improved brightness, longer wavelengths and fluorescence resonance energy transfer. *Current Biology* **6**, 178-182 (1996).
25. Ong, I.L.H. & Yang, K.L. Recent developments in protease activity assays and sensors. *Analyst* **142**, 1867-1881 (2017).
26. Phan, J. et al. Structural basis for the substrate specificity of tobacco etch virus protease. *Journal of Biological Chemistry* **277**, 50564-50572 (2002).
27. Parks, T.D., Leuther, K.K., Howard, E.D., Johnston, S.A. & Dougherty, W.G. Release of proteins and peptides from fusion proteins using a recombinant plant virus proteinase. *Analytical Biochemistry* **216**, 413-417 (1994).
28. Lakshmanan, A. et al. Preparation of biogenic gas vesicle nanostructures for use as contrast agents for ultrasound and MRI. *Nature Protocols* **12**, 2050 (2017).
29. Goll, D.E., Thompson, V.F., Li, H., Wei, W.E.I. & Cong, J. The calpain system. *Physiological Reviews* **83**, 731-801 (2003).
30. Ono, Y. & Sorimachi, H. Calpains—an elaborate proteolytic system. *Biochimica et Biophysica Acta (BBA)-Proteins and Proteomics* **1824**, 224-236 (2012).
31. Ono, Y., Saido, T.C. & Sorimachi, H. Calpain research for drug discovery: challenges and potential. *Nature Reviews Drug Discovery* **15**, 854-876 (2016).
32. Suzuki, S. et al. Development of an artificial calcium-dependent transcription factor to detect sustained intracellular calcium elevation. *ACS Synthetic Biology* **3**, 717-722 (2014).

33. Sauer, R.T. et al. Sculpting the proteome with AAA(+) proteases and disassembly machines. *Cell* **119**, 9-18 (2004).
34. Baker, T.A. & Sauer, R.T. ClpXP, an ATP-powered unfolding and protein-degradation machine. *Biochimica et Biophysica Acta (BBA)-Molecular Cell Research* **1823**, 15-28 (2012).
35. Sonnenborn, U. & Schulze, J. The non-pathogenic Escherichia coli strain Nissle 1917–features of a versatile probiotic. *Microbial Ecology in Health and Disease* **21**, 122-158 (2009).
36. Danino, T. et al. Programmable probiotics for detection of cancer in urine. *Science Translational Medicine* **7**, 289ra84 (2015).
37. Blum-Oehler, G. et al. Development of strain-specific PCR reactions for the detection of the probiotic Escherichia coli strain Nissle 1917 in fecal samples. *Research in Microbiology* **154**, 59-66 (2003).
38. Elowitz, M.B. & Leibler, S. A synthetic oscillatory network of transcriptional regulators. *Nature* **403**, 335-338 (2000).
39. Khalil, A.S. & Collins, J.J. Synthetic biology: applications come of age. *Nature Reviews Genetics* **11**, 367-379 (2010).
40. Tigges, M., Marquez-Lago, T.T., Stelling, J. & Fussenegger, M. A tunable synthetic mammalian oscillator. *Nature* **457**, 309-312 (2009).
41. Mark Welch, J.L., Hasegawa, Y., McNulty, N.P., Gordon, J.I. & Borisy, G.G. Spatial organization of a model 15-member human gut microbiota established in gnotobiotic mice. *Proceedings of the National Academy of Sciences* **114**, E9105-E9114 (2017).
42. Geva-Zatorsky, N. et al. In vivo imaging and tracking of host-microbiota interactions via metabolic labeling of gut anaerobic bacteria. *Nature Medicine* **21**, 1091-100 (2015).
43. Foucault, M.L., Thomas, L., Goussard, S., Branchini, B.R. & Grillot-Courvalin, C. In vivo bioluminescence imaging for the study of intestinal colonization by Escherichia coli in mice. *Applied and Environmental Microbiology* **76**, 264-74 (2010).
44. Round, J.L. & Mazmanian, S.K. The gut microbiota shapes intestinal immune responses during health and disease. *Nature Reviews Immunology* **9**, 313-323 (2009).
45. Derrien, M. & Vlieg, J.E.T.V. Fate, activity, and impact of ingested bacteria within the human gut microbiota. *Trends in Microbiology* **23**, 354-366 (2015).
46. Steidler, L. et al. Treatment of murine colitis by Lactococcus lactis secreting interleukin-10. *Science* **289**, 1352-1355 (2000).
47. Daniel, C., Roussel, Y., Kleerebezem, M. & Pot, B. Recombinant lactic acid bacteria as mucosal biotherapeutic agents. *Trends in Biotechnology* **29**, 499-508 (2011).

48. Muradali, D. & Goldberg, D.R. US of gastrointestinal tract disease. *Radiographics* **35**, 50-68 (2015).

49. Machtaler, S., Knieling, F., Luong, R., Tian, L. & Willmann, J.K. Assessment of inflammation in an acute on chronic model of inflammatory bowel disease with ultrasound molecular imaging. *Theranostics* **5**, 1175 (2015).

50. Farhadi, A., Ho, G.H., Sawyer, D.P., Bourdeau, R.W. & Shapiro, M.G. Ultrasound imaging of gene expression in mammalian cells. *Science* **365**, 1469 (2019).

3.5 Methods

3.5.1 Design and cloning of genetic constructs

All gene sequences were codon optimized for *E.Coli* expression and inserted into their plasmid backbones via Gibson Assembly or KLD Mutagenesis using enzymes from New England Biolabs and custom primers from Integrated DNA Technologies. The protease recognition sequences for TEV protease and μ-calpain, flanked by flexible linkers, were introduced by substitution-insertion into the second repeat of the wild-type Ana *gvpC* gene sequence in a pET28a expression vector (Novagen) driven by a T7 promoter and lac operator. The ssrA degradation tag for the ClpXP bacterial proteasome was appended to the C-terminus of Ana *gvpC* using a short flexible linker. The acoustic sensor gene for intracellular protease sensing of ClpXP was constructed by modifying of the acoustic reporter gene cluster *ARG1*[8], by addition of the ssrA degradation tag to the C-terminal of *gvpC* using a linker sequence. For expression in *E.coli* Nissle 1917 cells, the pET28a T7 promoter was replaced by the T5 promoter. For inducible expression of *clpX* and *clpP*, the genes encoding those two proteins were cloned from the *E. coli* Nissle 1917 genome into a modified pTARA backbone under a P_{BAD} promoter and araBAD operon. For dynamic regulation of intracellular sensing, the wild-type GvpC sequence was cloned into a modified pTARA backbone under a pTet promoter and tetracycline operator. The complete list and source of plasmids used in this study is given in **Supplementary Table 1**. Plasmid constructs were cloned using NEB Turbo *E. Coli* (New England Biolabs) and sequence-validated.

3.5.2 Construction of *clpX*$^-$ *clpP*$^-$ strain of *E.coli* Nissle 1917 (Δ*clpXP*)

The knockout of *clpX* and *clpP* in *E.coli* Nissle (ECN) was accomplished by Lambda Red recombineering using previously published methods[51]. A FRT-flanked *cat* gene was recombined into ECN genome to replace the *clpX* and *clpP* genes, and the integrated *cat* gene was then removed by the *FLP* recombinase from pE-FLP[52] to yield the Δ*clpXP* strain. More information on the recombineering plasmids used in this study and their source is provided in **Supplementary Table 1**.

3.5.3 GV expression, purification and quantification

For *in vitro* assays, GVs were harvested and purified from confluent *Ana* cultures using previously published protocols[12,28]. Briefly, Ana cells were grown in Gorham's media supplemented with BG-11 solution (Sigma) and 10 mM sodium bicarbonate at 25°C, 1% CO_2 and 100 rpm shaking, under a 14h light and 10h dark cycle. Confluent cultures were transferred to sterile separating funnels and left undisturbed for 2-3 days to allow buoyant *Ana* cells expressing GVs to float to the top and for their subnatant to be drained. Hypertonic lysis with 10% Solulyse (Genlantis) and 500 mM sorbitol was used to release and harvest the Ana GVs. Purified GVs were obtained through 3-4 rounds of centrifugally assisted floatation,

with removal of the subnatant and resuspension in phosphate buffered saline (PBS, Corning) after each round.

For expression of acoustic reporter/sensor genes (*ARG/ASG*) in bacteria, wild-type *E. Coli* Nissle 1917 cells (Ardeypharm GmbH) were made electrocompetent and transformed with the genetic constructs. After electroporation, cells were rescued in SOC media supplemented with 2% glucose for 1h at 37°C. Transformed cells were grown for 12-16 hours at 37°C in 5 mL of LB medium supplemented with 50 μg/mL kanamycin and 2% glucose. Large-scale cultures for expression were prepared by a 1:100 dilution of the starter culture in LB medium containing 50 μg/mL kanamycin and 0.2% glucose. Cells were grown at 37°C to an OD_{600nm} of 0.2-0.3, then induced with 3μM Isopropyl β-D-1-thiogalactopyranoside (IPTG) and allowed to grow for 22 hrs at 30°C. Buoyant *E.Coli* Nissle cells expressing GVs were isolated from the rest of the culture by centrifugally assisted floatation in 50 mL conical tubes at 300g for 3-4 hrs, with a liquid column height less than 10 cm to prevent GV collapse by hydrostatic pressure.

The concentration of Ana GVs was determined by measurement of their optical density (OD) at 500 nm (OD_{500}) using a Nanodrop spectrophotometer (Thermo Fisher Scientific), using the resuspension buffer or collapsed GVs as the blank. As established in previous work[28], the concentration of GVs at OD_{500} = 1 is approximately 114 pM and the gas fraction is 0.0417%. The OD of buoyant cells expressing GVs were quantified at 600 nm using the Nanodrop.

3.5.4 Bacterial expression and purification of GvpC variants

For expression of Ana GvpC variants, plasmids were transformed into chemically competent BL21(DE3) cells (Invitrogen) and grown overnight for 14-16 h at 37°C in 5 mL starter cultures in LB medium with 50 μg/mL kanamycin. Starter cultures were diluted 1:250 in Terrific Broth (Sigma) and allowed to grow at 37°C (250 rpm shaking) to reach an OD_{600nm} of 0.4-0.7. Protein expression was induced by addition of 1 mM IPTG, and the cultures were transferred to 30°C. Cells were harvested by centrifugation at 5500g after 6-8 hours. For the GvpC-ssrA variant, expression was carried out at 25°C for 8 hours to reduce the effect of protease degradation and obtain sufficient protein yield.

GvpC was purified from inclusion bodies by lysing the cells at room temperature using Solulyse (Genlantis), supplemented with lysozyme (400 μg/mL) and DNase I (10 μg/mL). Inclusion body pellets were isolated by centrifugation at 27,000g for 15 mins and then resuspended in a solubilization buffer comprising 20 mM Tris-HCl buffer with 500 mM NaCl and 6 M urea (pH: 8.0), before incubation with Ni-NTA resin (Qiagen) for 2 h at 4°C. The wash and elution buffers were of the same composition as the solubilization buffer, but with 20mM and 250 mM imidazole respectively. The concentration of the purified

protein was assayed using the Bradford Reagent (Sigma). Purified GvpC variants were verified to be >95% pure by SDS-PAGE analysis.

3.5.5 Preparation of gas vesicles for *in vitro* protease assays

Engineered GVs having protease-sensitive or wild-type GvpC were prepared using urea stripping and GvpC re-addition[12,28]. Briefly, Ana GVs were stripped of their native outer layer of GvpC by treatment with 6M urea solution buffered with 100 mM Tris- HCl (pH:8-8.5). Two rounds of centrifugally assisted floatation with removal of the subnatant liquid after each round were performed to ensure complete removal of native GvpC. Recombinant Ana GvpC variants purified from inclusion bodies were then added to the stripped Ana GVs in 6 M urea a 2-3x molar excess concentration determined after accounting for 1:25 binding ratio of GvpC: GvpA. For a twofold stoichiometric excess of GvpC relative to binding sites on an average Ana GV, the quantity of recombinant GvpC (in nmol) to be added to stripped GVs was calculated according to the formula: 2 * OD * 198 nM * volume of GVs (in liters). The mixture of stripped GVs (OD_{500nm} = 1-2) and recombinant GvpC in 6 M urea buffer was loaded into dialysis pouches made of regenerated cellulose membrane with a 6-8 kDa M.W. cutoff (Spectrum Labs). The GvpC was allowed to slowly refold onto the surface of the stripped GVs by dialysis in 4 L PBS for at least 12 h at 4 °C. Dialyzed GV samples were subjected to two or more rounds of centrifugally assisted floatation at 300 g for 3-4 h to remove any excess unbound GvpC. Engineered GVs were resuspended in PBS after subnatant removal and quantified using pressure-sensitive OD measurements at 500 nm using a Nanodrop.

3.5.6 Pressurized absorbance spectroscopy

Purified, engineered Ana GVs were diluted in experimental buffers to an OD_{500nm} ~ 0.2-0.4, and 400 µL of the diluted sample was loaded into a flow-through quartz cuvette with a pathlength of 1 cm (Hellma Analytics). Buoyant *E.Coli* Nissle cells expressing GVs were diluted to an OD_{600nm} of ~ 1 in PBS for measurements. A 1.5 MPa nitrogen gas source was used to apply hydrostatic pressure in the cuvette through a single valve pressure controller (PC series, Alicat Scientific), while a microspectrometer (STS-VIS, Ocean Optics) measured the OD of the sample at 500 nm (for Ana GVs) or 600 nm (for Nissle cells). The hydrostatic pressure was increased from 0 to 1 MPa in 20 kPa increments with a 7 second equilibration period at each pressure before OD measurement. Each set of measurements was normalized by scaling to the Min-Max measurement value, and the data was fitted using the Boltzmann sigmoid function $f(P) = 1 + e^{(P-P_c)/\Delta P^{-1}}$, with the midpoint of normalized OD change (P_c) and the 95% confidence intervals, rounded to the nearest integer, reported in the figures.

3.5.7 TEM sample preparation and imaging

Freshly diluted samples of engineered Ana GVs (OD_{500nm} ~ 0.3) in 10 mM HEPES buffer containing 150 mM NaCl (pH 8) were used for TEM. 2 µL of the sample was added to Formvar/carbon 200 mesh grids (Ted Pella) that were rendered hydrophilic by glow discharging (Emitek K100X). 2% uranyl acetate was added for negative staining. Images were acquired using the FEI Tecnai T12 LaB6 120kV TEM equipped with a Gatan Ultrascan 2k X 2k CCD and 'Leginon' automated data collection software suite.

3.5.8 Dynamic light scattering (DLS) measurements

Engineered Ana GVs were diluted to an OD_{500nm} ~ 0.2 in experimental buffers. 150-200 µL of the sample was loaded into a disposable cuvette (Eppendorf UVette®) and the particle size was measured using the ZetaPALS particle sizing software (Brookhaven instruments) with an angle of 90 ° and refractive index of 1.33.

3.5.9 Denaturing polyacrylamide gel electrophoresis (SDS-PAGE)

GV samples were OD_{500nm} matched and mixed 1:1 with 2x Laemmli buffer (Bio-Rad), containing SDS and 2-mercaptoethanol. The samples were then boiled at 95°C for 5 minutes and loaded into a pre-made polyacrylamide gel (Bio-Rad) immersed in 1x Tris-Glycine-SDS Buffer. 10 uL of Precision Plus Protein™ Dual Color Standards (Bio-Rad) was loaded as the ladder. Electrophoresis was performed at 120V for 55 minutes, after which the gel was washed in DI water for 15 minutes to remove excess SDS and commassie-stained for 1 hour in a rocker-shaker using the SimplyBlue SafeStain (Invitrogen). The gel was allowed to de-stain overnight in DI water before imaging using a Bio-Rad ChemiDoc™ imaging system.

3.5.10 *In vitro* protease assays

For *in vitro* assays with the TEV endopeptidase, recombinant TEV protease (R&D Systems, Cat. No. 4469-TP-200) was incubated (25% v/v fraction) with engineered Ana GVs resuspended in PBS (final OD_{500nm} in reaction mixture = 5-6) at 30°C for 14-16 h. This corresponds to a TEV concentration of 0.1~0.125 mg/mL (depending on the lot), within the range used in previous studies with this enzyme[53,54]. Engineered GVs with wild-type GvpC and TEV protease heat-inactivated at 80°C for 20-30 mins were used as the controls.

For *in vitro* assays with calpain, calpain-1 from porcine erythrocytes (Millipore Sigma, Cat. No. 208712) was incubated in a 10% v/v fraction with engineered Ana GVs in a reaction mixture containing 50 mM Tris-HCl, 50 mM NaCl, 5 mM 2-mercaptoethanol, 1 mM EDTA and 1 mM EGTA and 5 mM Ca^{2+} (pH: 7.5) This corresponds to a calpain concentration of ≥ 0.168 units per µl, with 1 unit defined by the manufacturer as sufficient to cleave 1 pmol of a control fluorogenic substrate in 1 min at 25˚C. The final concentration of engineered GVs in the reaction mixture was OD_{500nm} ~ 6 and the protease assay was carried

out at 25°C for 14-16h. Negative controls included the same reaction mixture without calpain, without calcium, or without calpain and calcium. Engineered GVs with WT-GvpC were used as additional negative controls.

For *in vitro* assays with ClpXP, a reconstituted cell-free transcription-translation (TX-TL) system adapted for ClpXP degradation assays[55] (gift from Zachary Sun and Richard Murray) was used. Briefly, cell-free extract was prepared by lysis of ExpressIQ *E.coli* cells (New England Biolabs), and mixed in a 44% v/v ratio with an energy source buffer, resulting in a master mix of extract and buffer comprising: 9.9 mg/mL protein, 1.5 mM each amino acid except leucine, 1.25 mM leucine, 9.5 mM Mg-glutamate, 95 mM K-glutamate, 0.33 mM DTT, 50 mM HEPES, 1.5 mM ATP and GTP, 0.9 mM CTP and UTP, 0.2 mg/mL tRNA, 0.26 mM CoA, 0.33 mM NAD, 0.75 mM cAMP, 0.068 mM folinic acid, 1 mM spermidine, 30 mM 3-PGA and 2% PEG-8000. For purified ClpX protein, a monomeric N-terminal deletion variant Flag-ClpXdeltaNLinkedHexamer-His6[56] (Addgene ID: 22143) was used. Post Ni-NTA purification, active fractions of ClpX hexamers with sizes above 250 kDa were isolated using a Supradex 2010/300 column, flash frozen at a concentration of 1.95 μM and stored at -80°C in a storage buffer consisting of: 50 mM Tris-Cl (pH 7.5), 100 mM NaCl, 1mM DTT, 1 mM EDTA and 2% DMSO. The final reaction mixture was prepared as follows: 75% v/v fraction of the master mix, 10% v/v of purified ClpX, 1nm of the purified pBEST-ClpP plasmid and engineered Ana GVs (concentration of OD_{500nm} = 2.5-2.7 in the reaction mixture). The mixture was made up to the final volume using ultrapure H_2O. The reaction was allowed to proceed at 30°C for 14-16 h. As a negative control, a protease inhibitor cocktail mixture (SIGMA*FAST*™, Millipore Sigma) was added to the reaction mixture at 1.65x the manufacturer-recommended concentration and pre-incubated at room temperature for 30 mins.

3.5.11 Dynamic sensing of ClpXP activity in Δ*clpXP E.Coli* Nissle 1917 cells

ClpXP *E. Coli* Nissle 1917 cells were made electrocompetent and co-transformed with the pET expression plasmid (Lac-driven) containing the *ASG* for ClpXP and a modified pTARA plasmid (pBAD-driven) containing the *clpX* and *clpP* genes. Electroporated cells were rescued in SOC media supplemented with 2% glucose for 2h at 37°C. Transformed cells were grown overnight at 37ºC in 5 mL LB medium supplemented with 50 μg/mL kanamycin, 25 μg/mL chloramphenicol and 2% glucose. Starter cultures were diluted 1:100 in LB medium with 50 μg/mL kanamycin, 25 μg/mL chloramphenicol and 0.2% glucose and allowed to grow at 37 °C to reach an OD_{600nm} of 0.2-0.3. *ASG* expression was induced with 3μM IPTG and the bacterial culture was transferred to the 30 °C incubator with 250 rpm shaking for 30 minutes. The culture was then split into two halves of equal volume, and one half was induced with 0.5% (weight fraction) L-arabinose for expression of ClpXP protease. Cultures with and without L-arabinose induction were allowed to grow for an additional 22 h at 30°C. Cultures were then spun down at 300 g in a refrigerated centrifuge

at 4 °C for 3-4 h in 50 mL conical tubes to isolate buoyant cells expressing GVs from the rest of the culture. The liquid column height was maintained at less than 10 cm to prevent GV collapse by hydrostatic pressure.

3.5.12 Dynamic sensing of circuit-driven gene expression in *E.Coli* Nissle 1917 cells

Electrocompetent *E. coli* Nissle cells were co-transformed with the pET expression plasmid (Lac-driven) containing the *ASG* for ClpXP and a modified pTARA plasmid[57] (Tet-driven) containing the WT Ana GvpC gene. Electroporated cells were rescued in SOC media supplemented with 2% glucose for 2h at 37°C. Transformed cells were grown overnight at 37ºC in 5 mL LB medium supplemented with 50 μg/mL kanamycin, 50 μg/mL chloramphenicol and 2% glucose. Starter cultures were diluted 1:100 in LB medium with 50 μg/mL kanamycin, 50 μg/mL chloramphenicol and 0.2% glucose and allowed to grow at 37 °C to reach an OD_{600nm} of 0.2-0.3. *ASG* expression was induced with 3 μM IPTG and the bacterial culture was transferred to 30 ºC incubator with 250 rpm shaking for 1.5-2 h. The culture was then split into two halves of equal volume, and one half was induced with 50 ng/mL aTc for expression of WT GvpC. Cultures with and without aTc induction were allowed to grow for an additional 20 h at 30°C. Cultures were then spun down at 300 g in a refrigerated centrifuge at 4 °C for 3-4 h in 50 mL conical tubes to isolate buoyant cells expressing GVs from the rest of the culture. The liquid column height was maintained at less than 10 cm to prevent GV collapse by hydrostatic pressure.

3.5.13 *In vitro* ultrasound imaging

Imaging phantoms were prepared by melting 1% agarose (w/v) in PBS and casting wells using a custom 3-D-printed template mold containing a 2-by-2 grid of cylindrical wells with 2 mm diameter and 1 mm spacing between the outer radii in the bulk material. Ana GV samples from *in vitro* assays or buoyant Nissle cells expressing GVs were mixed 1:1 with 1% molten agarose solution at 42°C and quickly loaded before solidification into the phantom wells. All samples and their controls were OD-matched using the Nanodrop prior to phantom loading, with the final concentration being OD_{500nm} = 2.2 for Ana GVs and OD_{600nm}= 1.0-1.5 for buoyant Nissle cells. Wells not containing sample were filled with plain 1% agarose. Hydrostatic collapse at 1.4 MPa was used to determine that the contribution to light scattering from GVs inside the cells was similar for those expressing the acoustic sensor gene and its wild-type *ARG* counterpart. The phantom was placed in a custom holder on top of an acoustic absorber material and immersed in PBS to acoustically couple the phantom to the ultrasound imaging transducer.

Imaging was performed using a Verasonics Vantage programmable ultrasound scanning system and a L22-14v 128-element linear array Verasonics transducer, with a specified pitch of 0.1 mm, an elevation focus of 8 mm, an elevation aperture of 1.5mm and a center frequency of 18.5 MHz with 67% -6 dB bandwidth. Linear imaging was performed using a conventional B-mode sequence with a 128-ray-lines

protocol. For each ray line, a single pulse was transmitted with an aperture of 40 elements. For nonlinear image acquisition, a custom cross-amplitude modulation (x-AM) sequence detailed in an earlier study[15], with an x-AM angle (θ) of 19.5° and an aperture of 65 elements, was used. Both B-mode and x-AM sequences were programmed to operate close to the center frequency of the transducer (15.625 MHz) and the center of the sample wells were aligned to the set transmit focus of 5 mm. Transmitted pressure at the focus was calibrated using a Precision Acoustics fiber-optic hydrophone system. Each image was an average of 50 accumulations. B-mode images were acquired at a transmit voltage of 1.6V (132 kPa), and an automated voltage ramp imaging script (programmed in MATLAB) was used to sequentially toggle between B-mode and x-AM acquisitions. The script acquired x-AM signals at each specified voltage step, immediately followed by a B-mode acquisition at 1.6V (132 kPa), before another x-AM acquisition at the next voltage step. For engineered Ana GVs subjected to *in vitro* protease assays, an x-AM voltage ramp sequence from 4V (230 kPa) to 10V (621 kPa) in 0.2V increments was used. For wild-type Nissle cells expressing GVs, an x-AM voltage ramp sequence from 7.5V (458 kPa) to 25V (1.6 MPa) in 0.5V increments was used. Samples were subjected to complete collapse at 25V with the B-mode sequence for 10 seconds, and the subsequent B-mode image acquired at 1.6V and x-AM image acquired at the highest voltage of the voltage ramp sequence was used as the blank for data processing. There was no significant difference between the signals acquired at specific acoustic pressures during a voltage ramp or after directly stepping to the same pressure (**Extended Data Fig. 3.9**).

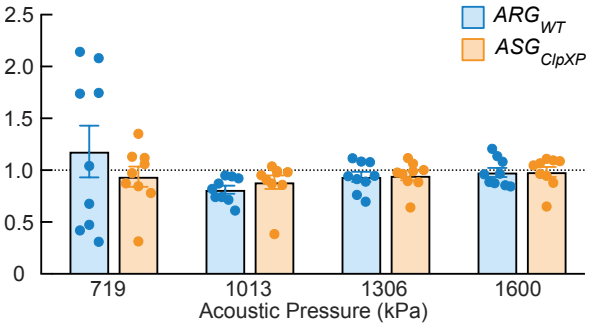

Extended Data Figure 3.9 | Absence of memory effect from imaging at sequentially increasing acoustic pressure. Ratio of sensor-specific signal (xAM/B-mode) acquired at the indicated acoustic pressures in the process of voltage ramping (comprising 36 points from 458 kPa to 1.6 MPa) or stepping the transducer output directly to corresponding pressure in a single step, for WT Nissle cells expressing either ARG_{WT} or ASG_{ClpXP}. N =3 biological replicates, with each N having 3 technical replicates. Individual dots represent each replicate, and the thick horizontal line indicates the mean. Error bars indicate SEM derived from biological replicates (see Online Methods).

Due to transducer failure, a replacement Verasonics transducer (L22-14vX) with similar specifications was used in experiments with Δ*clpXP* cells. The transmitted pressure at the focus was calibrated in the same way as the L22-14v. B-mode images were acquired at a transmit voltage of 1.6V (309 kPa), and an x-AM voltage ramp sequence from 6V (502 kPa) to 25V (2.52 MPa) was used. The imaging protocol was otherwise unchanged.

3.5.14 *In vivo* ultrasound imaging

All *in vivo* experiments were performed on C57BL/6J male mice, aged 14–34 weeks, under a protocol approved by the Institutional Animal Care and Use Committee of the California Institute of Technology. No randomization or blinding were necessary in this study. Mice were anesthetized with 1–2% isoflurane, maintained at 37 °C on a heating pad, depilated over the imaged region, and enema was performed by injecting PBS to expel gas and solid contents in mice colon. For imaging of *E. coli* in the gastrointestinal tract, mice were placed in a supine position, with the ultrasound transducer positioned on the lower abdomen, transverse to the colon such that the transmit focus of 5 mm was close to the center of the colon lumen. Prior to imaging, two variants of buoyancy-enriched *E. coli* Nissle 1917 were mixed in a 1:1 ratio with 4% agarose in PBS at 42 °C, for a final bacterial concentration of 1.5E9 cells ml^{-1}. An 8-gauge gavage needle was filled with the mixture of agarose and bacteria of one cell population. Before it solidified, a 14-gauge needle was placed inside the 8-gauge needle to form a hollow lumen within the gel. After the agarose–bacteria mixture solidified at room temperature for 10 min, the 14-gauge needle was removed. The hollow lumen was then filled with the agarose–bacteria of the other cell population. After it solidified, the complete cylindrical agarose gel was injected into the colon of the mouse with a PBS back-filled syringe. For the colon imaging, imaging planes were selected to avoid gas bubbles in the field of view. In all *in vivo* experiments, three transducers were used, including two L22-14v and one L22-14vX, due to transducer failures unrelated to this study. B-mode images were acquired at 1.9V (corresponding to 162 kPa in water) for L22-14v, and 1.6V (309 kPa in water) for L22-14vX. x-AM images were acquired at 20V (1.27 MPa in water) for L22-14v and 15V (1.56 MPa in water) for L22-14vX, with other parameters being the same as those used for *in vitro* imaging. B-mode anatomical imaging was performed at 7.4V using the 'L22-14v WideBeamSC' script provided by Verasonics.

3.5.15 Image processing and data analysis

All *in vitro* and *in vivo* ultrasound images were processed using MATLAB. Regions of interest (ROIs) were manually defined so as to adequately capture the signals from each sample well or region of the colon. The sample ROI dimensions (1.2 mm × 1.2 mm square) were the same for all *in vitro* phantom experiments. The noise ROI was manually selected from the background for each pair of sample wells. For the *in vivo* experiments, circular ROIs were manually defined to avoid edge effects from the skin or colon wall, and the tissue ROIs were defined as the rest of the region within the same depth range of the signal ROIs. For each ROI, the mean pixel intensity was calculated, and the pressure-sensitive ultrasound intensity ($\Delta I = I_{\mathrm{intact}} - I_{\mathrm{collapsed}}$) was calculated by subtracting the mean pixel intensity of the collapsed image from the mean pixel intensity of the intact image. The contrast-to-noise ratio (CNR) was calculated for each sample well by taking the mean intensity of the sample ROI over the mean intensity of the noise ROI. The x-AM

by B-mode ratio at a specific voltage (or applied acoustic pressure) was calculated with the following formula:

$$\frac{\Delta I_{x-AM}(V)}{\Delta I_{B-mode}(V)}$$

where $\Delta I_{x-AM}(V)$ is the pressure-sensitive nonlinear ultrasound intensity acquired by the x-AM sequence at a certain voltage V, and $\Delta I_{B-mode}(V)$ is the pressure-sensitive linear ultrasound intensity of the B-mode acquisitions at 1.6V (132 kPa) following the x-AM acquisitions at the voltage V. All images were pseudo-colored (bone colormap for B-mode images, hot colormap for x-AM images), with the maximum and minimum levels indicated in the accompanying color bars.

3.5.16 Statistical analysis

Data is plotted as the mean $\pm$ standard error of the mean (SEM). Sample size is N=3 biological replicates in all *in vitro* experiments unless otherwise stated. For each biological replicate, there were technical replicates to accommodate for variability in experimental procedures such as sample loading and pipetting. SEM was calculated by taking the values for the biological replicates, each of which was the mean of its technical replicates. The numbers of biological and technical replicates were chosen based on preliminary experiments such that they would be sufficient to report significant differences in mean values. Individual data for each replicate is given in **Extended Data Figures 1-9** in the form of scatter plots. P values, for determining the statistical significance for the *in vivo* data, were calculated using a two-tailed paired t-test.

Methods-only references

51. Datsenko, K.A. & Wanner, B.L. One-step inactivation of chromosomal genes in Escherichia coli K-12 using PCR products. *Proceedings of the National Academy of Sciences* **97**, 6640-6645 (2000).
52. St-Pierre, F. et al. One-step cloning and chromosomal integration of DNA. *ACS Synthetic Biology* **2**, 537-541 (2013).
53. Raran-Kurussi, S., Cherry, S., Zhang, D. & Waugh, D.S. Removal of Affinity Tags with TEV Protease. in *Heterologous Gene Expression in E.coli: Methods and Protocols* (ed. Burgess-Brown, N.A.) 221-230 (Springer New York, New York, NY, 2017).
54. Sequeira, A.F. et al. Gene design, fusion technology and TEV cleavage conditions influence the purification of oxidized disulphide-rich venom peptides in Escherichia coli. *Microbial Cell Factories* **16**, 4 (2017).
55. Zachary, Z.S., Jongmin, K., Vipul, S. & Richard, M.M. Protein degradation in a TX-TL cell-free expression system using ClpXP protease. *bioRxiv* (2015).

56. Martin, A., Baker, T.A. & Sauer, R.T. Rebuilt AAA + motors reveal operating principles for ATP-fuelled machines. *Nature* **437**, 1115-1120 (2005).

57. Wycuff, D.R. & Matthews, K.S. Generation of an AraC-araBAD promoter-regulated T7 expression system. *Analytical Biochemistry* **277**, 67-73 (2000).

3.6 Supplementary Material

Plasmid Name	Description and Purpose	Transcriptional regulators	Output gene product(s)	Insertions/Tags (including linkers)	Reference Information
WT C-His Ana GvpC in pET28a	Ana *gvpC* used as wild-type control for TEV and calpain sensor	pT7, LacO	WT C-His Ana GvpC	SLE-His6 at C-terminus	Addgene ID# 85732
WT N-His Ana GvpC in pET28a	Ana *gvpC* used as wild-type control for ClpXP sensor	pT7, LacO	WT N-His-Ana-GvpC	G-His6-SG at N-terminus	Addgene ID# 153294
C-His-GvpC-TEV	Ana *gvpC* with TEV cleavage site	pT7, LacO	C-His Ana GvpC with TEV cleavage site	SLE-His6 at C-terminus, GSGSGSG-ENLYFQG-SGSGSG in GvpC repeat 2	Addgene ID# 153296
C-His-GvpC-Calpain	Ana *gvpC* with calpain cleavage site	pT7, LacO	C-His Ana GvpC with calpain cleavage site	SLE-His6 at C-terminus, GSGSG-QQEVYGMMPRD-GSGSG in GvpC repeat 2	Addgene ID# 153295
N-His-GvpC-ssrA	Ana *gvpC* with ssrA degradation tag	pT7, LacO	N-His Ana GvpC with ssrA degradation tag	G-His6-SG at N-terminus, SG-AANDENYALAA at C-terminus	Addgene ID# 153297
pBEST_OR2_OR1-Pr-UTR1_ClpP-T500	*clpP* plasmid for use in the cell-free TX-TL system	OR2-OR1-Pr	ClpP		Addgene ID# 153302
pACYC-FLAG-dN6-His	*clpX* plasmid for use in the cell-free TX-TL system	pT7, LacO	Flag-ClpXdeltaNLinkedHexamer-His6	Flag tag at N-terminus His6 at C-terminus	Addgene ID# 22143

				L20 linkers	
pET28a_T5-ARG1	Original acoustic reporter gene construct (ARG_{WT})	pT5, LacO	Ana GvpA, WT Ana GvpC, Mega GvpR-U		Addgene ID # 106476
pET28a-T5-ASG_ClpXP	Acoustic sensor gene for ClpXP (ASG_{ClpXP})	pT5, LacO	Ana GvpA, dGvpC, Mega GvpR-U	SG-AANDENYALAA at C-terminus	Addgene ID# 153299
pKD3	Frt-flanked cat cassette for recombineering		CAT		Addgene ID # 45604
pKD46	Plasmid that carries the Lambda Red recombineering system	pBAD, araBAD operon	Gam, Beta, Exo		Coli Genetic Stock Center
pE-FLP	*FLP* recombinase to remove the integration module in reombineering	pE	FLP		Addgene ID # 45978
araBAD-BCD20-ClpP-BCD17-ClpX	Expression of *clpX* and *clpP* under araBAD promoter	pBAD, araBAD operon	ClpX, ClpP		Addgene ID # 153301
pTetR-BCD2-Ana GvpC	Wild-type Ana *gvpC* under Tet promoter	pTet, TetO	WT Ana GvpC		Addgene ID # 153298

Supplementary Table 3.1: List and features of genetic constructs used in this study.

pKD3[1] was a gift from Barry L. Wanner (Addgene plasmid # 45604 ; http://n2t.net/addgene:45604 ; RRID:Addgene_45604). pKD46[1] was obtained from the Coli Genetic Stock Center (CGSC, https://cgsc.biology.yale.edu/Site.php?ID=64672).

pE-FLP[2] was a gift from Drew Endy & Keith Shearwin (Addgene plasmid # 45978;http://n2t.net/addgene:45978 ; RRID:Addgene_45978).

The pBEST_OR2-OR1-Pr-UTR1_ClpP-T500 was a gift from Zachary Sun and Richard Murray[3].

pACYC-FLAG-dN6-His[4] was a gift from Robert Sauer (Addgene plasmid # 22143 ; http://n2t.net/addgene:22143 ; RRID:Addgene_22143)

The pTARA backbone was modified to make the araBAD-BCD20-ClpP-BCD17-ClpX and pTEtR-BCD2-Ana GvpC constructs. pTARA[5] was a gift from Kathleen Matthews (Addgene plasmid # 31491; http://n2t.net/addgene:31491 ; RRID:Addgene_31491).

REFERENCES FOR SUPPLEMENTARY INFORMATION:

1. Datsenko, K.A. & Wanner, B.L. One-step inactivation of chromosomal genes in Escherichia coli K-12 using PCR products. *Proceedings of the National Academy of Sciences* **97**, 6640-6645 (2000).
2. St-Pierre, F. et al. One-step cloning and chromosomal integration of DNA. *ACS Synthetic Biology* **2**, 537-541 (2013).
3. Zachary, Z.S., Jongmin, K., Vipul, S. & Richard, M.M. Protein degradation in a TX-TL cell-free expression system using ClpXP protease. *bioRxiv* (2015).
4. Martin, A., Baker, T.A. & Sauer, R.T. Rebuilt AAA + motors reveal operating principles for ATP-fuelled machines. *Nature* **437**, 1115-1120 (2005).
5. Wycuff, D.R. & Matthews, K.S. Generation of an AraC-araBAD promoter-regulated T7 expression system. *Analytical Biochemistry* **277**, 67-73 (2000).

Chapter 4

ULTRASENSITIVE ULTRASOUND IMAGING OF GENE EXPRESSION WITH SIGNAL UNMIXING

This chapter is in large part a reformatted version of the manuscript entitled "Ultrasensitive Ultrasound Imaging of Gene Expression with Signal Unmixing" submitted by Sawyer, D. P., Bar-Zion, A., Farhadi, A., Lee-Gosselin, A., Shrivaei, S. and Shapiro, M. G. to *Nature Methods* and currently under peer review. Under the supervision of Mikhail Shapiro, my contributions to this work were to conceive, design, and conduct the experiments, design and optimize the ultrasound pulse sequence and reconstruction algorithm, analyzed the data, and write the manuscript. Thanks to Avinoam Bar-Zion for assisting with the preparation of engineered bacterial cells, Arash Farhadi for preparation of the engineered mammalian cells, Audrey Lee-Gosselin for assistance with the animal experiments, and Shirin Shrivaei for performing the flow cytometry experiments.

Additionally, section 4.3.6 includes previously-unpublished data demonstrating the ability of BURST+ to detect single GVs in free suspension.

4.1 Abstract

Acoustic reporter genes (ARGs) enable biomedical ultrasound to image gene expression in genetically modified cells, facilitating the study of cellular function in deep tissues inaccessible with conventional optical techniques. ARGs encode air-filled protein nanostructures known as gas vesicles, which scatter sound waves, enabling the bacterial or mammalian cells expressing them to be visualized with ultrasound. Despite the promise of this technology for biological research and potential clinical applications, the sensitivity with which ARG-expressing cells can be visualized is currently limited, with a published detection limit for bacteria on the order of 10^8 cells/ml. Overcoming this limit is critical to enabling the use of ARGs in the broadest range of potential applications. Here, we present BURST – an ARG imaging paradigm that improves cellular sensitivity by more than 1000-fold. BURST takes advantage of the unique temporal signal pattern produced by gas vesicles as they collapse under acoustic pressure above a genetically defined threshold. By extracting the unique pattern of this signal from total scattering using template-based unmixing, BURST dramatically boosts the sensitivity of ultrasound to image ARG-

expressing cells, as demonstrated *in vitro* and *in vivo* in the mouse gastrointestinal tract. Furthermore, in dilute cell suspensions, BURST imaging enables the detection of gene expression in individual bacteria and mammalian cells. The resulting capabilities for ultrasensitive and single-cell imaging greatly expand the potential utility of ultrasound for non-invasive imaging of cellular function.

4.2 Introduction

The green fluorescent protein and its analogs allow biologists to visualize gene expression and other cellular processes under an optical microscope[1]. However, the scattering of light by tissue limits the use of such optical reporter genes in intact animals[2]. In contrast, ultrasound can propagate centimeters deep into biological tissues without losing coherence, enabling the noninvasive imaging of whole organs and organisms with excellent spatial and temporal resolution (~100 μm and ~1 ms, respectively)[3,4]. Recently the first acoustic reporter genes (ARGs) were developed for ultrasound imaging based on air-filled protein nanostructures called gas vesicles, or GVs[5]. When expressed in bacteria[6] or mammalian cells[7], ARGs allow the location and function of these cells to be visualized with ultrasound deep inside host organisms.

One of the main factors determining the utility of reporter genes is the sensitivity with which they can be detected. In previous work, ARG expression was detectable in bacteria using conventional ultrasound imaging at a concentration of 10^8 cells/ml[6]. While this density is relevant for certain *in vivo* scenarios, many applications would benefit from the ability to detect smaller numbers of cells. For example, many natural and engineered gastrointestinal (GI) microbes, which play critical roles in health and disease, must be studied within the context of the intact mammalian GI tract, which they populate at local concentrations spanning several orders of magnitude [8,9,10,11,12,13]. Visualizing the spatial dynamics of such microbes *in vivo* requires extending the sensitivity of ARG-based cellular imaging by a factor of 100–1000 while dealing with background scattering from anatomical structures. Furthermore, in some applications, it may be necessary to detect individual genetically labeled cells. Developing such capabilities requires large improvements in sensitivity and specificity compared to existing ARG imaging techniques[14,15,6,7].

To address this need, we introduce BURST (Burst Ultrasound Reconstructed with Signal Templates) – an ultrasensitive imaging paradigm tailored to ARGs, which improves cellular imaging sensitivity by more than 1000-fold. BURST imaging exploits the strong, transient signals generated during sudden GV collapse under acoustic pressure by unmixing the temporal dynamics of such signals from background scattering. Applied to imaging engineered commensal bacteria, BURST detects cells at concentrations below 10^5 cells/ml in tissue-mimicking phantoms and visualizes cells during their passage through the mouse GI tract. Furthermore, BURST can detect ultrasound signals from individual bacteria and mammalian cells, enabling

quantitative single-cell imaging. Just as the broad application of fluorescent imaging required major advances in both fluorescent proteins and optical detection methods (such as multiphoton microscopy), the development of BURST imaging complements recent advances in ARGs to greatly broaden the potential applications of biomolecular ultrasound.

4.3 Results

4.3.1 The BURST paradigm for selective imaging of ARG-expressing cells

BURST creates GV-specific ultrasound images by exploiting the phenomenon of GV collapse. GVs comprise a 2 nm-thick protein shell enclosing a hollow, air-filled compartment with dimensions on the order of 200 nm[16,17] (**Fig. 4.1a**, top). GVs self-assemble inside cells from the constituent proteins encoded in ARGs[6,7]. When these nanostructures are exposed to pressures above their genetically defined collapse threshold, their shell breaks (**Fig. 4.1a**, bottom) and their air contents are rapidly dissolved into the surrounding media. The collapse of GVs under acoustic pressure generates a strong transient ultrasound signal[7,18]. In BURST imaging, we rapidly acquire a series of ultrasound images during which the transmit pressure undergoes a step-change from a value below the GV collapse threshold to above it (**Fig. 4.1b**). This step-change generates a transient collapse-based signal increase in voxels containing GVs, while the signal from non-GV linear scatterers steps up and persists with the higher applied pressure (**Fig. 4.1b**). The images acquired during this pulse train combine to form a time-series vector for each voxel in the field of view (**Fig. 4.1, c-d**). In BURST signal processing, we decompose these vectors into weighted sums of template vectors representing the expected signal patterns of GVs, linear scatterers and background noise/offset, allowing us to generate images specific to each source of signal (**Fig. 4.1e**). We hypothesized that by effectively isolating the strong signal impulse generated by GVs at the moment of their collapse, while subtracting background linear contrast, BURST imaging would significantly improve the detection sensitivity of GV-expressing cells. Importantly, GV collapse is well-tolerated by both bacterial and mammalian cells, which can subsequently re-express new GVs to allow additional imaging[6,7].

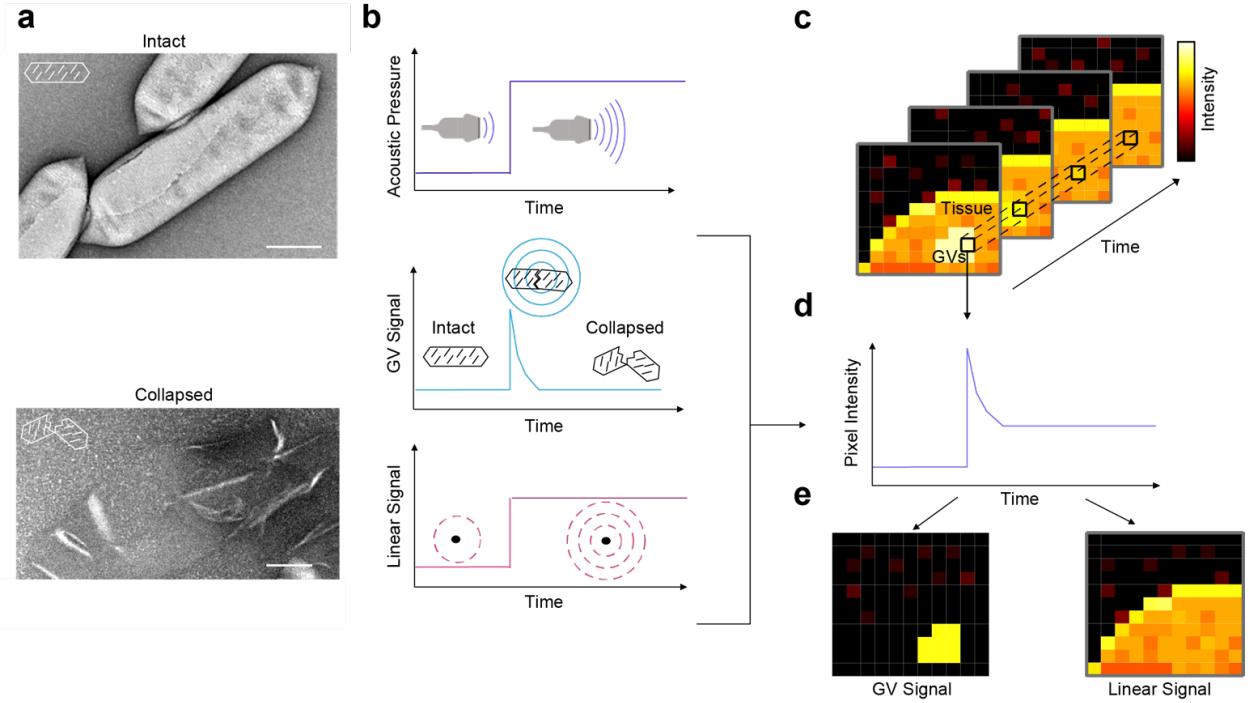

Figure 4.1 | BURST paradigm. (**a**) TEM images of intact (top) and collapsed (bottom) GVs from *Anabaena flos-aquae*. Scale bars: 100 nm. (**b**) Illustration of the BURST pulse sequence, showing the step change in applied acoustic pressure (top), the resulting transient increase in GV signal (middle) and the persistent increase in linear scatterer signal (bottom). (**c**) Illustration of an image time series generated by the high-pressure segment of the BURST sequence applied to a hypothetical target, which consists of scattering tissue with ARG-expressing cells located at the center. (**d**) Illustration of intensity time course for a pixel location in the region containing GVs. (**e**) Illustration of the result of the signal template unmixing algorithm applied to the image timeseries, generating separate images representing the contribution of GV signal (left) and linear signal (right) to the recorded image timeseries.

Temporal modulation of contrast agent signals has been used to enhance the detection of synthetic ultrasound contrast agents such as microbubbles[19] and nanodroplets[20], and has formed the basis for improved sensitivity and resolution in photoacoustic imaging[21,22] and fluorescence microscopy[23]. However, each class of reporters requires a unique approach based on their physical properties. A method like BURST, tailored to ARGs, has not been established, and is uniquely enabled by the monodisperse, highly nonlinear pressure response of GVs.

To test the BURST protocol, we prepared gel phantoms containing pairs of rectangular wells filled with either ARG-expressing *E. coli* Nissle cells or red fluorescent protein (RFP)-expressing controls (**Fig. 4.2a**). The cells were embedded in an agarose-based tissue-mimicking material (TMM)[24] with strong linear scatterers providing background contrast. For initial experiments, we used bacteria at a concentrations of 10^7 cells/ml, which is 10-fold lower than the previously published *in vitro* detection limit[6]. The phantoms were imaged at 6 MHz, using a single-cycle transmit waveform to maximize axial resolution. Parabolically focused B-mode pulses were used to achieve the peak positive pressure (PPP)

needed for GV collapse. Frames were acquired every 9 ms to minimize any impact from motion. In the initial low-pressure frame (0.27 MPa PPP), little signal was observed in either well (**Fig. 4.2b**). In the second frame, acquired at the stepped-up pressure of 4.3 MPa, both samples showed significant signal, with the ARG-expressing cells enhanced by 9 dB relative to RFP controls. By the next frame, this signal difference disappeared, as expected with GV collapse, leaving behind the linear scattering from the TMM.

The temporal pattern of signal in the ARG-expressing well is clearly distinguishable from the RFP control (**Fig. 4.2c**). The former shows a spike in signal in the first high-pressure frame, followed by decay to a stable plateau, while the latter shows a simple step-function jump. Using the BURST algorithm, we decomposed the signal vector in each well into its contributions from GVs, linear scatterers and noise (**Fig. 4.2d**). Performing this operation for each pixel in our field of view, we obtained images corresponding to each signal type (**Fig. 4.2, e-f**). The image corresponding to GV-specific signal shows very clear contrast between the well containing ARG-expressing cells and the control well, with a contrast-to-tissue ratio (CTR) of 32 dB (**Fig. 4.2e**). Meanwhile, the image corresponding to the linear scattering component showed a similar level of signal in each well, consistent with both wells having the same cell density and TMM composition (**Fig. 4.2f**).

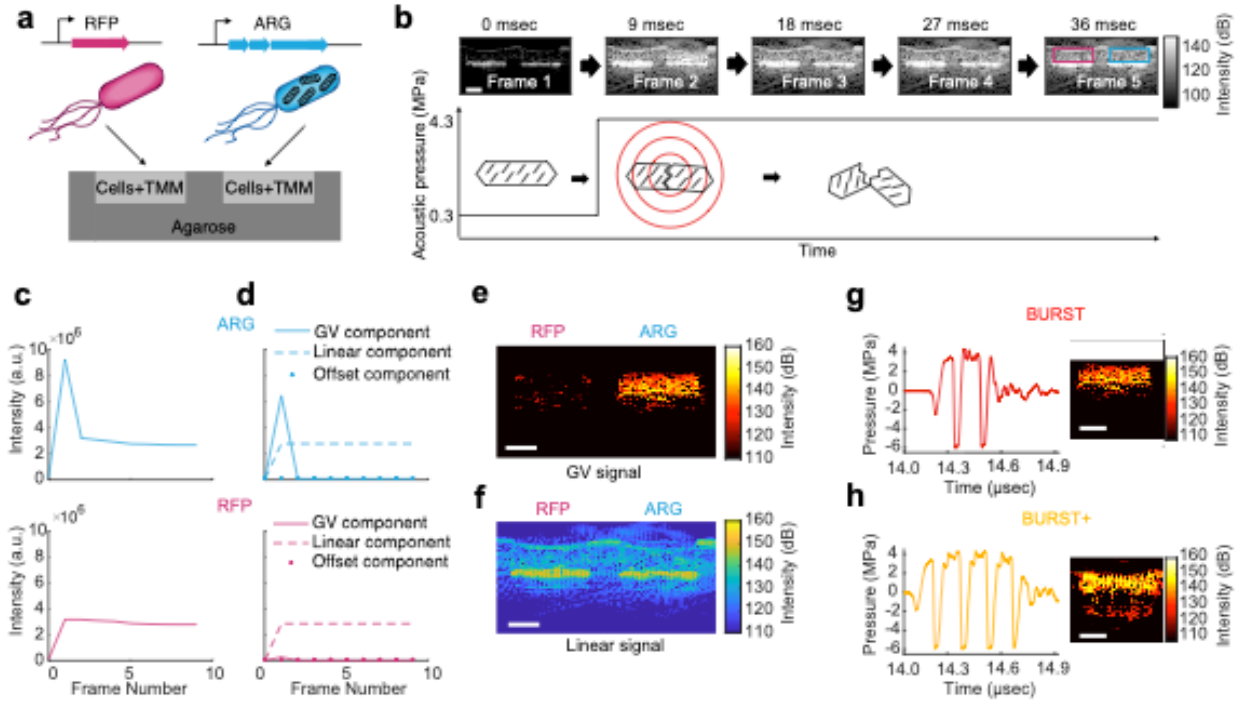

Figure 4.2 | BURST imaging of ARG-expressing cells. (**a**) Illustration of the agarose gel phantom containing cells engineered to express RFP or ARG, mixed with tissue-mimicking material (TMM). (**b**) Representative images from frames 1-5 of a BURST sequence applied to a 1% agarose phantom with wells containing TMM mixed with 10^7 cells/ml RFP-expressing (left) or ARG-expressing *E. coli* Nissle cells (right). The acoustic pressure is ramped from 0.27 MPa in the first frame to 4.3 MPa for the remaining 4 frames, as shown in the illustrated plot below the images.

Scale bars: 2 mm. (**c**) Mean pixel intensity vs. frame number in ROIs containing RFP or ARG1-expressing cells, outlined in (b). (**d**) Decomposition of the time traces in (c) using the template unmixing algorithm. (**e**) Output of the template unmixing algorithm applied pixel-wise to the full field of view, showing the estimated contribution of GV signal to every pixel. (**f**) Estimated contribution of linear tissue signal to every pixel. (**g**) Fiberoptic hydrophone measurement of the acoustic waveform used in the BURST high-pressure transmit, and the resulting BURST image of a phantom identical to the one described in (a). (**h**) Acoustic waveform for BURST+ and the corresponding image. All scale bars: 2 mm.

In addition to our basic BURST paradigm, which uses a single-cycle transmit waveform (**Fig. 4.2g**), we hypothesized that we could further boost detection sensitivity by extending the transmit waveform to multiple cycles. This hypothesis is based on the fact that following GV collapse, the air contained inside GVs is liberated as free nanobubbles, which can be cavitated with extended pulses[18]. Such nanobubbles normally dissolve on the millisecond timescale, as evidenced by the disappearance of GV contrast by the second frame following acoustic collapse (**Fig. 4.2b**). However, a pulse containing multiple cycles can stably cavitate the released nanobubbles, producing additional signal. To test this possibility, we extended the transmitted waveform to 3 cycles, naming the resulting imaging mode BURST+ (**Fig. 4.2h**). The measured output of the transducer is slightly extended due to ringdown. The number of cycles was set to 3 to enable nanobubble cavitation while preserving axial resolution. As hypothesized, ARG-expressing Nissle cells (at 10^7 cells/ml) imaged with BURST+ showed a signal enhancement of 6 dB relative to BURST. Detailed acoustic measurements confirmed that the BURST+ signal is predominantly generated by sustained stable cavitation of liberated nanobubbles, while BURST signal is generated by more transient dynamics (**Supplementary Fig. 4.1**).

4.3.2 *In vitro* detection limit for BURST imaging

To determine the cellular detection limits for BURST and BURST+, we used these techniques to image tissue-mimicking agarose phantoms containing ARG-expressing and RFP-expressing *E. coli* Nissle cells at concentrations ranging from 10^3 cells/ml to 10^8 cells/ml. In conventional B-mode images, it was challenging to make out clear GV contrast at any cell concentration (**Fig. 4.3a**). However, BURST images showed clear GV contrast down to 10^5 cells/ml (**Fig. 4.3b**), while BURST+ images showed clear GV contrast down to 10^4 cells/ml (**Fig. 4.3c**). This represents improvements of 1000-fold and 10,000-fold, respectively, over the previously reported detection limit[6]. Quantification across multiple replicates (**Fig. 4.3d**) confirms these detection thresholds with a mean CTR greater than 6 dB.

BURST and BURST+ signals increased with cell concentration up to approximately 10^6 cells/ml and thereafter plateaued. This plateauing is most likely due to acoustic shielding, in which collapsing GVs absorb energy from the acoustic waveform, preventing downstream GV collapse. Due to this effect, which increases with cell concentration, full collapse does not occur in the first high-pressure frame at concentrations of 10^7 cells/ml and above, resulting in pixel vectors that are assigned lower GV signal

weights in template unmixing (**Supplementary Fig. 4.2**). On the lower end of the concentration range, we noted that BURST+ images at 10^4 cells/ml appeared to show punctate clusters (**Fig. 4.3c**, second-to-bottom row). Since, at this dilution, we expect the imaged field of view to contain on the order of 100 cells, this suggested that BURST+ imaging may be capable of detecting signal from individual cells – a possibility examined further below.

While these experiments used TMM phantoms to identify detection limits relevant for *in vivo* imaging, in certain locations such as major blood vessels or other fluid compartments, the cells may be surrounded by a low-scattering medium. In agarose phantoms mimicking such conditions, the unmixed signals from ARG-expressing cells were reliably detectable at cell concentrations down to 10^3 cells/ml (**Supplementary Fig. 4.3**).

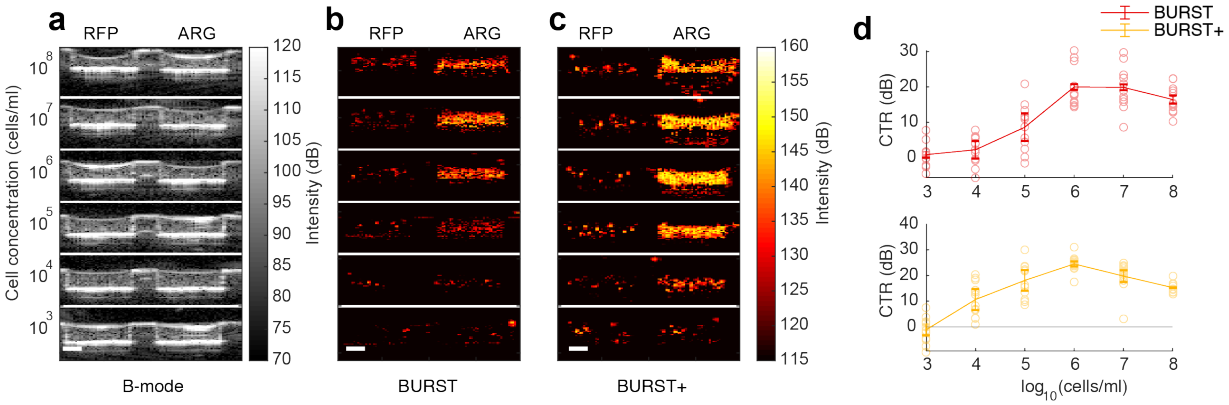

Figure 4.3 | Detection sensitivity of BURST imaging. (**a-c**) Ultrasound images of rectangular wells containing *E. coli* Nissle cells embedded with tissue-mimicking material (TMM) in an agarose phantom. The left well contains cells expressing RFP, and the right well contains cells expressing ARG. Rows correspond to cell concentrations ranging over six orders of magnitude. (**a**) B-mode images. (**b**) BURST images. (**c**) BURST+ images. The top edge of each image corresponds to a depth of 17.5 mm, the bottom to a depth of 23 mm. Scalebars: 2 mm. (**d**) Mean contrast-to-tissue ratio (CTR) vs log cell concentration for BURST and BURST+ on TMM-embedded cells. N = 12 wells (4 from each of 3 biological replicates). CTR represents the mean intensity of the ARG well relative to the mean intensity of the RFP well. Error bars represent SEM.

4.3.3 *In vivo* BURST imaging of bacterial passage through the small intestine

Having demonstrated the ability of BURST imaging to provide sensitive imaging of bacterial gene expression *in vitro*, we set out to test the ability of this method to visualize cells in a living animal. Bacteria play major roles in the mammalian microbiome, influencing everything from metabolism and immunity to neurological function[8,9,10,11,12,13]. In addition, many synthetic biology efforts are focused on engineering bacterial cells to act as diagnostic or therapeutic agents in the GI tract after oral administration[13]. Previously, ARG-expressing *E. coli* were imaged in the mouse colon after direct rectal injection in clean agarose phantoms containing 10^9 cells/ml[6]. However, imaging living cells in the much more complex environment

of the small intestine during their passage through this GI segment following oral administration was impossible.

To evaluate the ability of BURST to image cells *in vivo* following oral administration, we gavaged wild-type mice with an attenuated strain of *Salmonella typhimurium* engineered to express ARGs, or with control cells expressing the luminescent LUX operon[6] (**Fig. 4.4a**). No fasting, bicarbonate administration, or other pretreatments were used. Two hours later, we acquired BURST images at multiple transverse planes covering the abdominal cavity of each mouse. Display images were generated by overlaying grayscale B-mode images with heatmaps representing the GV-specific BURST signal (**Fig. 4.4, b-e**).

In all but one mouse gavaged with ARG-expressing cells, we observed contiguous patches of supra-threshold BURST signal with dimensions of approximately 2 mm × 1 mm, located 1 mm below the abdominal wall and spanning several contiguous frames in the abdomen (**Fig. 4.4b**). The anatomical region containing this signal corresponds to the expected location of the small intestine[25]. No significant BURST signal was observed in the abdominal cavities of control mice gavaged with LUX-expressing cells (**Fig. 4.4c**). Aggregating the mean BURST CTR in the upper abdominal cavity in each image plane across mice shows a consistent signal in the ARG-expressing group for all image planes spanning 16 mm to 22 mm below the rib cage (**Fig. 4.4f**). These results validate the ability of BURST imaging to reliably visualize ARG expression in live cells passing through the mouse GI tract.

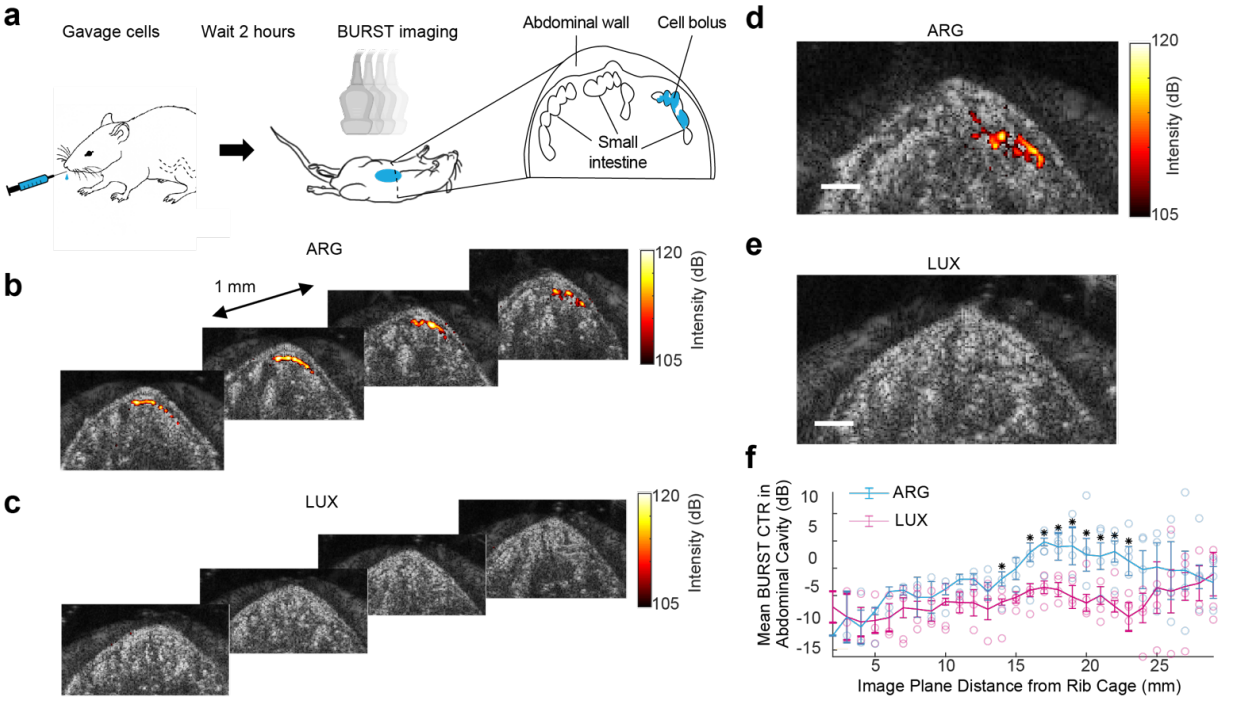

Figure 4.4 | BURST imaging of orally gavaged cells. (**a**) Illustration of the oral gavage experiment and the expected distribution of ARG-expressing cells as viewed in a cross section of the mouse abdomen. (**b-c**) Coronal BURST images (heat colormap) of the abdomen overlaid on the corresponding anatomical B-mode images (grayscale),

acquired 2 hours after oral gavage of 2 x 10^8 ARG-expressing (**b**) or LUX-expressing (**c**) *S. typhimurium* cells. The four images correspond to coronal planes 18 mm to 21 mm caudal to the rib cage. (**d-e**) Magnified images of coronal planes directly preceding those in (b-c) (17 mm). (**f**) BURST CTR as a function of image plane location in mice gavaged with ARG-expressing or LUX-expressing cells. The CTR is calculated based the mean intensity of ROIs manually drawn to encompass the ventral half of the abdominal cavity. Tissue ROIs encompassed a rectangular region in the dorsal half of the abdominal cavity. Error bars represent SEM. N = 4 mice. Asterisks indicate $p < 0.05$. Exact permutation test.

4.3.4 BURST+ imaging enables single-cell detection

The observation of punctate signals in BURST+ images at cell densities of 10^3 – 10^4 cells/ml (**Fig. 4.3d** and **Supplementary Fig. 4.1**) suggested that this imaging method may be capable of detecting signals from individual ARG-expressing cells. To test this hypothesis, we used BURST+ to image dilute samples of ARG-expressing and RFP-expressing Nissle cells, suspending them in degassed phosphate-buffered saline (PBS) at concentrations below 500 cells/ml (**Fig. 4.5a**). Suspending the cells in liquid buffer allowed us to thoroughly degas the medium to eliminate most microscopic air bubbles, which could otherwise act as confounding sources of signal. Based on hydrophone measurements of the beam profile of BURST+ transmit pulses, we estimated that cells in a 1 mm × 19.5 mm × 2 mm field of view (FOV) would experience sufficient pressure to generate collapse-dependent signal. Combining this volume with optical cell counts under fluorescence microscopy (for which cells were labeled with a synthetic dye), we could estimate the expected ground truth number of cells per image for each cell concentration.

BURST+ images of ARG-expressing cells showed clear punctate signals, the number of which increased with the cell concentration (**Fig. 4.5b**). In contrast, RFP-expressing controls rarely showed any such signals (**Fig. 4.5c**). To quantify the number of signal sources in our field of view, we counted all contiguous signals distinct from background noise, regardless of their size. In suspensions of ARG-expressing cells, the number of distinct sources increased linearly with cell concentration (R=0.86) and closely matched the number of cells expected from optical counting (**Fig. 4.5d**). In contrast, RFP-expressing controls had few signals and no significant dependence on cell concentration (R=0.08).

Following the successful single-cell imaging of bacterial cells, we tested the ability of BURST imaging to detect GV expression in individual mammalian cells, which are larger than bacteria but have lower GV expression levels[7]. We imaged suspensions of HEK cells genetically engineered to express either mammalian acoustic reporter genes (mARGs), or the control fluorophore mCherry. Cell concentrations were measured with optical cytometry. Punctate signal sources could clearly be seen in BURST+ images of suspended mARG-expressing cells, with the number of such sources increasing linearly with cell concentration (R=0.79) (**Fig. 4.5e**). Similar sources were rarely seen with mCherry control cells, and their number did not correlate with cell concentration (R=0.07) (**Fig. 4.5f**). The number of ultrasound sources counted for mARG-expressing cells constituted only about half the number of cells

expected based on optical counting. We suspect that this discrepancy arose due to the heterogeneity of gene expression in this cell line (in which, unlike the bacterial samples, we have no way to pre-select cells for imaging based on ascertained GV expression). Nevertheless, the fact that the number of punctate signals was of the expected order of magnitude and scaled linearly with concentration demonstrates that BURST+ detects single-cell signals from both ARG expressing bacteria and mammalian cells.

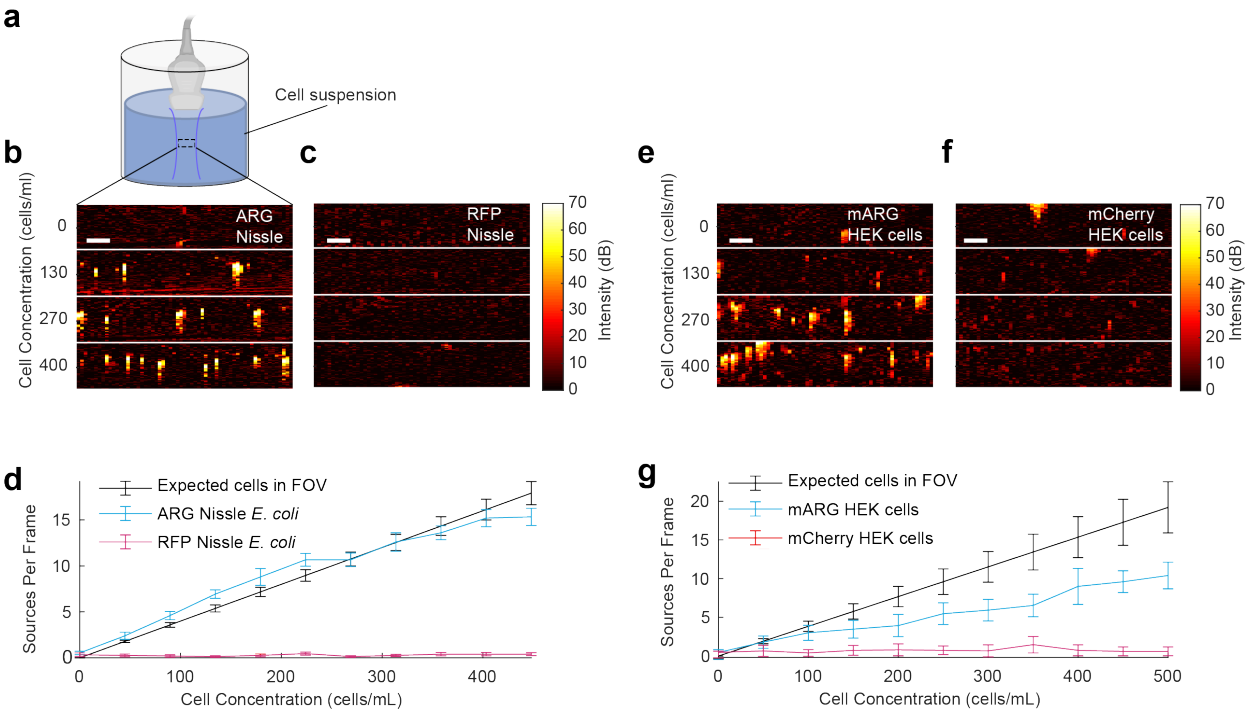

Figure 4.5 | Single cell imaging using BURST. (**a**) Illustration of the experimental setup, in which bacterial or mammalian cells are suspended in liquid at dilute concentrations while being imaged in the focal zone of the transducer. (**b**) Representative BURST+ images showing single sources in liquid buffer suspension of ARG-expressing *E. coli* Nissle cells at the indicated concentrations. (**c**) Representative BURST+ images of RFP-expressing *E. coli* Nissle cells. (**d**) Average number of single sources counted in images acquired with BURST+ vs. cell concentration for ARG- and RFP-expressing *E. coli* Nissle cells. Error bars represent SEM. N = 3 biological replicates. Mean counts from 5 frames were used for each biological replicate. A independent estimate of the expected number of cells in the transducer's field of view, based on cell counting by fluorescence microscopy, is also plotted for comparison. (**e**) Representative BURST+ images of suspended mARG-expressing HEK cells at the indicated concentrations. (**f**) Representative BURST+ images of mCherry-expressing HEK cells. (**g**) Average number of single sources counted in images acquired with BURST+ vs. cell concentration for mARG and mCherry-expressing HEK cells. Error bars represent SEM for N = 4 biological replicates. Mean counts from 5 frames were used for each biological replicate.

4.3.5 BURST imaging preserves cell viability

For BURST imaging of ARG-expressing cells to enable long-term studies with multiple imaging time points, it is important for this imaging mode to preserve the viability of imaged cells. To assess the cytocompatibility of BURST imaging, we quantified the viability of bacterial and mammalian cells after exposure to this imaging mode. First, to assay the effects of BURST and BURST+ imaging on bacterial

population growth and confirm ARG re-expression after imaging, we cultured ARG Nissle as colonies embedded in soft hydrogel media and applied BURST+ to half the sample (**Fig. 4.6a**). After 23 hours, colony growth was indistinguishable on the ultrasound-treated and untreated halves of the sample, as visualized with optical microscopy (**Fig. 4.6, b-e**). Moreover, strong GV-specific BURST+ signal was observed from the colonies with BURST+ imaging at this time point, confirming GV re-expression (**Supplementary Fig. 4.4**). Similar results were obtained with two additional plates.

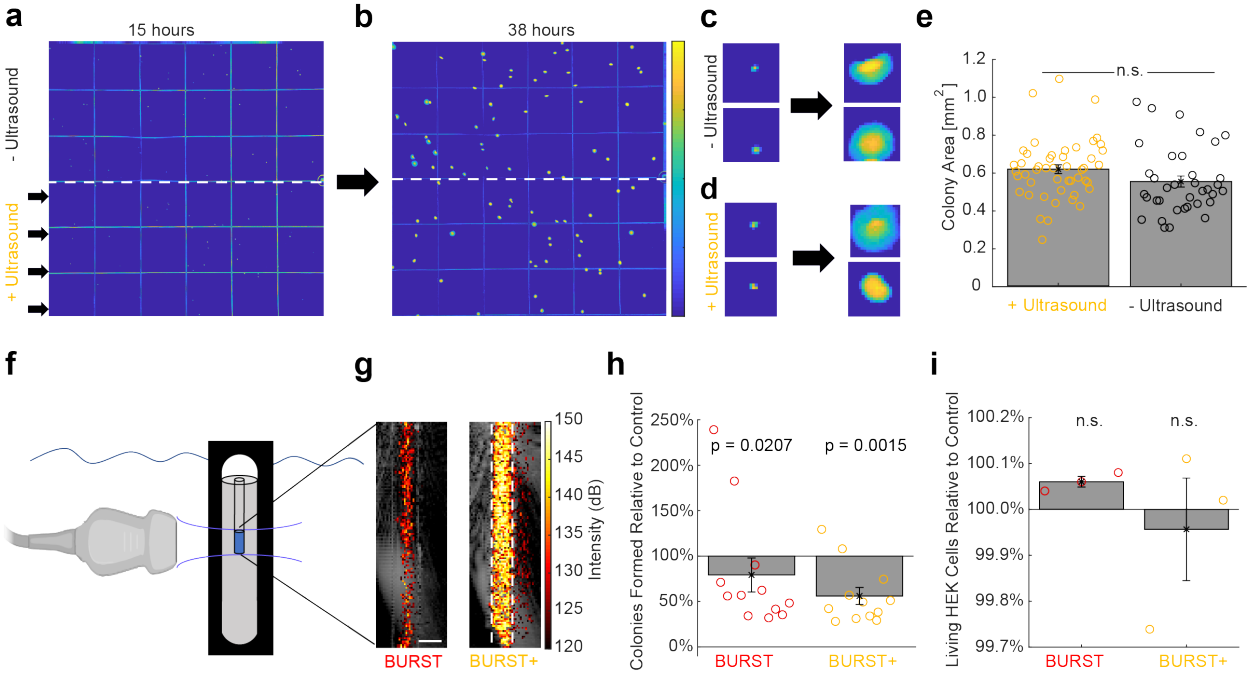

Figure 4.6 | Effects of BURST imaging on cell viability. (**a**) Darkfield optical image of ARG-expressing *E. coli* Nissle colonies on an agar plate 15 h after seeding. Width of 1 square is 12.7 mm. (**b**) Image of the same plate 23 h after application of BURST+ to the bottom half. (**c**) Representative magnified images of colonies from the top half of the plate in (a) (left) and (b) (right). (**d**) Representative magnified images of colonies from the bottom half of the plate in (a) (left) and (b) (right). (**e**) Area of colonies exposed or not exposed to BURST+ at the 38 hour time point. (**f**) Illustration of the experimental setup for single-cell viability. An acoustic cuvette with mylar windows is filled with 1% agarose and submerged in a water tank. A 2 mm diameter cylindrical inclusion in the agarose is filled with a suspension of GV-expressing cells (1×10^5 ARG Nissle cells/ml or 2.5×10^5 mARG HEK cells/ml) and imaged with BURST, BURST+, or 0.3 MPa B-mode as a control. (**g**) Representative BURST and BURST+ images of ARG Nissle samples overlaid on a grayscale B-mode image. The edges of the cylindrical inclusion are indicated with dashed white lines. Scale bars: 2 mm. (**h**) Colony forming units of ARG-expressing *E. coli* Nissle cells for the samples exposed to BURST and BURST+ relative to B-mode controls. Error bars represent SEM. N = 12 samples from 6 biological replicates. Approximate permutation test with 10^7 permutations. (**i**) Viable mARG-expressing HEK cells, as measured by flow cytometry, after exposure to BURST and BURST+, relative to B-mode controls. Error bars: SEM. N = 3 biological replicates. Exact permutation test.

To assess the impact of BURST and BURST+ imaging on bacterial cells in liquid suspension, we loaded ARG-expressing Nissle cells into a 2 mm cylindrical well within an agarose phantom (**Fig. 4.6f**) and applied BURST, BURST+, or 0.3 MPa linear imaging pulses (**Fig. 4.6g**). After imaging, we plated the

bacteria on selective solid media and counting the number of colonies formed after 20 hours. Both BURST and BURST+ produced a measurable decrease in the number of bacterial colonies relative to low-pressure controls, with an average reduction of 21% for BURST and 44% for BURST+ (**Fig. 4.6h**). This reduction may be indicative of the different acoustic or mechanical conditions experienced by individual cells in liquid compared to solid bacterial colonies, where no viability effects were observed. The colony results are arguably more relevant to most envisioned applications involving BURST imaging of bacteria inside mammalian hosts, where these cells typically inhabit crowded solid or gel-like environments[40,4212]. In addition, even in the liquid scenario, the exponential proliferation and saturating growth of bacteria would quickly make up for a modest reduction in the number of viable cells upon imaging.

To test the effects of BURST and BURST+ on the viability of mARG-expressing mammalian cells, we exposed liquid suspensions of mARG-expressing HEK cells to these imaging modes in the same apparatus as described above for bacteria. Following ultrasound exposure, we counted the number of live (metabolically active) and dead cells using flow cytometry. We observed no significant difference in the viability of cells exposed to either BURST or BURST+ relative to the low-pressure controls (**Fig. 4.6i**). The robustness of mammalian cells to these imaging modes may be due to the relatively small fraction of their cytosol being occupied by GVs[7] (<0.003%, compared to up to 10% for bacteria). Altogether, these results demonstrate that BURST and BURST+ preserve cellular viability to a level acceptable for most biological imaging applications.

4.3.6 BURST+ imaging enables detection of single gas vesicles

The successful detection of single ARG-expressing cells in BURST+ images (**Fig. 4.5**) demonstrated that this imaging method is capable of detecting signals from small numbers of GVs closely packed inside cells, but did not establish the minimum number of GVs per voxel required to generate detectable signal. To investigate this question, we used an experimental setup similar to that described in Section 4.3.4 to acquire BURST+ images of GVs purified from *Anabaena flos-aquae* cyanobacteria (Ana GVs)[26] at varying concentrations in the range of 10^2-10^3 GVs/ml, using pre-collapsed Ana GVs as controls. Because the gas inside free Ana GVs is known to equilibrate with the gas concentration in the surrounding medium in as little as 46 μs[16], exposing the GVs to degassed buffer would result in the pressure inside the GVs dropping below atmospheric pressure, potentially causing pre-mature collapse or loss of some acoustic properties. Based on these considerations, we chose not to degas the liquid buffer used in this experiment. To estimate the expected number of gas vesicles in the FOV for each concentration, we measured the optical density (OD) of our sample and used a previously-published conversion factor between OD and molarity for Ana GVs based on electron microscopy[26].

BURST+ images of intact GVs showed clear punctate signals, the number of which increased with the GV concentration (**Fig. 4.7a**). In contrast, collapsed GV controls showed a consistently small number of such signals that did not increase with GV concentration (**Fig. 4.7b**). The larger number of punctate signals observed in the control condition of this experiment (1.3 ± 1.2 signals/frame) compared with the single-cell detection experiment (0.3 ± 0.6) signals/frame) is expected based on our use of non-degassed buffer. In suspensions of intact Ana GVs, the number of distinct sources increased linearly with cell concentration (R = 0.83) and closely matched the number of GVs expected from electron microscopy counting (**Fig. 4.7c**). In contrast, collapsed controls had few signals and no significant dependence on cell concentration (R = -0.16). These results demonstrate that BURST+ detects signals from single Ana GVs.

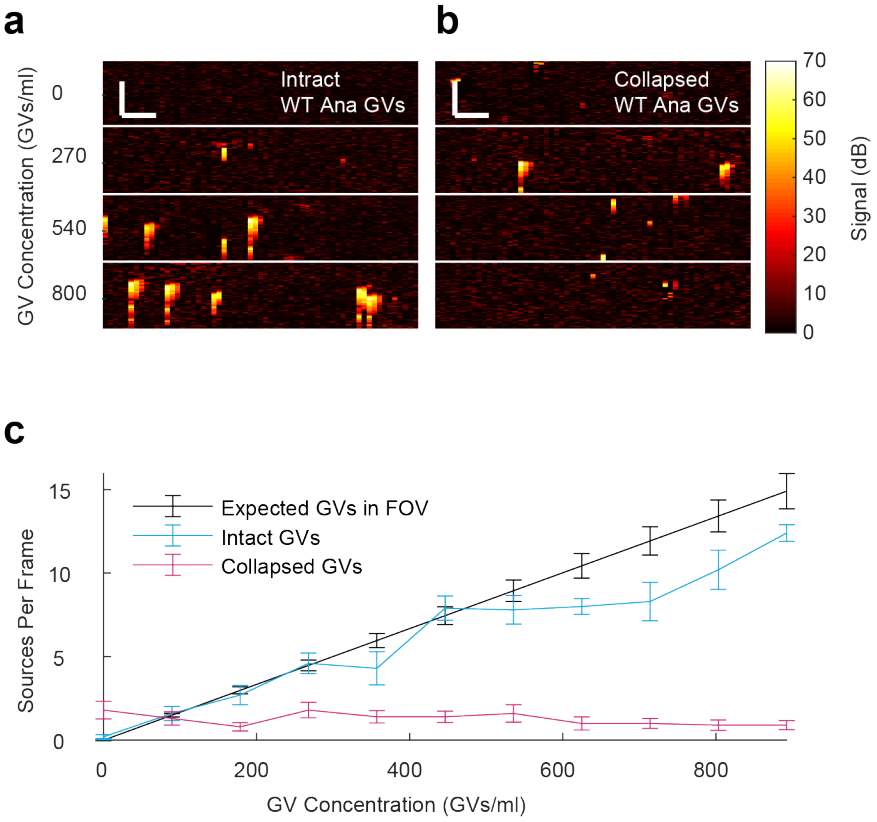

Figure 4.7 | Single gas vesicle imaging using BURST. (**a**) Representative BURST+ images showing single sources in liquid buffer suspension of intact gas vesicles purified from *Anabaena flos-aquae* cyanobacteria (Ana GVs) at the indicated concentrations. (**b**) Representative BURST+ images of pre-collapsed Ana GVs. (**c**) Average number of single sources counted in images acquired with BURST+ vs. GV concentration for intact and collapsed Ana GVs. Error bars represent SEM. N = 5 replicates. An independent estimate of the expected number of GVs in the transducer's field of view, based on GV counting under electron microscopy, is also plotted for comparison.

4.4 Discussion

Taken together, the results of this study demonstrate the ability of the BURST imaging paradigm to provide ultrasensitive ultrasound imaging of gene expression with an improvement of more than 1000-fold compared to the state of the art. BURST achieves this unprecedented sensitivity by taking advantage of the unique temporal signal generated by monodisperse populations of collapsing GVs, unmixed from both

surrounding and co-localized scatterers using a simple linear algorithm. This advance complements rapidly progressing efforts to develop and apply ARGs and GVs to a broad range of biological applications[4,6,7,18,27,28,29] and will immediately enable the imaging of these acoustic biomolecules with dramatically increased sensitivity and specificity without changes to their composition. Moreover, we expect the sensitivity of BURST to lower the barrier for initial applications of ARG-based imaging in challenging settings by facilitating the detection of low ARG expression levels or small ARG-labeled cell densities.

Several future improvements would help BURST imaging achieve widespread use. First, to enable rapid BURST imaging over a large field of view, it would be useful to develop ultrasound imaging transducers capable of higher transmit pressures. In the present study, transmitted beams had to be focused to a relatively small section of the available field of view to achieve the pressure needed to generate BURST signals. With stronger transducers, less focusing would be required, allowing more efficient scanning. At the same time, the pressure requirement could be reduced by engineering ARGs to encode GVs with lower critical collapse pressures. For example, the acoustic collapse mid-point of the ARGs used in this study is 2.7 MPa[6], whereas certain engineered GVs collapse at pressures below 0.6 MPa[27]. Lower pressure would also be expected to mitigate the already-minor effects of BURST imaging on cell viability, which itself should be extended to investigate other potential cellular side-effects in specific application scenarios.

More broadly, the BURST paradigm presented in this work demonstrates the potential of novel imaging techniques, developed in parallel with biological reagents, to expand the scope of GV and ARG capabilities. The engineering of fluorescent proteins with improved and novel properties, such as selective photoactivation[1,30], went hand-in-hand with complementary innovations in microscopy and image processing, such as PALM[31], STORM[32], and light sheet microscopy[33], resulting in ever-improving resolution, scale, and information content. We envision a similar synergy in the evolution of acoustic proteins and ultrasound imaging techniques.

4.5 Methods

4.5.1 Bacterial expression

Plasmids encoding ARGs were transformed into chemically competent *E. coli* Nissle 1917 (Ardeypharm GmbH) and grown in 5 ml starter cultures in LB medium with 50 μg/ml kanamycin, 2% glucose for 16 h at 37 °C. Large-scale cultures in LB medium containing 50 μg/ml kanamycin and 0.2% glucose were inoculated at a ratio of 1:100 with the starter culture. Cells were grown at 37 °C to OD600nm = 0.3, then induced with 3 μM IPTG. Cells were cultured for 22 h at 30 °C, then centrifugated for 4 hours at 150 x g and 4 °C to enrich for buoyant cells. Cells in the buoyant fraction were used for experiments involving

agarose phantoms. Neutrally buoyant cells in the supernatant below the buoyant fraction were used for all other experiments involving ARG-expressing Nissle cells. The same expression protocol was followed to produce mRFP-expressing Nissle cells, except that cells were resuspended from the pellet in PBS following centrifugation.

GV-expressing *Salmonella typhimurium* of the attenuated, tumor-homing strain ELH1301[34] were produced by transforming cells with a plasmid encoding an engineered genetic construct comprising either a GV operon or, as a control, a NanoLuc luciferase. Constructs were assembled using Gibson cloning. The genetic constructs were cloned into the pTD103 plasmid (gift from J. Hasty), with expression driven by a luxI promoter upon induction with 3nM N-(β-ketocaproyl)-l- homoserine lactone (AHL). The cells were cultured for 24 hours at 30 °C after induction, then centrifugated for 4 hours at 150 x g and 4 °C to enrich for buoyant cells. Cells in the buoyant fraction were used for *in vivo* experiments.

In experiments employing multiple bacterial biological replicates, replicates correspond to cells cultured from separate colonies from the same transformation.

4.5.2 Mammalian cell expression

mARG-expressing and mCherry-expressing HEK cells were previously described[7]. Briefly, HEK293tetON cells were genetically engineered with mARG gene cassettes (Addgene 134343, 134344 and 134345) using the piggyBac transposase system and a monoclonal culture was created by flow cytometry (BD FACSAria III). Similarly, mCherry-expressing cells were created by genetically engineering HEK293tetON cells with mCherry using the piggyBac transposase system. Cell cultures were maintained in DMEM supplemented with 10% tetracycline-free FBS (Clontech) and penicillin/streptomycin. For BURST imaging, both cells were seeded in 10 cm plates, and once they reached 70-80% confluency treated with 1 µg/mL doxycycline and 5 mM sodium butyrate for 72 hours. Cells were then trypsinized and resuspended in media before being stained 1:1 with Trypan blue dye and counted using a disposable hemocytometer (C-chip DHC S02, Incyto) under a brightfield microscope.

4.5.3 Ultrasound pulse sequence and data acquisition

Ultrasound imaging for all experiments was performed using a Verasonics Vantage programmable ultrasound scanning system. *In vitro* experiments were done using an L10-4v 128-element linear array transducer (Verasonics). Image acquisition was performed using a custom imaging script with a 64-ray-lines protocol with a synthetic aperture of 65 elements to form a focused excitation beam. The programmable transmit focus was set to 20 mm to be aligned with the fixed elevation focus of the transducer. The transmit waveform was set to a frequency of 6 MHz, 67% intra-pulse duty cycle resulting in sinusoidal pulses. BURST pulse sequences consisted of a single low-pressure frame (transducer voltage

= 1.6 V, peak positive pressure = 0.27 MPa) followed by five high-pressure frames (transducer voltage = 50 V, peak positive pressure = 4.3 MPa). The frame rate was 111 Hz. A similar imaging sequence was used for the *in vivo* experiments, with some modifications detailed below in the relevant section.

4.5.4 BURST processing algorithm

BURST images are generated by applying a temporal template unmixing algorithm across individual pixel locations in the frame stack. The input to the algorithm at the single pixel level consists of a 6-element vector, corresponding to pixel values in each frame. The parameters of the algorithm are the following template vectors for GVs ($\boldsymbol{u_g} = [0\ 1\ 0\ 0\ 0\ 0]^T$), linear scatterers ($\boldsymbol{u_s} = [0\ 1\ 1\ 1\ 1\ 1]^T$) and offset ($\boldsymbol{u_o} = [1\ 1\ 1\ 1\ 1\ 1]^T$).

The template unmixing model is represented by the linear equation $\boldsymbol{Uw} = \boldsymbol{p}$, where the template vectors are concatenated into the template matrix $\boldsymbol{U} = [\boldsymbol{u_s}\ \boldsymbol{u_o}\ \boldsymbol{u_g}]$, and $\boldsymbol{w}$ contains the weights for each template. For each pixel vector $\boldsymbol{p}$, least squares solution for the template weights is obtained by the pseudoinverse:

$$\boldsymbol{w} = (\boldsymbol{U}^T\boldsymbol{U})^{-1}\boldsymbol{U}^T\boldsymbol{p}$$

The w_g component of $\boldsymbol{w} = [w_s\ w_o\ w_g]$ was selected as the output of the algorithm. More generally, $\boldsymbol{U}$ can be an $n \times m$ matrix, where n is the length of $\boldsymbol{p}$ and the number of image frames and m is the length of $\boldsymbol{w}$ and the number of signal templates.

In theory, because negative weights have no meaning in this model, a proper estimation of the template weights would require the appropriate constrained linear least squares solution, which is typically two orders of magnitude slower to compute. However, it was found empirically that setting all negative values of the unconstrained solution to zero results in a final image that is not appreciably different from that obtained using the constrained solution. The template unmixing algorithm was applied offline to acquired BURST data. All image processing was implemented in MATLAB.

4.5.5 *In vitro* phantom imaging

Phantoms for imaging were prepared by melting 1% (w/v) agarose in PBS and casting wells using a custom 3D-printed template with 48 wells with dimensions of 6 mm × 5 mm × 2 mm. ARG- and RFP-expressing Nissle cells (at 2× the final concentration and at 25 °C) were mixed in a 1:1 ratio with molten agarose or molten TMM (at 2× the final concentration and at 56 °C) and immediately loaded into the phantom. The concentration of cells was determined before diluting and loading by measuring their OD_{600nm}. TMM consisted of 1% (w/v) agarose, 0.53% (w/v) 37 μm silicon carbide, 0.94% (w/v) 3 μm aluminum oxide, 0.88% (w/v) 0.3 μm aluminum oxide, and 96.65% (w/v) PBS, similar to the TMM described by Ramnarine

et al. (2001)[24] but with lower agarose content and no glycerol or antibiotic. Special care was taken to thoroughly degas the molten agarose to reduce the number of microbubbles present in the gel.

4.5.6 *In vivo* imaging

All *in vivo* experiments were performed on female BALB/cJ mice under a protocol approved by the Institutional Animal Care and Use Committee of the California Institute of Technology. No randomization or blinding were necessary in this study. Mice were anesthetized with 1–2% isoflurane, maintained at 37 °C on a heating pad, depilated over the imaged region, and imaged using an L11-4v transducer attached to a manipulator. For imaging of gavaged *Salmonella typhimurium* in the gastrointestinal tract, mice were placed in a supine position, with the ultrasound transducer positioned over the upper abdomen such that the transmit focus of 12 mm was close to the top of the abdominal wall. Two hours prior to imaging, mice were gavaged with 200 μl of buoyancy-enriched *Salmonella typhimurium* at a concentration of 10^9 cells/ml.

To mitigate tissue motion during *in vivo* imaging, a rapid BURST script was implemented that transmits and acquires three 32-element aperture focused beams at a time, improving the frame rate by a factor of 3 to 333 Hz. To maximize spatial resolution, the transmit waveform was set to a frequency of 11.4 MHz. The transmit focus was set at 12 mm to match the expected location of the small intestine relative to the transducer, which had to be positioned in relatively close proximity to maintain acoustic coupling.

Prior to processing with template unmixing, a 2×2 median filter followed by a gaussian blur filter with $\sigma = 1$ was applied to each 2D image frame of each image plane of each mouse. The images output from template unmixing were then concatenated into a 3D array to which a $1 \times 1 \times 3$ median filter was applied to remove isolated motion artifacts. The resulting 2D BURST images were then dB-scaled and overlaid on the square-root-scaled B-mode image representing frame 1 in the corresponding timeseries. The BURST images were overlaid in locations where the BURST image pixel values exceeded a threshold of 105 dB, which was chosen as the minimum threshold at which no residual motion artifacts were visible in the dorsal half of the abdominal cavity, where no BURST signal was expected. BURST images were pseudo-colored with the hot colormap and B-mode images with the gray colormap. Quantification was performed by manually drawing an ROI covering the ventral half of the abdominal cavity in each image plane for each mouse.

4.5.7 Single-source counting

Hydrophone measurements of the ultrasound transducer's acoustic field were used to estimate the out-of-plane dimension of the 3D field-of-view (FOV) in which ARG-expressing cells are expected to experience collapse dependent signal (2 mm). The out-of-plane FOV boundaries were defined as the displacement at which the peak positive acoustic pressure is equal to the acoustic collapse mid-point of the *E. coli*-expressed

ARGs used in this study[6]. These measurements were performed using a fiber-optic hydrophone system with a tapered sensor tip (Precision Acoustics) immersed in a tank filled with water that had been conditioned overnight using an AQUAS-10 water conditioner (Onda). The lateral dimension of the FOV (19.5 mm) was determined by the number of ray lines used to form the ultrasound image. The axial dimension (1 mm) was set by restricting the axial region of the BURST images displayed for counting to this size, which was chosen to cover the region around the transducer focus over which the mean BURST signal intensity was relatively constant.

Prior to counting, cells were diluted to an estimated 10^6 cells/ml and were then incubated at 25 °C for 30 min with BacLight Green fluorescent dye (Invitrogen). 10 µl of the cell suspension was loaded onto a C-Chip hemocytometer (SKC, Inc.) and cells were counted at 10x magnification with an Observer.A1 microscope (Zeiss).

For validation of single-cell detection, the L10-4v transducer was mounted on a BiSlide computer-controlled 3D translatable stage (Velmex) above a 4 L container containing 3.8 L water that had been circulated through the water conditioner for 1 hour. 200 ml of 20x PBS was then gently added to the water, with the mouth of the PBS-containing bottle at the level of the surface of the water to avoid creating bubbles. A piece of acoustic absorber material was placed at the bottom of the bucket to reduce reflections. A MATLAB script was written to control the Verasonics system in tandem with the BiSlide stage, which was programmed to move 1 cm after each BURST+ acquisition. After each set of BURST+ acquisitions (starting with plain PBS), 30 µl of 10^6 cells/ml ARG-expressing Nissle cell suspension was added to the bucket, which was gently stirred with a glass rod. A separate bucket with freshly conditioned water and buffer was used for the RFP control cells.

We wrote a MATLAB script to display a 1 mm × 19.5 mm segment, centered at the point of highest average intensity, of all BURST images (all replicates, all concentrations, and RFP vs. ARG cells) in a random order, blinding the experimenter to the condition when performing source counting.

4.5.8 Collapse signal characterization

Collapse signal characterization experiments were performed with the same liquid buffer suspension setup and protocol used for single-source validation, apart from the variations in sequence parameters described in Supplementary Fig. 4.1.

To capture the sub-millisecond dissolution times of the nanobubbles, an ultrafast version of the BURST+ pulse sequence was implemented in which the full timeseries of low- and high-pressure acquisitions is done for each ray line, rather than for each frame. This results in a significantly shorter delay

between frames for any given location in the image at the expense of significantly longer delays between separate ray lines.

4.5.9 Bacterial colony growth assay

ARG Nissle cells were transformed as described above. The transformation mix after recovery was plated on a 4-layer LB-Agar plate. In addition to LB and 50 μg/ml kanamycin, the first (bottom) layer contained 1% agarose and 7.5 μM IPTG; the second layer 1% agarose and 1% glucose; and the third layer 0.25% agarose, 1% glucose, and 10 cells/ml of the transformed Nissle. The fourth (top) layer contained 0.25% agarose in PBS with 1% glucose and 50 μg/ml kanamycin. The first and second layers were 4 mm thick and the third and fourth layers were 1 mm thick.

After culturing for 15 h at 30 °C, a darkfield optical image of the plate was acquired using a gel imager (BioRad). The plate was then immersed in PBS to allow acoustic coupling to the L10-4v transducer. The transducer was connected to the BiSlide motor stage and aligned perpendicular to the plane of the plate at a distance of 20 mm from the LB-Agar layer containing the ARG-expressing colonies. One half of the plate was exposed to BURST+ by applying the sequence to planes spaced by 1 mm across the plate. The plate was incubated for an additional 23 h at 30 °C.

A second darkfield optical image of the plate was acquired following the second round of incubation. The BURST+ plate scan was then repeated to obtain images confirming GV re-expression.

4.5.10 Bacterial colony-forming assay

Neutrally buoyant ARG Nissle cells were exposed to ultrasound inside cylindrical inclusions in agarose gel in 3D-printed acoustic cuvettes with windows covered by mylar. Each cuvette was filled with molten 1% agarose gel and a 3D-printed cylindrical plug was used to cast a cylindrical inclusion with 40 mm length and 2 mm diameter. Each ARG Nissle sample was diluted to 10^5 cells/ml in PBS. 50 μL of the resulting suspension was loaded into the inclusion in the acoustic cuvette, which was placed in a water tank. The L10-4v transducer was attached to an XSlide translatable motor stage (Velmex), submerged in a water tank, and aligned such that the 20 mm transducer focus was positioned at the center of the inclusion. A single pulse sequence was applied to each sample, using either BURST+, BURST, or, in the control case, B-mode with 3 cycles and a PPP of 0.3 MPa. 20 μL of sample was then extracted from the inclusion and diluted with PBS to 10^4 cells/ml. 100 μL of this dilution was plated on Lennox LB agar with 50 μg/ml kanamycin and 2% glucose. Plates were incubated for 20 hours at 30 °C.

Cell viability was measured by counting the number of colonies formed from samples exposed to BURST or BURST+ and dividing by the number of colonies formed from the same biological replicate exposed to the control condition.

4.5.11 Mammalian cell viability assay

HEK cells from an mARG-expressing cell line were trypsinized and pelleted by centrifugation at 400 g for 4 min at 4 °C. The pelleted cells were then resuspended in PBS and diluted to a concentration of 2.5×10^5 cells/ml. These samples were then exposed to ultrasound and collected with the same protocol used for ARG-expressing bacteria described above.

After ultrasound exposure, cells were stained with Zombie NIR viability dye (BioLegend Inc.) following the manufacturer's protocol. Relative cell death was measured using the Beckman Coutler Cytoflex Flow Cytometer (Beckman Coutler Inc.) based on Zombie NIR fluorescence. This assay was validated with a positive control condition in which HEK cells were incubated at 80 °C for 1 minute, resulting in 100% measured cell death.

References

1. Tsien, R. Y. The Green Fluorescent Protein. *Annual Review of Biochemistry* **67**, 509–544 (1998).
2. Ntziachristos, V. Going deeper than microscopy: the optical imaging frontier in biology. *Nature Methods* **7**, 603–614 (2010).
3. Piraner, D. I. *et al.* Going Deeper: Biomolecular Tools for Acoustic and Magnetic Imaging and Control of Cellular Function. *Biochemistry* **56**, 5202–5209 (2017).
4. Maresca, D. *et al.* Biomolecular Ultrasound and Sonogenetics. *Annu. Rev. Chem. Biomol. Eng.* (2018) doi:10.1146/annurev-chembioeng-060817-084034.
5. Shapiro, M. G. *et al.* Biogenic gas nanostructures as ultrasonic molecular reporters. *Nature Nanotechnology* **9**, 311–316 (2014).
6. Bourdeau, R. W. *et al.* Acoustic reporter genes for noninvasive imaging of microorganisms in mammalian hosts. *Nature* **553**, 86–90 (2018).
7. Farhadi, A., Ho, G. H., Sawyer, D. P., Bourdeau, R. W. & Shapiro, M. G. Ultrasound imaging of gene expression in mammalian cells. *Science* **365**, 1469–1475 (2019).
8. Round, J. L. & Mazmanian, S. K. The gut microbiota shapes intestinal immune responses during health and disease. *Nature Reviews Immunology* **9**, 313–323 (2009).

9. Derrien, M. & van Hylckama Vlieg, J. E. T. Fate, activity, and impact of ingested bacteria within the human gut microbiota. *Trends in Microbiology* **23**, 354–366 (2015).

10. Simon, G. L. & Gorbach, S. L. Intestinal flora in health and disease. *Gastroenterology* **86**, 174–193 (1984).

11. Savage, D. C. Microbial ecology of the gastrointestinal tract. *Annual review of microbiology* **31**, 107–133 (1977).

12. Donaldson, G. P., Lee, S. M. & Mazmanian, S. K. Gut biogeography of the bacterial microbiota. *Nature Reviews Microbiology* **14**, 20–32 (2016).

13. Riglar, D. T. & Silver, P. A. Engineering bacteria for diagnostic and therapeutic applications. *Nature Reviews Microbiology* **16**, 214–225 (2018).

14. Maresca, D. *et al.* Nonlinear ultrasound imaging of nanoscale acoustic biomolecules. *Appl. Phys. Lett.* **110**, 073704 (2017).

15. Maresca, D., Sawyer, D. P., Renaud, G., Lee-Gosselin, A. & Shapiro, M. G. Nonlinear X-Wave Ultrasound Imaging of Acoustic Biomolecules. *Phys. Rev. X* **8**, 041002 (2018).

16. Walsby, A. E. Gas vesicles. *Microbiology and Molecular Biology Reviews* **58**, 94–144 (1994).

17. Pfeifer, F. Haloarchaea and the Formation of Gas Vesicles. *Life* **5**, 385–402 (2015).

18. Bar-Zion, A. *et al.* Acoustically Detonated Biomolecules for Genetically Encodable Inertial Cavitation. *bioRxiv* 620567 (2019).

19. Demené, C. *et al.* Spatiotemporal Clutter Filtering of Ultrafast Ultrasound Data Highly Increases Doppler and fUltrasound Sensitivity. *IEEE Transactions on Medical Imaging* **34**, 2271–2285 (2015).

20. Sheeran, P. S. & Dayton, P. A. Phase-change contrast agents for imaging and therapy. *Curr. Pharm. Des.* **18**, 2152–2165 (2012).

21. Stiel, A. C. *et al.* High-contrast imaging of reversibly switchable fluorescent proteins via temporally unmixed multispectral optoacoustic tomography. *Opt. Lett., OL* **40**, 367–370 (2015).

22. Yao, J. *et al.* Multiscale photoacoustic tomography using reversibly switchable bacterial phytochrome as a near-infrared photochromic probe. *Nature Methods* **13**, 67–73 (2016).

23. Patterson, G., Davidson, M., Manley, S. & Lippincott-Schwartz, J. Superresolution Imaging using Single-Molecule Localization. *Annual Review of Physical Chemistry* **61**, 345–367 (2010).

24. Ramnarine, K. V., Anderson, T. & Hoskins, P. R. Construction and geometric stability of physiological flow rate wall-less stenosis phantoms. *Ultrasound in medicine & biology* **27**, 245–250 (2001).

25. Zhang, Y. *et al.* Non-invasive multimodal functional imaging of the intestine with frozen micellar naphthalocyanines. *Nature Nanotechnology* **9**, 631–638 (2014).

26. Lakshmanan, A. *et al.* Preparation of biogenic gas vesicle nanostructures for use as contrast agents for ultrasound and MRI. *Nature Protocols* **12**, 2050–2080 (2017).

27. Lakshmanan, A. *et al.* Molecular Engineering of Acoustic Protein Nanostructures. *ACS Nano* **10**, 7314–7322 (2016).

28. Maresca, D. *et al.* Acoustic biomolecules enhance hemodynamic functional ultrasound imaging of neural activity. *NeuroImage* **209**, 116467 (2020).

29. Lu, G. J., Farhadi, A., Mukherjee, A. & Shapiro, M. G. Proteins, air and water: reporter genes for ultrasound and magnetic resonance imaging. *Current Opinion in Chemical Biology* **45**, 57–63 (2018).

30. Lippincott-Schwartz, J. & Patterson, G. H. Development and Use of Fluorescent Protein Markers in Living Cells. *Science* **300**, 87–91 (2003).

31. Betzig, E. *et al.* Imaging Intracellular Fluorescent Proteins at Nanometer Resolution. *Science* **313**, 1642–1645 (2006).

32. Rust, M. J., Bates, M. & Zhuang, X. Sub-diffraction-limit imaging by stochastic optical reconstruction microscopy (STORM). *Nat Methods* **3**, 793–796 (2006).

33. Keller, P. J., Schmidt, A. D., Wittbrodt, J. & Stelzer, E. H. K. Reconstruction of Zebrafish Early Embryonic Development by Scanned Light Sheet Microscopy. *Science* **322**, 1065–1069 (2008).

34. Danino, T., Lo, J., Prindle, A., Hasty, J. & Bhatia, S. N. In Vivo Gene Expression Dynamics of Tumor-Targeted Bacteria. *ACS Synth. Biol.* **1**, 465–470 (2012).

35. Chen, W.-S., Matula, T. J. & Crum, L. A. The disappearance of ultrasound contrast bubbles: Observations of bubble dissolution and cavitation nucleation. *Ultrasound in medicine & biology* **28**, 793–803 (2002).

4.6 Supplementary Material

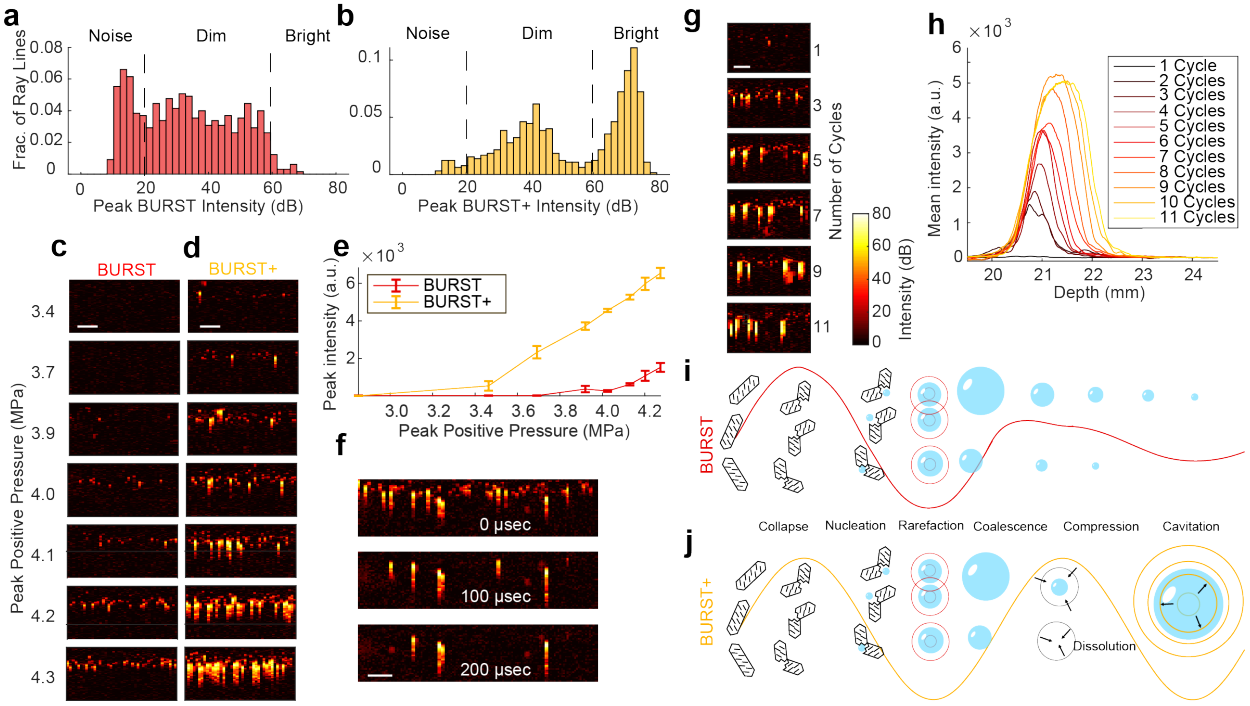

Supplementary Figure 4.1 | Collapse signal generation mechanism. The imaging target for all panels is ARG *E. coli* Nissle at 10^3 cells/ml in suspension. All images are displayed in dB scale with the same colormap shown in the bottom right of panel (g) (min: 0 dB, max: 80 dB). All scalebars are 2 mm. (**a**) Distribution of BURST ray line peak intensities (i.e. maxima over columns of pixels) for PPP = 4.3 MPa. N = 650. (**b**) Distribution of BURST+ ray line peak intensities for PPP = 4.3 MPa. N = 650. (**c**) BURST pressure ramp images with PPP ranging from 3.4 MPa to 4.3 MPa. (**d**) BURST+ pressure ramp with the same pressures as in (c). (**e**) Peak image intensity vs PPP for BURST and BURST+. Error bars: SEM. N = 10 BURST acquisitions. (**f**) Image time series acquired with an ultrafast implementation of BURST+, with 1 frame/100 µsec, at 4.3 MPa. (**g**) Cycle ramp images with the number of transmit waveform cycles ranging from 0.5 cycles to 10.5 cycles and PPP held constant at 4.0 MPa. (**h**) Mean intensity of cycle ramp images vs. depth. Traces are averaged over 10 replicates. Error bars not shown for clarity. (**i**) Proposed mechanism to account for the presence of dim signals, but not bright signals, in BURST. (**j**) Proposed mechanism to account for the presence of both dim and bright sources in BURST+ and pulse sequences with more than one cycle.

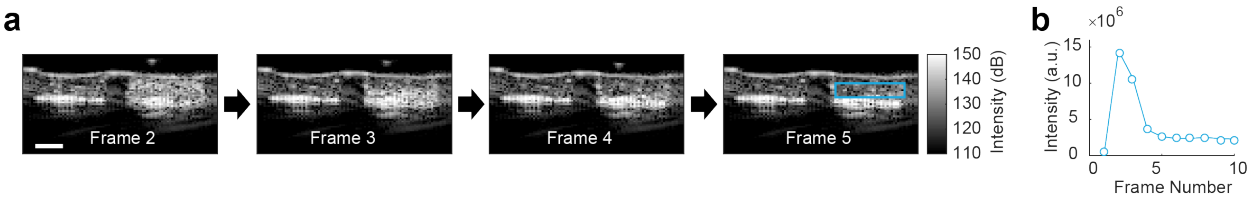

Supplementary Figure 4.2 | Acoustic shielding in BURST sequence at high ARG-expressing cell concentration. (**a**) Images from the high-pressure frames (frames 2-5) of a BURST+ sequence applied to a 1% agarose phantom with wells containing tissue-mimicking scatterers mixed with 10^8 cells/ml RFP-expressing *E. coli* Nissle (left) and ARG-expressing *E. coli* Nissle (right). Scale bars: 2 mm. (**b**) Mean pixel intensity vs. frame number for the ARG well, corresponding to the ROI of the same color in Frame 5 of the previous panel.

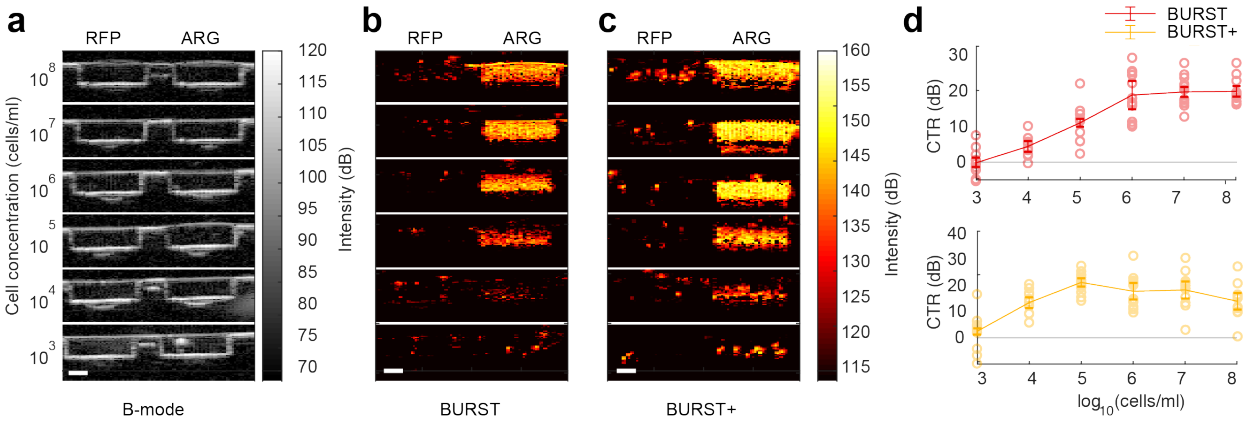

Supplementary Figure 4.3 | *In vitro* BURST imaging of ARG-expressing bacteria in plain agarose gel. (**a-c**) Array of ultrasound images of a cross section of rectangular wells containing Nissle *E. coli* embedded in 1% agarose wells within an agarose phantom. Each image contains a pair of wells, the left well containing RFP-expressing Nissle, the right well containing ARG-expressing Nissle. Rows correspond to cell concentrations, which range over six orders of magnitude. (**a**) B-mode images. (**b**) BURST images. (**c**) BURST+ images. The top edge of each image corresponds to a depth of 17.5 mm, the bottom to a depth of 23 mm. The left edge of each image corresponds to a lateral coordinate of -7 mm, the right to +7 mm. Scalebars: 2 mm. (**d**) Mean CTR vs log cell concentration for BURST and BURST+ on agarose-embedded cells. N = 12 wells, 4 from each of 3 biological replicates. CTR values represent the mean intensity of the ARG well relative to the mean intensity of the RFP well.

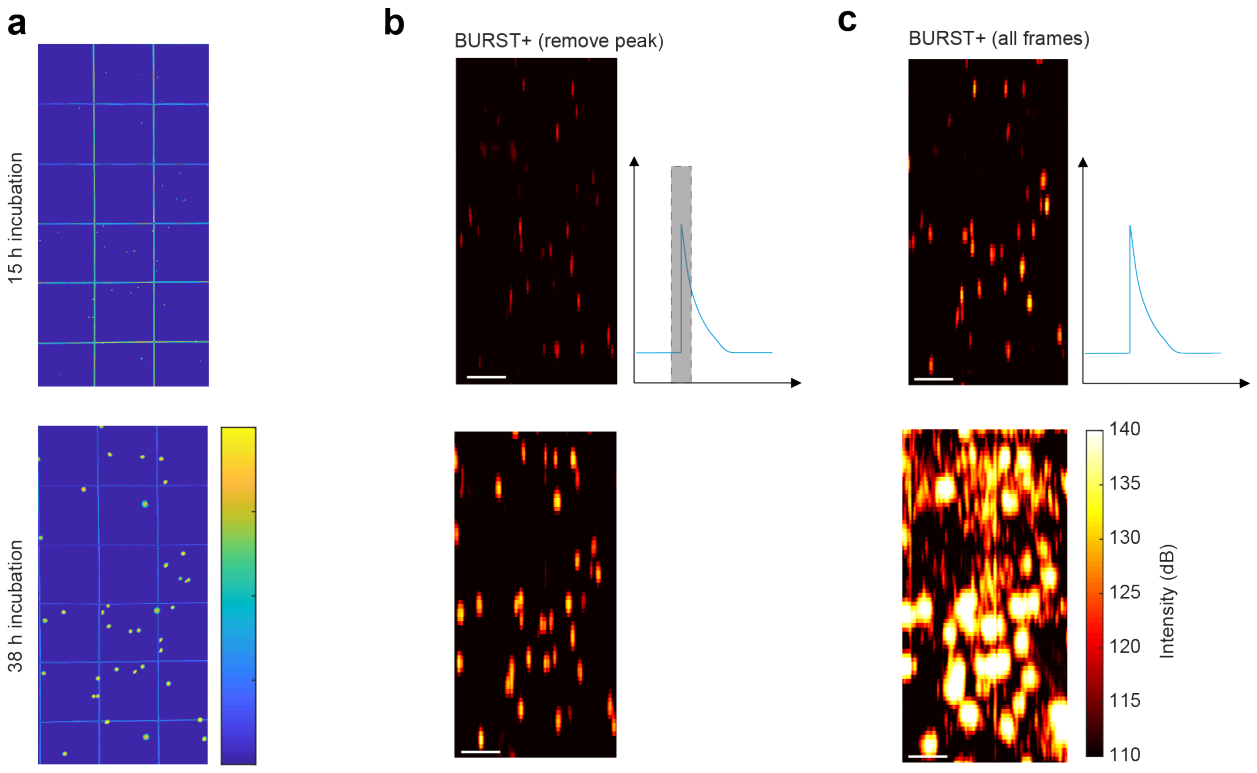

Supplementary Figure 4.4 | ARG Nissle colonies continue to grow and re-express GVs after exposure to BURST+. (**a**) Darkfield optical images of the half of the plate exposed to BURST+ after incubation at 30 °C for a total of 15 h (top) and 38 h (bottom). (**b**) BURST+ composite ultrasound images of the plate after 15 h (top) and 38 h (bottom), with the first collapse frame removed prior to template unmixing to reduce BURST signal area and allow easy comparison of signal spatial distribution with the optical image. The composite image was formed by taking the maximum of each BURST image plane along the axial dimension and concatenating the resulting rows of pixels to form 2D composite image. Prior to dB scaling, a 3×3 median filter was applied to the composite image, followed by a Gaussian filter with $\sigma = 1$. (**c**) The same BURST+ ultrasound images with all frames included in template unmixing. Due to the extremely high concentration of GV-expressing cells in the colonies, the BURST signal generated in the first collapse frame has an area significantly larger than the colony itself. This spatial broadening could be caused by the increased probability of a sufficient number of GVs stochastically collapsing at a lower pressure, thereby expanding the effective point spread function of the ultrasound beam. Scale bars: 10 mm.

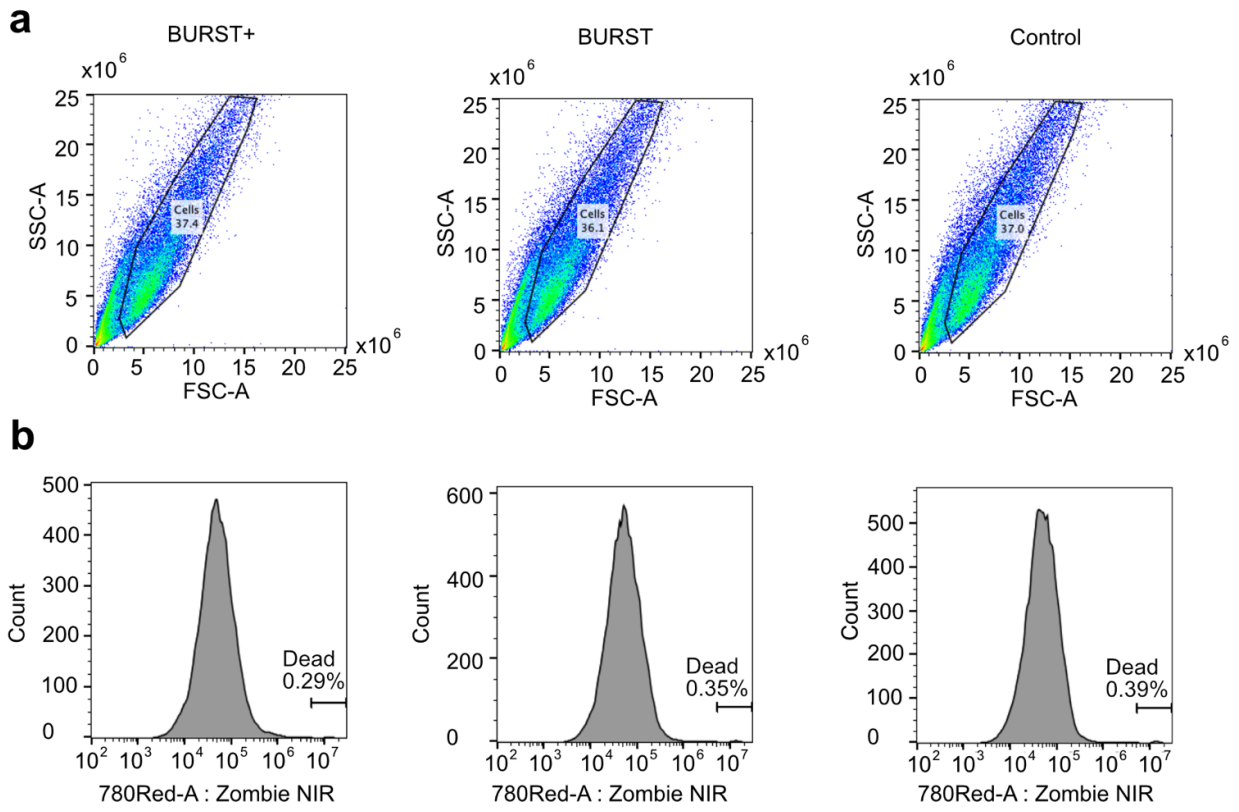

Supplementary Figure 4.5 | Gating strategy for quantifying cell death in mArg-HEK cells. (**a**) SSC-FSC gating for cell populations exposed to BURST+, BURST, and low-pressure control. (**b**) The corresponding Zombie NIR fluorescence histograms for each population. Cell death was quantified by gating the fraction of cells that emitted Zombie NIR fluorescence. The cutoff was the same for all samples.

Supplementary Note 1: Collapse signal generation mechanism

In performing the single cell detection experiments, we observed that the BURST signals from single cells tended to fall into two distinct categories: small, point-like "dim" signals of moderate intensity between 20 dB and 60 dB, and larger, elongated "bright" signals with intensities of 60 dB to 80 dB (**Fig 4.5, b, e**). Analysis of the signal intensity distributions for BURST and BURST+ applied to cells in liquid suspension revealed that BURST generated predominantly dim signals (**Supplementary Fig. 4.1a**) and that BURST+ generated predominantly bright signals, though dim signals were also present (**Supplementary Fig. 4.1b**). An understanding of the mechanisms behind these acoustic phenomena would allow us to better predict the performance of BURST and BURST+ in novel settings.

As a starting point for investigation, we hypothesized three mechanisms by which acoustic collapse of GVs might result in strong, transient ultrasound signal: 1) the same linear scattering that creates contrast when imaging below the collapse threshold of the GV, 2) an acoustic wave generated by the rapid volume change that occurs during GV collapse, or 3) cavitation of nanobubbles liberated from the GVs following

collapse. In the case of (1), the signal strength is due to an increase in scattering amplitude in proportion to the higher pressures applied, while the signal transience is explained by collapse of the GVs after the initial scattering event. For (3), signal transience would result from the sub-millisecond dissolution times of the nanobubbles.

To test these hypotheses, we imaged ARG Nissle in liquid buffer suspension at 10^3 cells/ml with a range of pulse sequences differing in pressure level, number of waveform cycles, and frame rate. We used the same setup and sample preparation protocol used for the single cell detection experiments. We first applied a pressure ramp with BURST and BURST+ to determine the pressure threshold at which different signal intensities are generated for each pulse sequence. Dim signals appeared in the BURST images at 3.7 MPa, but remained very sparse up to 3.9 MPa (**Supplementary Fig. 4.1c**). Bright signals did not appear in any BURST images. Both dim signals and bright signals appeared in BURST+ images at 3.4 MPa, although bright signals were very sparse, with less than one per frame at this pressure. Bright signals appeared consistently in BURST+ frames at 3.9 MPa and gradually increased in number at higher pressures (**Supplementary Fig. 4.1d**). Since BURST and BURST+ have identical pressure maxima and minima, these results suggest the larger number of cycles in BURST+ is necessary for the generation of bright signals and increases the generation of dim signals. Interestingly, although the 50% acoustic collapse pressure threshold of GVs expressed in ARG Nissle is 2.5 MPa, neither pulse sequence generated observable signal at 2.8 MPa. One explanation for this is that GV collapse is a stochastic event that occurs with probability proportional to both PPP and duration of insonation. However, both bright and dim signals are only observed in the first collapse frame for all pressure levels, which suggests that all GVs in the field of view collapse after the first pulse but, depending on the pulse parameters and GV characteristics, may not generate signal. This suggests that mechanism (2) is unlikely for bright or dim signals since it predicts that GV collapse is a sufficient condition for signal generation.

Although both bright and dim signals increased in number at higher pressures (**Supplementary Fig. 4.1c-d**), the peak intensity of the bright signals increased in direct proportion to the increase in pressure (**Supplementary Fig. 4.1e**). The number of dim signals, in contrast, increased with pressure while their intensity remained relatively constant up to 4.1 MPa. If the dim signals were generated by mechanism (1), we would expect to observe the opposite: there should be scattering from all cells in the field of view at an intensity that increases proportionally with incident pressure. Instead, our observations are consistent with a stochastic collapse model in which GVs in a given cell generate collapse signal with a probability proportional to the peak positive acoustic pressure. The stochasticity may be intrinsic to the physical process of collapse or may result from variability in shape, size, and number of expressed GVs. In either case, we may rule out mechanism (1) for both bright and dim signals. The evidence thus far suggests that both the

bright and dim signals are generated from mechanism (3): the interaction of liberated nanobubbles with the high-pressure acoustic waveform. However, this does not explain their markedly different characteristics.

To investigate the temporal properties of the bright and dim signals, we designed an ultrafast implementation of BURST+ with an inter-frame delay of 100 μsec. Although both bright and dim signals appear transient in the standard BURST+ pulse sequence with an inter-frame delay on the order of 10 msec, the ultrafast sequence showed that many bright signals persist after several high-pressure transmits (**Supplementary Fig. 4.1f**). In contrast, the band of dim signals always vanishes after the first high-pressure frame. Because mechanisms (1) and (2) depend on an irreversible collapse of the GV shell, this provides further evidence against their involvement in generation of the bright signals.

To obtain a tighter upper bound on the persistence time of the dim signals, we applied a cycle ramp with numbers of cycles ranging from 1 to 12. We held PPP constant at 4.0 MPa for each pulse sequence since this pressure level maximized visibility of individual bright and dim sources in the same frame. Both the intensity and size of the bright signals increased in proportion to the number of cycles (**Supplementary Fig. 4.1g-h**) Interestingly, after 2 cycles, more cycles did not obviously increase the number of either bright or dim signals (**Supplementary Fig. 4.1g**), suggesting a regime change in the signal generation mechanism caused by the presence of more than one cycle. The size of the dim signals, in contrast, did not change with the number of cycles, remaining at approximately the size of 1 wavelength (250 μm in this case). This implies that if the dim sources are generated by microbubbles, their dissolution times must be less than 500 nsec.

Physical modeling of GV collapse and nanobubble nucleation, dissolution, and cavitation will likely be required to elucidate the differences between the bright and dim signal generation mechanisms. While such modeling is beyond the scope of this work, we propose here a qualitative model that may account for our observations. It has been shown that, when insonated at 5 MHz with PPP > 4 MPa, microbubbles below a threshold radius of 800 nm decay as $1/R^6$ while larger bubbles undergo resonance enhancement[35], increasing in size through rectified diffusion. Under this proposed mechanism, all nanobubbles liberated by the first positive half-cycle initially have radii below the 800 nm decay threshold, as predicted by typical GV volume[26]. During the first negative half-cycle, rarefaction of these nanobubbles generates the dim signals and also generates bubbles with radii above the decay threshold due to rectified diffusion or coalescence of the nanobubbles. In the case of multi-cycle waveforms, subsequent cycles result in cavitation of the larger bubbles, which generates the bright signals (**Supplementary Fig. 4.1i**). In contrast, single-cycle waveforms do not generate bright signals because there are no subsequent cycles to cavitate the larger bubbles that form following the first negative half-cycle (**Supplementary Fig. 4.1j**). In this case, the dim signals generated by multi-cycle waveforms would be due to nanobubbles that remain below the decay threshold following the first negative half cycle.

References

1. Tsien, R. Y. The Green Fluorescent Protein. *Annual Review of Biochemistry* **67**, 509–544 (1998).
2. Ntziachristos, V. Going deeper than microscopy: the optical imaging frontier in biology. *Nature Methods* **7**, 603–614 (2010).
3. Piraner, D. I. *et al.* Going Deeper: Biomolecular Tools for Acoustic and Magnetic Imaging and Control of Cellular Function. *Biochemistry* **56**, 5202–5209 (2017).
4. Maresca, D. *et al.* Biomolecular Ultrasound and Sonogenetics. *Annu. Rev. Chem. Biomol. Eng.* (2018) doi:10.1146/annurev-chembioeng-060817-084034.
5. Shapiro, M. G. *et al.* Biogenic gas nanostructures as ultrasonic molecular reporters. *Nature Nanotechnology* **9**, 311–316 (2014).
6. Bourdeau, R. W. *et al.* Acoustic reporter genes for noninvasive imaging of microorganisms in mammalian hosts. *Nature* **553**, 86–90 (2018).
7. Farhadi, A., Ho, G. H., Sawyer, D. P., Bourdeau, R. W. & Shapiro, M. G. Ultrasound imaging of gene expression in mammalian cells. *Science* **365**, 1469–1475 (2019).
8. Round, J. L. & Mazmanian, S. K. The gut microbiota shapes intestinal immune responses during health and disease. *Nature Reviews Immunology* **9**, 313–323 (2009).
9. Derrien, M. & van Hylckama Vlieg, J. E. T. Fate, activity, and impact of ingested bacteria within the human gut microbiota. *Trends in Microbiology* **23**, 354–366 (2015).
10. Simon, G. L. & Gorbach, S. L. Intestinal flora in health and disease. *Gastroenterology* **86**, 174–193 (1984).
11. Savage, D. C. Microbial ecology of the gastrointestinal tract. *Annual review of microbiology* **31**, 107–133 (1977).
12. Donaldson, G. P., Lee, S. M. & Mazmanian, S. K. Gut biogeography of the bacterial microbiota. *Nature Reviews Microbiology* **14**, 20–32 (2016).

13. Riglar, D. T. & Silver, P. A. Engineering bacteria for diagnostic and therapeutic applications. *Nature Reviews Microbiology* **16**, 214–225 (2018).

14. Maresca, D. *et al.* Nonlinear ultrasound imaging of nanoscale acoustic biomolecules. *Appl. Phys. Lett.* **110**, 073704 (2017).

15. Maresca, D., Sawyer, D. P., Renaud, G., Lee-Gosselin, A. & Shapiro, M. G. Nonlinear X-Wave Ultrasound Imaging of Acoustic Biomolecules. *Phys. Rev. X* **8**, 041002 (2018).

16. Walsby, A. E. Gas vesicles. *Microbiology and Molecular Biology Reviews* **58**, 94–144 (1994).

17. Pfeifer, F. Haloarchaea and the Formation of Gas Vesicles. *Life* **5**, 385–402 (2015).

18. Bar-Zion, A. *et al.* Acoustically Detonated Biomolecules for Genetically Encodable Inertial Cavitation. *bioRxiv* 620567 (2019).

19. Demené, C. *et al.* Spatiotemporal Clutter Filtering of Ultrafast Ultrasound Data Highly Increases Doppler and fUltrasound Sensitivity. *IEEE Transactions on Medical Imaging* **34**, 2271–2285 (2015).

20. Sheeran, P. S. & Dayton, P. A. Phase-change contrast agents for imaging and therapy. *Curr. Pharm. Des.* **18**, 2152–2165 (2012).

21. Stiel, A. C. *et al.* High-contrast imaging of reversibly switchable fluorescent proteins via temporally unmixed multispectral optoacoustic tomography. *Opt. Lett., OL* **40**, 367–370 (2015).

22. Yao, J. *et al.* Multiscale photoacoustic tomography using reversibly switchable bacterial phytochrome as a near-infrared photochromic probe. *Nature Methods* **13**, 67–73 (2016).

23. Patterson, G., Davidson, M., Manley, S. & Lippincott-Schwartz, J. Superresolution Imaging using Single-Molecule Localization. *Annual Review of Physical Chemistry* **61**, 345–367 (2010).

24. Ramnarine, K. V., Anderson, T. & Hoskins, P. R. Construction and geometric stability of physiological flow rate wall-less stenosis phantoms. *Ultrasound in medicine & biology* **27**, 245–250 (2001).

25. Zhang, Y. *et al.* Non-invasive multimodal functional imaging of the intestine with frozen micellar naphthalocyanines. *Nature Nanotechnology* **9**, 631–638 (2014).

26. Lakshmanan, A. *et al.* Preparation of biogenic gas vesicle nanostructures for use as contrast agents for ultrasound and MRI. *Nature Protocols* **12**, 2050–2080 (2017).
27. Lakshmanan, A. *et al.* Molecular Engineering of Acoustic Protein Nanostructures. *ACS Nano* **10**, 7314–7322 (2016).
28. Maresca, D. *et al.* Acoustic biomolecules enhance hemodynamic functional ultrasound imaging of neural activity. *NeuroImage* **209**, 116467 (2020).
29. Lu, G. J., Farhadi, A., Mukherjee, A. & Shapiro, M. G. Proteins, air and water: reporter genes for ultrasound and magnetic resonance imaging. *Current Opinion in Chemical Biology* **45**, 57–63 (2018).
30. Lippincott-Schwartz, J. & Patterson, G. H. Development and Use of Fluorescent Protein Markers in Living Cells. *Science* **300**, 87–91 (2003).
31. Betzig, E. *et al.* Imaging Intracellular Fluorescent Proteins at Nanometer Resolution. *Science* **313**, 1642–1645 (2006).
32. Rust, M. J., Bates, M. & Zhuang, X. Sub-diffraction-limit imaging by stochastic optical reconstruction microscopy (STORM). *Nat Methods* **3**, 793–796 (2006).
33. Keller, P. J., Schmidt, A. D., Wittbrodt, J. & Stelzer, E. H. K. Reconstruction of Zebrafish Early Embryonic Development by Scanned Light Sheet Microscopy. *Science* **322**, 1065–1069 (2008).
34. Danino, T., Lo, J., Prindle, A., Hasty, J. & Bhatia, S. N. In Vivo Gene Expression Dynamics of Tumor-Targeted Bacteria. *ACS Synth. Biol.* **1**, 465–470 (2012).
35. Chen, W.-S., Matula, T. J. & Crum, L. A. The disappearance of ultrasound contrast bubbles: Observations of bubble dissolution and cavitation nucleation. *Ultrasound in medicine & biology* **28**, 793–803 (2002).

Chapter 5

ULTRASOUND IMAGING OF GENE EXPRESSION IN MAMMALIAN CELLS

This chapter is in large part a reformatted version of the manuscript entitled "Ultrasound Imaging of Gene Expression in Mammalian Cells" published by Farhadi, A., Ho, G. H., Sawyer, D. P., Bourdeau, R. W. and Shapiro, M. G. in *Science*. Under the supervision of Mikhail Shapiro, my contributions to the work were to help design and optimize the ultrasound pulse sequence and assist with writing the manuscript.

Working as a collaborator on this project taught me valuable lessons about the impact of imaging capabilities on the development of novel tools in synthetic biology. The expression of gas vesicles (GVs) in mammalian cells was a tremendous achievement, but it was made especially difficult by the low expression levels. This challenge necessitated the development of an early destructive imaging protocol that extracted more signal from the GVs during collapse. However, it was only after developing this protocol further and experimenting with different pulse sequence parameters and reconstruction methods that I was able to develop this protocol into BURST and improve its specificity and sensitivity by multiple orders of magnitude. And yet, without the unmet need of improved imaging sensitivity, BURST likely would never have been developed. This is in contrast to how, in the case of xAM, the imaging technique created an opportunity for novel acoustic biosensors. In this way, I now appreciate how the innovation feedback loop works from both directions.

5.1 Abstract

The study of cellular processes occurring inside intact organisms requires methods to visualize cellular functions such as gene expression in deep tissues. Ultrasound is a widely used biomedical technology enabling non-invasive imaging with high spatial and temporal resolution. However, no genetically encoded molecular reporters are available to connect ultrasound contrast to gene expression in mammalian cells. To address this limitation, we introduce mammalian acoustic reporter genes. Starting with a gene cluster derived from bacteria, we engineered a eukaryotic genetic program whose introduction into mammalian cells results in the expression of intracellular air-filled protein nanostructures called gas vesicles, which produce ultrasound contrast. Mammalian acoustic reporter genes allow cells to be visualized at volumetric densities below 0.5% and permit high-resolution imaging of gene expression in living animals.

5.2 Introduction

The study of cellular function within the context of intact living organisms is a grand challenge in biological research and synthetic biology[1]. Addressing this challenge requires imaging tools to visualize specific cells in tissues ranging from the developing brain to tumors, and to monitor gene- and cell-based therapeutic agents *in vivo*[2]. However, most common methods for imaging cellular processes such as gene expression rely on fluorescent or luminescent proteins, which have limited performance in intact animals due to the poor penetration of light in biological tissue[3,4]. On the other hand, ultrasound easily penetrates most tissues, enabling deep non-invasive imaging with excellent spatial and temporal resolution (~100 μm and ~1 ms, respectively)[2,5]. These capabilities, along with its safety, portability and low cost, have made ultrasound a widely used technology in biomedicine. Despite these advantages, to date ultrasound has played a relatively small role in cellular imaging due to the lack of appropriate genetically encoded reporters.

Recently, biomolecular contrast agents for ultrasound were introduced based on gas vesicles, air-filled protein nanostructures which evolved in certain waterborne bacteria and archaea to provide cellular buoyancy[6,7]. Gas vesicles comprise a 2 nm-thick protein shell enclosing a gas compartment with dimensions on the order of 100 nm. The acoustic impedance mismatch between their gas interior and surrounding aqueous media allows gas vesicles to strongly scatter sound waves and thereby serve as ultrasound contrast agents[8–12]. In their native organisms, gas vesicles are encoded by clusters of 8-14 genes, including one or two primary structural proteins, and several other essential genes encoding putative assembly factors or minor shell constituents.

The use of gas vesicles as reporter genes requires the heterologous expression of their cognate multi-gene operon in a new cellular host, ensuring proper transcription and translation of each gene, functional folding of each corresponding protein and appropriate stoichiometry and co-localization of the constituents for gas vesicle assembly. Recently, a genetic engineering effort succeeded in expressing gas vesicles as acoustic reporter genes (ARGs) in commensal bacteria, allowing their imaging in the mouse gastrointestinal tract[13]. If ARGs could be developed for mammalian cells, this would enable the study of how such cells develop, function and malfunction within the context of model organisms and enable the *in vivo* imaging of mammalian cells engineered to perform diagnostic or therapeutic functions[14–16]. However, developing ARGs for mammalian cells represents an even greater synthetic biology challenge due to the differences in transcription, translation, co-localization and protein folding between prokaryotes and eukaryotes[17–19]. To our knowledge, no genetic operon larger than 6 genes has been moved between these domains of life[20].

5.3 Results

Here, we describe the expression of ARGs in mammalian cells to enable ultrasound imaging of mammalian gene expression. To identify a set of genes capable of encoding gas vesicle assembly in mammalian cells,

we synthesized individual gas vesicle genes from three different microbial species using codons optimized for human expression, cloned each gene into a separate monocistronic plasmid and transiently co-transfected mixtures of the genes from each species into HEK293T cells (**Fig. 5.1A**). After allowing 72 hours for protein expression, we gently lysed the cells (~2x10^6 cells per sample), and centrifugated the lysate to enrich for buoyant particles, which would include any gas vesicles. The top fraction of the centrifugated lysate was then screened for gas vesicles using transmission electron microscopy (TEM). These experiments took advantage of the intrinsic stochasticity of transient co-transfection, in terms of the ratios of genes and the overall DNA quantity delivered to each cell, to simultaneously sample a broad range of gene stoichiometries and expression levels without prior knowledge of parameters leading to gas vesicle formation.

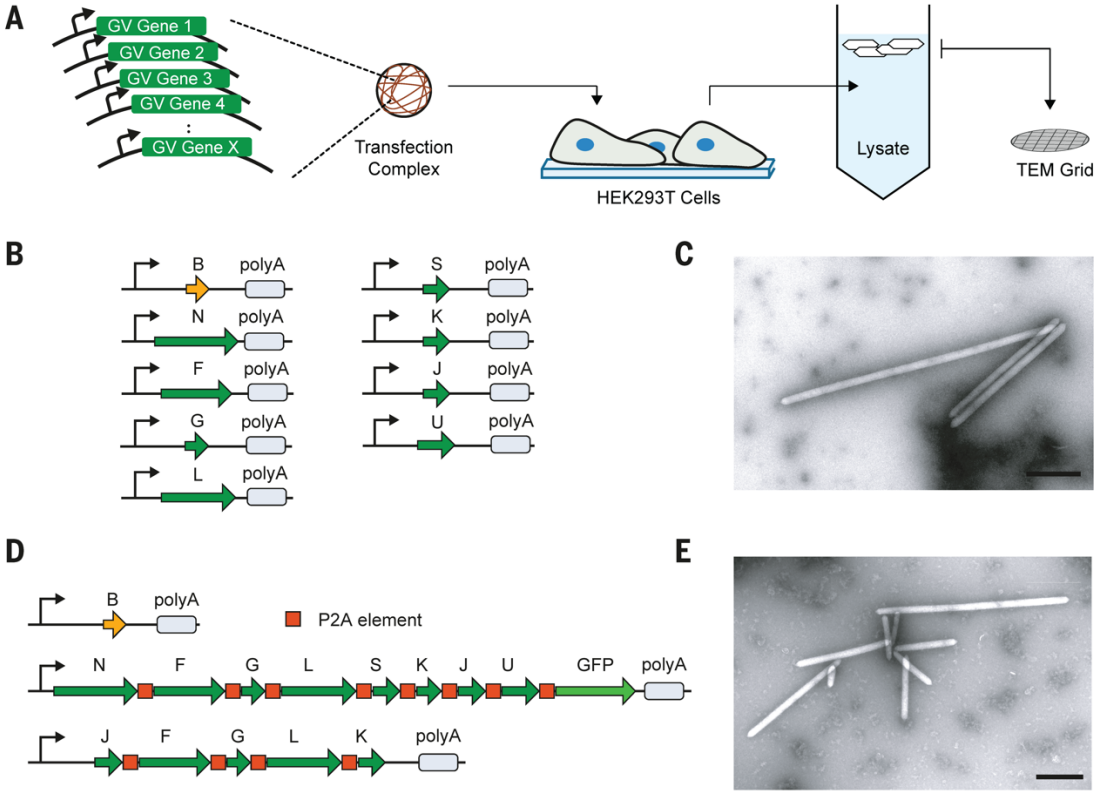

Figure 5.1 | Engineering of mammalian acoustic reporter genes. (**A**) Schematic of the transient co-transfection assay used to identify combinations of genes capable of producing gas vesicles in mammalian cells. (**B**) Schematic of nine genes from *B. megaterium* capable of encoding gas vesicle expression in mammalian cells. Thin arrow denotes CMV promoter. polyA denotes SV40 polyadenylation element. (**C**) Representative TEM image of purified gas vesicles expressed in HEK293T cells. (**D**) Gene cassettes comprising the mammalian acoustic reporter gene construct, mARG. (**E**) Representative TEM image of gas vesicles purified from HEK293T cells transiently transfected with mARGs for 72 hours. All scale bars represent 500 nm.

The co-transfection of the gas vesicle genes from *Halobacterium salinarum* and *Anabaena flos-aquae* did not lead to the formation of detectable gas vesicles. However, the co-transfection of 9 gas vesicle-

forming genes from *Bacillus megaterium* (**Fig. 5.1B**) resulted in the production of unmistakable gas vesicles as evidenced by their appearance in TEM images (**Fig. 5.1C**). The 9 genes originate from an eleven-gene *B. megaterium* gene cluster previously used to express gas vesicles in *E. coli*[13,21], with the exception of *GvpR* and *GvpT*, which were found to be unnecessary for gas vesicle formation (**Supplementary Fig. 5.1**).

Using the 9 genes identified in our stochastic screen, we set out to construct a polycistronic mammalian operon for consistent gas vesicle expression by joining these genes using the viral co-translational self-cleavage peptide P2A[22]. Having determined that all genes except *GvpB* could tolerate P2A peptide additions (**Supplementary Fig. 5.2** and **Supplementary Table 5.1**), we constructed a polycistronic plasmid containing the 8 P2A-tolerant gas vesicle genes connected by P2A sequences, and co-transfected it into HEK293T cells together with a plasmid encoding *GvpB*. Unfortunately, this did not result in the production of gas vesicles. We hypothesized that one or more of the genes in our polycistronic plasmid was expressed at an insufficient level, and used a complementation assay to identify *GvpJ, GvpF, GvpG, GvpL* and *GvpK* as bottleneck genes (**Supplementary Fig. 5.3**). This led us to construct a polycistronic "booster" plasmid containing these five genes, ordered to minimize P2A modifications to *GvpJ* and G*vpK*, which were found to be most limiting. The co-transfection of the booster plasmid together with the two plasmids above (**Fig. 5.1D**) enabled robust expression of gas vesicles in cells (**Fig. 5.1E**). We named this set of three genetic constructs mammalian acoustic reporter genes, or mARGs.

After establishing polycistronic constructs for mammalian gas vesicle assembly, we used an integrase[23,24] to incorporate them into the cellular genome for stable expression under a doxycycline-inducible TRE3G promoter, with fluorescent proteins added to each construct as transfection indicators (**Fig. 5.2A**). We transfected these plasmids into HEK293-tetON cells and used flow cytometry to sort cells according to their expression level of each fluorescent reporter. We found that the cell population combining the strongest expression of each construct produced the largest quantity of gas vesicles (**Fig. 5.2B, Supplementary Fig. 5.4, A-D**). To ensure that mARG expression was not limited to HEK293 cells, we also transfected Chinese hamster ovary cells (CHO-K1), and obtained similar results (**Supplementary Fig. 5.4, E-G**).

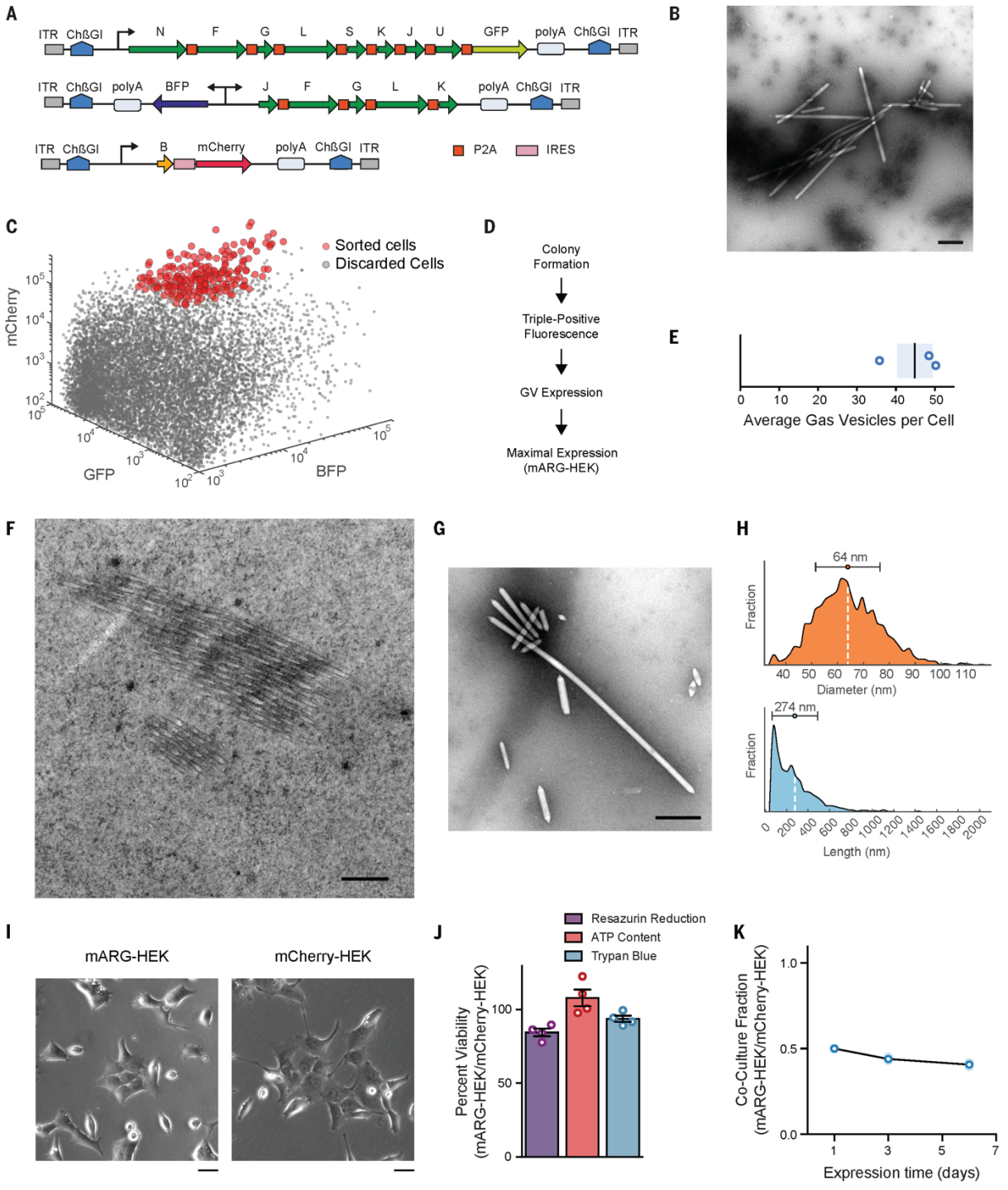

Figure 5.2 | Formation, properties and non-toxicity of gas vesicles in cells with genome-integrated mammalian acoustic reporter genes. (**A**) Schematic of mARG constructs used for genomic integration into cells with the piggyBac transposase system. ITR, inverted terminal repeat; ChβGI, Chicken beta-globin insulator; GFP, Emerald green fluorescent protein; BFP, enhanced blue fluorescent protein 2. (**B**) Representative TEM image of buoyancy-enriched lysate from HEK293-tetON cells transfected with the constructs in (A) and sorted for high expression of all three operons. (**C**) Fluorescence-activated cell sorting of HEK293-tetON cells transfected with the constructs in (A). Red circles denote individual cells selected by sorting to form monoclonal cell lines. (**D**) Selection process for

monoclonal cell lines, including assays for viability, fluorescence intensity and gas vesicle yield. (**E**) Number of gas vesicles expressed by monoclonal HEK293-tetON cells after 72 hours of induced expression, as counted in lysates using TEM. Bar represents the mean and the shaded area represents SEM (n=3, each from two technical replicates). (**F**) Representative TEM image of a 60-nm section through an mARG-HEK cell showing an angled slice through two bundles of gas vesicles in the cytosol. (**G**) Representative TEM image of gas vesicles purified from mARG-HEK cells. (**H**) Size distribution of gas vesicles expressed in mARG-HEK cells. The mean and standard deviation of both distributions is illustrated as a circle and with error bars. (n=1828) (**I**) Phase contrast images of mARG-HEK and mCherry-HEK cells 72 hours after induction with 1 μg/mL doxycycline and 5 mM sodium butyrate. (**J**) Cell viability of mARG-HEK cells relative to mCherry-HEK cells after 72 hours of gene expression. Error bars indicate SEM. (**K**) Fraction of mARG-HEK cells in co-culture with mARG-mCherry cells seeded in equal numbers over 6 days of gene expression (n=3 biological replicates, each from 4 technical replicates, with darker symbols showing the mean). Scale bars in **B**, **F**, **G** represent 500 nm. Scale bar in **I** represents 20 μm.

To generate a stable monoclonal cell line expressing mARGs for detailed analysis, we sorted individual high-expression HEK293-tetON cells for monoclonal growth (**Fig. 5.2C**), producing 30 cell lines, which we screened for viability, fluorescence and gas vesicle formation (**Fig. 5.2D**, **Supplementary Table 5.2**). The number of gas vesicles per cell was then estimated from TEM images, and a cell line yielding the largest quantity of gas vesicles was selected and named mARG-HEK. When induced for 72 hours with 1 μg/mL of doxycycline and 5 mM sodium butyrate (to reduce epigenetic silencing), this cell line produced on average 45 gas vesicles per cell (**Fig. 5.2E**). Using thin-section TEM, gas vesicles could clearly be seen in the cytosol of individual mARG-HEK cells (**Fig. 5.2F**). From TEM images of cell lysates, we measured the average dimensions of gas vesicles produced in this cell line to be 64 ± 12 nm wide (standard deviation, n=1828) and 274 ± 212 nm long (standard deviation, n=1828), with some reaching lengths greater than 1 micron (aspect ratios greater than 30) (**Fig. 5.2, G-H**). This corresponds to an average gas vesicle volume of 0.605 attoliters. Together, the 45 gas vesicles expressed in an average mARG-HEK cell are expected to occupy just 0.0027% of the cell's cytosolic volume.

The expression of gas vesicles did not change the gross morphology of mARG-HEK cells (**Fig. 5.2I**), and was non-toxic as determined by three different assays (**Fig. 5.2J**), as compared to a similarly prepared control cell line (mCherry-HEK) (**Supplementary Fig. 5.5 A-B**). During a 6-day co-culture, mARG-HEK cells showed only a minor growth disadvantage compared to mCherry-HEK cells (**Fig. 5.2K**). As expected, both engineered cell lines grew more slowly than wild-type HEK293T cells (**Supplementary Fig. 5.6**).

Having engineered mARG-HEK cells, we sought to image their expression of acoustic reporters with ultrasound. Gas vesicles encoded by the *B. megaterium* gene cluster are expected to produce linear ultrasound scattering[21]. However, since mammalian cells themselves also produce significant linear contrast, detecting gas vesicles expressed in such cells using linear methods is challenging. To enable more selective imaging of mARG-expression, we took advantage of the ability of gas vesicles to collapse irreversibly above specific ultrasound pressure thresholds[8,9,13,21]. A switch in the incident ultrasound pressure from below to above such a threshold results in a strong transient signal from the gas vesicles,

which decays to a lower level in the next ultrasound frame due to immediate dissolution of their gas contents and the elimination of ultrasound scattering (**Fig. 5.3, A-B**). Meanwhile, background tissue scattering rises with the increase in incident pressure and remains constant at the new level. Thus, images formed by taking the difference in signal between the collapsing and post-collapse frames reveal specifically the presence of gas vesicles.

We implemented this collapse-based imaging approach using an amplitude modulation pulse sequence[10], which we found to provide the best cancellation of non-gas vesicle signals. When hydrogels containing mARG-HEK cells were imaged using this technique at 18 MHz, they were easily distinguishable from mCherry-HEK controls based on their contrast dynamics (**Fig. 5.3C**). Critically, while this imaging paradigm requires the collapse of gas vesicles inside cells, this does not affect cell viability (**Fig. 5.3D**).

To test if mARGs can faithfully monitor circuit-driven gene expression[25,26], we measured the dynamic ultrasound response of mARG-HEK cells under the control of a doxycycline-inducible promoter (**Fig. 5.3E**). After induction with 1 μg/mL doxycycline, the cells showed a gradual buildup of ultrasound signal, with clear contrast appearing on day two and increasing over the next 4 days (**Fig. 5.3F**). These kinetics are similar to those observed with fluorescent indicators (**Supplementary Fig. 5.7A**). When the gene circuit was driven using a range of inducer concentrations, the ultrasound contrast followed the expected transfer function of the promoter (**Fig. 5.3G, Supplementary Fig. 5.7B**).

To determine how sensitively mARG-expressing cells could be detected in a mixed cell population, we combined mARG-HEK cells with mCherry-HEK cells at varying ratios. We were able to detect the presence of mARG-expressing cells in these mixtures down to 2.5% of total cells (**Fig. 5.3H**), corresponding to less than 0.5% volumetric density, or approximately 3 cells or 135 gas vesicles per voxel with dimensions of 100 μm. A similar voxel-averaged concentration of gas vesicles was detectable in a monoculture of mARG-HEK cells induced to express 1.4 ± 0.6 gas vesicles per cell (**Supplementary Fig. 5.8**).

In many imaging experiments, the output of a gene circuit is read out only once. However, in some cases it may be desirable to track gene expression over time. We therefore tested whether mARG-expressing cells in which the gas vesicles have been collapsed during imaging could re-express these reporters to allow additional imaging. mARG-HEK cells cultured a nutrient-supported hydrogel produced clear ultrasound contrast 3 days after induction, and were able to re-express their acoustic reporters over 3 additional days (**Fig. 5.3, I-J**).

Having engineered mammalian cells to stably express gas vesicles and characterized their ability to produce ultrasound contrast *in vitro*, we next tested the ability of mARG expression to be visualized *in vivo* with high spatial resolution. We formed model tumor xenografts in immunocompromised mice by

inoculating mARG-HEK cells in Matrigel subcutaneously in their left flanks (**Fig. 5.4A**). In the same mice, the right flanks were inoculated with mCherry-HEK control cells. We induced reporter gene expression in both tumors for 4 days through systemic injections of doxycycline and sodium butyrate (**Fig. 5.4B**). We expected these nascent tumors to be mostly vascularized at their perimeter, resulting in the strongest inducible gene expression at the tumor periphery (**Fig. 5.4A**). Ultrasound, with its sub-100-μm spatial resolution (at 18 MHz), should be able to discern this gene expression pattern, whereas attaining such resolution would be challenging with optical techniques.

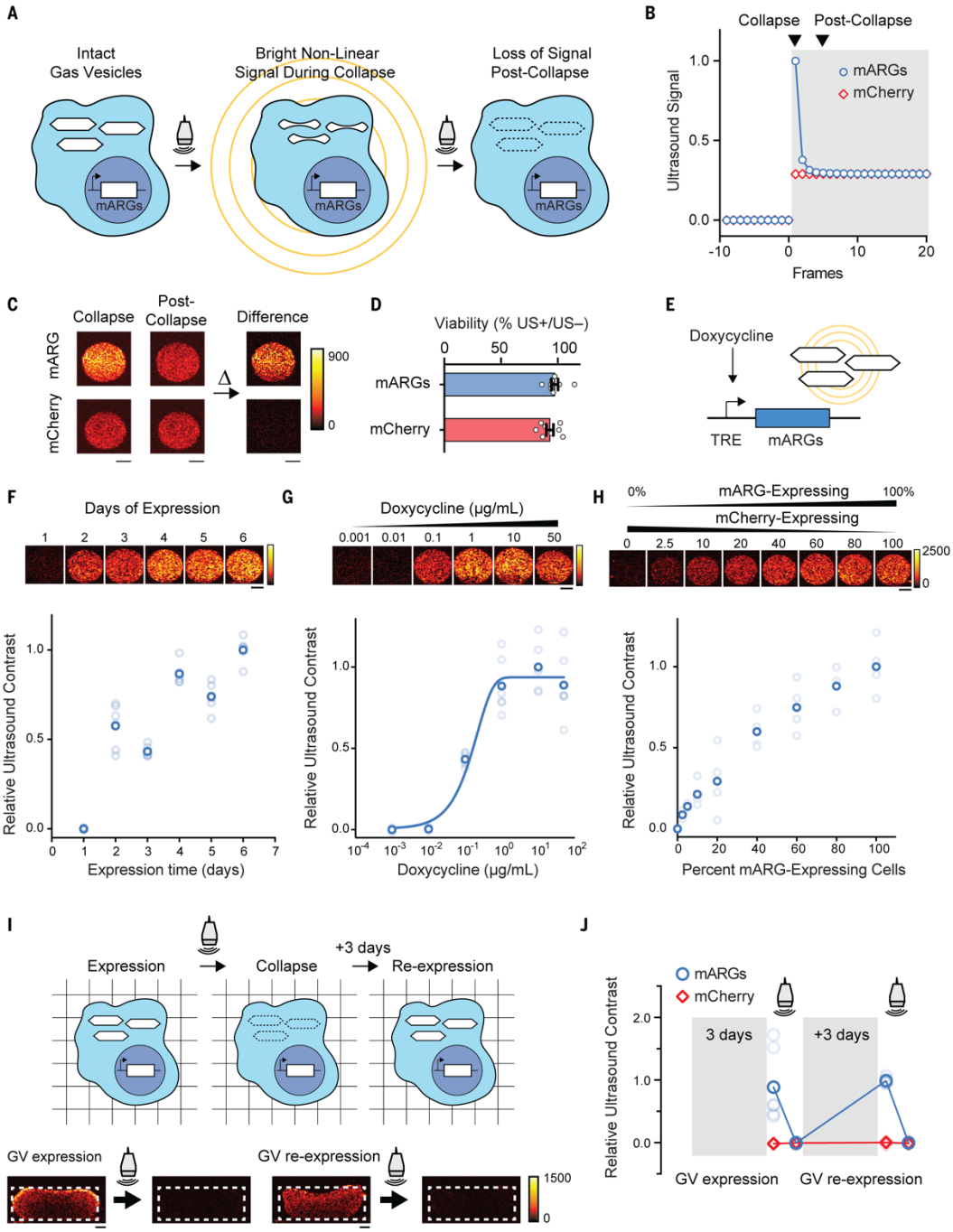

Figure 5.3 | Ultrasound imaging of mammalian gene expression *in vitro*. (**A**) Illustration of the collapse-based ultrasound imaging paradigm used to generate gas vesicle-specific ultrasound contrast from mARG-expressing cells. (**B**) Representative non-linear signal recorded during a step change in the incident acoustic pressure, from 0.27 MPa in the white-shaded region to 1.57 MPa in the grey-shaded region. (**C**) Representative collapse and post-collapse ultrasound images of mARG-HEK and mCherry-HEK cells acquired during this ultrasound imaging paradigm and their difference, indicating gas vesicle-specific contrast. (**D**) Cellular viability after being insonated under 3.2 MPa acoustic pressures, as measured using the MTT assay. (**E**) Schematic of a chemically inducible gene circuit with mARG expression as its output. All three mARG cassettes in mARG-HEK cells are under the control of the doxycycline-inducible TRE3G promoter (TRE), with expression triggered by incubation with doxycycline. (**F**) Representative ultrasound images and contrast measurements in mARG-HEK cells as a function of time following induction with 1 μg/mL of doxycycline and 5 mM sodium butyrate (n=6, with the darker dots showing the mean). (**G**)

Representative ultrasound images and contrast measurements in mARG-HEK cells as a function of doxycycline induction concentrations. Cells were allowed to express gas vesicles for 72 hours in the presence of 5 mM sodium butyrate. (n=6, with the darker dots showing the mean). A sigmoidal function is fitted as a visual guide. (**H**) Representative ultrasound images and contrast measurements in mARG-HEK cells mixed with mCherry-HEK cells in varying proportions. Cells were induced with 1 μg/mL of doxycycline and 5 mM sodium butyrate for 72 hours prior to imaging. (n=4, with the darker dots showing the mean) (**I**) Schematic and representative ultrasound images from mARG-HEK cells in Matrigel re-expressing gas vesicles after acoustic collapse. Cells were induced with 1 μg/mL of doxycycline and 5 mM sodium butyrate for 72 hours before and after 3.2 MPa acoustic insonation. Ultrasound images were acquired after an additional 72 hours in culture following collapse. (**J**) Ultrasound contrast in mARG-HEK and mCherry-HEK cells after initial expression, after collapse, after re-expression and after second collapse. (n=7, with the darker dots showing the mean). GV, gas vesicles. All scale bars represent 1 mm.

After 4 days of induction, we observed clear ultrasound contrast in the flank inoculated with mARG-HEK cells, which was absent from the contralateral side (**Fig. 5.4, C-D**). As expected, the pattern observed with ultrasound revealed mARG expression at the perimeter of the tumor, while the core remained dark, and the imaging of adjacent ultrasound planes revealed this pattern of gene expression to persist across the tumor mass (**Fig. 5.4E, Supplementary Fig. 5.9**).

The ultrasound-observed spatial distribution of gene expression was consistent with the low vascularity in the tumor core, as observed with Doppler ultrasound (**Supplementary Fig. 5.10**). The peripheral gene expression pattern was confirmed with subsequent histological examination of the tissue (**Fig. 5.4F, Supplementary Fig. 5.11**). In comparison, our *in vivo* fluorescence images just showed the presence of signal somewhere in the tissue and not its precise distribution (**Fig. 5.4G**). These results, which were consistent across 5 animals (**Supplementary Fig. 5.12A**), demonstrate that mARGs enable gene expression imaging *in vivo* and highlight the ability of ultrasound to visualize intricate patterns of gene expression non-invasively. We imaged 3 of the animals again after an additional 4 days to look for re-expression of the collapsed gas vesicles, and observed ultrasound contrast in each case (**Supplementary Fig. 5.12B**).

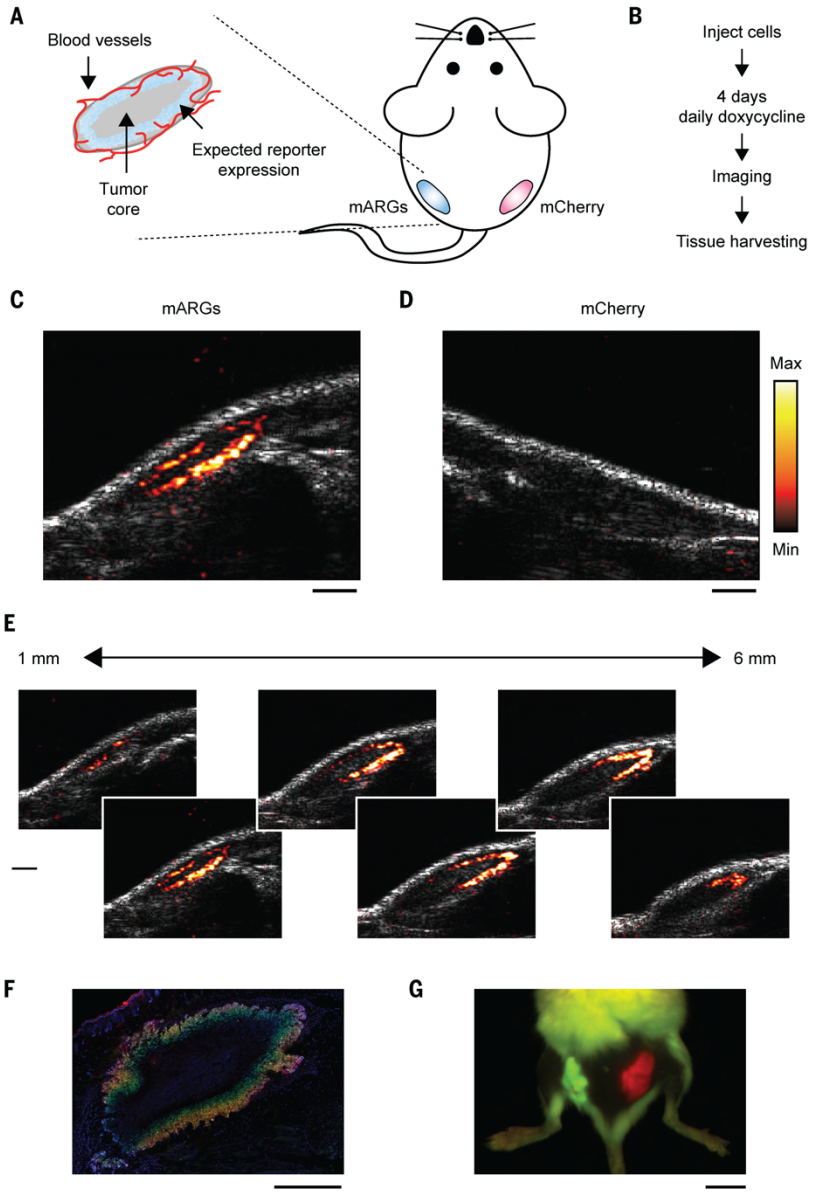

Figure 5.4 | Ultrasound imaging of mammalian gene expression *in vivo*. (**A**) Diagram of a mouse implanted with a subcutaneous tumor model, and the expected spatial pattern of vascularization and doxycycline-induced reporter gene expression. (**B**) Experimental timeline. (**C**) Representative ultrasound image of tumors containing mARG-HEK cells after 4 days of doxycycline administration. mARG-specific contrast shown in the hot colormap is overlaid on an anatomical B-mode image showing the background anatomy. (**D**) Representative ultrasound image of tumors containing mCherry-HEK cells after 4 days of doxycycline administration. (**E**) Ultrasound images of adjacent planes in the mARG-HEK tumor acquired at 1 mm intervals. The minimum and maximum values of color bars in C-E are 4000 and 40000 au, respectively. (**F**) Representative fluorescence image of a histological tissue section of an mARG-HEK tumor. Blue color shows the TO-PRO3 nucleus stain, green color shows GFP fluorescence and red color shows mCherry fluorescence. (**G**) Fluorescence image of a mouse implanted with mARG-HEK and mCherry-HEK tumors on the left and right flanks, respectively, after 4 days of expression. Scale bars for are 1 mm for **C-F** and 1 cm for **G**.

5.4 Discussion

Our results establish the ability of an engineered genetic construct encoding prokaryote-derived gas vesicles to serve as a mammalian reporter gene for ultrasound, providing the ability to monitor cellular location and function inside living organisms. mARGs provide many of the capabilities associated with established genetically encoded optical reporters, including imaging cellular dynamics via promoter-driven expression and mapping cellular populations in complex samples. While optical reporter genes mainly provide these

capabilities in culture and surgically accessed tissues, mARGs enable gene expression to be resolved non-invasively *in vivo*.

While the genetic constructs described in this work should be immediately useful in a variety of contexts, significant scope exists for further optimization to make acoustic reporter genes as widely useful as GFP[5,11]. For example, accelerating mARG expression beyond the day-scale kinetics shown in this study and developing sensitive imaging paradigms that do not require gas vesicle collapse would enable the imaging of more dynamic cellular processes. In addition, while this study demonstrated essential mARG functionality with clonally selected cell lines, the expression of mARGs in primary cells, their delivery to endogenous cells via viral vectors, and their expression in transgenic animals would greatly expand the utility of this technology. To facilitate such uses, it would be helpful to further condense the mARG constructs. For example, genes could be consolidated into fewer clusters, and preliminary experiments show that *gvpB* can be combined with the 8-gene polycistron encoding *gvpN-gvpU* via an internal ribosome entry sequence (IRES) (**Supplementary Fig. 5.13**). In addition, the total length of the coding sequence contained in mARG could be reduced from 7.6 kb to 4.8 kb by eliminating the need for redundant booster genes, relying instead on non-coding elements such as different-strength promoters to tune expression stoichiometry. Further optimization of mARG genetic constructs is also needed to reduce epigenetic silencing and metabolic burden[27–29]. Just as the engineering of GFP over many years yielded brighter and more colorful reporters enabling new uses of fluorescence microscopy, further engineering of the genetic constructs comprising mARGs would help cellular ultrasound penetrate and enable new areas of mammalian biology and biomedicine.

5.5 Methods

5.5.1 Chemicals, cell lines and synthesized DNA

All chemicals were purchased from Sigma Aldrich unless otherwise noted. HEK293T and CHO-K1 cell lines were ordered from American Type Culture Collection (ATCC) and HEK293-tetON cells and CHO-tetON cells were purchased from Clontech (Takara Bio). Synthetic DNA was ordered from Twist Bioscience.

5.5.2 Cloning

Monocistronic plasmids used for transient transfection of HEK293T cells of gas vesicle genes used the pCMVSport backbone. Codon optimized gas vesicle genes were assembled in each plasmid using Gibson assembly. To test the effect of N- and C-terminal P2A modification each *B. megaterium* gas vesicle gene on the pNL29 plasmid (addgene 91696) was individually cloned using standard mutagenesis

techniques. To test the N-terminal modification, the CCT codon was inserted following the start codon. To test the C-terminal modification, a linker-P2A sequence (GGAGCGCCAGGTTCCGGG-GCTACTAACTTCAGCCTCCTTAAACAGGCCGGCGA CGTGGAAGAGAATCCTGGC) was inserted upstream of the stop codon for each gene.

The polycistronic plasmid containing GvpN, GvpF, GvpG, GvpL, GvpS, GvpK, GvpJ, GvpU and Emerald GFP (EmGFP) were codon optimized, and synthesized in three fragments. The three fragments were Gibson assembled in the pCMVSport plasmid. The booster plasmid was assembled by multi-fragment Gibson assembly from PCR amplified fragments of the above plasmid.

The piggyBac transposon system (System Biosciences) was used to genomically integrate the mARG cassettes. To clone the mARG cassettes to the piggyBac transposon backbone, the plasmid was first digested using the SpeI and HpaI restriction enzymes and the mARG cassettes were Gibson assembled in the backbone. For doxycycline-inducible expression, the CMV promoter upstream of the gas vesicle genes was replaced with the TRE3G promoter. Internal ribosome entry site (IRES) and mCherry were cloned downstream GvpB as a marker for genomic integration. For the booster plasmid, CMVmin followed by enhanced BFP2 (eBFP2) and a polyadenylation element were cloned in the reverse direction upstream of the TRE3G promoter (creating a bi-directional doxycycline-inducible promoter) and used as a marker for genomic integration. A piggyBac transposon plasmid containing TRE3G and mCherry was Gibson assembled similarly to above.

5.5.3 Cell culture, transient transfection and TEM analysis

HEK293T and CHO-K1 cells were cultured in DMEM with 10% FBS and penicillin/streptomycin and seeded in a 6-well plate for transfection experiments. When the cells reached 70-80% confluency, 2 µg of total DNA (comprising the indicated mixtures of plasmids) was complexed with 2.58 µg polyethyleneimine (PEI-MAX; Polysciences Inc.) per µg of DNA, added to the cell culture, and incubated for 12-18 hours. The transfection of monocistronic plasmids encoding *Halobacterium salinarum*, *Anabaena flos-aquae* and *Bacillus megaterium* were all at equal molar ratios. Thereafter, the media containing the PEI-DNA complex was changed with fresh media. Cells were allowed to express the recombinant proteins for 72 hours.

To look for gas vesicles, fully confluent cells cultured in 6-well plates were lysed with 400 µL of Solulyse-M (Genlantis Inc) per well for one hour at 4 °C. The lysate was then transferred to 2 mL tubes, diluted with 800 µL of 10 mM HEPES buffer at pH 8.0 and centrifugated overnight at 300 g and 8 °C. Then, 60 µL of the supernatant was transferred to a fresh tube to be analyzed using transmission electron microscopy (TEM).

From this top fraction, 2 µL of sample was added to Formvar/carbon 200 mesh grids (Ted Pella) that were rendered hydrophilic by glow discharging (Emitek K100X). The samples were then stained with 2% uranyl acetate. The samples were imaged on a FEI Tecnai T12 transmission electron microscope equipped with a Gatan Ultrascan CCD.

To estimate gas vesicle yield and analyze size distribution, the cells were seeded in 6-well plates and gas vesicle expression was induced with 1 µg/mL of doxycycline and 5 mM sodium butyrate for 72 hours. The cells were lysed using Solulyse-M and buoyancy enriched at 300 g at 8 ˚C overnight. The top fraction of the supernatant was mixed with 2M urea and spotted on Formvar/carbon grids. The TEM grids were washed with water before staining with 2% uranyl acetate. To calculate gas vesicle yield per cell, the total number of gas vesicles per sub-grid on the TEM grid was manually counted and related via lysate volume to the number of source cells. Gas vesicle size distribution was quantified using FIJI[30].

To visualize gas vesicles inside cells, mARG-HEK cells were seeded in 6-well plates and allowed to express gas vesicles for 72 hours. The cells were fixed in 1.25% glutaraldehyde in PBS, post-fixed in 1% aqueous osmium tetroxide, reduced with ferrocyanide and block-stained in 1% uranyl acetate (all reagents from Electron Microscopy Sciences). The material was then dehydrated through a graded ethanol series and embedded in Eponate12 (Ted Pella). Sections were cut 60 nm thin onto formvar-filmed copper grids, stained with 2% uranyl acetate and Reynolds lead citrate, and imaged at 80 kV in a Zeiss EM10C (Oberkochen) equipped with an ES1000W Erlangshen CCD camera (Gatan).

5.5.4 Genomic integration and FACS

HEK293-tetON and CHO-tetON cells were used for genomic integration of the mARGs. The cells were cultured in a 6-well plate containing 2 mL DMEM with 10% tetracycline-free FBS (Clontech) and penicillin/streptomycin. Cells were transfected with the piggyBac transposon backbone containing the mARGs and the piggyBac transposase plasmid at a transposon:transposase molar ration of 2.5:1. Transfection was conducted using parameters mentioned above and the cells were allowed to incubate for 72 hours. Cells were induced with 1 µg/mL of doxycycline 24 hours prior to FACS (BD FACSAria III). Polyclonal subpopulations of mARG-expressing HEK293-tetON cells were sorted into the following four bins: (subtype 1) cells with eBFP2 fluorescence greater than 10^4 and EmGFP fluorescence greater than 10^4 and mCherry fluorescence greater than $2x10^4$ au, (subtype 2) cells with eBFP2 fluorescence between $3x10^3$ and $2x10^4$ and EmGFP fluorescence between $2x10^3$ and $2x10^4$ and mCherry fluorescence between $2x10^3$ and $2x10^4$ au, (subtype 3) cells with eBFP2 fluorescence between 10^3 and $6x10^3$ and EmGFP fluorescence between $2x10^2$ and 10^3 and mCherry fluorescence greater than $2x10^4$ au, (subtype 4) cells with eBFP2 fluorescence greater than 10^4 and EmGFP fluorescence greater than $2x10^4$ and mCherry fluorescence between $2x10^3$ and $2x10^4$ au. CHO-tetON cells were transfected with mARGs and the piggyBac transposase

plasmid similar to above. mARG-expressing CHO-tetON cells with eBFP2 fluorescence greater than 10^4, EmGFP fluorescence greater than 10^4 and mCherry fluorescence greater than $2x10^4$ au were sorted.

For monoclonal cell lines, naïve HEK293-tetON cells were transfected with mARGs and the piggyBac transposase similar to above. mARG-expressing cells with eBFP2 fluorescence greater than 10^4, EmGFP fluorescence greater than 10^4 and mCherry fluorescence greater than $2x10^4$ au were sorted. 576 cells were sorted in individual wells of 96-well plate and the surviving 30 cells were analyzed for gas vesicle expression as described above.

To generate mCherry-HEK cells, HEK293-tetON cells were transfected with piggyBac transposon plasmid containing TRE3G promoter driving mCherry and the transposase plasmid similar to above. mCherry-HEK cells were sorted from cells with mCherry fluorescence between $1.5x10^4$ and 10^5 au.

Monoclonal cell lines (mARG-HEK and mCherry-HEK cells) were maintained in tetracycline-free media without butyrate and all imaging and toxicity experiments were conducted with cells that were less than 16 generations.

5.5.5 In vitro toxicity assays

The viability of the mARG-expressing cells was determined using three different assays involving cellular metabolic activity (resazurin reduction, MTT assay), quantification of cellular ATP content (CellTiter-Glo, Promega Corp.), and dye exclusion (Trypan Blue, Caisson Labs). The measurements were all quantified as percent viability compared to control cells that expressed mCherry only (mCherry-HEK). For the MTT and CellTiter-Glo assays, cells were grown in 96-well plates and induced with 1 µg/mL doxycycline and 5 mM sodium butyrate for 72 hours. They were then treated with reagents according the manufacturers' protocols. Luminescence (CellTiter-Glo) and absorbance at 540 nm (MTT) was measured using a SpectraMax M5 spectrophotometer (Molecular Devices). For the Trypan Blue assay, the cells were first grown in 6-well plates and treated with 1 µg/mL doxycycline and 5 mM sodium butyrate for 72 hours. They were then trypsinized and resuspended in media before being stained 1:1 with Trypan Blue dye. Ten µL of the solution was loaded in a disposable hemocytometer (C-chip DHC S02, Incyto) and total cell count and blue-stained dead cells were quantified by bright field microscopy. Cellular morphology was imaged from mARG-HEK and mCherry-HEK cells after 3 days of expression with 1 µg/mL doxycycline and 5 mM sodium butyrate. Phase images were acquired using a Zeiss Axio Observer with a 20x objective. For the co-culture cell competition assay, cells were counted and $2x10^5$ cells from each type were mixed together and seeded in 6-well plates. One day after seeding, cells were induced with 1 µg/mL doxycycline and 5 mM sodium butyrate and the media was exchanged daily. At each time point, cells were trypsinized and sorted using the MACSQuant VYB Flow Cytometer (Miltenyi Biotech) to quantify relative cell ratios. At one day and three days post induction, cells were passaged to ensure continuous exponential growth.

5.5.6 *In vitro* ultrasound imaging

To create phantoms for *in vitro* ultrasound imaging, wells were casted with molten 1% w/v agarose in PBS using a custom 3D-printed template. mARG-HEK and mCherry-HEK cells were allowed to express their transgenes using the specified inducer concentrations and expression duration. They were then trypsinized and counted via disposable hemocytometers in bright field microscopy. Next, cells were mixed at a 1:1 ratio with 50 °C agarose and loaded into the wells before solidification. The volume of each well was 60 µl and contained $6x10^6$ cells. The phantoms were submerged in PBS, and ultrasound images were acquired using a Verasonics Vantage programmable ultrasound scanning system and L22-14v 128-element linear array transducer with a 0.10-mm pitch, an 8-mm elevation focus, a 1.5-mm elevation aperture, and a center frequency of 18.5 MHz with 67% −6 dB bandwidth (Verasonics, Kirkland, WA). Each frame was formed from 89 focused beam ray lines, each with a 40-element aperture and 8 mm focus. A 3-half-cycle transmit waveform at 17.9 MHz was applied to each active array element. For each ray line, the amplitude modulation (AM) code was implemented using one transmit with all elements in the active aperture followed by 2 transmits in which first the odd- and then the even-numbered elements are silenced (*10*). Each image captured a circular cross-section of a well with a 4-mm diameter and center positioned at a depth of 8 mm. In AM mode, the signal was acquired at 0.27 MPa (2V) for 10 frames and the acoustic pressure was increased to 1.57 MPa (10V) to collect 46 additional frames. Ultrasound images were constructed by subtracting the collapsing frame by frame 4 post-collapse.

For Fig. 5.3, F-H, the high gas vesicle content of some samples resulted in acoustic shielding and a residual amount of gas vesicles remained intact after 46 frames of insonation at 1.57 MPa. To fully collapse all the gas vesicles and collect the background signal, the acoustic pressure was increased to 3.2 MPa (25V), then a second set of images was acquired with 10 frames at 0.27 MPa and 46 frames at 1.57 MPa. Gas vesicle-specific signal was determined by subtracting the total ultrasound signal from the 46 frames acquired before 3.2 MPa ultrasound by the total ultrasound signal from the 46 frames post collapse.

5.5.7 Cytotoxicity assay on cells exposed to ultrasound

mARG-HEK and mCherry-HEK cells were cultured on custom made Mylar-bottom 24-well plates. Cells were cultured on fibronectin-coated Mylar films until they reached 80% confluency and induced for gas vesicle expression (1 µg/mL doxycycline and 5 mM sodium butyrate) for 3 days. The cells were then insonated from the bottom using an L22-14v 128-element linear array transducer (Verasonics). The transducer was mounted on a computer-controlled 3D translatable stage (Velmex). The bottom of the plates was acoustically coupled to the transducer with water and positioned 8 mm away from the transducer face. The cells were exposed to 3.2 MPa of pressure and the transducer was translated at a rate of 3.8 mm/s. The

plates were returned to the incubator for 24 hours. Cytotoxicity was then assayed using resazurin reduction (MTT) on cells exposed to ultrasound and compared to non-insonated control cells.

5.5.8 3D cell culture and *in vitro* acoustic recovery after collapse

mARG-HEK and mCherry-HEK cells were mixed in Matrigel (Corning) containing 1 µg/mL of doxycycline and 5 mM sodium butyrate. The cell-laden hydrogels were placed in a 1% w/v agarose base to prevent cell migration out of the hydrogel and to separate the cells away from the bottom of the plates during imaging. Cells were cultured for total of 6 days and imaged every 3 days from the top using an L22-14v 128-element linear array transducer (Verasonics). The transducer was wiped with 70% ethanol, and imaging was conducted in a laminar flow biosafety cabinet to preserve sterility. After imaging, to ensure complete collapse of all gas vesicles in the cells, the entire hydrogel was exposed to 3.2 MPa ultrasound and the transducer was translated three times across the gel at a rate of 1-2 mm/s. The culture media was changed daily and contained 1 µg/mL of doxycycline and 5 mM sodium butyrate.

5.5.9 I*n vivo* expression of gas vesicles and ultrasound imaging

All *in vivo* experiments were performed on NOD SCID mice (NOD.CD17 *Prkdc*^{scid}/*NCrCr*l; Charles River), aged 10-15 weeks, under a protocol approved by the Institutional Animal Care and Use of Committee of the California Institute of Technology. mARG-HEK and mCherry-HEK cells were cultured in tetracycline-free media in T225 flasks. 1-1.2x10^7 cells were trypsinized and the 200 µl cell-pellet was mixed with 200 µl Matrigel (Corning) containing 5 mM sodium butyrate. The mixture of mARG-HEK cells and Matrigel was injected subcutaneously in the left flank of mice and the mixture of mCherry-HEK cells and Matrigel was injected subcutaneously in the right flank of mice. Starting from the day of tumor inoculation, mice we interperitoneally injected with 200 µl of saline containing 75 µg doxycycline and 25 mg of sodium butyrate daily. The lower half of mice were depilated to allow for fluorescence imaging and ultrasound coupling.

For ultrasound imaging, the mice were anesthetized with 2% isoflurane and maintained at 37˚C using a heating pad. Ultrasound imaging was carried out using the pulse sequence described above with an L22-14v transducer attached to a custom-made manual translation stage. Using B-mode ultrasound imaging, the center of the tumor was positioned approximately 8 mm from the surface of the transducer, and gas vesicle-specific ultrasound images were acquired. The transducer was translated laterally with 1 mm steps to collect ultrasound images of most of the tumor.

High framerate ultrasound datasets for Doppler imaging were acquired with the same ultrasound transducer and scanner. The Doppler pulse sequence consisted of 11 tilted plane wave transmissions (varying from -10 to 10 degrees) at a 5.5 kHz framerate, leading to a 500 Hz framerate after coherent

compounding. Plane wave transmissions lasted 0.5 s (or 250 frames). A power Doppler image representing blood flow was computed from each ensemble of 250 frames using a singular value decomposition filter that separates clutter from red blood cell echoes[31].

To obtain tissue samples after the mice were euthanized, tumors were resected and placed in 3.7% formaldehyde solution (4˚C) for 24 hours and transferred to sterile 30% sucrose for an additional 24 hours. Tumors were embedded in OCT compound (Tissue-Tek), flash frozen and sectioned to 60 μm slices using a Cryostat (Leica CM3050). Sections were stained with TO-PRO3 nucleus stain, mounted (Fluoromount Aqueous Mounting Medium) and imaged using a Zeiss LSM 800 confocal microscope.

References

1. Tsien, R. Y. Imagining imaging's future. *Nat Rev Mol Cell Biol* **Suppl**, SS16-21 (2003).
2. Piraner, D. I. *et al.* Going Deeper: Biomolecular Tools for Acoustic and Magnetic Imaging and Control of Cellular Function. *Biochemistry* **56**, 5202–5209 (2017).
3. Chu, J. *et al.* A bright cyan-excitable orange fluorescent protein facilitates dual-emission microscopy and enhances bioluminescence imaging in vivo. *Nature biotechnology* **34**, 760–767 (2016).
4. Santos, E. B. *et al.* Sensitive in vivo imaging of T cells using a membrane-bound Gaussia princeps luciferase. *Nature Medicine* **15**, 338–344 (2009).
5. Maresca, D. *et al.* Biomolecular Ultrasound and Sonogenetics. *Annu. Rev. Chem. Biomol. Eng.* (2018) doi:10.1146/annurev-chembioeng-060817-084034.
6. Pfeifer, F. Distribution, formation and regulation of gas vesicles. *Nature Reviews Microbiology* **10**, 705–715 (2012).
7. Walsby, A. E. Gas vesicles. *Microbiology and Molecular Biology Reviews* **58**, 94–144 (1994).
8. Shapiro, M. G. *et al.* Biogenic gas nanostructures as ultrasonic molecular reporters. *Nature Nanotechnology* **9**, 311–316 (2014).
9. Lakshmanan, A. *et al.* Molecular Engineering of Acoustic Protein Nanostructures. *ACS Nano* **10**, 7314–7322 (2016).
10. Maresca, D. *et al.* Nonlinear ultrasound imaging of nanoscale acoustic biomolecules. *Appl. Phys. Lett.* **110**, 073704 (2017).
11. Maresca, D., Sawyer, D. P., Renaud, G., Lee-Gosselin, A. & Shapiro, M. G. Nonlinear X-Wave Ultrasound Imaging of Acoustic Biomolecules. *Phys. Rev. X* **8**, 041002 (2018).
12. Lu, G. J., Farhadi, A., Mukherjee, A. & Shapiro, M. G. Proteins, air and water: reporter genes for ultrasound and magnetic resonance imaging. *Current Opinion in Chemical Biology* **45**, 57–63 (2018).
13. Bourdeau, R. W. *et al.* Acoustic reporter genes for noninvasive imaging of microorganisms in mammalian hosts. *Nature* **553**, 86–90 (2018).

14. Davis, M. M., Tato, C. M. & Furman, D. Systems immunology: just getting started. *Nature immunology* **18**, 725 (2017).
15. Maguire, Y. G. *et al.* Physical principles for scalable neural recording. *Frontiers in computational neuroscience* **7**, 137 (2013).
16. Schroeder, T. Imaging stem-cell-driven regeneration in mammals. *Nature* **453**, 345–351 (2008).
17. Gradinaru, V. *et al.* Molecular and Cellular Approaches for Diversifying and Extending Optogenetics. *Cell* **141**, 154–165 (2010).
18. Shieh, Y.-W. *et al.* Operon structure and cotranslational subunit association direct protein assembly in bacteria. *Science* **350**, 678–680 (2015).
19. Natan, E., Wells, J. N., Teichmann, S. A. & Marsh, J. A. Regulation, evolution and consequences of cotranslational protein complex assembly. *Current Opinion in Structural Biology* **42**, 90–97 (2017).
20. Close, D. M. *et al.* Autonomous Bioluminescent Expression of the Bacterial Luciferase Gene Cassette (lux) in a Mammalian Cell Line. *PLOS ONE* **5**, e12441 (2010).
21. Farhadi, A. *et al.* Recombinantly expressed gas vesicles as nanoscale contrast agents for ultrasound and hyperpolarized MRI. *AIChE Journal* **0**,.
22. Szymczak, A. L. & Vignali, D. A. Development of 2A peptide-based strategies in the design of multicistronic vectors. *Expert Opinion on Biological Therapy* **5**, 627–638 (2005).
23. Ding, S. *et al.* Efficient Transposition of the piggyBac (PB) Transposon in Mammalian Cells and Mice. *Cell* **122**, 473–483 (2005).
24. Wilson, M. H., Coates, C. J. & George, A. L. PiggyBac Transposon-mediated Gene Transfer in Human Cells. *Molecular Therapy* **15**, 139–145 (2007).
25. Elowitz, M. B. & Leibler, S. A synthetic oscillatory network of transcriptional regulators. *Nature* **403**, 335–338 (2000).
26. Gardner, T. S., Cantor, C. R. & Collins, J. J. Construction of a genetic toggle switch in Escherichia coli. *Nature* **403**, 339–342 (2000).

27. Gaidukov, L. *et al.* A multi-landing pad DNA integration platform for mammalian cell engineering. *Nucleic Acids Res* **46**, 4072–4086 (2018).

28. Jusiak, B. *et al.* Comparison of Integrases Identifies Bxb1-GA Mutant as the Most Efficient Site-Specific Integrase System in Mammalian Cells. *ACS Synth. Biol.* **8**, 16–24 (2019).

29. Neville, J. J., Orlando, J., Mann, K., McCloskey, B. & Antoniou, M. N. Ubiquitous Chromatin-opening Elements (UCOEs): Applications in biomanufacturing and gene therapy. *Biotechnology Advances* **35**, 557–564 (2017).

30. Schindelin, J. *et al.* Fiji: an open-source platform for biological-image analysis. *Nature Methods* **9**, 676–682 (2012).

31. Demené, C. *et al.* Spatiotemporal Clutter Filtering of Ultrafast Ultrasound Data Highly Increases Doppler and fUltrasound Sensitivity. *IEEE Transactions on Medical Imaging* **34**, 2271–2285 (2015).

5.6 Supplementary Material

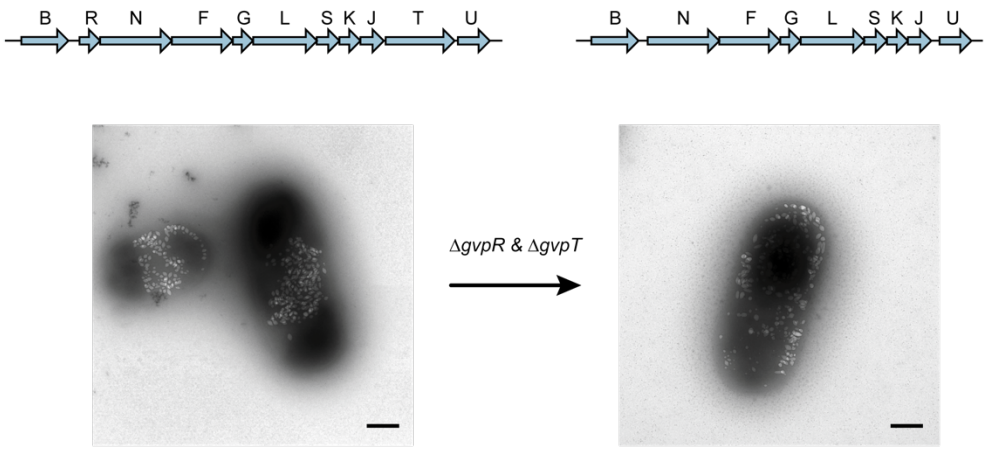

Supplementary Figure 5.1 – G*vpR* and G*vpT* genes in the *B. megaterium* gene cluster are not necessary for gas vesicle formation. Schematic of bacterial gas vesicle gene clusters used for heterologous expression of gas vesicles in *E. coli* (top). Representative whole cell TEM images of *E. coli* Rosetta 2(DE3)pLysS cells after expression of gas vesicles genes for 22 hours (bottom). Scale bars represent 500 nm. Expression performed as in Farhadi *et al.* (*21*) and TEM imaging as in Bourdeau *et al.* (*13*).

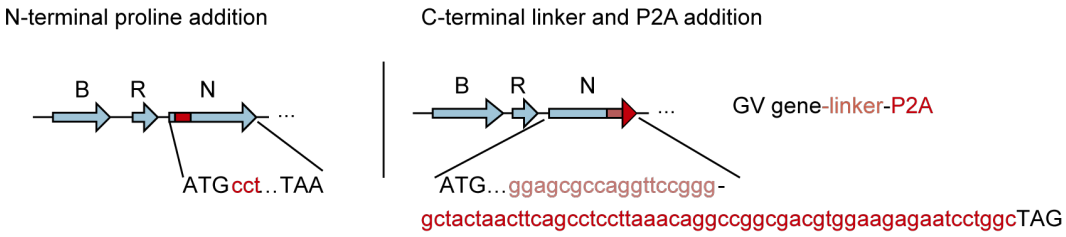

Supplementary Figure 5.2 – Assay for tolerability of P2A peptide additions. Illustration of gas vesicle gene cluster with N- or C-terminal modifications of each gene to test tolerability of P2A peptides, tested one-by-one in *E. coli*.

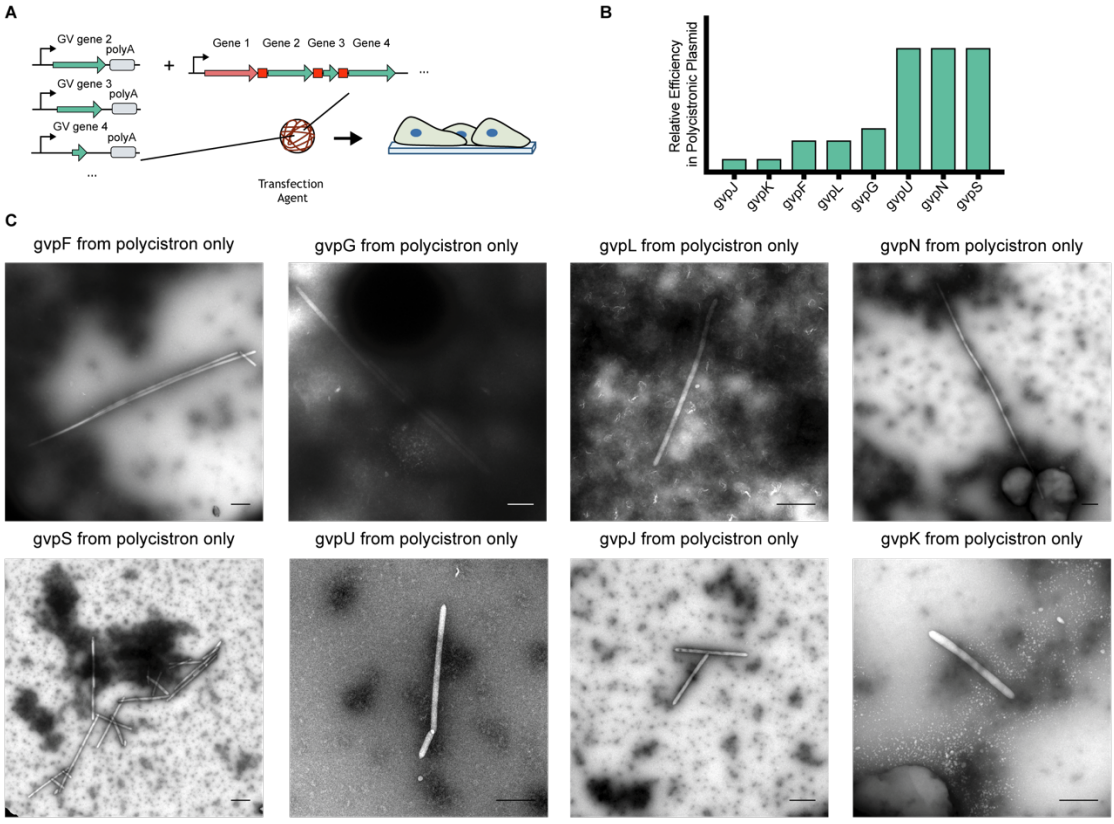

Supplementary Figure 5.3 – Identification of bottleneck genes on the polycistronic gas vesicle gene plasmid. (**A**) Schematic of the experiment. To test the efficiency with which gas vesicles could be formed when a given gene was supplied only on the polycistronic plasmid, and thereby identify "bottleneck" genes, cells were co-transfected with a monocistronic plasmid containing G*vpB*, 7 other monocistronic plasmids including all but the gene being assayed, and the polycistronic plasmid. (**B**) Qualitative estimate of the relative number of gas vesicles produced when each indicated gene was supplied solely by the polycistronic plasmid. (**C**) Representative TEM images of gas vesicles in the lysate of HEK293T cells for all 8 assays. Scale bars represent 500 nm. These results suggest that *GvpN*, *GvpS* and *GvpU* supplied in either monocistronic or polycistronic form supported abundant gas vesicle assembly. However, the production of gas vesicles was significantly reduced when *GvpJ, GvpF, GvpG, GvpL* or *GvpK* was supplied from the polycistronic vector. We therefore suspected that these genes represented a bottleneck in gas vesicle formation.

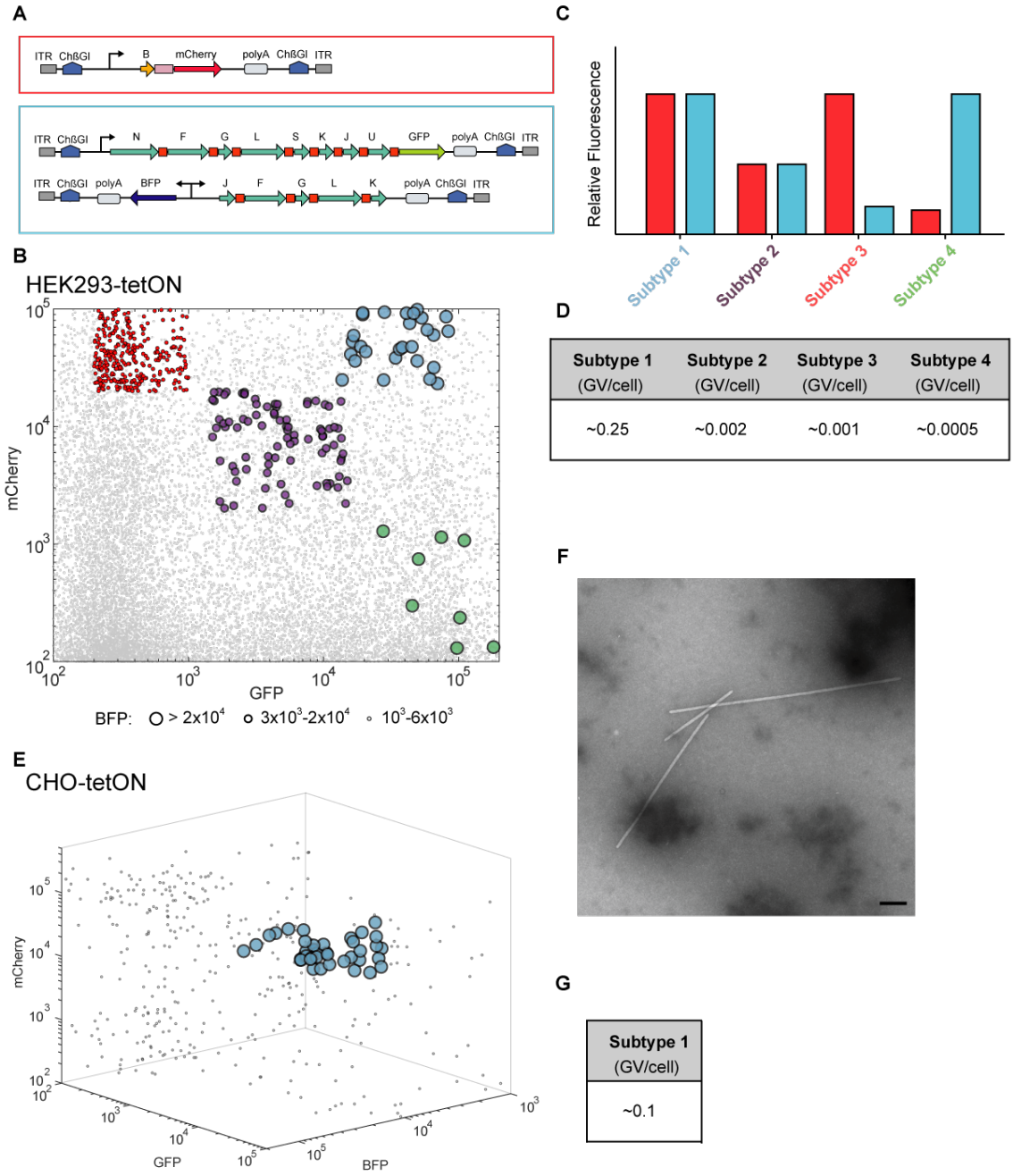

Supplementary Figure 5.4 – Fluorescence activated cell sorting of HEK293-tetON and CHO-tetON cells transfected with integrating mARG constructs. (**A**) Diagram of the integrating constructs used to generate polyclonal cell lines. (**B**) FACS of mARG-expressing HEK293-tetON cells. Colored data indicate cells sorted for each group and gray dots are unsorted population. (**C**) Illustration of the four polyclonal subtypes sorted to study the impact of polycistron stoichiometry on gas vesicle expression. Red bars indicate mCherry expression; cyan bars indicate EmGFP and eBFP2 expression. (**D**) Approximate gas vesicle yield from polyclonal cells in each subtype. (**E**) FACS of mARG-expressing CHO-tetON cells. Colored data indicate cells sorted in subtype 1 and gray dots are unsorted cells. (**F**) Representative TEM image of buoyancy-enriched lysate from CHO-tetON cells sorted as indicated in (E). Scale bar represents 500 nm. (**G**) Approximate gas vesicle yield for the sorted mARG-expressing CHO-tetON cells.

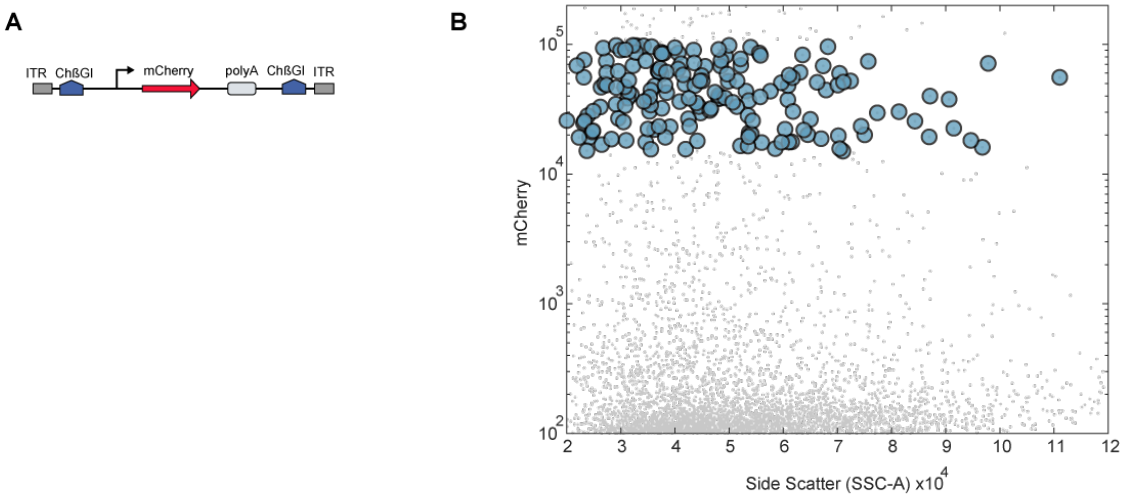

Supplementary Figure 5.5 – Genetic construct and sorting of mCherry-HEK cell line. (**A**) Genetic construct for stable genomic integration of mCherry containing a TRE3G promoter upstream and SV40 polyadenylation element downstream of mCherry. (**B**) FACS of mCherry cells, with selected cells indicated with blue dots.

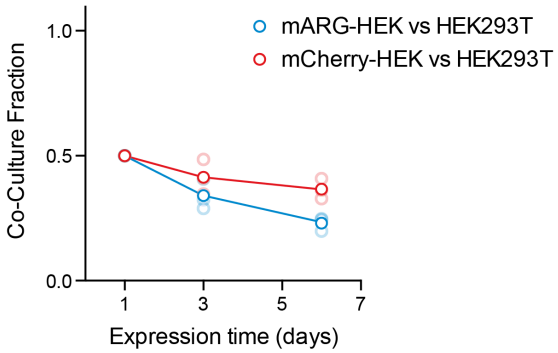

Supplementary Figure 5.6 – Co-culture of reporter gene expressing cells with HEK293T cells. Fraction of mARG-HEK cells in co-culture with HEK293T cells (blue) or mARG-mCherry cells in co-culture with HEK293T cells (red) seeded in equal numbers over 6 days of gene expression (n=3 biological replicates, each from 4 technical replicates, with darker dots showing the mean).

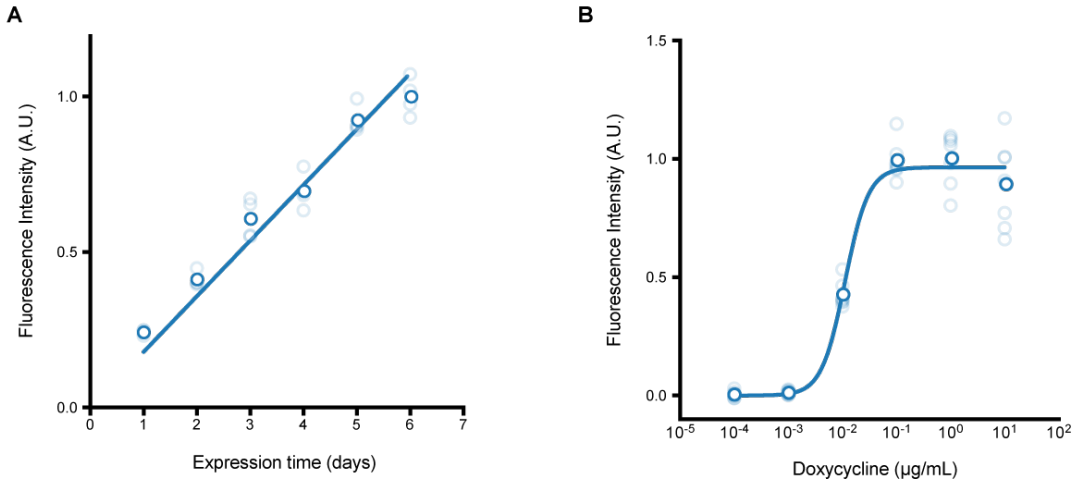

Supplementary Figure 5.7 – Fluorescence measurements of gene expression as a function of time and inducer concentration in mARG-HEK cells. (**A**) mCherry fluorescence of mARG-HEK cells induced with 1 µg/mL doxycycline and 5 mM sodium butyrate at the indicated times after induction (n=4, with the darker dots showing the mean). (**B**) mCherry fluorescence of mARG-HEK cells with the indicated inducer concentration and 5 mM sodium butyrate after 72 hours of induction (n=7, with the darker dots showing the mean).

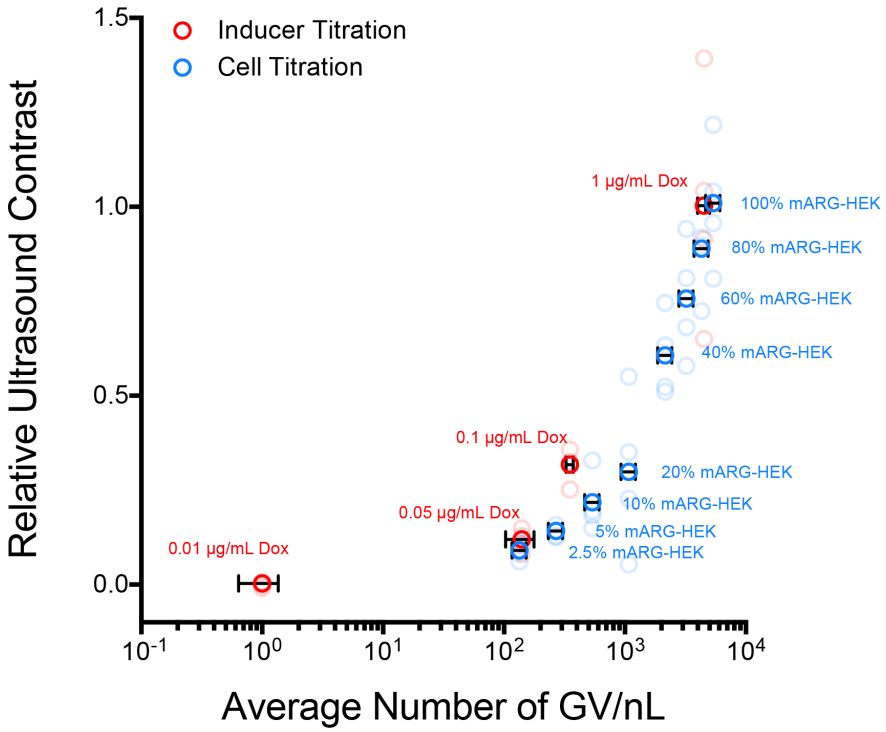

Supplementary Figure 5.8 – Dependence of ultrasound contrast on gas vesicle density. Relative ultrasound contrast produced by mARG-HEK cells in hydrogel as a function of the estimated average number of gas vesicles (GV) per nanoliter present after a monoculture of mARG-HEK cells was induced with different concentrations of doxycycline, or after fully-induced mARG-HEK cells were mixed with mCherry-HEK cells at different ratios. Blue symbols represent results from mARG-HEK cells induced with 1 µg/mL doxycycline for 3 days (producing on average 45 gas vesicles per cell) mixed with mCherry-HEK cells (expressing no gas vesicles) in varying proportions, as presented in Fig. 5.3H. Red symbols represent results from mARG-HEK cells induced with 0.01, 0.05, 0.1 and 1 µg/mL doxycycline for 3 days; expressing on average 0.01 ± 0.004, 1.4 ± 0.4, 3.5 ± 0.3, 45 ± 5.1 (mean ± SEM) gas vesicles per cell, respectively, as quantified by TEM. All cells were cultured with 5 mM sodium butyrate during expression. The number of gas vesicles was quantified after 72 hours of induced expression, as counted in lysates using TEM. Ultrasound contrast was normalized to the maximum in each type of titration. Dark symbols show the mean of ultrasound contrast for 4 replicates. Error bars represent SEM of 4 biological replicates for 0.01, 0.05, 0.1 µg/mL induction and n=3 biological replicates (each from two technical replicates) for 1 µg/mL samples.

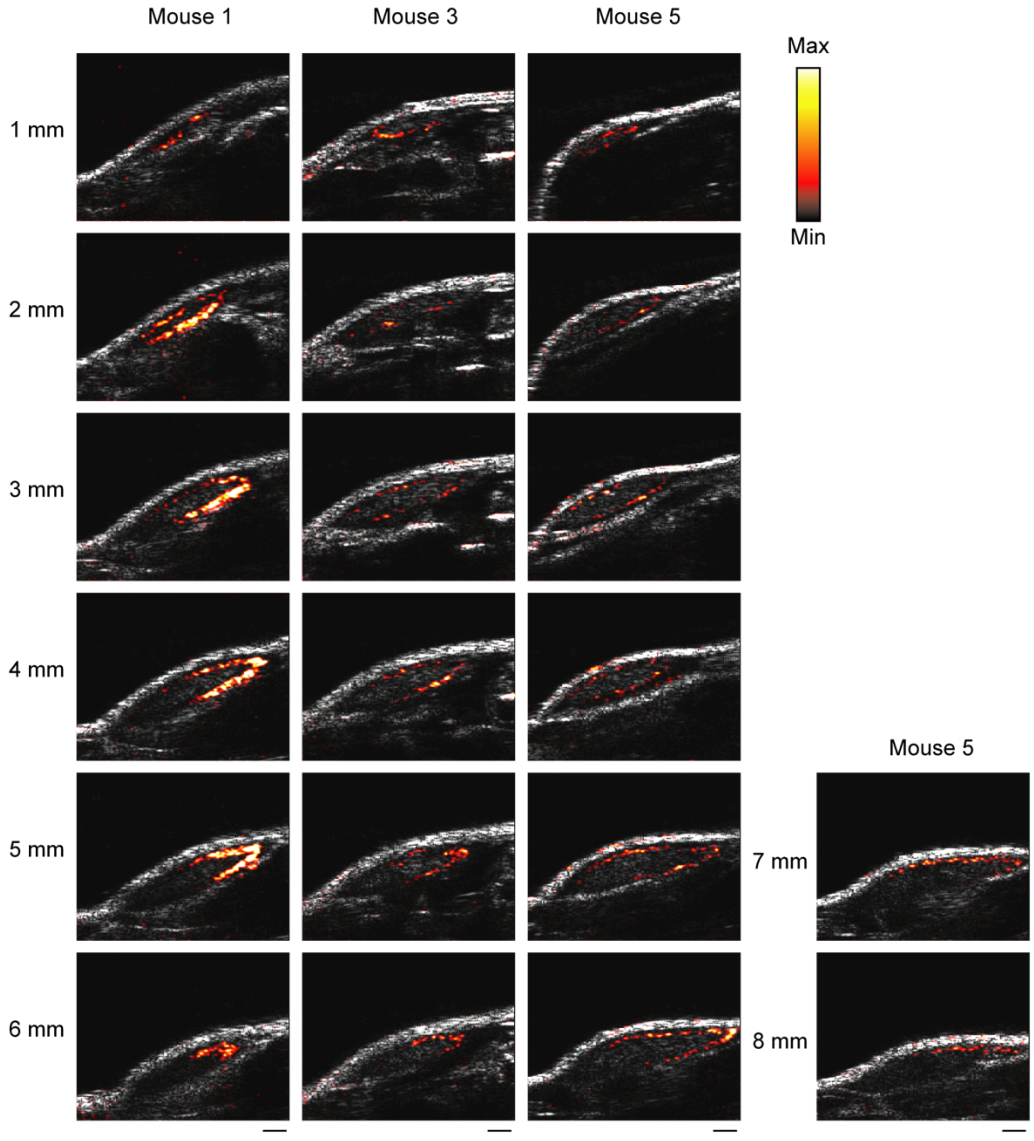

Supplementary Figure 5.9 – Additional examples of *in vivo* ultrasound images of adjacent planes in mARG-HEK tumors acquired at 1 mm intervals. For each imaging slice the difference heatmap of nonlinear signal between frame 1 and frame 4 is overlaid on grayscale anatomical scale. Minimum and maximum values of color bar are 4000 and 40000, respectively. Scale bars are 1 mm.

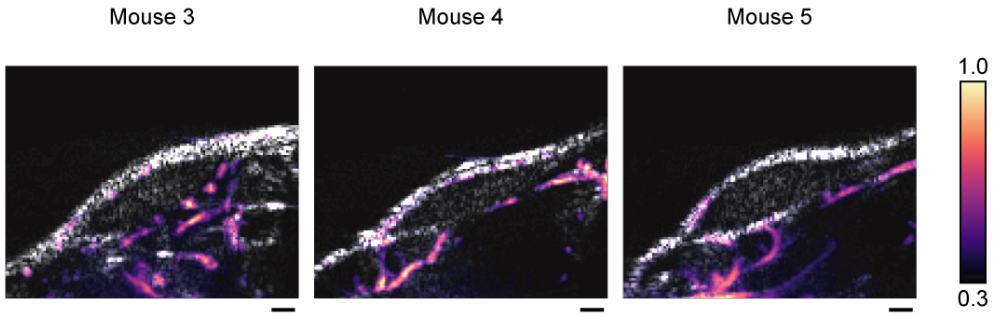

Supplementary Figure 5.10 – Representative Doppler ultrasound images of tumors containing mARG-HEK cells. Doppler ultrasound images were acquired using 250 frames of ultrafast planewaves at 25V and used to reconstruct vascular maps plotted as normalized power doppler signal overlaid on anatomical images in grayscale. Scale bars represent 1 mm.

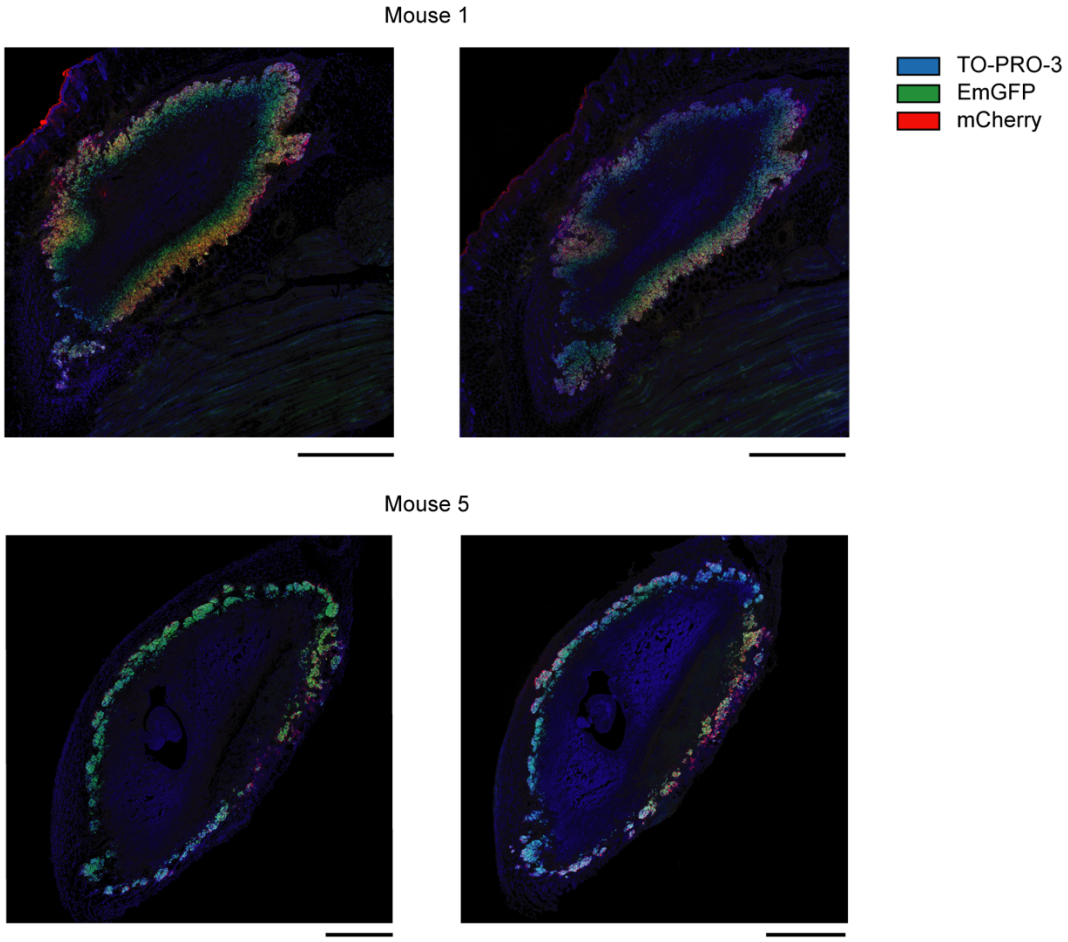

Supplementary Figure 5.11 – Representative histology sections of tumors containing mARG-HEK cells. For each mouse, two neighboring sections are presented. Blue color indicates cell nuclear staining using TO-PRO-3, green color represents GFP fluorescence and red color represents mCherry fluorescence. All scale bars are 1 mm.

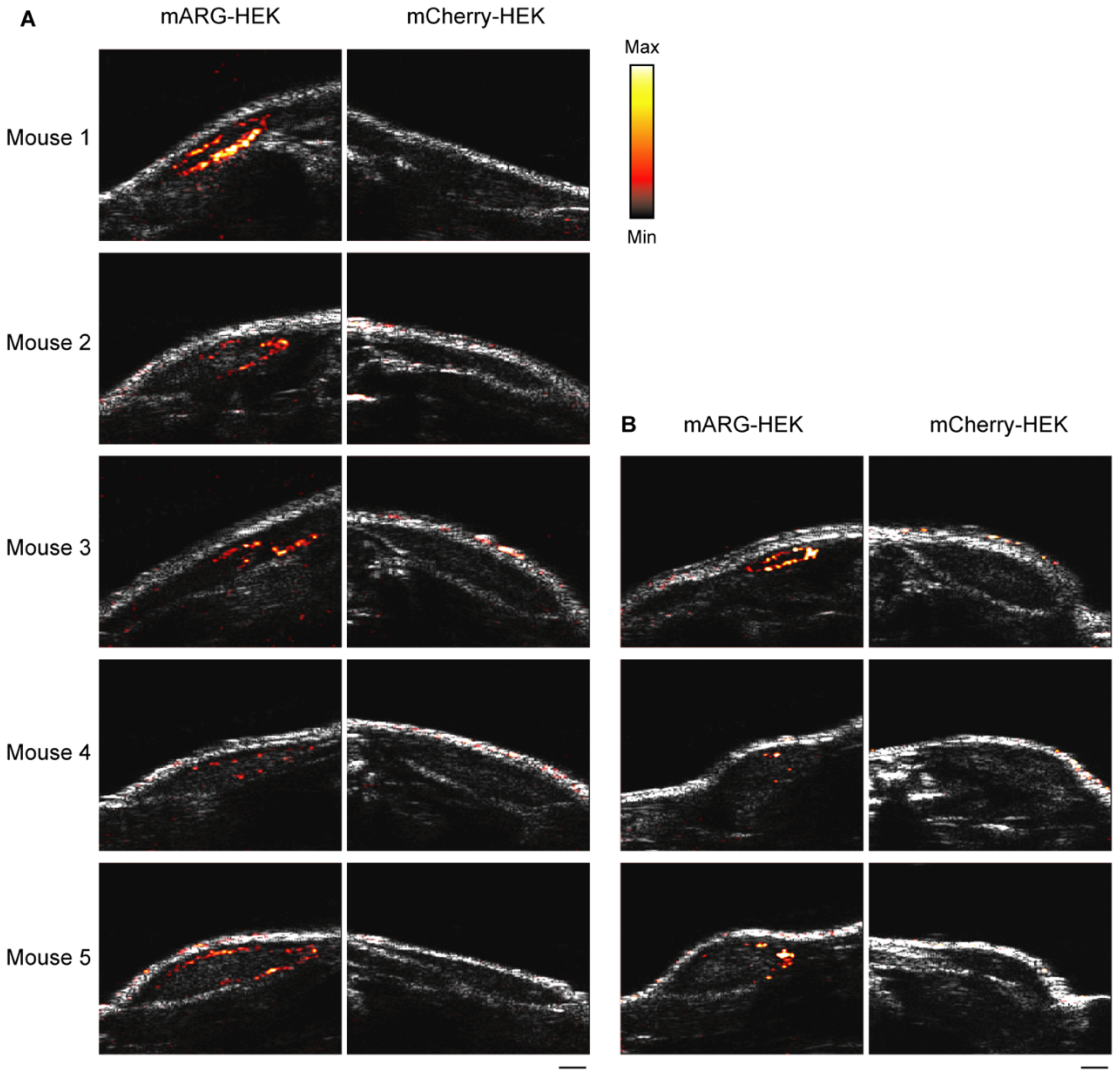

Supplementary Figure 5.12 – Biological replicates of *in vivo* ultrasound imaging of gene expression. (**A**) The left column shows ultrasound images of tumors containing mARG-HEK cells after 4 days of doxycycline administration. The right column shows ultrasound images of tumors containing mCherry-HEK cells after 4 days of doxycycline administration. After imaging the tumors were insonated with 3.2 MPa of ultrasound to collapse the expressed gas vesicles. (**B**) The left column shows ultrasound images of tumors containing mARG-HEK cells re-expressing gas vesicles after an additional 4 days of doxycycline administration. The right column shows ultrasound images of tumors containing mCherry-HEK cells after an additional 4 days of doxycycline administration. Difference heatmap of nonlinear signal between frame 1 and frame 4 is overlaid on a grayscale anatomical ultrasound image. Min and max on color bar represent 4000 and 40000, respectively. Scale bars represent 1 mm.

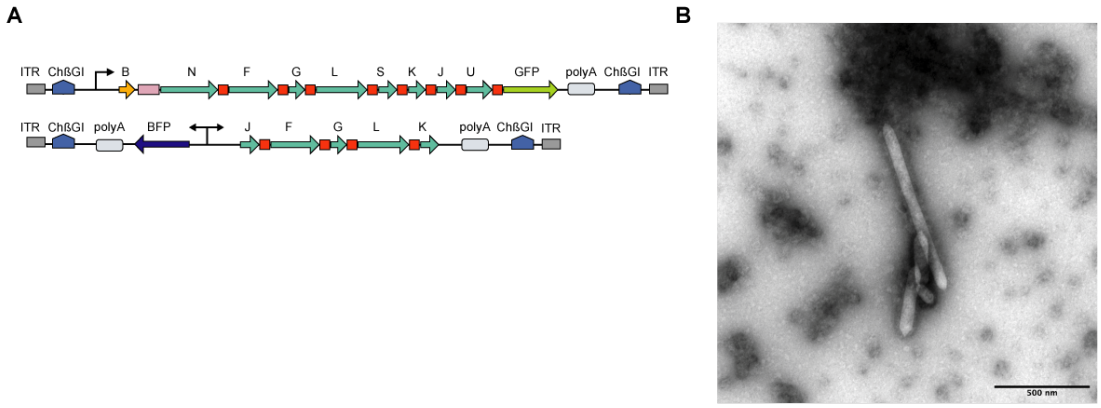

Supplementary Figure 5.13 – Consolidated mARG construct comprising 2 gene cassettes enables mammalian gas vesicle expression. (**A**) Schematic of two gene cassettes integrated to the genome of HEK293-tetON cells. In the top construct G*vpB* is separated from G*vpN* by an internal ribosome entry sequence (shown in purple). (**B**) Representative TEM image of GVs in the lysate of HEK293-tetON cells transfected with the constructs in (A) and induced with 1 µg/mL doxycycline.

Gene	GVs after N-term addition?	GVs after C-term addition?
GvpB	--	No
GvpR	Yes	Yes
GvpN	Yes	Yes
GvpF	Yes	Yes
GvpG	Yes	Yes
GvpL	Yes	Yes
GvpS	Yes	Yes
GvpK	Yes	Yes
GvpJ	Yes	Yes
GvpT	Yes	Yes
GvpU	Yes	Yes

Supplementary Table 5.1 – Tolerability of P2A peptide additions to *B. megaterium* gas vesicle genes. Each gene of the *B. megaterium* gene cluster was modified with an N-terminal proline after the start codon or with a linker and P2A peptide at the C-terminus, resulting in a total of 21 unique GV gene clusters as illustrated in Supplementary Fig. 5.2. *E. coli* were transformed with each plasmid and gas vesicles were induced for expression for a total of 22 hours and assayed for the presence of gas vesicles using TEM. The table indicates whether gas vesicles were observed by TEM. Expression and TEM imaging performed as in Farhadi *et al.* (*21*).

Collected from FACS	Formed colonies	Triple positive fluorescence	Formed GVs (TEM)	>1 GVs/cell
576	30	21	12	6

Supplementary Table 5.2 – Selection funnel for monoclonal mARG-HEK cells. The numbers indicate the number of cells or cell lines selected at each stage.

References

30. J. Schindelin *et al.*, Fiji: an open-source platform for biological-image analysis. *Nat Methods* **9**, 676-682 (2012).
31. C. Demene *et al.*, Spatiotemporal Clutter Filtering of Ultrafast Ultrasound Data Highly Increases Doppler and fUltrasound Sensitivity. *IEEE Trans Med Imaging* **34**, 2271-2285 (2015).

Chapter 6

CONCLUSIONS AND FUTURE DIRECTIONS

This thesis describes some of the initial work on the design of pulse sequences and algorithms for enhancing the capabilities of noninvasive ultrasound imaging of gas vesicles and acoustic reporter genes. Chapter 2 introduced xAM, a pulse sequence that achieves high specificity imaging of harmonic gas vesicles by using the transient interaction of axisymmetric, cross-propagating plane waves to eliminate artifacts caused by nonlinear wave propagation. Chapter 3 presented an application of xAM to the visualization of the dynamic biomolecular process of proteolytic enzyme activity deep inside living animals. Chapter 4 introduced BURST, an imaging paradigm that improves the sensitivity of gas vesicle imaging by a factor of at least 1000 and enables the detection of single ARG-expressing cells as well as single gas vesicles in liquid suspension by inducing and capturing transient cavitation events following gas vesicle collapse and unmixing their temporal dynamics from background signal. Chapter 5 described the application of an early implementation of BURST to visualize the dynamics of expression of the first mammalian acoustic reporter genes and to image vascularization patterns in tumors expressing mammalian acoustic reporter genes. Currently, out of all known methods for ultrasound imaging of gas vesicles, xAM and BURST provide the best specificity and sensitivity, two metrics fundamental to the quality of all forms of measurement. As such, the number of applications of these methods can be expected to increase in proportion to the number of research directions utilizing gas vesicles and acoustic reporter genes.

Nevertheless, a number of limitations remain for both xAM and BURST, some of which can be obviated with improvements in hardware, others of which may be overcome with advances in gas vesicle and acoustic reporter gene engineering, and still others that will require entirely novel imaging approaches to surpass. Several of these limitations, along with possible future directions for addressing them, are discussed below.

6.1 Future Directions for xAM

The most pressing limitation of xAM is the low framerate of live imaging in its current implementation, which is typically 1 to 5 Hz. While this framerate is sufficient for stationary targets, it makes *in vivo* imaging difficult in the presence of tissue motion. This limitation arises because xAM image lines are not formed along the propagation direction of the ultrasonic waves, but along the line at which the two cross-propagating plane-waves intersect. This makes xAM incompatible with the proprietary pixel-oriented

software beamforming algorithm implemented on Verasonics ultrasound systems[1] that normally enables reconstruction at high frame rates. Without the bottleneck of software beamforming, xAM could in principle be used to acquire a 10-mm-deep image with 64 ray lines at 400 Hz. Consequently, addressing this limitation is largely an engineering challenge, albeit one that requires some effort at algorithmic optimization in a compiled programming language and knowledge of parallel computing.

Increasing the framerate of xAM by two orders of magnitude in this way would make *in vivo* imaging more robust and also create opportunities for experimenting with in-software compounding methods to improve CNR and artifact cancellation. One interesting idea would be to use non-axisymmetric plane waves that cross-propagate at different angles and combine the resulting echoes similar to compounding with tilted plane waves. Of course, this would necessitate a new beamforming strategy because the ray lines would no longer be perpendicular to the axis of the transducer array.

Once the beamforming bottleneck is addressed, the framerate of xAM will be limited by the fact that it forms images on the basis of ray lines from separates sets of transmits. To match the frame rates used in ultrafast doppler[2] and super-localization[3] applications, the xAM framerate would need to be improved by a further two orders of magnitude. One way to do this would be to use a planar ultrasound array and transmit an X-wave on each row of the array simultaneously.

Another limitation of xAM is its non-adjustable depth of field for a given aperture and cross-propagation angle, given by the following equation,

$$\frac{D}{2}\cot\theta$$

where D is the aperture size. At the empirically optimal angle of 19.5° and a 6.5 mm aperture, this translates to a maximum depth of 9.1 mm, though intensity of the beam begins to fade around 7 mm. This is 50% to 90% of the maximum attenuation-limited depth for *in vivo* imaging with 18 MHz ultrasound, which is typically 10 to 15 mm. Because both probe element spacing and the attenuation-limited depth increase with ultrasound frequency, the portion of the potential depth of field compromised by this limitation should be roughly constant for different probes. The only way to increase the maximum depth for a given angle is to increase the programmed aperture, which reduces the lateral field of view. To circumvent this trade-off, a linear array with a larger number of elements could be used.

6.3 Future Directions for BURST

A notable limitation of BURST is its sensitivity to motion of the imaging target, which required a modified pulse sequence and additional post-processing steps to remove motion artifacts for *in vivo* experiments, as described in Section 4.5.6. While the BURST frames are acquired at a reasonable rate of 111 Hz, the pixel-

based template unmixing algorithm assumes that no tissue displacement larger than 300 µm occurs over the full series of frames, which requires a much higher framerate than simply matching the Nyquist frequency of tissue motion. One strategy to address this would be to apply tissue motion corrections methods developed for ultrasound super-localization, which also relies on a stack of frames and is susceptible to motion artifacts[4,5]. Another interesting approach would be to use multi-pixel signal templates capable of unmixing signals based on spatial characteristics, allowing templates to correspond to patterns of tissue motion as well other spurious signal sources such as bubbles. However, this would increase complexity and would likely require learning templates from *in vivo* data, which may not be available in sufficient quantities to prevent overfitting. Alternatively, the framerate could be increased by two orders of magnitude by applying the sequence of voltages to each ray line at a time, rather than transmitting every ray line at each voltage value. Of course, this would also increase the time between ray line acquisitions by two orders of magnitude, which could lead to visible discontinuities in BURST signal between ray lines, but the threshold for tolerable motion levels would be much higher for this effect, and it would likely be preferable to the false positive BURST signal caused by motion artifacts in the original sequence. However, this method could reduce total BURST signal by collapsing gas vesicles adjacent to the current ray line and allowing the liberated nanobubbles to dissolve before being insonified.

Another potential limitation of BURST could be specific frequency requirements, though more experiments are needed to determine the effects of frequency on BURST signal. Using our L10-4v probe, we found that BURST was significantly more effective at transmit waveform frequencies in the range of 5 MHz to 7 MHz (unpublished data), but this may simply be due to the probe's center frequency of 6 MHz as these experiments did not control for pressure. More research is needed to determine both the effect of transmitted waveform frequency on BURST signal intensity as well as the full frequency spectrum of received BURST signal.

A third limitation of BURST is its narrow axial field of view, which is restricted to 2 mm, less than 10% of the available field of view, due to the need for highly focused beams to achieve the required pressure levels. The axial field of view is also limited to half the width of the probe due to the need for a large aperture to produced sharply focused beams, though this is comparable to the lateral field of view of xAM.

All three of these limitations could be overcome by developing a custom transducer capable of achieving peak positive pressures in the range of 3.4 MPa to 4.3 MPa throughout the image plane using only plane waves. This would allow each BURST frame to be acquired in a single transmit, obviating the need for focused beams and allowing for ultrafast frame rates. This could also allow the receive function to be performed with a separate probe, whose specifications would no longer be constrained by the frequency and peak pressure requirements of the transmit waveform. Moreover, 100% of the receiving probe's axial and lateral fields of view could be utilized.

Of course, the primary limitation of BURST is the irreversible collapse of gas vesicles required to generate the strong signal responsible for this method's dramatically increased sensitivity. This limits the potential of BURST to image targets over time. Unfortunately, this is a fundamental limitation of BURST, which generates signal through the transient cavitation of nanobubbles liberated from collapsed gas vesicles. However, it may still be possible to apply BURST to enable high sensitivity in multiplexed gas vesicle imaging[6] and in the acoustic biosensor imaging described in Chapter 3 through the development of gas vesicles with higher collapse pressure. As shown in Supplementary Figure 4.1, BURST+ requires a peak positive pressure of at least 3.4 MPa to generate detectable collapse signal. Because the gas vesicles used in that experiment have an acoustic collapse midpoint of 2.6 MPa[7], this result suggests that, at least at a frequency of 6 MHz, a peak positive pressure greater than 3.4 MPa may be required to initiate the transient cavitation events responsible for strong BURST+ signal and that the gas vesicle collapse threshold may not be the limiting factor.

If this is the case, new gas vesicle variants with acoustic collapse thresholds above 3.4 MPa could enable BURST to be used for ultrasensitive multiplexed collapse imaging. Though no gas vesicle variants with acoustic collapse thresholds in this range are currently known, the wide spread of collapse thresholds for currently-characterized gas vesicles over an order of magnitude[8] suggests that such variants could be produced through directed evolution. Noting that a given reporter gene variant typically produces gas vesicles with a distribution of sizes and collapse pressures, variants with narrow distributions would be advantageous for multiplexed imaging.

A more ambitious direction would be to engineer or evolve gas vesicles whose high collapse threshold is conditional on the binding of GvpC. In Ana gas vesicles, removal of GvpC reduces the acoustic collapse midpoint by 300 kPa, which, considering the distribution of collapse thresholds for Ana gas vesicles with intact GvpC, is a shift of two standard deviations[6]. The prospects for developing a high-threshold variant with this property are less certain because the gas vesicles with the highest known collapse thresholds are small in size and do not bind with GvpC, but there is no reason to believe evolving such a variant would not be possible. If such a high-threshold, GvpC-strengthened gas vesicle were developed and engineered to have biomolecular sensing capabilities similar to those described in Chapter 3, it could enable ultrasensitive imaging of not only gene expression, but other biomolecular processes as well.

Finally, while BURST will always be a destructive imaging method, it may be possible to design a novel, non-destructive pulse sequence that still improves sensitivity by multiple orders of magnitude, as will be explored in the final section below.

6.3 Challenges and Opportunities for Novel Imaging Methods

As described above, there are several opportunities for extending the capabilities of xAM and BURST, but some limitations will require novel imaging methods to overcome. The destructive nature of BURST is one such limitation, making the development of a non-destructive method with similar sensitivity a high-impact objective. BURST is capable of detecting single gas vesicles, a surprising capability made possible by transient cavitation of nanobubbles liberated from collapsed gas vesicles. In contrast, echoes from the scattering of a sub-collapse-threshold acoustic wave on a single gas vesicle would be below the noise floor of an ultrasound probe.

One method often used to detect very weak signals buried in noise is lock-in detection[9], in which the amplitude of a sinusoidal signal confounded by noise is measured by comparison to a reference signal with the same phase and frequency. This process efficiently cancels noise by integrating only those components of the input signal with the same phase as the reference signal, such that the measurement SNR increases in direct proportion to the integration time. For comparison, SNR increases in proportion to the square root of the integration time for detection methods that are not phase-sensitive. However, lock-in detection is rarely used in contrast-enhanced ultrasound imaging because clutter signal from tissue, which does have the same phase as contrast agent signal, is a much stronger source of confounding than noise, even in AM and other contrast imaging modes.

Dual-frequency transducers have recently been used to generate echoes from contrast agents at low frequencies while recording their nonlinear echoes at frequencies several times higher[10]. Nonlinear contrast agent signal remains detectable while tissue signal is strongly attenuated at the higher-order harmonics. In a study with microbubbles, a CTR of 25.5 was achieved by transmitting at 1.5 MHz center frequency with a peak acoustic pressure of 1600 kPa and receiving at 10 MHz center frequency[11]. Because tissue nonlinearity increases with pressure, we could expect to achieve significantly higher CTR by using 350 kPa to induce buckling in stripped Ana gas vesicles. Because dual-frequency imaging experiments have only been performed with receive-to-transmit center frequency ratios at which contrast agent signal remains above the noise floor, it may be possible to reduce tissue signal further relative to contrast agent signal by using even higher center frequency ratios. Combining dual-frequency transducers with gas vesicles and lock-in detection could therefore be a promising direction for achieving non-destructive ultrasensitive imaging, especially in areas of the body with low scattering, such as the brain and blood vessels.

Ultimately, as innovations in imaging methods are iteratively developed alongside innovations in gas vesicle and acoustic reporter gene engineering, I anticipate that many of the remaining barriers to robust noninvasive imaging of cellular function will buckle and collapse.

References

1. Daigle, R. E. Ultrasound imaging system with pixel oriented processing. (2012).
2. Errico, C. *et al.* Transcranial functional ultrasound imaging of the brain using microbubble-enhanced ultrasensitive Doppler. *NeuroImage* **124**, 752–761 (2016).
3. Errico, C. *et al.* Ultrafast ultrasound localization microscopy for deep super-resolution vascular imaging. *Nature* **527**, 499–502 (2015).
4. Harput, S. *et al.* Two-Stage Motion Correction for Super-Resolution Ultrasound Imaging in Human Lower Limb. *IEEE Transactions on Ultrasonics, Ferroelectrics, and Frequency Control* **65**, 803–814 (2018).
5. Hingot, V., Errico, C., Tanter, M. & Couture, O. Subwavelength motion-correction for ultrafast ultrasound localization microscopy. *Ultrasonics* **77**, 17–21 (2017).
6. Lakshmanan, A. *et al.* Molecular Engineering of Acoustic Protein Nanostructures. *ACS Nano* **10**, 7314–7322 (2016).
7. Bourdeau, R. W. *et al.* Acoustic reporter genes for noninvasive imaging of microorganisms in mammalian hosts. *Nature* **553**, 86–90 (2018).
8. Lakshmanan, A. *et al.* Preparation of biogenic gas vesicle nanostructures for use as contrast agents for ultrasound and MRI. *Nature Protocols* **12**, 2050–2080 (2017).
9. Scofield, J. H. Frequency-domain description of a lock-in amplifier. *American Journal of Physics* **62**, 129–133 (1994).
10. Martin, K. H. *et al.* Dual-Frequency Piezoelectric Transducers for Contrast Enhanced Ultrasound Imaging. *Sensors* **14**, 20825–20842 (2014).
11. Lindsey, B. D., Rojas, J. D., Martin, K. H., Shelton, S. E. & Dayton, P. A. Acoustic characterization of contrast-to-tissue ratio and axial resolution for dual-frequency contrast-specific acoustic angiography imaging. *IEEE Transactions on Ultrasonics, Ferroelectrics, and Frequency Control* **61**, 1668–1687 (2014).